

MEASUREMENT AND COMPUTATION OF LOSSES FROM A
TRANSONIC TURBINE VANE CASCADE

MEASURE ET ÉVALUATION NUMÉRIQUE DE LA PERTE D'UNE
GRILLE D'AUBE FIXE DE TURBINE EN RÉGIME TRANSSONIQUE

A Thesis Submitted

to the Division of Graduate Studies of the Royal Military College of Canada

by

Stephen Arthur Andrews, B.Sc.

In Partial Fulfillment of the Requirements for the Degree of

Master of Applied Science

11 May, 2009

© This thesis may be used within the Department of National
Defence but copyright for open publication remains the property of the author.

**ROYAL MILITARY COLLEGE OF CANADA
COLLÈGE MILITAIRE ROYAL DU CANADA**

**DIVISION OF GRADUATE STUDIES AND RESEARCH
DIVISION DES ÉTUDES SUPÉRIEURES ET DE LA RECHERCHE**

This is to certify that the thesis prepared by / Ceci certifie que la thèse rédigée par

STEPHEN ARTHUR ANDREWS

entitled / intitulée

**MEASUREMENT AND COMPUTATION OF LOSSES FROM A
TRANSONIC TURBINE VANE CASCADE**

complies with the Royal Military College of Canada regulations and that it meets the accepted standards of the Graduate School with respect to quality, and, in the case of a doctoral thesis, originality, / satisfait aux règlements du Collège militaire royal du Canada et qu'elle respecte les normes acceptées par la Faculté des études supérieures quant à la qualité et, dans le cas d'une thèse de doctorat, l'originalité,

for the degree of / pour le diplôme de

MASTER OF APPLIED SCIENCE

Signed by the final examining committee:

Signé par les membres du comité examinateur de la soutenance de thèse :

_____, Chair / Président
Dr. Allister MacIntyre

_____, External Examiner / Examineur externe
Dr. Michael Benner

_____, Main Supervisor / Directeur de thèse principal
Dr. William D. E. Allan

Dr. Ali Mahallati, Dr. Xiaohua Wu, Dr. Emily Corcoran

Approved by the Head of Department: / Approuvé par le Directeur du Département:

_____, Date: _____
Dr. Habib Benabdallah

This thesis is not to be regarded as classified.
Cette thèse n'est pas considérée comme à publication restreinte.

Dr. William D. E. Allan

Acknowledgments

I would like to thank my two supervisors, Dr. W. Allan and Dr. A. Mahallati, both of whom taught me a lot about fluid dynamics and a little bit about life. Additionally, Dr. LaViolette has always been extremely generous in providing advice on all aspects of this project.

Additional thanks go to the excellent technicians at the National Research Council of Canada, especially Paul Hunt, Derek Winfield and Dave Carey. Their hard work and patience were invaluable to the experimental portion of this research.

Finally, thanks are due to the Gas Turbine Laboratory of the National Research Council of Canada and the Department of National Defense Aerospace Engineering Research Advisory Council for providing funding for this work.

Abstract

Andrews, Stephen Arthur. MSc. Royal Military College of Canada, 11 May, 2009.
Measurement and Computation of Losses from a Transonic Turbine Vane Cascade.
Supervised by Dr. William D. E. Allan and Dr. Ali Mahallati.

Experimental and numerical studies were performed on a cascade of first stage nozzle guide vanes operating at transonic speeds. Detailed pressure measurements on the blade surface and in the wake, as well as oil film and schlieren flow visualization were combined with computational predictions to examine the aerodynamic performance of the blades. Experimental data were collected between Mach 0.3 and 1.3, while computational predictions extended this range to Mach 1.7.

The analysis was focused on examining the behaviour of the blade losses with increasing Mach number. The losses reached a local maximum at an exit Mach number of unity and experienced a subsequent decrease or plateau with increasing Mach number. The computational results showed that this transonic loss plateau existed until the exit Mach number exceeded 1.4.

Investigations into the aerodynamic performance of the blade showed that the base pressure had a strong influence on the behaviour of the losses. At supersonic speeds, shocks and shock-boundary layer interactions were also important contributors to the loss.

Steady and unsteady computational models showed excellent qualitative and fair quantitative agreement with the experimental data. Empirical correlations for the losses under-predicted the experimental measurements.

The behaviour of the aerodynamic losses from the nozzle guide vane under investigation showed that there was a potential advantage, or at least no penalty, to operating at exit Mach numbers higher than the design value of 1.16. If the mating rotor could tolerate the increased inlet speed, this could result in an increase in stage

efficiency.

Keywords: Turbine, Stator, Transonic, Loss, Base Pressure, Shock-Boundary Layer Interaction, Wake, Experiment, Computational Fluid Dynamics

Resumé

Andrews, Stephen Arthur. MAsc. Collège militaire royal du Canada, 11 May, 2009.
Measure et évaluation numérique de la perte d'une grille d'aube fixe de turbine en régime transsonique. Thèse dirigée par Dr. William D. E. Allan

Des études expérimentales et numériques ont été réalisées sur une grille d'aube représentant les aubes fixe d'une turbine à des vitesses transsoniques. Des mesures de pression détaillées sur la surface de l'aube ainsi que dans son sillage, en plus de méthodes de visualisations comme la strioscopie et les films d'huile sont combinés avec des prédictions numériques pour examiner la performance aérodynamique des aubes. Les données expérimentales furent recueillies entre Mach 0.3 et 1.3 alors que les prédictions numériques étendent cette gamme jusqu'à Mach 1.7.

L'analyse se concentra sur la corrélation des pertes en fonction du nombre de Mach Croissant. Les pertes ont atteint un maximum at un nombre de Mach unitaire à la sortie et dépendamment de la définition de perte employée, montre une diminution suivie d'un plateau á mesure que le nombre de Mach augmente. Les résultats numériques démontrent que le plateau s'étend jusqu'à Mach 1.4

L'étude de la performance aérodynamique de l'aube montre que la pression du culot a une forte influence sur les pertes. Aux vitesses supersoniques, l'interaction entre les ondes de choc et la couche limite contribue aussi grandement aux pertes. Les pertes engendrées dans la couche limite non décollé ont très peu d'effets sur la performance de l'aube.

Les modèles numériques, stationnaire et instationnaire, montrent un excellent accord qualitatif et une bonne représentation quantitative des données expérimentales. Les corrélations empiriques pour les pertes sous-estiment les valeurs expérimentales.

La perte aérodynamique résultant des aubes étudiées montre qu'il y a un avantage ou du moins aucun désavantage à utiliser ces aubes à des nombres de Mach à la sortie

plus grandes que celle de conception soit 1.16. Si le rotor couplé a ce stator peut accepter cette vitesse accrue, ceci pourrait accroître le rendement de l'étage.

Mots clés : Turbine, Stator, pertes transsoniques, pression du culot, Interaction onde de choc couche limite, Sillage, expérience, Dynamique des fluides numériques

Table of Contents

Acknowledgments	iii
Abstract	iv
Resumé	vi
List of Tables	xi
List of Figures	xii
List of Symbols	xv
Chapter 1. Introduction	1
Chapter 2. Literature review	5
2.1. Sources of Loss in Transonic Blades	6
2.1.1. Boundary Layer Loss	6
2.1.2. Shocks and Shock Boundary Layer Interaction	8
2.1.3. Base Pressure	13
2.1.4. Trailing Edge Cooling Injection	17
2.1.5. Secondary Losses	19
2.1.6. Combined Effects	19
2.2. Overview of Previous Studies on Transonic Vanes at NRC	21
2.2.1. Highly Loaded Turbine Test Rig (HLTTR)	21
2.2.2. Transonic Planar Cascade	23
2.3. Correlations to Predict Losses	25
Chapter 3. Experimental Setup and Measurement Methods	29
3.1. Experimental Facility	29
3.1.1. Test Section	30
3.1.2. Blade Geometry	31
3.2. Instrumentation	33
3.2.1. Vane Surface Static Pressures	33
3.2.2. Sidewall Static Pressure	34
3.2.3. Transonic Flow Probe	35
3.2.4. Temperature Measurement	35
3.2.5. Pressure Measurement	35
3.2.6. Linear Traverse Mechanism	36
3.3. Data Acquisition	38
3.4. Flow Visualization	39
3.5. Finger Probe	41
3.5.1. Other designs of Transonic Pressure Probes	41

3.5.2.	Probe Design	42
3.5.3.	Calibration Method	43
3.5.4.	Calibration Results	44
3.6.	Data Reduction Procedures	51
3.6.1.	Mach Numbers	51
3.6.2.	Finger Probe Data Reduction	53
3.6.3.	Mass-Averaged Loss Calculation	54
3.6.4.	Mixed-Out Profile Loss Calculation	55
3.6.5.	Entropy Generation	56
3.7.	Flow Quality within the Transonic Linear Cascade	56
3.7.1.	Periodicity/Uniformity	57
3.7.2.	Suction Surface Static Pressures	62
3.7.3.	Flow Two Dimensionality	65
3.7.4.	Probe Interactions	68
Chapter 4.	Computational Setup	71
4.1.	Governing Equations	71
4.2.	Numerical Model	72
4.3.	Boundary Conditions	74
4.4.	Solution Procedure	74
4.5.	Mesh Quality	77
4.5.1.	Grid Independence study	77
4.6.	Post-Processing	79
Chapter 5.	Results	80
5.1.	Surface Flow Visualization	81
5.1.1.	Subsonic Flow at $Ma = 0.7$	82
5.1.2.	Transonic Flow at $Ma = 1.16$	82
5.2.	Passage Flow Visualization	84
5.2.1.	Experimental Schlieren Images	84
5.2.2.	Computed Schlieren Images	87
5.3.	Blade Surface Static Pressure Distribution	91
5.3.1.	Subsonic Flow	92
5.3.2.	Transonic Flow	96
5.4.	Base Pressure	101
5.5.	Wake Traverses	105
5.5.1.	Outlet Flow Angles	106
5.5.2.	Total Pressure	112
5.5.3.	Mass-Averaged and Mixed-Out Results	113
Chapter 6.	Discussion	116
6.1.	Transonic loss Behaviour	116
6.1.1.	Confirming the Behaviour of the Losses	116
6.1.2.	Possible Causes for the Minimum	117
6.1.3.	Shocks and Shock Boundary Layer Interaction	117
6.1.4.	Base Pressure	119

6.2. Empirical and Computational Predictions of Losses	122
6.2.1. Empirical Predictions of Total Pressure Loss Coefficient	123
6.2.2. Empirical Predictions of Base Pressure Coefficient	123
6.2.3. Predictive Ability of Computational Methods	124
Chapter 7. Conclusions and Recommendations	128
7.1. Recommendations for Future Work	129
References	132
Appendix A. Flow Quality in Transonic Calibration Tunnel	137
A.1. Calibration Tunnel Design	137
A.2. Flow Quality in the Calibration Tunnel	138
A.2.1. Test Section Mach Number	139
A.2.2. Angle History	142
Appendix B. Probe Accuracy	146
Appendix C. Uncertainty Calculations	149
C.1. Uncertainty in Measurements	149
C.2. Uncertainty in Mass Averaged Quantities	150
C.3. Uncertainty in Local Mach Number	151
C.4. Uncertainty in Axial Velocity-Density Ratio	152
Appendix D. Supplemental Figures	153
D.1. Traverses	153
D.2. Blade Loadings	156
D.3. Computed Passage Flow Visualization	161
Appendix E. MatLab Data Reduction Code	170
E.1. Mixed out Profile Loss	170
E.2. Mass Averaged Loss	171
E.3. Finger Probe Analysis	172
Appendix F. Coordinates	178
F.1. Blade Geometry	178
F.2. Static Pressure Taps	181
Curriculum Vitae	182

List of Tables

Table 3.1.	Blade geometry	33
Table 3.2.	Losses from north and south passages	62
Table 4.1.	Exit Mach numbers for CFD simulations	76
Table 4.2.	Inlet flow angles	76
Table 5.1.	Test Conditions	80
Table 5.2.	Variations of Reynolds number	81
Table 5.3.	Shock position determined by various methods	97
Table 6.1.	Comparison of experiments to computational and empirical predictions	122
Table A.1.	Effect of Different Reference Pressures	140
Table C.1.	95% confidence intervals on measured quantities	149
Table F.1.	Blade coordinates	178
Table F.2.	Blade surface pressure tap locations	181

List of Figures

Figure 1.1.	Pratt and Whitney Canada PT6A42 gas turbine[49]	2
Figure 2.1.	Effect of Reynolds number on boundary layer loss [20]	7
Figure 2.2.	Effect of pressure gradient on boundary layer loss [20]	8
Figure 2.3.	Trailing edge shock structure[22]	9
Figure 2.4.	Oblique shock-boundary layer interaction model [63]	11
Figure 2.5.	Schlieren image of shock boundary layer interaction [61]	12
Figure 2.6.	Sieverding correlation	16
Figure 2.7.	Loss breakdown by source	20
Figure 2.8.	Transonic loss behavior	22
Figure 2.9.	Previous data from the transonic linear cascade [10]	25
Figure 3.1.	Layout of a generic linear cascade	29
Figure 3.2.	Overall view of the transonic linear cascade	30
Figure 3.3.	Blade geometry	32
Figure 3.4.	Static tap locations	34
Figure 3.5.	Data acquisition system	36
Figure 3.6.	Photograph of linear traverse mechanism	37
Figure 3.7.	Method of alignment of transonic flow probe	38
Figure 3.8.	Procedure for applying oil-pigment mixture to blades	40
Figure 3.9.	A view of the NRC finger probe	42
Figure 3.10.	Plot of calibration coefficients (before cascade tests)	45
Figure 3.11.	Plot of calibration coefficients (after cascade tests)	46
Figure 3.12.	Variations in K_ϕ between calibrations	47
Figure 3.13.	Static probe behaviour at zero flow angle	48
Figure 3.14.	Shock attachment Mach number	49
Figure 3.15.	Mach number, no probe	53
Figure 3.16.	Mach number, with probe	53
Figure 3.17.	Inlet sidewall static pressure measurements	59
Figure 3.18.	Midspan inlet traverses at $Ma = 1.16$	60
Figure 3.19.	Exit sidewall dynamic pressure coefficients	61
Figure 3.20.	Mid-passage Traverses with optimal tailboard positions	63
Figure 3.21.	Difference in suction surface static pressures at $Ma = 1.16$	64
Figure 3.22.	Blade surface flow pattern at $Ma = 0.7$	66
Figure 3.23.	Axial Velocity-Density Ratio changes with Mach number	67
Figure 3.24.	Effect of probe position on surface Mach number distributions	69
Figure 3.25.	Effect of probe position on cascade Mach number	70
Figure 4.1.	Computational domain	75
Figure 4.2.	Computational mesh	78

Figure 5.1.	Oil-film flow visualization results	83
Figure 5.2.	Vortex observed at Mach 1.16	84
Figure 5.3.	Experimental schlieren images	86
Figure 5.4.	Computed passage flow field at $Ma = 0.70$	89
Figure 5.5.	Computed passage flow field at $Ma = 1.16$	90
Figure 5.6.	Detailed view of Total Gradient at the Passage Throat for $Ma =$ 1.16	91
Figure 5.7.	Local Mach numbers for subsonic flow	93
Figure 5.8.	Measured and predicted surface Mach number at $Ma = 0.7$	94
Figure 5.9.	Local slope of suction surface	95
Figure 5.10.	Local Mach numbers for transonic flow	97
Figure 5.11.	Measured and predicted surface Mach number at $Ma = 1.0- 1.31$	99
Figure 5.12.	Detail of Figure 5.11	100
Figure 5.13.	Base pressure coefficient as measured and computed at various Mach numbers	102
Figure 5.14.	Base pressure history over time for unsteady simulations	104
Figure 5.15.	Comparison of Sieverding correlation to experimental and compu- tational results	105
Figure 5.16.	Measured and computed Wake flowfield for $Ma = 0.30$	107
Figure 5.17.	Measured and computed wake flowfield for $Ma = 0.70$	108
Figure 5.18.	Measured and computed wake flowfield for $Ma = 1.16$	109
Figure 5.19.	Effect of Mach number on mixed out flow angle	110
Figure 5.20.	Graphical determination of the exit metal angle	111
Figure 5.21.	Blade performance	114
Figure 6.1.	Gerrard[28] model of vortex formation.	121
Figure 6.2.	Comparison of experimental and computed normalized total pres- sure loss	126
Figure A.1.	Schematic of the NRC transonic probe calibration tunnel	137
Figure A.2.	Finger probe installed in traverse mechanism	138
Figure A.3.	Layout of static pressure taps on calibration tunnel endwall	140
Figure A.4.	Static pressure distribution on calibration tunnel endwalls	141
Figure A.5.	Effect of probe angle on tunnel Mach number	143
Figure A.6.	Effect of probe angle on tunnel Mach number	145
Figure B.1.	Validation using calibration data	147
Figure B.2.	Pre-traverse calibration validation using new data	148
Figure D.1.	Experimental and computed wake flowfield for $Ma = 1.0$	154
Figure D.2.	Experimental and computed wake flowfield for $Ma = 1.31$	155
Figure D.3.	Measured and predicted surface Mach number at $Ma = 0.3$	157
Figure D.4.	Measured and predicted surface Mach number at $Ma = 0.5$	158
Figure D.5.	Measured and predicted surface Mach number at $Ma = 0.9$	159
Figure D.6.	Measured and predicted surface Mach number at $Ma = 1.4$	160
Figure D.7.	Computed steady passage flow field at $Ma = 0.3$	161
Figure D.8.	Computed steady passage flow field at $Ma = 0.5$	162

Figure D.9. Computed steady passage flow field at $Ma = 0.9$	163
Figure D.10. Computed steady passage flow field at $Ma = 1.00$	164
Figure D.11. Computed steady passage flow field at $Ma = 1.31$	165
Figure D.12. Computed steady passage flow field at $Ma = 1.4$	166
Figure D.13. Computed steady passage flow field at $Ma = 1.5$	167
Figure D.14. Computed steady passage flow field at $Ma = 1.6$	168
Figure D.15. Computed steady passage flow field at $Ma = 1.7$	169

List of Symbols

Latin Symbols

A	Passage area	[m]
a	Local speed of sound	[m/s]
C_x	Axial chord	[m]
C	True chord	[m]
e	Radius of curvature	[m]
e_o	Internal energy	[kJ]
f	Vortex shedding frequency	[Hz]
ht	Span	[m]
h	Enthalpy	[kJ/kg]
K	Calibration coefficient	[-]
k	Turbulent kinetic energy	[kJ/kg]
\dot{m}	Mass flow	[kg/s]
n	Generic counter	[-]
o	Throat opening	[m]
P	Pressure	[Pa]
R	Universal gas constant	[kJ/kgK]
s	Pitch or Enthalpy	[m or kJ/kgK]
T	Temperature	[K]
t	Time	[s]
u	Velocity	[m/s]
x	Generic spatial position	[m]
y	Pitchwise position	[m]

Greek Symbols

α	Flow angle	[°]
α_g	Gauging angle	[°]
β	Metal angle	[°]
γ	Specific heat ratio	[-]
Δ	Discrete change in a property	[-]
δ	Deviation angle	[°]
δ_{te}	Trailing edge wedge angle	[°]
ϵ	Angle of curvature	[°]
ν	Kinematic viscosity	[m ² /s]
μ	Dynamic viscosity	[kg/m s]
ω	Specific turbulence dissipation rate	[-]
ϕ	Incidence angle on probe	[°]
ϕ_{te}	Trailing edge diameter	[m]

ψ	Generic flow property	NA
ρ	Density	[kg/m ³]
η	Efficiency	[-]
ι	Incidence angle	[°]
τ	Reynolds stress	[kPa]
ζ	Entropy generation coefficient	[-]
ζ_{st}	Stagger angle	[°]

Subscripts

1	Value at the inlet
2	Value at the exit
<i>Amecke</i>	Value according to Amecke and Šafařík
<i>b</i>	Value at the trailing edge
<i>c</i>	Value measured at center pressure port
<i>char</i>	Characteristic value
<i>i</i>	Local value
<i>L</i>	Value measured at left pressure port
<i>m</i>	Value at the mixed-out plane
<i>o</i>	Stagnation value
<i>R</i>	Value measured at right pressure port
<i>s</i>	Static value
<i>st</i>	Value measured at static pressure port

Superscripts

*	Value at the throat
---	---------------------

Dimensionless Groups

Cq	Dynamic pressure coefficient	Equation 3.17
Cd	Boundary layer loss coefficient	
Cp_b	Base pressure coefficient	Equation 2.5
Ma	Mach number	Equation 3.9
Re	Reynolds number	Equation 5.1
Su	Strouhal number	Equation 5.2
Y_t	Total pressure loss coefficient	Equation 2.3

Chapter 1

Introduction

Gas turbines are a major source of power for both propulsion in the air and at sea and for the generation of electricity on land. In these varied roles, gas turbines consume a significant fraction of the world's hydrocarbons. For this reason, an improvement in the efficiency of a gas turbine component, which may be trivial in other applications, can lead to an appreciable fuel saving over the life of the engine.

Essentially, a gas turbine consists of three core components: compressor, combustion chamber and turbine. The compressor uses part of the power generated by the turbine to compress the air. The combustion chamber adds additional internal energy to the flow before it is expanded through the turbine to produce the power required by the compressor. After the turbine, the remaining energy in the flow can be used to power an additional turbine or the flow can be expanded through a nozzle to produce thrust. A gas turbine, representative of an engine for a light aircraft or helicopter, is shown in Figure 1.1.

Most axial turbine stages consist of a pair of blades. The first set of blades, called stators, nozzles or vanes, accelerates and turns the flow. This imparts significant angular momentum to the flow before it enters the second set of blades, known as the rotor. The large change in angular momentum across the rotor is used to produce useful work.

The overall amount of energy within the fluid at any point in a turbine is often quantified in terms of total enthalpy. This measure combines all forms of available energy in the fluid; pressure, internal and kinetic, into one quantity. The work extracted by a turbine can be measured as the difference in total enthalpy between the stator inlet and rotor exit. Thus, the efficiency of a turbine is defined as the amount of work extracted from the fluid compared to the amount of work which could have been extracted for the same drop in total pressure by an adiabatic, isentropic process.

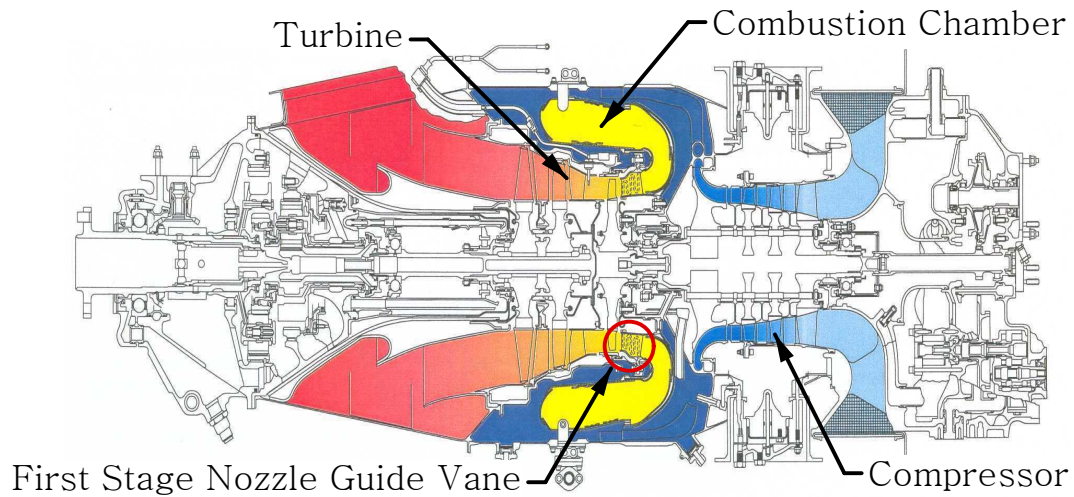


Figure 1.1: Pratt and Whitney Canada PT6A42 gas turbine[49]

Turbine blades are designed to operate most efficiently at specific flow conditions. However, most gas turbines, especially those used for air and sea transportation, must operate at a variety of power settings which can change the Reynolds number, Mach number and incidence angle on the blades. The performance of first stage nozzle guide vanes is most sensitive to changes in the exit Mach number. Therefore, the present research set out to examine how variations of the exit Mach number from design conditions affected the losses generated by the vanes.

A series of experimental investigations in a linear cascade were performed on a midspan profile from a first stage nozzle guide vane of a high pressure turbine. Though the real flow through most high pressure turbine stages is a three-dimensional phenomenon, the flow conditions within a linear cascade can come close to replicating the flow which exists at the mid-span of a real blade. In order for the cascade to model accurately the midspan flow within the engine, the flow within each passage must be similar to replicate the infinite row of blades present in an annular turbine stage. Additionally, the midspan flow in both the engine and cascade must be primarily two-dimensional. Through careful design and testing these flow conditions can be achieved. As such, for decades, linear cascades have been used extensively in the design of turbomachinery blading.

The experimental results were supplemented by computational simulations of the same flow. Commercially available computational fluid dynamics software, *Fluent 6.3*, was used to perform both steady state and time-dependent simulations.

Typically, measurements in a cascade are performed in two planes; at the inlet and at the exit of the blade row. Often, information at the exit plane is represented as values which would exist at a theoretical *mixed-out* plane. This plane would be located at some infinite distance downstream of the cascade where the inhomogeneous flow present at the exit plane has completely mixed out into a homogeneous flow.

Flow conditions at the exit plane were measured using a three-hole pressure probe, designed for use in transonic flows and calibrated between Mach 0.1 and Mach 1.2. The experimental measurements were performed between Mach 0.3 and Mach 1.3. Computational simulations were carried out up to Mach 1.7. In addition to the traverses at the exit plane, the surface static pressures on the blade were measured and oil film and schlieren photography were employed to visualize the flow.

The present study used these detailed experimental methods to explore the effect of varying exit Mach numbers on the magnitudes of the losses generated in a linear cascade of first stage nozzle guide vanes. In addition to the magnitude of the losses, the local flow features which caused these losses were identified. Comparison of the computational predictions to the experimental results allowed certain features of the flow to be described in greater detail. Additionally, the computational results showed the current ability of commercial codes to predict the behaviour of transonic flows through cascades. Empirical correlations for the total pressure loss and base pressure were compared to the experimental data to examine their applicability to transonic flows.

This thesis is divided into seven chapters. Chapter two will provide information on the present understanding of loss generation from turbine vanes. The experimental techniques and data reduction methods will be introduced in the third chapter, followed by a discussion of the computational methods in chapter four. The results from each of the various tests performed on the cascade will be discussed in detail in chapter five. Chapter six will bring together both the experimental and compu-

tational results to describe the mechanisms responsible for the losses produced by the blading. Chapter seven will summarize all the findings and make recommendations for improvements in the experimental and computational methods as well as suggesting directions for future work.

Chapter 2

Literature review

This chapter presents an overview of the previous literature, both experimental and computational, that is related to losses in transonic cascades. The main objective of the current work was to examine the magnitude and sources of loss within a cascade of transonic turbine vanes. The experiments were performed in a linear cascade which has had a long history of use examining various phenomena encountered in transonic turbines. As such, this literature review will first examine the sources of losses within a turbine blade passage, making reference to the many experiments performed on transonic blading in the past. Subsequently, the relevant experiments performed on transonic turbine blades at the National Research Council of Canada will be examined in detail.

The stated objective of this work was to measure aerodynamic losses, which are typically meant as any departure from the behaviour which would be observed in an isentropic flow. Aerodynamic losses occur when the kinetic or pressure energy of the flow is converted into internal energy through an irreversible process. In an adiabatic process, such as expansion through a turbine, entropy production is a direct measure of irreversibilities, or losses. In his thorough review of the sources of losses in turbomachines, Denton [20] argued for losses to be defined as the generation of entropy. He noted that a thermodynamic property such as entropy or enthalpy is a more useful design tool as it relates directly to the efficiency of the blade row.

For adiabatic flow, the generation of entropy can be expressed using Equation 2.1 [20]. Knowing this, the entropy production coefficient, ζ , could be calculated according to Equation 2.2 [20].

$$\Delta s = -R \ln \left(\frac{P_{o2}}{P_{o1}} \right) \quad (2.1)$$

$$\zeta = \frac{T_2 \Delta s}{h_{o2} - h_2} \quad (2.2)$$

However, Denton's advocacy of the use of entropy generation to track losses has failed to deter most researchers from the much more common approach of using total pressure deficit to quantify losses. The most popular expression of total pressure losses normalizes the difference between a characteristic inlet and exit total pressures by the exit dynamic pressure [6]. This is expressed in Equation 2.3.

$$Y_t = \frac{(Po_1 - Po_2)}{(Po_2 - Ps_2)} \quad (2.3)$$

Unless explicitly stated otherwise, the losses in this review refer to a total pressure loss defined according to Equation 2.3.

2.1 Sources of Loss in Transonic Blades

The losses generated by a row of blades are a result of several inter-related mechanisms. Though no one mechanism exists in isolation from the others, it is necessary to discuss each separately for the sake of clarity. The four major groups of losses are: boundary layer losses, shock losses, base pressure losses and secondary flow losses.

2.1.1 Boundary Layer Loss

Boundary layer losses refers to the entropy generated within the boundary layers on the blade and is often termed skin friction drag. Additional losses can be incurred when a boundary layer separates from the surface of the blade. Though there are many blades where boundary layer separation occurs without any external influence, at the incidence angle the present work examined, only shock-induced boundary layer separation was observed. Therefore, this section will deal with the losses incurred in undisturbed boundary layers, while the effects of separation will be discussed with reference to shock-boundary layer interaction.

The discussion of losses in undisturbed boundary layers draws on the thorough review of this subject performed by Denton [20]. Denton quantified the entropy generated in boundary layers using a dissipation coefficient, C_d , *i.e.* a local rate of entropy production in the boundary layer normalized by characteristic boundary layer properties.

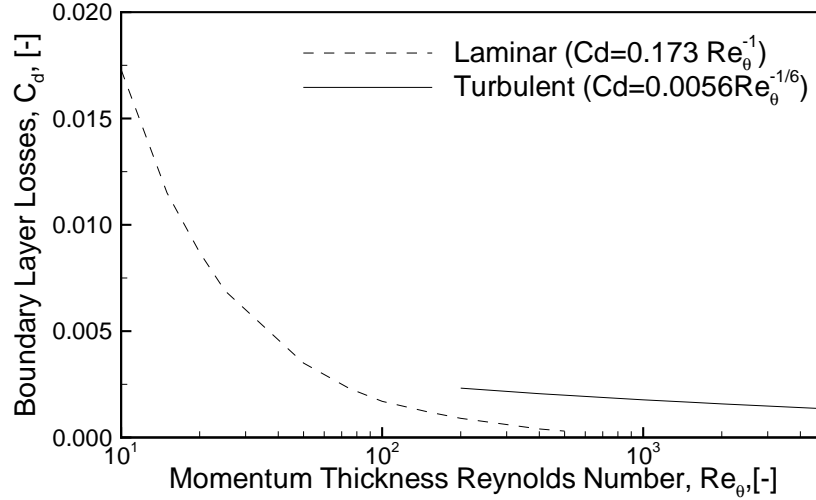


Figure 2.1: Effect of Reynolds number on boundary layer loss [20]

The effect of the momentum thickness-based Reynolds number and pressure gradients on C_d was described by Denton. The momentum thickness based Reynolds number, Re_θ , normalized the product of the momentum thickness and the velocity at the edge of the boundary layer by the local kinematic viscosity. Figure 2.1 [20] shows the effect of Re_θ on the dissipation coefficient. The figure shows how two different correlations for boundary layer loss were affected by the Reynolds number. The correlation used for laminar flow was taken from Truckenbrodt [65], and the turbulent correlation was from Schlichting [54].

Similar to the classic Moody diagram, there is a sharp decrease in viscous dissipation, quantified in this case by C_d , as the Reynolds number increases in the laminar range. This is followed by a sudden jump to a higher loss level once the transition to turbulence occurs, with an increasing turbulent Reynolds number causing a gradual reduction in the level of viscous dissipation. Therefore, there is an advantage in keeping the boundary layer laminar for as long as possible in order to benefit from the lower loss levels.

Figure 2.2 [20], shows a calculation of the effect of a favorable (accelerating) or adverse (diffusing) pressure gradient on the loss in a turbulent boundary layer. The values plotted for different pressure gradients were determined using a computational method presented by Cebeci and Carr [12] and Schlichting's [54] correlation for turbu-

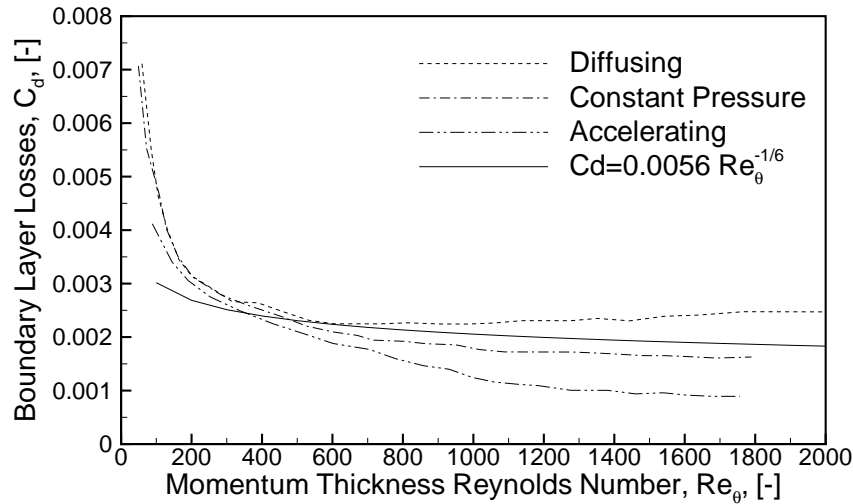


Figure 2.2: Effect of pressure gradient on boundary layer loss [20]

lent flow is also plotted for comparison. There is lower loss in an accelerating region than in a decelerating one. It also shows that the correlation given in Figure 2.1 agreed very well with the calculations past Re_θ of 500.

The discussion of skin friction losses can be greatly simplified by the observation that skin friction losses do not vary with increasing turbulent Reynolds numbers to the same degree as other sources of loss in transonic turbine blading [41]. Though the flow rate and pressure gradient do affect the loss magnitude, in many cases the variations they cause were insignificant, so that the boundary layer losses can be assumed to be constant without greatly influencing the prediction of overall loss [20]. Denton and Cumpsty [21] stated that for a turbulent boundary layer, it was appropriate to assume that C_d remained essentially constant regardless of turbulent Reynolds number variations.

2.1.2 Shocks and Shock Boundary Layer Interaction

In turbine blades with supersonic exit Mach numbers, a shock system will form at the trailing edge. The shocks originate from flow around the trailing edge which many authors, including Stanewsky [63], model as backwards-facing step. The effect of shocks is further complicated by the fact that turbine blades do not exist in isolation but are affected by the flow from adjacent blades. In the transonic regime, most blade

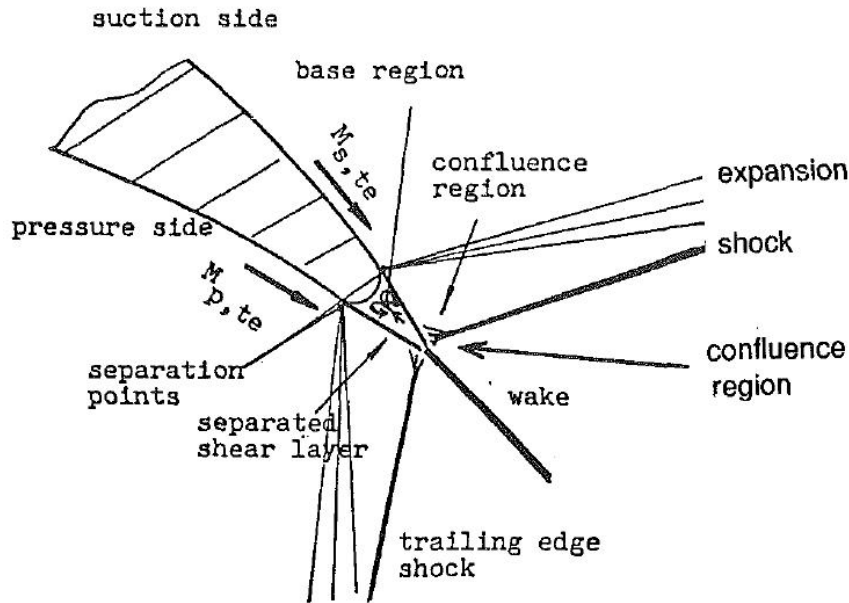


Figure 2.3: Trailing edge shock structure[22]

designs will have the pressure side trailing edge shock of an adjacent blade impinge on their suction surface [63]. The effect of the interaction between the incident shock and the boundary layer can be a major source of loss in the transonic regime [41]. This section first examines the effects of the shock wave and subsequently the effect that impinging shock waves have on the boundary layer.

The basic structure of a trailing edge shock system, illustrated by Figure 2.3, is taken from the work of Denton and Xu [22]. There is a set of expansion waves which are caused by the flow turning towards the chord line at the beginning of the trailing edge radius. The suction side and pressure side flows converge at a point downstream from the trailing edge and here the flow turns back to the downstream direction, forming an oblique shock. The position of this point of confluence is of great interest as it determines the angles through which the expansion waves and oblique shocks would turn an inviscid flow and thus also determines their strength.

Between the two converging streams lies a triangular, low velocity, region bounded by two strong shear layers. Sieverding *et al.* [58] showed that in flows approaching the limit loading, past which the entire passage is choked, there was an additional lip shock present. The lip shock was needed to adjust the pressure of flow to the value

in the base triangle region. The behavior of the flow near the trailing edge will be explored further in Section 2.1.3.

Shocks are obvious sources of entropy generation [5], and thus losses, in the flow. However the loss across an oblique shock is not as simple to calculate as that from a normal shock since the loss is dependent on both the Mach number and the angle that the shock wave makes with the flow. This angle is a function of both the Mach number and the angle through which the flow is being turned. As the Mach number increases, for a constant turning angle, the shock will tilt downstream. This shock swing behavior is predicted by oblique shock relations and was seen in a series of schlieren images taken by Graham and Kost [30] and independently by Carscallen *et al.* [10].

However, Denton [20] noted that at transonic Mach numbers, the losses induced by shock-boundary layer interaction are just as significant as the losses introduced by the shock itself. Therefore, the effect of shock-boundary layer interaction on the losses from the blade must be examined.

A thorough review of shock-boundary layer interaction in transonic flows was performed by Stanewsky in 1973 [63]. His model for the behavior of an incident oblique shock wave on a flat plate boundary layer is shown in Figure 2.4. For comparison, a real schlieren picture of a shock interacting with the boundary layer of a turbine blade, taken from Sonoda *et al.* [61], is shown in Figure 2.5.

The most notable feature of both the model and the image is the generation of multiple reflected compression shocks and expansion waves; opposed to the single reflected compression wave predicted by inviscid flow. The origin of this interesting viscous behavior is the effective displacement thickness of the separation bubble.

This behaviour is initiated by a small local separation developing due to the boundary layer's inability to remain attached across the pressure rise created by the incident trailing edge shock, which originated from the adjacent blade. This separated region cannot convect mass or momentum downstream so the flow must be diverted around it to maintain continuity. In doing this, the flow is turned towards the passage and, in the supersonic region of the boundary layer, this creates an oblique shock wave.

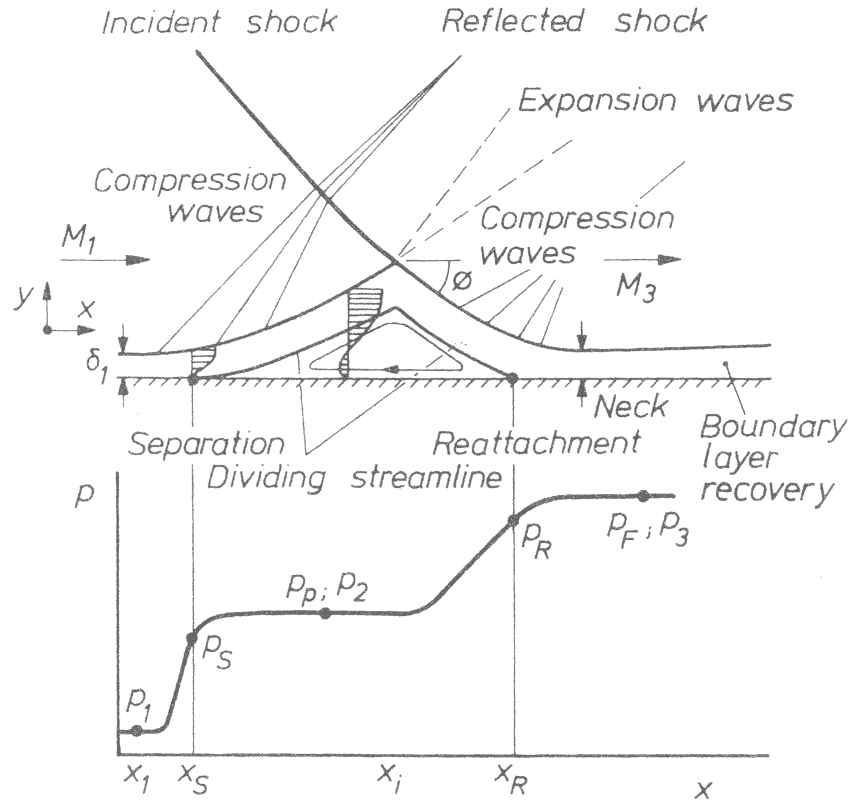


Figure 2.4: Oblique shock-boundary layer interaction model [63]

If the flow re-attaches, the separation bubble will be finite and at some point begin to shrink. As it does, the flow is turned back towards the blade and an expansion fan is created. After the separation bubble, the flow is turned back to follow the blade and a second oblique shock wave is created [63].

In the schlieren image from Sonoda *et al.* [61], Figure 2.5, this behavior can be clearly seen. The separation bubble (C) is quite large so the first oblique shock (B) is formed upstream of the incident trailing edge shock (A). The expansion fan (D) is formed at the point of maximum thickness of the separation bubble. Finally, the second oblique shock (E) occurs almost at the trailing edge where the separated flow finally reattaches.

A major assumption of the preceding discussion is that the flow would re-attach to the airfoil at some point downstream. The many test pilots who were victims of the early flight research on transonic airfoils would attest that this is not always the case. The ability of the flow to re-attach to the blade is affected strongly by

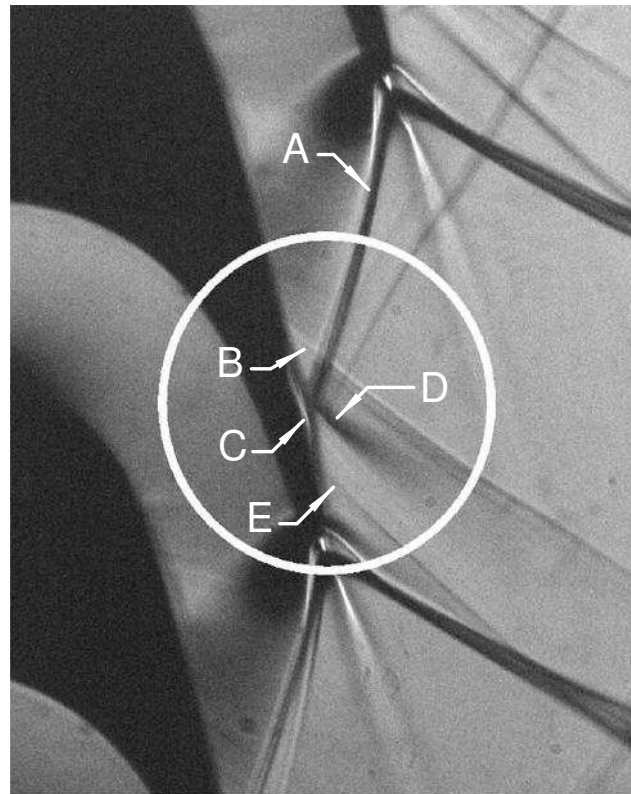


Figure 2.5: Schlieren image of shock boundary layer interaction [61]

the strength of the incident shock as well as the state of the boundary layer, (i.e. laminar, transitional or turbulent). The physics of how flow reattaches to the blade is beyond the scope of this review. In general, however, the strength of the shock directly affects the flow's ability to re-attach since it sets the pressure rise which the boundary layer must overcome. Laminar boundary layers will separate more easily than turbulent ones and will also be less likely to re-attach to the blade [63]. The degree of turbulence in the boundary layer is an important parameter in the process of flow reattachment. Turbulent mixing is the process that allows an exchange of momentum from the energetic bulk flow to low momentum shear layer, allowing it to overcome the adverse pressure gradient.

The difference that a laminar versus turbulent shock-boundary layer interaction has on a blade's performance was discussed by Sonoda *et al.* [61]. They compared one blade with laminar flow up to the shock impingement point to another which promoted

transition earlier on the blade. The ensuing reduction of the size of the separated zone was in part responsible for a 17% reduction in losses. This example shows that though Section 2.1.1 indicated that a laminar boundary layer would have a lower viscous loss, the added loss incurred by a laminar shock-boundary layer interaction may make a turbulent boundary layer preferable on areas of a blade where these interactions may occur.

One interesting feature of Figure 2.4 which has not yet been examined is the pressure distribution within the region affected by the shock. The pressure distribution shows a sharp compression at the source of the first shock wave reflection. This is followed by an isobaric region in the separation bubble which is terminated by a gradual compression due to the second reflected shock wave. Experimental pressure distributions of the shock-affected region of a turbine blade's suction surface were collected by Dietrichs *et al.* [23]. They showed that the pressure distribution seen in the flat plate model agreed well with the behaviour observed on a real airfoil.

2.1.3 Base Pressure

Shock waves are not the only source of loss originating from the trailing edge. The trailing edge of the blade is surrounded by a region of low pressure fluid. This entropy generated in this region leads to *base pressure* losses. There is an additional source of loss at the trailing edge which termed the *mixing loss*. Mixing losses are a result of the entropy generated as the shear layers from the pressure and suction surfaces meet and begin to mix out to restore a uniform velocity stream. The mixing loss is present in all airfoils and its main driving force is the difference in velocity between the pressure and suction surfaces at the trailing edge. The strong resulting velocity gradients will create irreversible losses of energy from the flow which cannot be recovered regardless of how long the flow is allowed to mix [1].

The base pressure loss is different than the mixing loss as it is possible to have a base pressure loss without the presence of a velocity gradient, such as in the flow behind a cylinder. In this case the driving force for the base pressure loss is the entropy produced by the separation of the flow on the decelerating region of the

cylinder. In turbine blades with trailing edge cooling, the thick trailing edge can act like a cylinder and the flow will separate before the pressure and suction side streams converge. Thus, the loss at the trailing edge is due to three phenomenon, shock waves, mixing loss and base pressure loss.

The importance of the base pressure loss is demonstrated by a simple model for the generation of entropy downstream of the trailing edge in incompressible flow. This model is given in Equation 2.4, whose derivation is shown in [20].

$$Y_t = -\frac{C_{pb} \phi_{te}}{o} + \frac{2\theta}{o} + \left(\frac{\delta^* + \phi_{te}}{o} \right)^2 \quad (2.4)$$

In Equation 2.4, θ was the boundary layer's momentum thickness, δ^* was the boundary layer's displacement thickness, o was the diameter of the throat and ϕ_{te} was the trailing edge diameter. C_{pb} was the base pressure coefficient, defined in Equation 2.5.

$$C_{pb} = \frac{P_b - P_2}{P_{o2} - P_2} \quad (2.5)$$

Since Equation 2.4 assumes incompressible flow it does not reflect the losses generated by trailing edge shocks, and is therefore only indicative of the base pressure and mixing losses downstream of the trailing edge.

It is important to note that in Equation 2.4 the base pressure was modified by the trailing edge to throat opening ratio, ϕ_{te}/o . Therefore, as the trailing edge diameter becomes small relative to the throat, the base pressure coefficient becomes less important. For this reason the significance of the base pressure depends on the blade geometry. Several researches have examined the contribution of base pressure to overall losses on real turbine blades. Corriveau and Sjolander [16] noted that the base pressure contributed to approximately one third of the total trailing edge loss. Using Equation 2.4, Jouini *et al.* [33] calculated that 80% of the difference in losses observed between two blade designs could be attributed to differences in the base pressure coefficient. Section 2.1.6 will show that the base pressure and mixing losses are major sources of losses at transonic speeds.

These two examples serve to show that accurate prediction of losses in a blade strongly depend on the base pressure information. Accordingly, there have been many efforts to predict the magnitude of the base pressure in transonic turbines. Sieverding *et al.* [58] proposed a correlation to which many subsequent researchers have compared their data. Sieverding's correlation relates the Mach number to the base pressure for various blade geometries. In this correlation, the base pressure was normalized by inlet total pressure, the Mach number was represented by the cascade static-to-total pressure ratio and geometry was indicated by the mean of the suction side curvature and the trailing edge wedge angle. The correlation was derived using data from a family of 16 different blades. The limitations that this blade family placed on the effective range of the correlation will be examined in Chapter 6.

Sieverding's correlation is reproduced in Figure 2.6. Jouini *et al.* [33], to the present author's knowledge, has had the most success in obtaining results which agreed with Sieverding's correlation. Xu and Denton [69] examined a family of four turbine blades and measured many different sources of loss, including the base pressure. They found that their results had very poor agreement with the Sieverding correlation. They recorded base pressures in excess of the exit static pressure while the correlation predicted the opposite trend.

Another group of researchers took a different approach to empirical modeling of the base pressure. Bölcs and Sari [7] used the method of characteristics to determine the Mach number at the point of confluence, or recompression Mach number. Section 2.1.2 showed this value was critical to the determination of the strength of the trailing edge compression and expansion waves. They then correlated the base pressure to that recompression Mach number, using a polynomial relationship. This relationship was found to be independent of the blade's geometry and the magnitude of losses in annular or linear cascades. However, this approach had the disadvantage of having to calculate the recompression Mach number using a numerical approach or the method of characteristics in order to obtain an estimate of the base pressure. The results from this correlation showed good agreement with the data of Xu and Denton [69], since the Bölcs and Sari correlation predicted base pressures higher than the

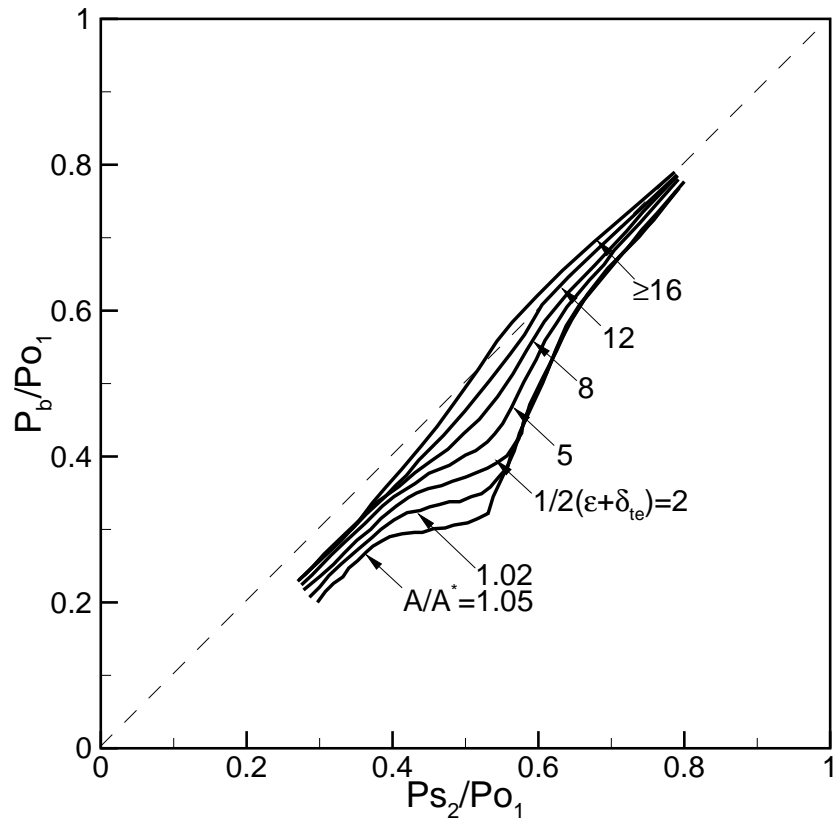


Figure 2.6: Sieverding correlation

exit static pressure.

There was a clear conflict between the correlation proposed by Sieverding *et al.* [58] and that of Bölcs and Sari [7]. The former predicted the base pressure to almost always be less than the exit static pressure, while the latter almost always predicted it to be greater. Both correlations appeared to be correct in certain circumstances as an independent experiment observed the predicted trend from each of these correlations. Jouini *et al.*'s data [33] matched the Sieverding correlations and Xu and Denton [69] agreed with Bölcs and Sari [7]. It is clear that there are some parameters that are not being accounted for in either of these correlations, making each valid for certain blade geometries and flow conditions. As there remained many gaps in the body of knowledge of base pressure, Sieverding expanded on his previous work and performed a more detailed experiment on the flow physics in the trailing edge region. The investigation of Sieverding *et al.* [57] did not lead to a clear outline of the parameters

that affected base pressure loss. However it highlighted several details of the trailing edge flow that helped to explain its behaviour.

Sieverding *et al.* [57] produced a series of continuous high speed schlieren images which were able to resolve the vortex shedding occurring at the trailing edge, which had previously been observed by Carscallen *et al.* [10]. Sieverding *et al.*'s [57] images were gathered at $Ma = 0.8$. It was observed that at this high subsonic Mach number, acoustic waves, or weak pressure discontinuities, were generated as the trailing edge shear layers oscillated, generating a vortex street. These acoustic waves were able to propagate upstream in the subsonic flow.

Sieverding *et al.* [57] instrumented the trailing edge of a turbine blade with a rotating trailing edge and recorded both the time-resolved and time-averaged base pressure around the trailing edge circle. They observed that the isobaric region recorded by Sieverding *et al.* in 1980 [58] at the trailing edge of a flat plate was not present. Rather, there was a significant pressure minimum at the center of the trailing edge arc, also known as the trailing edge tip. One reason for this difference was that the 1980 experiment was performed on a flat plate, while Sieverding *et al.*'s 2003 tests were performed on a real blade. This could affect vortex shedding as a flat plate has symmetric boundary layers while a turbine blade has significantly different boundary layers on the pressure and suction surface at the trailing edge plane. Additionally, Sieverding *et al.*'s [58] 1980 experiment was performed in supersonic flow while the 2003 tests [57] were performed at Mach 0.8. Raffel and Kost [51] also observed an isobaric region behind a flat plate at various supersonic exit Mach numbers. However, no other research has examined the pressure distribution around a real blade's trailing edge in supersonic flow conditions, or examined if the isobaric region behind a flat plate is present in subsonic flow.

2.1.4 Trailing Edge Cooling Injection

Equation 2.4 showed that the base pressure's contribution to the losses from the blade was strongly dependent on the trailing edge to throat-opening ratio. In the absence of other design constraints, it would appear preferable to have a very sharp trailing edge

to minimize base pressure losses. In fact, this is the approach taken in compressor and low pressure turbine blades. However, high pressure turbine blades operate in an environment where the mean temperature of the passage flow is in excess of that which the blade materials can safely tolerate. Extremely thin geometries are simply not practical since the extremities will adopt the temperature of the surrounding flow, some form of cooling is necessary to prevent a catastrophic failure of the blade. Almost every commonly used cooling scheme employs some form of trailing edge coolant ejection which necessitates a thicker trailing edge than is aerodynamically desirable. The current tests model the presence of such a thick trailing edge, but not the introduction of cooling air. This air would have a different stagnation temperature and pressure as well as Mach number than the main flow. This section will briefly examine the effects that coolant injection has on the blade losses in order to understand how the test profile would perform in a real engine environment.

When losses are defined in terms of thermodynamic properties the presence of trailing edge cooling can affect it in two ways. First, the introduction of low-energy fluid into a turbine stage will reduce the blade's base thermodynamic efficiency. This effect was discussed by Denton [20]. Secondly, the injection will affect the aerodynamic performance of the blade by locally disturbing the flow with high momentum jets. This topic has been examined by many authors, amongst them Reiss and Bölcs [52] who examined only coolant schemes that avoided injection at the trailing edge. They reported that trailing edge injection can increase losses while in some situations, losses could be reduced by leading edge injection.

Xu and Denton [69] noted that for the case of coolant injection from discrete ports, the base pressure was increased. Though Section 2.1.3 indicated that this effect, in isolation, would reduce the magnitude of losses, the experimental results showed that the losses increased. This was due, in part, to the additional mixing within the flow. The coolant disturbed the exit flow to the point that no region of two dimensional flow existed in the cooled blades. Reiss and Bölcs [52] examined the effect of trailing edge injection over a range of coolant mass-flow rates. They noted that there was an optimum coolant mass flow that minimized losses at a level below

the no-injection condition. However, for larger mass flow rates the losses increased, as Xu and Denton [69] observed. Reiss and Böles [52] attributed the minimum in loss to interactions between the injected coolant and the trailing edge vortex shedding. This behaviour has also been observed by Motallebi and Norbury [43], in an investigation on an isolated airfoil with trailing edge injection. Motallebi and Norbury [43] noted that when the mass flow of coolant was less than a critical value, the coolant flow would suppress the trailing edge vortex street, this had the effect of increasing the base pressure. This critical value varied with supersonic Mach number but remained around 5–7% of the inlet mass flow rate. Subsequent increases of mass flow past this critical value resulted in a reduction in base pressure. Recall from section Section 2.1.3 that a lower base pressure led to an increase in losses.

2.1.5 Secondary Losses

One final source of losses in stationary turbine blades are those which arise due to secondary flow. Secondary losses primarily result from the generation of large scale vorticity within the blade passage. In stationary blades, the two major sources of this vorticity are stagnation pressure gradients within the boundary layer and the cross-passage pressure difference. This group of losses encompasses a great many separate loss-generating mechanisms and is worthy of an entire chapter to give even a cursory outline of these complex, inter related entropy generators, (as was done in [6]). However, the present work explicitly aims not to measure the effects of secondary losses. Therefore, though it is acknowledged that this source will affect the three dimensional losses from the blading, secondary flows will have a negligible impact on the midspan losses of the vanes under investigation and thus will not be considered in the present work.

2.1.6 Combined Effects

In the introduction to this discussion of sources of loss on transonic blades, it was noted that there was significant interaction between all the loss mechanisms. This

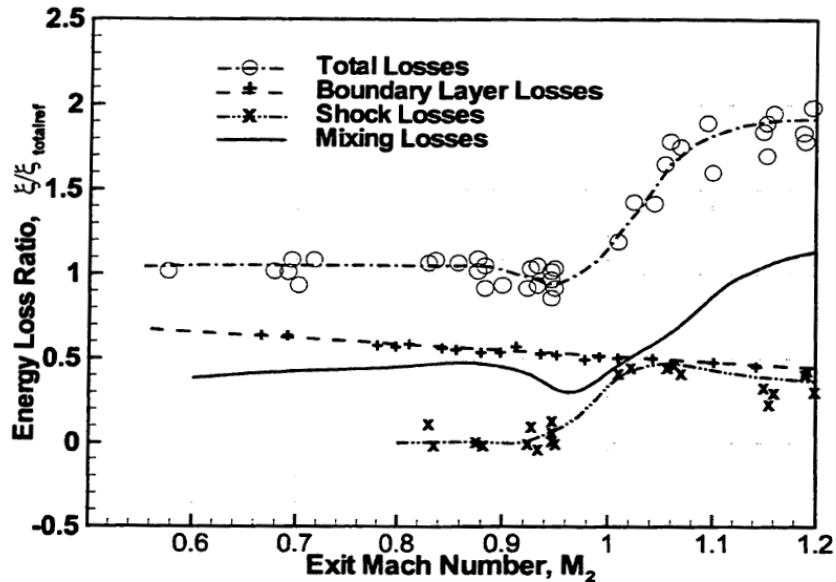


Figure 2.7: Loss breakdown by source

section will discuss the relative importance of each mechanism to the overall losses as well as show some interesting results caused by these interactions.

Figure 2.7, taken from Mee *et al.* [41], shows one interpretation of the relative importance of the various loss generating mechanisms. Mee *et al.*'s choice of loss coefficient is based on entropy generation rather than total pressure losses. Here $\xi = 1 - \eta$ where η is defined in Equation 2.6 and ξ_{ref} represents the losses at a reference condition.

$$\eta = \frac{h_{o2} - h_2}{h_{o2} - h_2 + \Delta s} \quad (2.6)$$

The boundary layer losses were calculated by measuring the momentum thickness on the pressure and suction surfaces of the blade at the start of the trailing edge radius. The shock losses were based on the total pressure measured outside the wake. Finally, the mixing losses were that part of the total losses that was neither boundary layer nor shock losses. There was one significant limitation in this approach. Mee *et al.* [41] noted that as the Mach number increased and shocks became more parallel to the flow, the trailing edge shocks crossed the measurement plane and some of the total pressure losses due to shocks was not accounted for as shock losses, but rather contributed to the mixing losses. As a result, it was unclear if the relative importance of the shock

losses truly decreased past Mach one, as Figure 2.7 shows, or if this was only due to the position of the shocks relative to the measuring plane. However, these results supported the observation alluded to in Section 2.1.1 that the changes boundary layer losses with increasing Mach number are small compared to the changes in the other sources of loss. Additionally it shows that between $Ma = 1$ and $Ma = 1.2$ there was a large ($\approx 100\%$) increase in the overall losses.

Other researchers, such as Graham and Kost [30] as well as Carscallen and Oosthuizen [11] have extended the Mach number range of their investigations past Mach 1.2 and have noted a unique trend of the losses with Mach number. Figure 2.8 from Graham and Kost's work [30], shows the losses measured on a turbine vane with a thick trailing edge, at two different incidence angles. It can be seen that the loss decreased past Mach one leading to a local minimum at Mach 1.1 before a sharp growth in losses at transonic speeds. The mechanism for this behavior will be explained more thoroughly with reference to the current results in Chapter 6. This interesting trend in transonic losses is not entirely without precedent, Anderson's discussion of supercritical airfoils [5] also showed that there was a local minimum in losses just before a steep transonic rise. However, this minimum occurred at high subsonic rather than low supersonic speeds.

2.2 Overview of Previous Studies on Transonic Vanes at NRC

2.2.1 Highly Loaded Turbine Test Rig (HLTTR)

The series of experiments which have been performed at NRC on the performance of highly loaded turbine vanes began with a project initiated by Pratt and Whitney Canada in the 1980's to investigate the performance of a single stage gas generator turbine. This research turbine was meant to be representative of the first stage of a small aircraft or helicopter engine. The turbine was designed to produce sufficient power to drive the compressor in a single turbine stage in order to reduce the weight and complexity of the engine. Additionally, it was designed to operate at a relatively low rotational speed to reduce component wear as well as the gyroscopic effect of

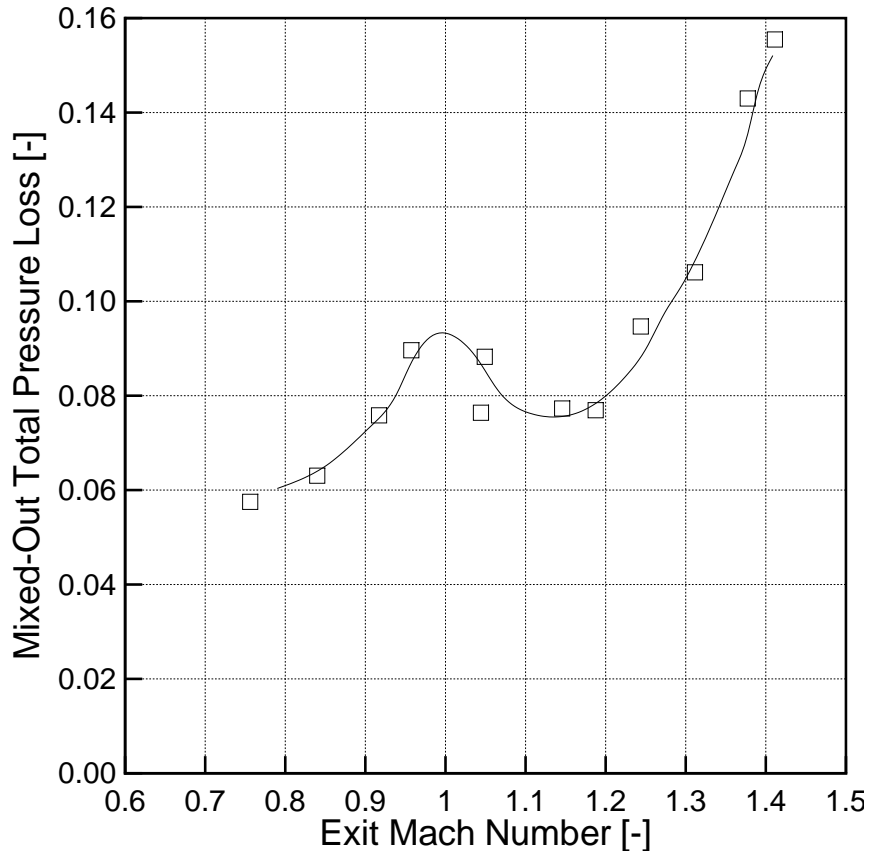


Figure 2.8: Transonic loss behavior

the engine on the handling characteristics of light helicopters. The combination of large work extraction and low rotational speed lead to very high stage loading. The original tests performed in the HLTTR were described by Moustapha *et al.* [45].

These tests took place in an annular rig with the capability to make measurements on either an annulus of stators or a complete turbine stage with a spinning rotor. The length scale of the blades was three times engine size to facilitate detailed measurements of the wake. A significant amount of effort was invested into studying the behavior of the stator in isolation. The effects of off-design Mach number, as well as endwall contouring, were explored in detail by Williamson and Moustapha [68] and Moustapha and Williamson [46]. It was found that the mid-span local isentropic Mach numbers would increase up to the passage throat and then, for nominally subsonic flow, they would decrease. In the case of nominally supersonic flow, the acceleration continued past the throat up to an certain position within the uncovered turning

region, past which the flow would decelerate. Flow visualization showed that this deceleration began at the location of impingement by an adjacent blade's trailing edge shock. The effect of Mach number on the losses was also investigated. Williamson and Moustapha [68] observed that the area-averaged value of the total pressure loss grew continuously with increasing Mach number. Another wake parameter that was investigated by Williamson and Moustapha [68] was the total temperature field. Surprisingly, it was found that there were gradients of total temperature in the wake of the blades; this was an unexpected result from an adiabatic blade passage. Since the instrumentation in the apparatus was too coarse to make any inference into the sources of these gradients, a new larger scale linear cascade was designed and commissioned.

2.2.2 Transonic Planar Cascade

The primary reason for commissioning the Transonic Linear Cascade was to investigate the causes of the total temperature gradients observed in the stator wake with the HLTTR. However, in its almost twenty years of operation at NRC, it has been used to examine many other unique phenomena in turbine vanes, especially those specific to blades with thick trailing edges.

Carscallen and Oosthuizen [11] were able to observe total temperature gradients in the vane wake and confirmed that they were not due simply to heat transfer from the cascade to the flow. In subsequent published discussions of the paper [11], the theory was proposed that the temperature non-uniformities were due to vortex shedding from the trailing edge.

Using high speed schlieren photography, these vortices were observed by Fleige [26] and Carscallen *et al.* [10] for a wide range of transonic Mach numbers. They reported that at a characteristic exit Mach number below $Ma = 0.7$ there was an intermittent von Kármán vortex street behind the blades. The vortex street was shed continuously between $Ma = 0.7$ and $Ma = 1.1$. Beyond $Ma = 1.1$, the vortex street was no longer purely of a von Kármán type, but rather took on one of several unique patterns. Similar shedding behavior was also reported in a numerical simulation of the cascade

performed by Currie and Carscallen [18].

Fleige [26, 10] further investigated the nature of the vorticity within the blade wake at $Ma = 1.16$ by taking 170 schlieren images over 35 minutes and sorting them according to the vortex pattern which was observable. He found that 44.5% of the time the wake had no discernable vortex structure. For 46.5% of the time a von Kármán type wake was present and for a final 9% of the time, a distinct yet non-von Kármán vortex street was observed. Essentially, the von Kármán vortex shedding at $Ma = 1.16$ was present 50% of the time [18].

The vortex behavior is significant when the mid-span losses and base pressure are examined. It was observed that there was a sharp drop in base pressure and a corresponding rise in mid span losses when the continuous von Kármán vortex street was present. As the von Kármán street degenerated into progressively more disordered vortex shedding patterns at high transonic Mach numbers, there was a rise in the base pressure which corresponded with a decrease in loss. This trend is shown in Figure 2.9, which reproduced the data of Carscallen *et al.* [10]. Though the preceding sections showed that there are many variables which can affect both the base pressure and midspan losses, the strong correlation between the changing modes of vortex shedding behind the blade and dramatic changes in the base pressure and loss suggests that these parameters may be strongly affected by the vortices.

It was observed that the vortex shedding at the trailing edge affected not only the total temperature but also the base pressure and loss. Therefore, this important phenomenon was investigated in more detail by Carscallen *et al.* [9] using a fast response total temperature probes. The vortex shedding was found to be occurring at 10kHz. In order to resolve the vortical structures a probe developed at Oxford University, which had a bandwidth of 87kHz, was employed. The total temperature redistribution detected by the time averaged results in [11] was observed in much greater detail. These results confirmed the theory raised by the original investigations [11], that the total temperature in the wake was redistributed by the Eckert Weis effect [9].

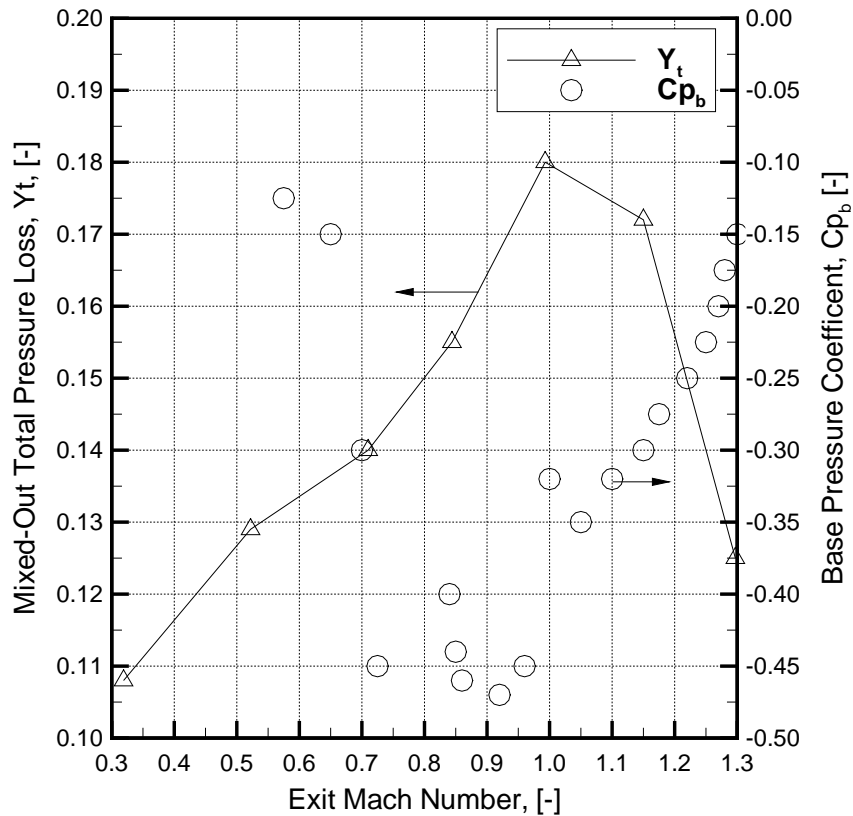


Figure 2.9: Previous data from the transonic linear cascade [10]

2.3 Correlations to Predict Losses

The preceding discussion of the sources of loss in turbine vanes demonstrated that the magnitude of the total pressure loss through a stator row is dependent on many different entropy generating mechanisms which are all inter-related to some degree. Though this complex flow has resisted any analytical solution, there are several empirical correlations in existence that aim to use the performance of previously tested blades to predict the behavior of new designs.

One of the most basic empirical loss correlations for turbines was proposed by Soderberg [24] which gave a rough estimate for the losses from both stator and rotor vanes. The design parameters which this correlation examined were the Reynolds number, the total fluid deflection within the blade, the thickness to chord ratio and the aspect ratio.

Since the Soderberg correlations was developed in the 1940's, more advanced empirical methods for predicting losses have been developed. Craig and Cox [17], developed a loss correlation for both steam and gas turbine blades which performed well over a wide range of Reynolds numbers and aspect ratios. The Craig and Cox model was updated by Chen [13] to better describe for the behaviour of steam turbine blades at transonic exit Mach numbers.

Another loss correlation was developed in the 1950's by Ainley and Mathieson [3] and has been continuously improved upon in the decades since its introduction. Dunham and Came [25] presented their work in the early 1970's which incorporated additional test data to reflect the rapid evolution in the performance of turbine blades. The next major review of the Ainley and Mathieson correlation was performed by Kacker and Okapuu [34] in the early 1980's. A more modern re-examination of this correlation was performed by Zhu and Sjolander [70] in 2005. This empirical loss correlations will be referred to as the Kacker and Okapuu (K&O) correlation, recognizing that many other authors have contributed to it.

Both the Kacker and Okapuu and Craig and Cox correlations claim to be able to predict the efficiency of *well designed* blading within $\pm 2\%$. However, the model proposed by Craig, Cox and Chen used data from both steam and gas turbines in its database of successful designs. The model developed by Ainley, Mathieson, Dunham, Came, Kacker, Okapuu, Zhu and Sjolander used only data from gas turbines. making it better suited to gas turbine applications, and is in common use in industry. For this reason, the Kacker and Okapuu loss correlation, in the form presented by Zhu and Sjolander, will be discussed in greater detail.

The method of applying the Kacker and Okapuu [34] correlation is described in by their 1982 paper [34]. Zhu and Sjolander [70] incorporated modern cascade data to adjust the correlations constants to better predict the performance of modern blading. The modifications are documented in [70]. The precise details of the correlations will not be repeated here. However, a brief discussion is necessary on the geometric and flow properties that the correlation treats as significant and what their influence is on the predicted losses.

The chosen loss correlation predicts the losses arising from several different, independent, sources and linearly combines them. The basic equation for the correlation is shown in Equation 2.7. Though determining the value of the terms on the right hand side is complex and non-linear, this equation shows how the basic correlation behaves.

$$Y_T = Y_p \times f_{Re} + Y'_{TET} + Y_s + Y_{TC} \quad (2.7)$$

Where:

- Y_p represents the profile losses. These losses are predicted based on the degree of reaction of the stage and the blade's pitch to chord ratio, exit flow angle and the inlet metal angle.
- f_{Re} modifies the profiles losses to account for Reynolds number based on the true chord and the exit plane velocity and gas properties.
- Y'_{TET} represents the trailing edge losses. This source of loss is modeled based on the trailing edge to throat-opening ratio, the exit Mach number, the amount of blade turning and the degree of blade reaction. This trailing edge modifier is solely meant to model the mixing/base pressure losses at the trailing edge, not the shock system.
- Y_s represents the secondary flow losses and is ignored for predicting the two dimensional losses at midspan.
- Y_{TC} represents the tip clearance flow losses and can be omitted for stationary blades.

For transonic flows there are two modifiers applied to the profile losses to account for compressibility effects: one modifier is meant to model the presence of shocks at the leading edge of the blade or within the passage. This modifier is strongly dependent on the inlet Mach number and is consequently very small in the current experiment. There is a second compressibility modifier which only applies to cases with supersonic exit Mach numbers and is meant to account for the presence of trailing

edge shocks in the uncovered part of the blade. The exit Mach number is the only variable that affects this modifier, and in the current experiment it is the dominant compressibility effect.

Experimental Setup and Measurement Methods

This chapter describes the experimental facility, the instrumentation and the data reduction techniques used for this investigation.

3.1 Experimental Facility

All the experiments were performed in the Transonic Linear Cascade located at the National Research Council of Canada (NRC) in Ottawa Ontario. Though Carscallen [8] described the design and commissioning of the cascade, the important details of this facility will be repeated here.

A layout of a linear cascade is shown in Figure 3.1. The coordinate system used in a cascade is also shown in this figure. In the present work, the two extremes in the pitchwise direction were labeled North and South. This convention will be used consistently throughout this work to avoid confusion when referring to pitchwise positions. Figure 3.1 also shows the location of the three measurement planes. The labeling of these planes will be as follows: the inlet plane is labeled 1, the exit plane 2 and the mixed out plane, m.

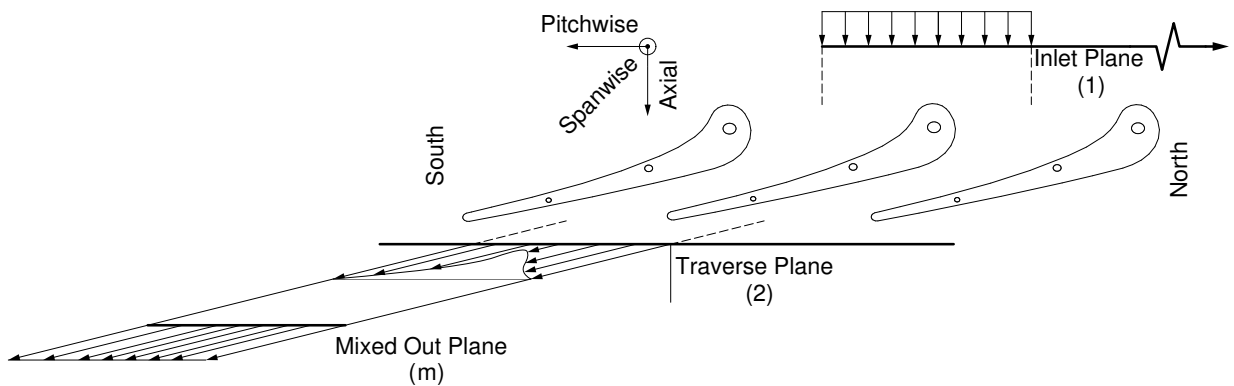


Figure 3.1: Layout of a generic linear cascade

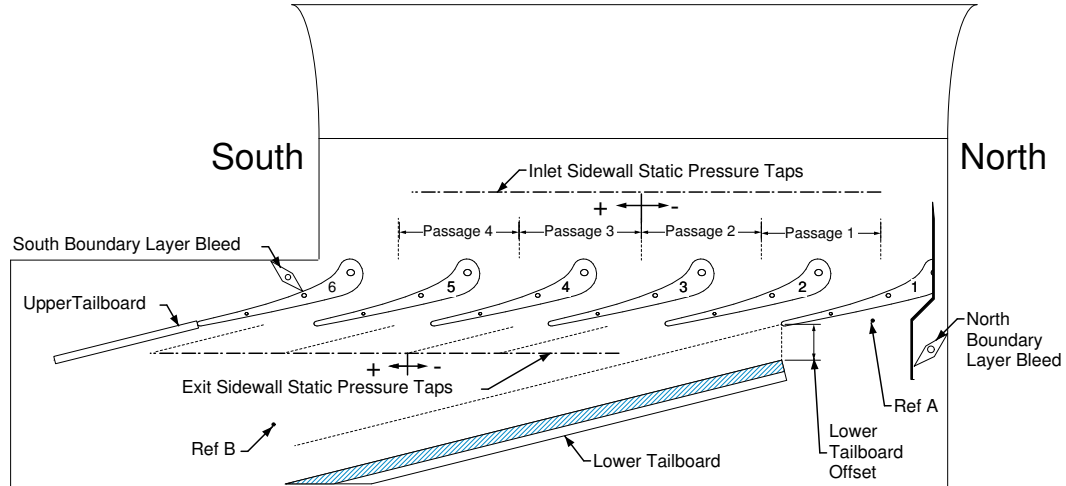


Figure 3.2: Overall view of the transonic linear cascade

Figure 3.2 shows a schematic of the transonic linear cascade. Air was drawn through the the Transonic Linear Cascade by a 2 MW Brown-Boveri exhauster, capable of delivering 4.5 kg/s of air at an absolute pressure of 50.8 mmHg at the exhauster inlet. However, the losses introduced in the ducting system between the exhauster and the cascade lead to a higher absolute pressure at the exit plane of the cascade. This caused the maximum exit Mach number from the cascade to be limited to $Ma = 1.4$.

3.1.1 Test Section

The inlet to the cascade was a bell-mouth formed by a 5 : 1 ellipse with mitered corners. Since the original intent of the cascade was to examine secondary flows within the blade passages, the cascade had a long inlet section so the sidewall boundary layers would grow to a thickness of 10% of the span by the start of the blade-row. Boundary layer bleeds were installed on the North and South side of the cascade to control the endwall boundary layers.

The cascade consisted of six blades forming five passages. The flow exiting the blade-row was guided by an upper and lower tailboard. The lower tailboard was perforated, with holes drilled perpendicular to the tailboard surface. This was intended to suppress the reflection of shock waves originating from the blade trailing edges

at supersonic speeds. The upper tailboard was not part of the cascade described in [8], it was added to improve the cascade periodicity. Unlike the lower tailboard, the upper tailboard was made of solid aluminum. Tests showed that the upper and lower tailboard were the only means of adjusting the periodicity of the cascade. The boundary layer bleeds did not have a significant effect.

3.1.2 Blade Geometry

The blade used in the current experiment was of the same design as that used by Carscallen *et al.* [11, 8, 10, 9]. However, there was one change to the as-manufactured blade geometry between the previous experiments and the current work. An imperfection at the beginning of the trailing edge radius was removed from the pressure surface. Previously there was a small rounded protrusion in this region. The blade used in the present experiments had a smooth transition from the pressure surface to the trailing edge circle as had been intended in the original blade design.

The blades which made up the cascade had some very aggressive design features. Section 2.2.1 discussed that the airfoil was the mid-span profile from the stator of a first stage turbine which was required to power the compressor of a gas turbine used in small air and rotor-craft. As such, it required aggressive cooling as well as a large amount of turning to allow the matching rotor to produce sufficient power in a single stage. The need for aggressive cooling led to the blade having a thick trailing edge ($\approx 20\%$ of the throat opening). The blade was designed to have a high suction surface curvature in the first $0.5 C_x$ of the blade, where most of the turning was desired. This led to the blade having low suction surface curvature downstream of the throat. There were several advantages to having low suction surface curvature downstream of the throat. Sieverding *et al.* [58] noted that low suction surface curvature was strongly correlated to a low base pressure losses. Graham and Kost [30] stated that the smaller the suction surface curvature, the easier it was for a separated boundary layer to re-attach to the blade. Finally, Ainley [2] noted that low suction surface curvature led to decreased flow deflection from the exit metal angle.

The blade geometry is shown in Figure 3.3, its design specifications are given in

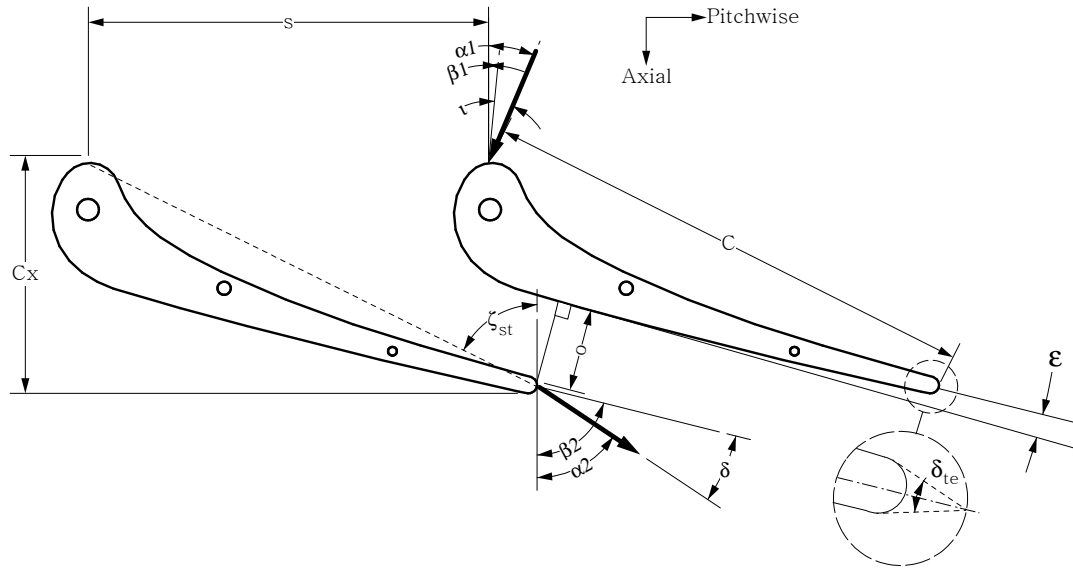


Figure 3.3: Blade geometry

Table 3.1. This table also contains several dimensionless ratios which are often used to characterize a blade's design.

Detailed blade coordinates are presented in Appendix F. The passage throat, labeled as o in Figure 3.3, was located at the start of the region of uncovered turning. The passage throat occurred at $0.57 C_x$, or 32% the suction surface length.

The aspect ratio of the airfoils was 1.74 based on axial chord. This was sufficient to allow for two-dimensional flow at the mid-span, as will be shown in subsequent sections.

The ratio of the throat opening to the pitch has been strongly correlated to the exit flow angle of turbine blades by Ainley [2]. Equation 3.1 uses this ratio to calculate the gauging angle which is used to predict the outlet flow angle.

$$\alpha_g = \cos^{-1} \left(\frac{o}{s} \right) \quad (3.1)$$

The suction surface curvature downstream of the throat was indicated in two ways. The most common was to calculate the uncovered turning. This was defined as the angle formed between a line tangent to the suction surface at the throat, and the exit metal angle, shown as ϵ in Figure 3.3. Another measure, called the suction surface

Table 3.1: Blade geometry

Property	Symbol	Value
Number of Vanes		6 mm
Axial Chord	C_x	84.6 mm
True Chord	C	175.3 mm
Span	ht	112.8 mm
Pitch	s	147.8 mm
Throat Opening	o	23.58 mm
Trailing Edge Diameter	ϕ_{te}	6.35 mm
Stagger Angle	ζ_{st}	64°
Inlet Metal Angle	β_i	0°
Nominal Incidence	ι	-10°
Outlet Metal Angle	β_e	76°
Mean SS Radius of Curvature	e	2000mm
Uncovered Turning Angle	ϵ	3°
Solidity	$\frac{C}{s}$	1.19
Trailing Edge Blockage	$\frac{\phi_{te}}{o}$	0.269
Aspect Ratio	$\frac{s}{C_x}$	1.74
SS Curvature Ratio	$\frac{s}{e}$	0.074
Gauging Angle	α_g	78.8°

curvature ratio, normalized the pitch by the mean radius of curvature on the suction surface downstream of the throat.

3.2 Instrumentation

3.2.1 Vane Surface Static Pressures

The static pressure profile along the surface of the blade was an important indicator of how the flow close to the blade was behaving. Static pressures were recorded at 26 points on the suction surface and 14 points on the pressure surface. Each static tap on the blade's surface had a diameter of 0.76 mm. Figure 3.4 shows the locations of the static taps around the blade and Table F.2 in Appendix F describes their locations on the blade.

Each blade in the cascade had only the pressure or suction surfaces instrumented.

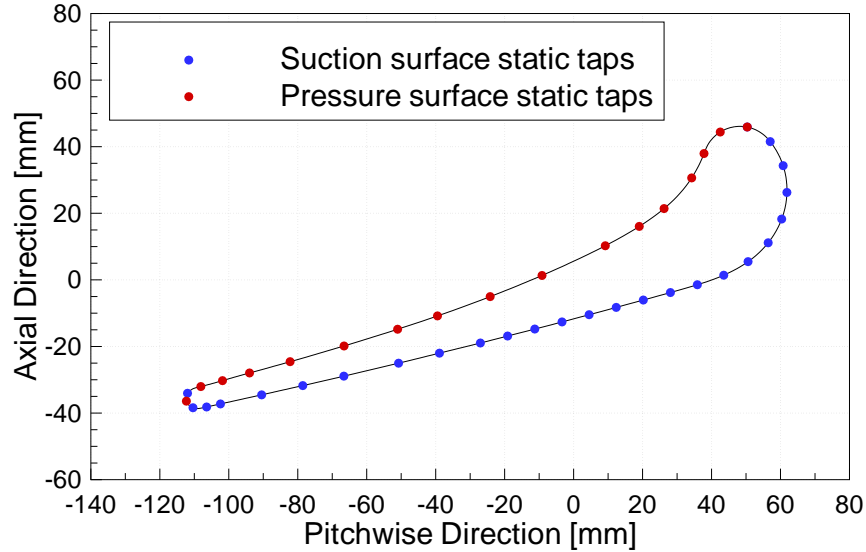


Figure 3.4: Static tap locations

All the data presented in this thesis came from surface pressure measurements taken from the pressure surface of the blade 3 and the suction surface of blade 4.

The three static taps located closest to the trailing edge on the blade were used to measure the base pressure on the airfoil. Many researchers, including Sieverding *et al.* [58] noted that the measurement of base pressure was affected if the diameter of the static pressure tap in the base region was large relative to the trailing edge thickness. The base pressure static tap in the current blades was only 0.635mm in diameter, representing only 10% ϕ_{te} .

3.2.2 Sidewall Static Pressure

To examine the quality of the inlet and exit flow, the sidewall static pressures were recorded at two locations. The inlet flow was measured at 14 equally spaced taps, placed in a line $1 C_x$ upstream of the blade's leading edge. The exit flow was measured at 16 locations placed $1.4 C_x$ downstream of the leading edge.

Two static taps were also installed to monitor the characteristic exit static pressure. The first location, termed *Ref. A* was located below the suction side of blade 1. The second location, termed *Ref B* was placed downstream of the exit static pressure taps. The locations of the inlet and exit static taps as well as the two characteristic

static pressures are shown in Figure 3.2. All endwall static taps had a diameter of 0.76 mm.

3.2.3 Transonic Flow Probe

A 3-hole type probe, designed for use in transonic flow, was traversed across two blade pitches at the inlet and exit planes. The exit plane was located so that the probe sensed the flow 1.4 axial chords downstream of the leading edge and the inlet plane was located so that the flow 1 axial chord upstream of the blade was measured. The details of the design, calibration and resulting accuracy of this custom pneumatic probe are presented in Section 3.5.

3.2.4 Temperature Measurement

The reference stagnation temperature was measured with a calibrated Guildline 9540 digital platinum resistance thermometer (S/N: 60400, Cal. due: March 14, 2009).

3.2.5 Pressure Measurement

The reference total pressure was measured with a calibrated Druck DPI 142 precision barometric indicator (S/N: 1422421697, Cal. due: May 26, 2009). The reference temperature and pressure data were transferred to the host computer via a PCI-GPIB (NI-488.2) card.

All pressure ports from the instrumented airfoils, the probe and the endwall were connected to pressure modules of a DSA 3016 HyScan pressure scanner. Each DSA 3016 module has sixteen ± 103.42 kPa (15 psi) temperature compensated transducers, with an accuracy of $\pm 0.05\%$ full scale. The tunnel static and stagnation pressures were measured on the last two transducers of the last module. Transducers were referenced to the reference total pressure and they were calibrated online, using a ± 103.42 kPa (15 psi) range calibrated Hyscan *SPC 3000 Servo Pressure Calibrator*. This calibrator was checked against the DPI 142 instrument, mentioned above. Transducers were re-zeroed at the beginning of each condition. This arrangement

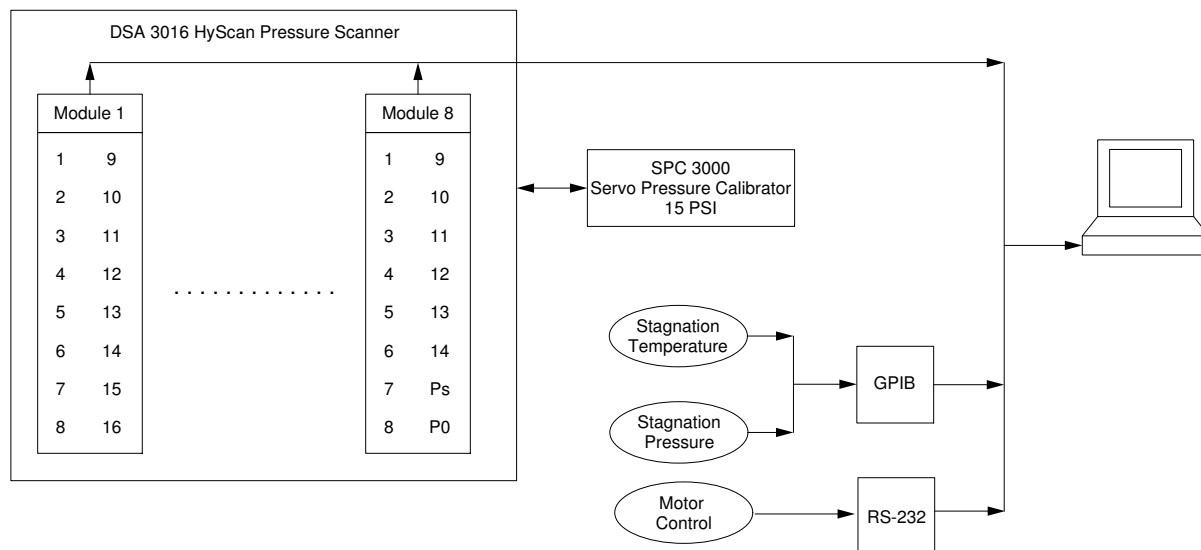


Figure 3.5: Data acquisition system

is illustrated in Figure 3.5. To minimize uncertainties, end-to-end calibrations were performed for all instruments involved in testing.

3.2.6 Linear Traverse Mechanism

The transonic flow probe was traversed using a linear traverse mechanism driven by a 400 step/rev stepper motor connected to a 20 rev/in lead screw. The probe could be rotated about its own axis by means of a manual rotary table. A slot 6.35 mm (0.25 in) wide and 508 mm (20 in) long was machined into the western sidewall to allow the probe to traverse across the third and fourth blade passages. This slot was sealed with a 19.5 mm (0.75 in) wide Teflon strip which was fixed to the probe stem. At the maximum Mach number setting, the suction on the Teflon created too substantial a resisting force for the stepper motor to overcome. This prevented the probe from traversing the exit plane. A second sealing strip of aluminum with a slot only one pitch long was placed between the Teflon and the cascade sidewall to reduce the force which the pressure was exerting on the Teflon. This arrangement is shown in Figure 3.6. This modification, along with only traversing in the flow direction, allowed the motor to completely overcome the suction on the Teflon strip and move

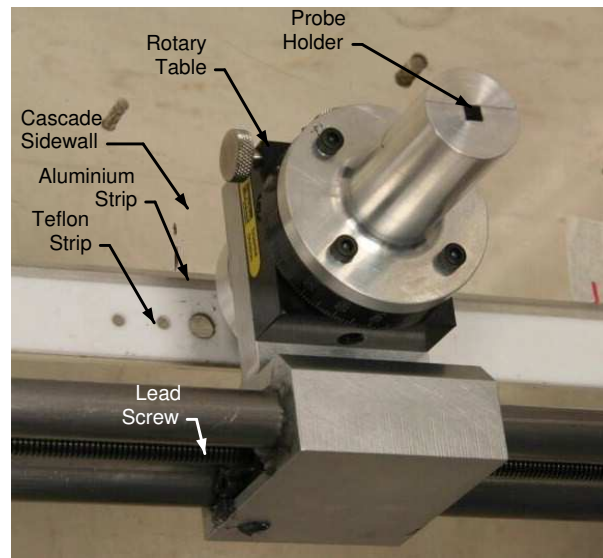


Figure 3.6: Photograph of linear traverse mechanism

the probe accurately and repeatably. The probe was zeroed along the traverse plane by using a stencil which was aligned with four of the dowel pin holes used to secure the blades. For the exit traverses, a line was extended from the trailing edge of the third blade at the metal angle (76°) and the probe was placed so that the center of the probe stem was coincident with the point where this line intersected the traverse plane. This arrangement is shown in Figure 3.7. The probe tip was then aligned with the metal angle. A similar technique was used to align the probe for the inlet traverses. In this case, the line was extended one axial chord upstream from the leading edge and was parallel to the cascade sidewalls.

The exit plane traverses were much finer than those at the inlet plane. The measurement positions for the exit flow were located at 49 unequally spaced points along the pitch. Within the wake, measurements were taken every 1% of the pitch. This spacing grew to 5% of the pitch outside the wake. The inlet traverses took measurements every 9% of the pitch.

Most traverses were performed from the middle of passage 3 to the middle of passage 4. The mid-passage locations are shown in Figure 3.7. The location of the original zeroing point was marked both on the sidewall and as an angular position on

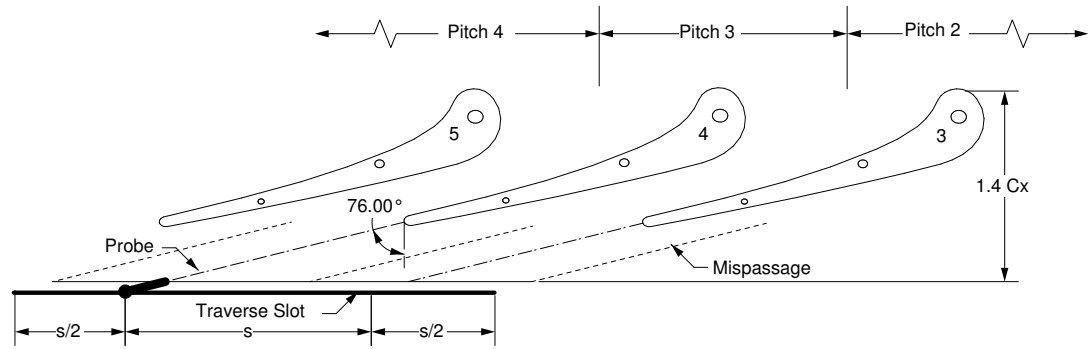


Figure 3.7: Method of alignment of transonic flow probe

the stepper motor shaft. Using these two markers, the presence of any bias errors in the probe's position could be observed when the probe returned to its zero position. In all cases, the misalignment of the stepper motor shaft from the zero position was imperceptible. Since one revolution of the shaft corresponded to 0.0635 mm of linear travel, visual inspection of the shaft alignment allowed the zero position to be checked with a high degree of accuracy.

3.3 Data Acquisition

The data acquisition system employed in the current experiment performed three main tasks; gathering pressure information, gathering temperature information and controlling the traverse mechanisms. The same equipment was used for both measurements within the cascade and the calibration tunnel.

The HyScan pressure scanner was setup to recorded 400 data points per measurement position. Each data point consisted of an average of 20 individual samples. Each sample was collected over 250 μ s. Low frequency measurements from both the Druck DPI 142 and Guildline 9540 were also gathered for every measurement position.

A Velmex stepper motor controller was used to control the linear traverse mechanism used on the transonic linear cascade as well as the angular traverse mechanism used in the probe calibration facility. The Velmex converted a digital signal containing the desired number of steps into a control signal to the stepper motor. Since it

was necessary that the number of steps be an integer, there was a small error introduced as the desired position was converted into steps. To prevent the accumulation of this small error affecting the results, all traverse positions were set to distances which corresponded to an integer number of steps.

All the data acquisition and control equipment was controlled by one personal computer using LabVIEW software. Figure 3.5 shows how the various systems worked together to collect data and control the experiment.

3.4 Flow Visualization

In addition to pressure measurements, flow visualization was used to examine the flow behaviour within the nozzle guide vane passage and interpret surface static pressure measurements. The flow visualization focused on two flow regions which strongly influenced the overall flow physics of the blade, the trailing edge flow and the shock-boundary layer interaction on the suction surface. This technique was also used to examine the extent of flow two-dimensionality in the passage.

One widely used surface flow visualization technique is the oil-film method. This method consists of coating the airfoil surface with a layer of oil that is mixed with powdered pigments. The mixture responds to the surface shear stress and hence it is removed from the surface in attached flows, but accumulates in the regions of flow separation. In the experiments reported here, a mixture of 15 mL of Alkali refined Linseed oil and 280 mg of Lampblack pigments was applied on the suction surface of the vane. The oil was applied in an extremely thin layer over the blade surface, with a minimal amount of oil placed on the leading edge.

Before the oil was applied, the blades were covered with a thin self-adhesive white vinyl sheet. This gave a uniform background over which the oil could be applied, enhancing the contrast of the images. The procedure for painting the blades is shown in Figure 3.8. The first step in the procedure was shown in Frame ‘A’. Applying four drops of oil from a $\frac{1}{2}$ in wide paintbrush provided sufficient oil to cover the entire suction surface. The oil was then spread along the surface of the blade until an even coating was achieved, shown in frame ‘B’. Any excess oil was removed with a paper

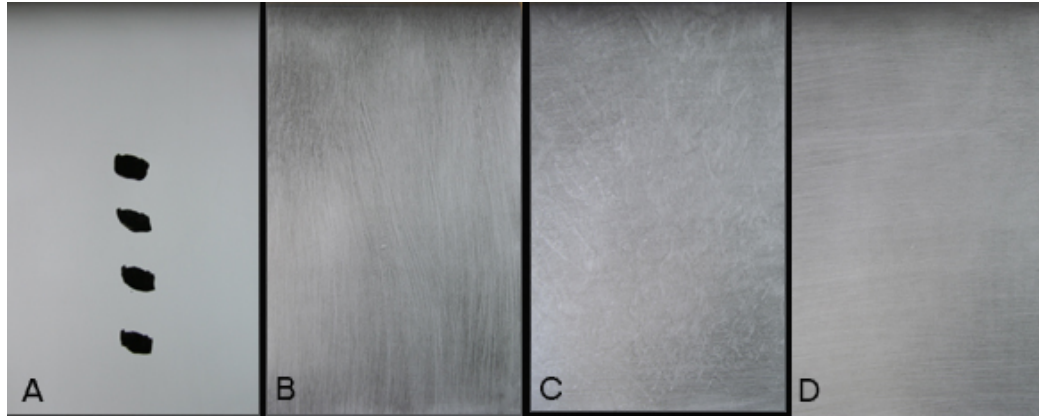


Figure 3.8: Procedure for applying oil-pigment mixture to blades

towel, shown in frame ‘C’. The oil was then spread in the spanwise direction so that the brush strokes would not be confused with streamlines. The finished blade is shown in frame ‘D’.

In supersonic flow, the presence of shock waves complicated the production of meaningful flow visualization images. The separation bubble, which formed at the impingement point of the shock wave, entrained some of the oil mixture. When the flow to the test section was shut off, the oil which had been trapped in the strong vorticity in the separated region was released and flowed downstream. This would result in large streaks of oil on the blade surface which were not indicative of the true behaviour of the flow. This streaking was eliminated using two techniques. The first was to apply only minimal amounts of oil to the leading edge, since most of the oil applied above the shock impingement point was entrained in the separation zone. The second technique was to briefly reduce the tunnel Mach number to a subsonic value after the supersonic flow pattern was established, and quickly return to the target Mach number. This swept the entrained oil downstream and the resulting streak was attenuated once the tunnel Mach number was returned to its original set-point. So long as the flow only spent fraction of the total test time at the subsonic Mach number, the resulting image was characteristic of the supersonic Mach number behaviour.

3.5 Finger Probe

A pressure probe was designed and calibrated at NRC to measure the total pressure, flow direction and velocity magnitude in subsonic and supersonic flows.

This section describes the various potential designs of transonic pressure probes, the mechanical design of the NRC finger probe, the facility used to calibrate the probe, the results from the calibration and a discussion on their accuracy.

3.5.1 Other designs of Transonic Pressure Probes

Various designs of transonic pressure probes have been used in the past for measurements in transonic cascades. Sieverding *et al.* [56] investigated four different probe designs in a 1974 report. One design they examined was termed a *cone probe* and was very similar to the current *finger probe*. Sieverding found no major flaws in the design of the cone probe. However, none of the five probes tested by Sieverding *et al.* [56] were found to be in all ways superior to any other design.

Other researchers who examined the wake of turbine blades used other probe designs. Xu and Denton [69] used a *Neptune Probe* in their investigation of losses from transonic turbine blading. The Neptune probe was described by Kiock *et al.* [35] and Sieverding [55]. The difference between the cone or finger probe and the Neptune probe lay in the number of separate sets of tubes, or *prongs* used to measure the flow properties. The cone and finger probe used two prongs, one to measure total pressure and flow direction and another to measure the static pressure. The Neptune probe measured each of these three properties on a separate prong. All three probe designs required the flow to be two-dimensional to achieve accurate measurements.

There were some designs of transonic flow probes which measured the flow's velocity, total pressure and incidence angle using only one prong. The DFVLR Göttingen transonic cascade [30, 23, 38] used a modified wedge type probe which was described in [56]. Povey *et al.* [48] used a true wedge probe in their transonic cascade measurements. The true wedge probe was the simplest design. However, the disadvantage of using a true wedge probe in transonic flow was its insensitivity to static pressure in

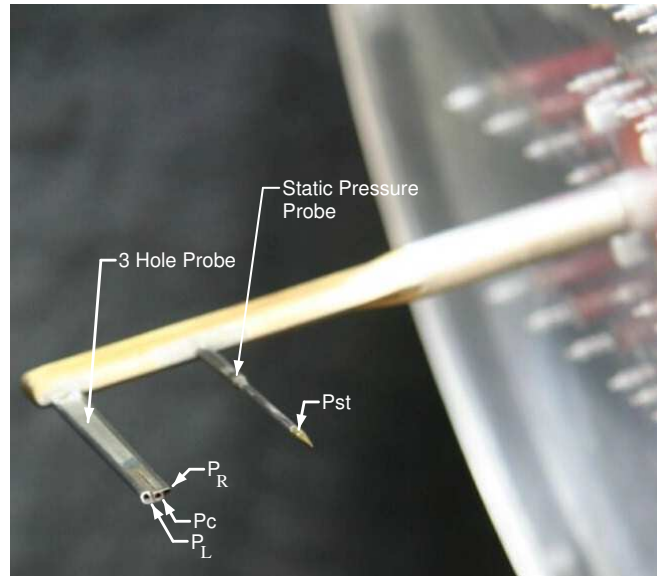


Figure 3.9: A view of the NRC finger probe

the transonic region. This was shown by Sieverding *et al.* [56]. The modified wedge probe used by DFVLR had adequate static pressure sensitivity across the Mach number range examined, but suffered from non-linear calibration behaviour [56].

All the probes which have been mentioned presented some degree of difficulty measuring the static pressure in the transonic region due to the unique behaviour of the flow over all styles of probes at these speeds. The nature of this issue and how it may be resolved will be discussed in Section 3.5.4.

3.5.2 Probe Design

The finger probe, shown in Figure 3.9, consisted of two prongs; one three-hole pressure probe to measure total pressure and flow angle and one static pressure probe. Following a design described by Spaid *et al.* [62], the three-hole probe comprised of three stainless steel tubes of 1.07 mm outer diameter and 0.68 mm inner diameter. The three tubes were first soldered together and machined in a plane parallel to the probe stem. The face angles of the two side tubes were then machined at $45 \pm 0.5^\circ$ with a wire EDM (Electronic Discharge Machine). The static probe was made of a 1.07 mm diameter stainless tube with a brass tip. Following the design of Huey [32],

the static probe tip had a 15° cone angle with four equally-spaced 0.25 mm holes drilled at 3.5 mm below the sharp tip. The three-hole and static probe prongs were 35 mm long, from the stem, and 15.9 mm apart. The probe stem was designed to minimize the blockage of the test section. The stem was made of a 125 mm long, 6.35 mm diameter, stainless steel tube terminated in a 40 mm thin wedge-shaped brass body, where the two probes were mounted. This arrangement allowed flow measurements with minimal blockage, especially downstream of the cascade. Since the probe holes were parallel to the vane wakes in the cascade, the effective probe diameter (assuming two-dimensional flow) was 1.07 mm, giving a probe tip to trailing edge ratio of 0.17.

3.5.3 Calibration Method

The probe was calibrated by recording the four probe pressures over a range of angles at each Mach number. A set of dimensionless numbers, given in Equations 3.2-3.8, were created which related these four measured pressures to the three known flow properties in the calibration tunnel, *i.e.*, the total pressure, static pressure and flow angle. The static pressure was often presented as a Mach number, calculated using the true total pressure. The design of the calibration tunnel as well as the uncertainty in the calibration conditions is presented in Appendix A. One calibration was performed before the probe was used for wake traverses and one after. These two calibrations were referred to as the pre-traverse calibration and post-traverse calibration respectively.

Equations 3.2 through Equation 3.7 were taken from Lewis' 1965 report [40] on the use of three hole probes in incompressible flow. The various K factors related the measured pressures from the probe to key flow conditions: total pressure, flow angle and Mach number. The K_ϕ coefficients were functions only of the measured probe pressures and were used to determine the flow angle. Once this was known, K_{23} could be used to determine the dynamic pressure. Subsequently, K_1 could be used to determine the total pressure. Equation 3.8 was added to allow the method of Lewis [40] to be extended to compressible flow.

$$K_1 = \frac{(P_c - P_s)}{(P_o - P_s)} \quad (3.2)$$

$$K_{12} = \frac{(P_c - P_L)}{(P_o - P_s)} \quad (3.3)$$

$$K_{13} = \frac{(P_c - P_R)}{(P_o - P_s)} \quad (3.4)$$

$$K_{23} = \frac{(P_L - P_R)}{(P_o - P_s)} \quad (3.5)$$

$$K_{\phi 1} = \frac{(P_c - P_L)}{(P_c - P_R)} \quad (3.6)$$

$$K_{\phi 2} = \frac{1}{K_{\phi 1}} = \frac{(P_c - P_R)}{(P_o - P_L)} \quad (3.7)$$

$$K_M = \frac{P_{st}}{P_c} \quad (3.8)$$

In the preceding equations, P_L , P_R , P_c and P_{st} were the measured probe pressures, as shown in Figure 3.9. P_o and P_s were the true total and static pressures measured in the test section of the calibration tunnel. The procedure for extracting the flow angle and Mach number using these parameters is given in Section 3.6.

3.5.4 Calibration Results

Calibration charts for the probe were created by calculating the values of Equation 3.2 through 3.8 for every Mach number and angle combination. Figure 3.10 shows the calibration coefficients for the pre-traverse calibration. Figure 3.11 shows the calibration coefficients for the post-traverse calibration, which was shown in Appendix A as the best set of data available.

There was a significant difference between sets of calibration data taken before and after the traverses. The most obvious difference was the discrepancy between the K_1 and K_M values at supersonic Mach numbers, as seen in Figure 3.11 and Figure 3.10. Another, more subtle, difference which was the behaviour of the K_ϕ coefficients. Figure 3.12 shows the K_ϕ values for a nominal Mach number of 1.22. The third-order approximation was the most appropriate for this data. The K_ϕ curves intersect at different points for the two sets of calibration data. This is significant since the

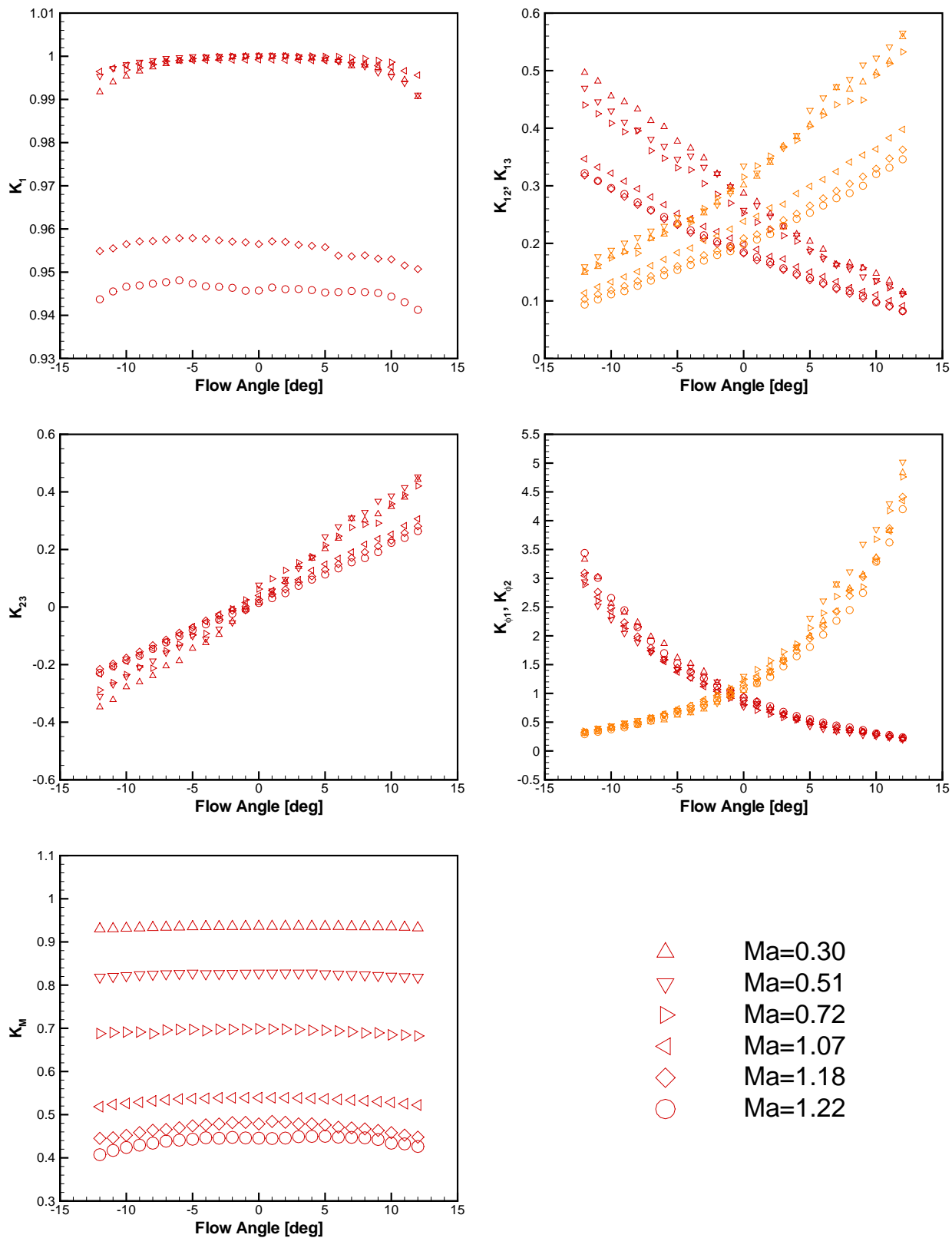


Figure 3.10: Plot of calibration coefficients (before cascade tests)

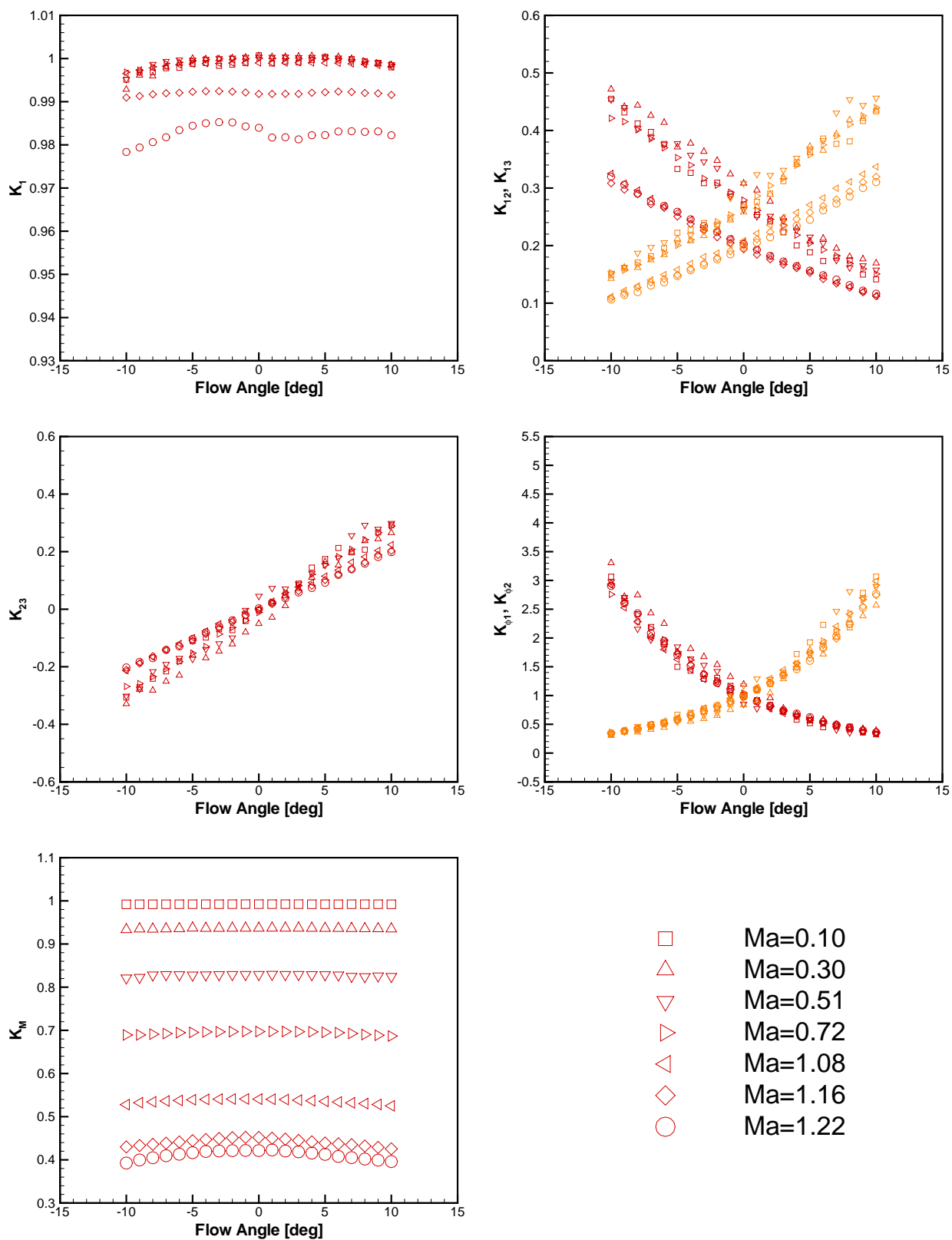


Figure 3.11: Plot of calibration coefficients (after cascade tests)

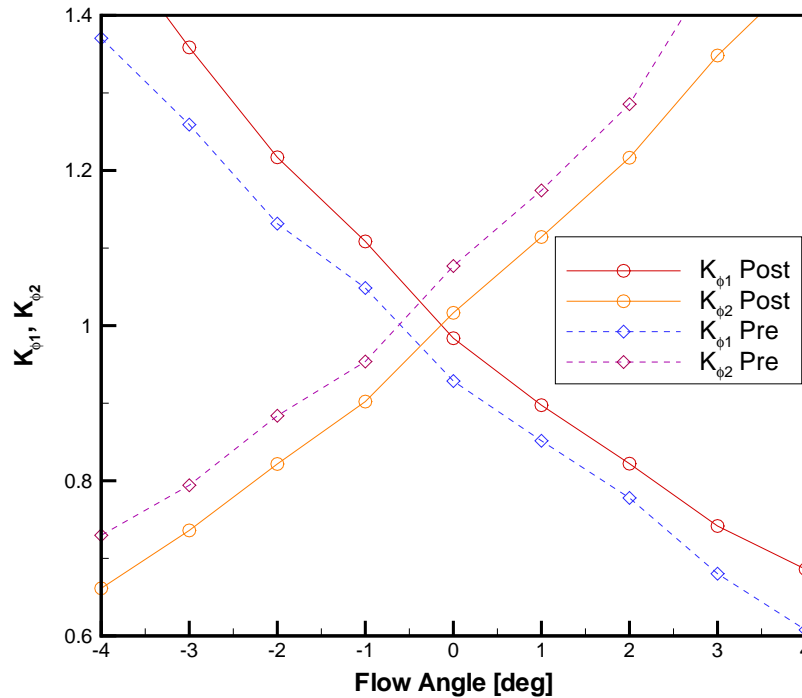


Figure 3.12: Variations in K_{ϕ} between calibrations

intersection point of the $K_{\phi 1}$ and $K_{\phi 2}$ curves indicated when $P_L = P_R$ and hence when the pressures are balanced across the probe tip. This shift indicated that the probe was physically altered over the course of the experiment. This was most likely caused by early attempts to set the probe angle by placing an inclinometer on the three hole probe. The slight force that the inclinometer placed on the probe may have caused it to deflect over time. Because of this, the data from the pre-traverse calibration was applied to the experiments performed soon after this calibration, while the post-traverse calibration was applied to experiments performed later in time. A discussion of the overall accuracy of the probe is given in Appendix B.

Appendix A discusses why data taken at $Ma = 1.19$ during the pre-traverse calibration data was not used in the data-reduction. There were also data taken at $Ma = 1.16$ which were discarded from data reduction. Figure 3.13 shows how K_M varied with Mach number at a zero flow angle in the first calibration. There is a sharp discontinuity between the $Ma = 1.16$ and 1.18 values. This discontinuity lead to there being three different Mach numbers which could correspond to certain

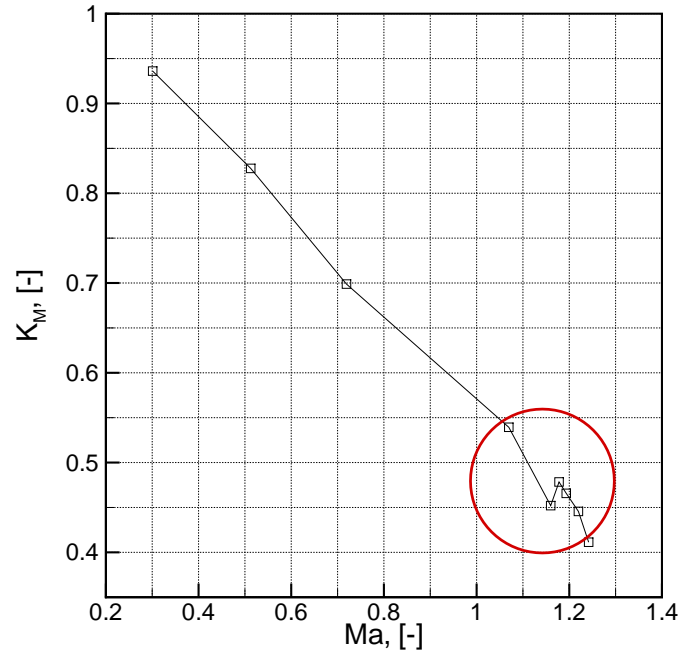


Figure 3.13: Static probe behaviour at zero flow angle

values of K_M , preventing an unique measure of static pressure. Sieverding *et al.* [56] noted this behaviour in the four probes which they examined. However, they made no mention of how they were able to find a unique value of their static pressure coefficient, equivalent to K_M , in this region.

The origin of this discontinuity lay in the transonic behaviour of the leading edge shock on the static pressure probe. According to the analytical work of Taylor and Maccoll [64], as the the incoming flow to an infinite cone approaches Mach one, a detached bow shock will form at an infinite distance from the tip of the cone. Once Mach one is exceeded, the bow shock will move towards the cone tip with increasing Mach number. At some critical Mach number, the shock will attach to the tip and behave like an oblique shock wave. The difference in behaviour between oblique shocks and bow shocks, which can be modeled as normal shocks, would change the static pressure measured by the static probe enough to cause the discontinuity observed in Figure 3.13. Solomon [60] compiled data on the Mach numbers where the transition from bow shock to oblique shock occurred for a variety of cone terminated cylinders in supersonic flow. The sharpest included cone angle which he examined was 25° .

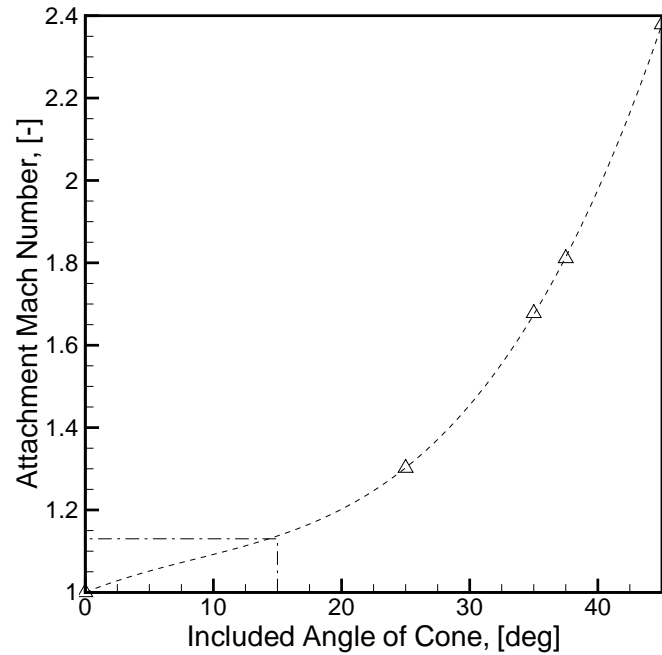


Figure 3.14: Shock attachment Mach number

A third-order polynomial was passed through his data, as shown in Figure 3.14, in order to extrapolate the behaviour at an included angle of 15° . To get a realistic extrapolation, an additional point was added to force the polynomial to reflect an oblique shock occurring at exactly Mach one for a cone with zero included angle. This is the behaviour that Taylor and Maccoll [64] predicted for infinite cones. The third order fit to this data was justified using the extra sum of squares method, which showed that there was a 94% probability that the increase in agreement between a third and second order polynomial was due to the suitability of the third order fit rather than to scatter in the data.

From Figure 3.14 the change from a bow shock to oblique shock was predicted to occur at $Ma = 1.14$ for an included cone angle of 15° . The discontinuity in the results occurred between $Ma = 1.16$ and $Ma = 1.18$ in the current data, presented in Figure 3.13. Since the behaviour in K_M changed little with flow angle, figure Figure 3.13 shows only the data from when the flow angle was zero. Considering that the Mach number at which the shock was predicted to attach was an extrapolation from various experimental and theoretical values, it was reasonable to assume that

the change in shock behaviour from a detached bow shock to an attached oblique shock was the source of the discontinuity seen in the current probe.

Though the preceding argument described a potential cause for the discontinuity, accounting for it presented additional difficulties. The challenge lay in the fact that the correction to obtain the true static pressure from the probe measurements was dependent on the nature of the shock wave forming on the static pressure probe. The correction was different for attached and detached shock waves. This problem was investigated by Kost [36], who added an additional static tap in the wake of the probe stem. He supported this decision by showing that the base pressure behind a cylinder varied linearly with Mach number. However, research presented in Section 2.1.3 indicated the relationship may not be as simple at transonic speeds.

Adding an additional static tap to the probe appeared to be a promising solution since it may not be possible to account for the shock position otherwise. If shock position were to be accounted for, it would be one of four variables that would need to be extracted from four pressure measurements (static pressure, total pressure and flow angle being the other three). Though it may appear that this could be possible by some unique combination of the four measured pressures, the left and right pressures in a three hole probe are not independent variables. Therefore there are only three truly independent measurements from which to extract four independent variables, which is fundamentally impossible. Adding the static pressure tap in the wake would provide an additional and independent measurement to allow a fourth variable to be extracted. Therefore, it was possible that adding an additional static tap in the wake of the probe stem would allow the finger probe to measure static pressure accurately, even in the Mach number range where the shock attachment occurred. However, geometric constraints of the current probe precluded adding an additional static tap without remanufacturing the entire probe. Hence, it is proposed to design a finger probe with a base-pressure static tap in the future.

To allow the probe to determine a unique Mach number in the transonic region, the calibration data from $Ma = 1.16$ were not used to form the calibration coefficients. This introduced an error in the measured Mach number. By removing the data at

$Ma = 1.16$, the calibration process ignored the discontinuity and linearly interpolated between the $Ma = 1.07$ and $Ma = 1.18$. The maximum Mach number error occurred when $K_M = 0.45$. In this case, flow would be measured as $Ma = 1.22$ when, in fact, it could have been only $Ma = 1.16$, creating an error of $Ma = 0.06$. If the static temperature of the flow were 298K, this would correspond to a 18 m/s (5%) error in velocity at $Ma = 1.16$. During the second calibration, only one point was collected between $Ma = 1.0$ and 1.22. Because of this, the discontinuity in K_M values seen previously could not be observed.

3.6 Data Reduction Procedures

In order to obtain information about aerodynamics of the nozzle guide vanes, the data collected from the experiments required a significant amount of post-processing. This section explains how these data reduction procedures were carried out.

3.6.1 Mach Numbers

Much of the data which will be presented about the flow around the blading will be presented as a Mach number. The Mach number is a dimensionless variable which relates the local flow velocity to the speed which pressure waves can travel in the local flow. Flow which has a local Mach number in excess of unity is termed supersonic flow and has markedly different behaviour than subsonic flow. These differences are well documented in any compressible flow textbook such that by Anderson [5] or Oosthuizen and Carscallen [47].

Flows with Mach numbers between roughly $Ma = 0.75$ and $Ma = 1.2$ are known as transonic flows. Though the upper and lower bounds on the transonic regime are arbitrary, they reflect the fact that flows at these speeds do not behave exactly like subsonic or supersonic flows. Such flows exhibit their own unique, and often complex, behaviour as the flow changes from behaving in a subsonic to a supersonic manner.

The Mach number was used in two different ways; the most common was as a *global* Mach number. This was a Mach number which was used to represent the

operating point of an experiment or simulation. The global Mach number was defined using Equation 3.9. The choice of appropriate characteristic static pressure, $P_{s_{char}}$, presented some difficulties which will be addressed subsequently. Unless it is stated otherwise, references to the Mach number always implies the global Mach number.

$$Ma_{global} = \sqrt{\frac{2}{\gamma - 1} \left[\left(\frac{Po_1}{P_{s_{char}}} \right)^{\frac{\gamma-1}{\gamma}} - 1 \right]} \quad (3.9)$$

Another use of the Mach number was as a *local* Mach number. This was used to show local velocities such as on the surface of the blades or in the wake downstream of the blading. This Mach number was computed using Equation 3.10.

$$Ma_{local} = \sqrt{\frac{2}{\gamma - 1} \left[\left(\frac{Po_{char}}{P_{s_{local}}} \right)^{\frac{\gamma-1}{\gamma}} - 1 \right]} \quad (3.10)$$

In Equation 3.10, the characteristic total pressure, Po_{char} , was often chosen as the inlet total pressure. The local static pressure, $P_{s_{local}}$, was the static pressure at the spacial position where the local Mach number was being evaluated. If the local Mach number is being used, this will be noted explicitly in subsequent chapters.

The global exit Mach number of the cascade was a non-trivial quantity to compute. There were four possibilities of reference static pressures which could be used: the first was a single static tap placed below the first airfoil. This was labeled *Ref A* in Figure 3.2. The second was a tap placed downstream of the traverse plane in the middle of the fourth passage, *Ref B* in Figure 3.2. A third option was to use the mean of the downstream static pressure taps. The final option was to use the minimum value of the downstream static taps. Figure 3.15 shows the exit Mach number calculated using each choice of characteristic static pressure. All four values agreed quite closely. However, Figure 3.16 shows the worst case scenario, when the probe was placed in the flow and located upstream of the *Ref B* static tap. It can be seen that this choice of static tap produced an erroneously high reading. For this reason, the *Ref A* static pressure tap location was employed in all experiments. Though this static tap was not in the most physically sensible location, it was immune to probe interference. Experiments without the probe present showed that this tap's

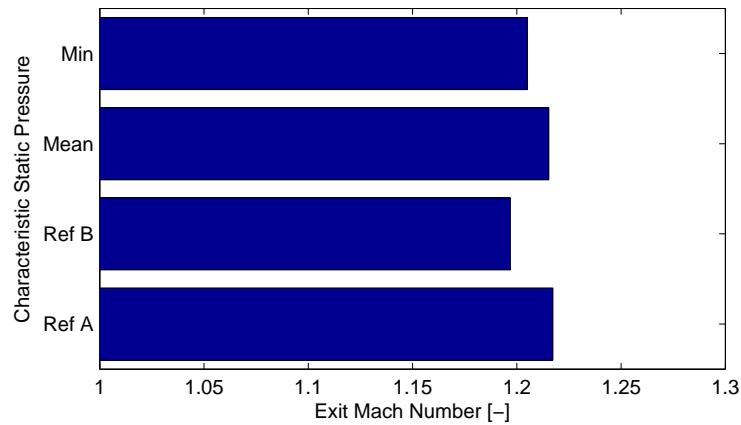


Figure 3.15: Effect of characteristic static pressure on global Mach number without upstream probe

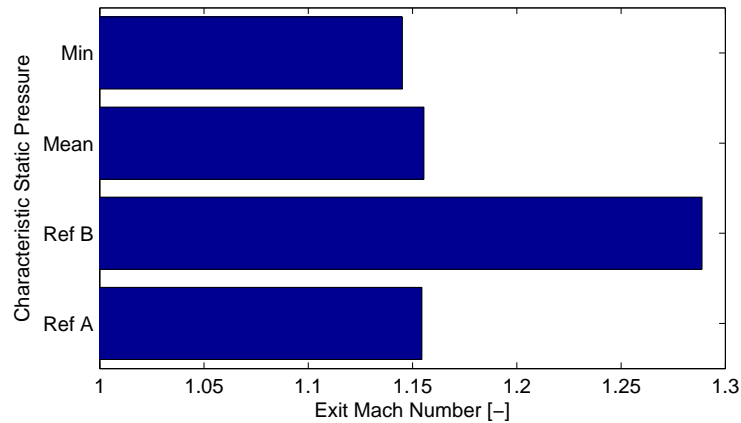


Figure 3.16: Effect of characteristic static pressure on global Mach number with upstream probe

readings were very close to taps in a more physically intuitive position.

3.6.2 Finger Probe Data Reduction

Section 3.5 highlighted the difficulties in obtaining a set of calibration data that would allow the flow angle and Mach number to be measured accurately. The actual method of using this calibration data to find these properties in an unknown flow will be explained here.

In incompressible flow, when the Mach number effects on the probe are negligible, the flow properties of total pressure, flow angle and Mach number could be extracted

from the four pressure measurements using the method outlined by Lewis [40].

However, the current experiments were not carried out in incompressible flow and the method of Lewis was modified in order to operate in compressible flows. The procedure became more complex once the Mach number effects were considered. The value of P_{st} from the static pressure prong was used to calculate the value of K_M . However, K_M also varied with angle, so an iterative process was required to determine the flow angle and Mach number simultaneously. First, the measured K_M was used to determine the Mach number, assuming that $\alpha = 0$. Using this guessed Mach number, the flow angle was determined using the known values of $K_{\phi 1}$ or $K_{\phi 2}$, whichever was smaller. The Mach number was then calculated again using the new value of α and the difference between the new and initial Mach numbers was computed. The process continued until the difference became less than a specific tolerance. For the data reduced here, this tolerance was set to 0.01. This was a reasonable value for the tolerance since it was the same as the uncertainty in the test section Mach number. Once the Mach number and angle were known, the dynamic and static pressures were calculated. The only added complexity was the need to for linear interpolation between calibration coefficients to obtain values for the measured Mach number and flow angle combination. This entire process was automated using a data reduction program implemented in *Matlab*. The source code is provided in Appendix E.3.

3.6.3 Mass-Averaged Loss Calculation

In order to determine the the midspan losses in a physically meaningful manner, the data from the wake traverses had to be mass averaged.

“For determining losses in turbomachinery flows, mass-averaging, as opposed to area- or arithmetic-averaging, is necessary because it produces integrated results that are consistent with the conservation equations [6].”

The differential mass flow at any traverse location $(\Delta\dot{m}_i)$, could be expressed in terms of the known wake properties using Equation 3.11

$$\Delta\dot{m}_i = \frac{Po_i}{\sqrt{To_i}} Ma_i \cos(\alpha) \sqrt{\frac{\gamma}{R}} \left(1 + \frac{(\gamma - 1)}{2} Ma_i^2 \right)^{\frac{1+\gamma}{2-2\gamma}} \quad (3.11)$$

Knowing the differential mass flow across the pitch, the mass-averaged value of any property, (ψ) , could be determined using Equation 3.12

$$\bar{\psi} = \frac{\int_0^1 (\psi_i \cdot \Delta\dot{m}_i) d\left(\frac{y}{s}\right)}{\int_0^1 \Delta\dot{m}_i d\left(\frac{y}{s}\right)} \quad (3.12)$$

The most important mass averaged property was the mass-averaged total pressure. The total pressure loss was computed by using the mass-averaged total and static pressure in Equation 2.3.

3.6.4 Mixed-Out Profile Loss Calculation

An alternative method of wake data reduction was a calculation of the mixed-out total pressure loss, using the process described by Amecke and Šafařík [4]. This method converts the inhomogeneous measured flow field to a homogeneous flow far downstream while conserving mass, momentum and energy. The mixed-out loss method has some advantages over the mass-averaged method of wake data reduction as it is independent of the axial location where the traverse is performed. This makes the mixed-out loss the best measurement for comparison with other researchers' loss data.

The method described by Amecke and Šafařík [4] had provisions for the introduction of a second species of gas as well as total temperature variations across the pitch, which were not used in the current computation of mixed-out loss. Though Section 2.2.2 noted that total temperature variations did occur in the wake, it was assumed that the fluctuations in total temperature would not affect the mixed-out value of loss, since the thermal energy in the wake was being redistributed by the vorticity in the wake rather than being added to the flow.

In order to calculate the total pressure loss in a manner consistent with the definition used by most authors, given in Equation 2.3, some modification to the equations given by Amecke and Šafařík were necessary.

Amecke and Šafařík, defined their loss term, ζ_{Amecke} as in Equation 3.13. To transform this into an expression comparable to Equation 2.3, it was necessary to

know the dynamic pressure at the exit plane, (Φ). Amecke and Šafařík calculated this using Equation 3.14.

$$\zeta_{Amecke} = 1 - \frac{P_{O_m}}{P_{O_i}} \quad (3.13)$$

$$\Phi = \frac{q_m}{P_{O_m}} = \text{Eqn.45 in [4]} \quad (3.14)$$

Knowing both ζ_{Amecke} and Φ , the total pressure loss coefficient, Y_t could be computed using Equation 3.15.

$$Y_t = \frac{\zeta_{Amecke}}{1 - \Phi (1 - \zeta_{Amecke})} \quad (3.15)$$

The algorithm used to compute the mixed out loss was implemented in *Matlab*, the source code is provided in Appendix E.1.

3.6.5 Entropy Generation

It has been mentioned previously in Chapter 2 that the total pressure loss coefficient, (Y_t), though the most common method used to quantify loss, was not the more meaningful measure of the blade's performance. The generation of entropy, defined in Equation 3.16, was a better overall measurement.

$$\zeta = \frac{2 \ln \left(\frac{P_{O_m}}{P_{O_1}} \right)}{\gamma Ma_m^2} \quad (3.16)$$

Assuming:

- Ideal gas.
- Adiabatic flow through the passage with no work extracted.

3.7 Flow Quality within the Transonic Linear Cascade

A linear cascade attempts to simulate the two dimensional flow over an infinite row of blades. This is meant to be indicative of how the flow would behave at a given cross section of a real three-dimensional blade. Before any investigation of the aerodynamic

performance of a blade within a cascade can be performed, it was necessary to examine how closely the cascade came to replicating two-dimensional periodic flow at mid-span.

To quantify this, three parameters were examined: the flow periodicity/uniformity, the similarity in suction surface pressures, and the flow two-dimensionality. The inlet flow uniformity and outlet flow periodicity were measures of how close the passages being examined came to recreating the behaviour which would be expected in an infinite blade-row. An ideal inlet flow for a nozzle guide vane would have uniform flow across the pitch, while the ideal flow at the exit would repeat itself periodically from passage to passage. Similarity of the pressure distributions on the suction surface of the blades was another measure of flow similarity between passages. The flow two-dimensionality indicated if there were any changes in the flow's velocity or direction across the spanwise. The linear cascade was designed to have two dimensional flow around the midspan.

3.7.1 Periodicity/Uniformity

Two tests were performed to quantify the degree of outlet flow periodicity and inlet flow uniformity in the cascade. The first set of tests were measurements of the inlet and outlet sidewall static taps located respectively one axial chord upstream and 1.4 axial chords downstream of the leading edge. Using these static taps, the upper and lower tailboards were adjusted to achieve the best possible periodicity.

After the tailboards were adjusted, the inlet and exit flow was traversed with the finger probe which resolved the local flow angle and Mach number. Detailed probe traverses were a much better measure of the flow conditions in the cascade. The following sections describe the adjustments which were made to the cascade to achieve periodic flow and the resulting flow quality measured by the finger probe. To examine the improvement in periodicity, the flow quality was compared to an initial case, where the upper and lower tailboards were set to the blade metal angle of 76° . Additionally, the north and south boundary layer bleeds were adjusted so that wool tufts, placed upstream of the first and sixth blades' leading edge, showed the flow

entering the end passages axially.

3.7.1.1 Inlet Flow

The inlet flow measured for the initial case is shown in Figure 3.17. The vertical axis presents dynamic pressure coefficients, Cq , which normalized the local dynamic pressure by the mean dynamic pressure at the inlet, as shown in Equation 3.17.

$$Cq = \frac{P_o - P_{s_i}}{P_o - \frac{1}{n} \sum_{i=1}^n P_{s(1,i)}} \quad (3.17)$$

The data in Figure 3.17 show a flow bias toward the south of the cascade. It was found that no adjustment to the north or south boundary layer bleed, nor to either upper or lower tailboard could produce a significant difference in this distribution. Neither did it change significantly with Mach number.

More detailed measurements, taken with the finger probe, are shown in Figure 3.18. They show the total pressure, the flow angle and the local Mach number across two pitches of the inlet plane. The pressure field upstream of the blades were clearly visible in this figure as well as the strong southward bias in flow direction, indicated by the flow angle remaining less than zero across the pitch.

3.7.1.2 Exit Flow

The exit flow measured for the initial case is shown in Figure 3.19a. The southward bias in Cq , observed at the inlet, was also present at the exit. Also, the depth of the velocity deficit in the wake regions varied between passages. To remedy this, the lower tailboard was relocated relative to the trailing edge of the first blade, as shown in Figure 3.2. Originally the tailboard was adjacent to the trailing edge with a small, (≈ 3 mm), positive step. This would prevent the proper shock structure forming behind the first blade, which would affect the suction surface of the second blade by changing its shock structure and this effect would propagate across the blade-row. If a sufficient number of blades were present, a periodic flow would eventually establish itself. However, since the current cascade had only six blades, it was important to set the shock structure of the first blade as accurately as possible. For this reason,

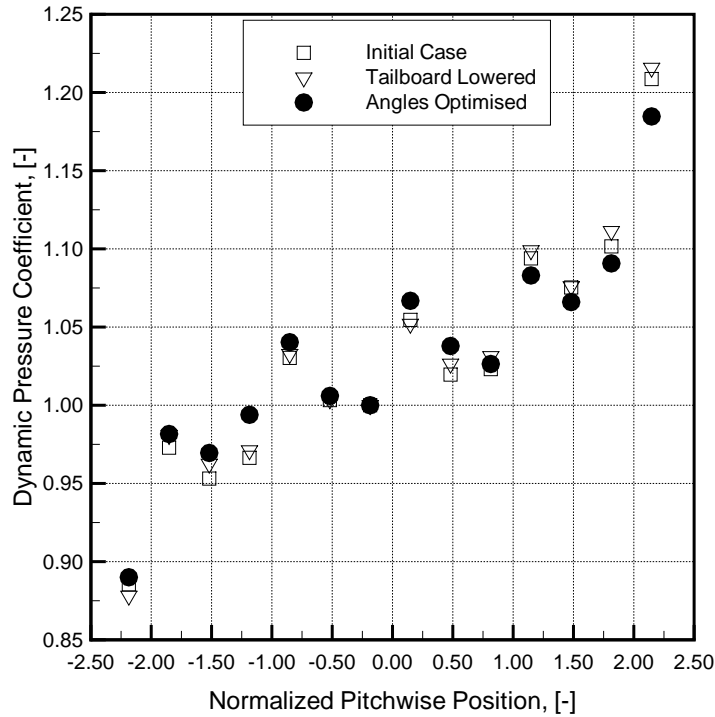
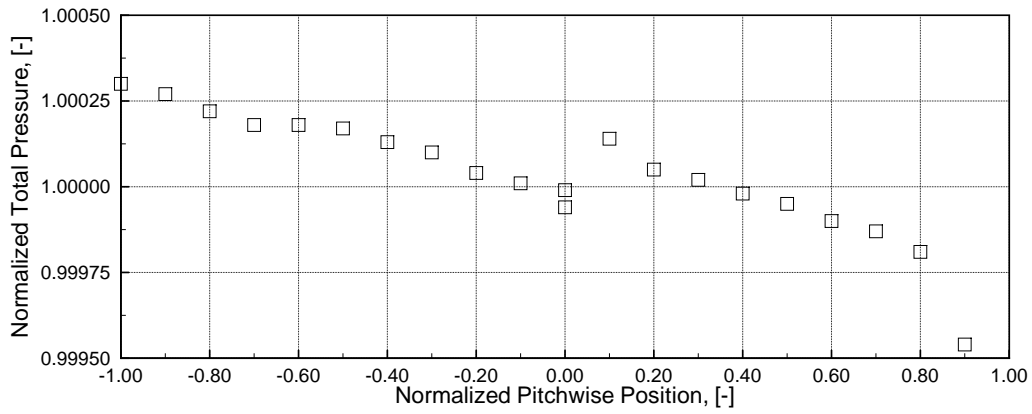


Figure 3.17: Sidewall static pressure measurements in the inlet plane at $Ma = 1.16$

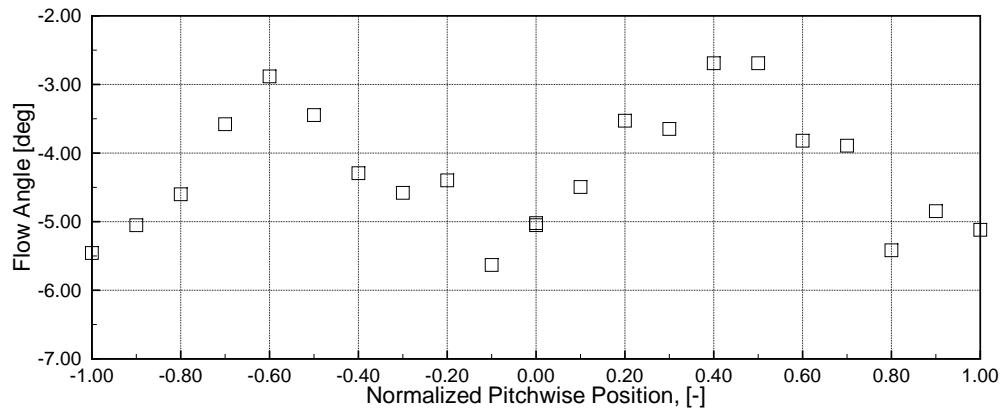
the tailboard was lowered by 20 mm. This would allow a shock structure that was similar to the characteristic pattern described in Section 2.1.2. This shock pattern was different from those of the other airfoils, since the boundary layer development on the pressure surface of the first blade was different than those on other airfoils. Figure 3.19b shows that by adjusting the tailboard location independently of the angle, the periodicity was improved.

However, the exit flow in Figure 3.19b showed room for improvement, therefore a range of upper and lower tailboard angles were examined over Mach numbers between $Ma = 0.1$ and $Ma = 1.4$. It was found that with the lower tailboard in its new position, one set of upper and lower tailboard angles provided acceptable outlet flow periodicity over the Mach number range examined. The lower tailboard was set at $14.5^\circ \pm 0.2^\circ$ and the upper tailboard was set at $9.4^\circ \pm 0.5^\circ$. Figure 3.19c shows the exit flow at $Ma = 1.16$ and Figure 3.19d shows the exit sidewall Cq distribution at $Ma = 0.1$, $Ma = 0.8$, $Ma = 1.16$ and $Ma = 1.43$.

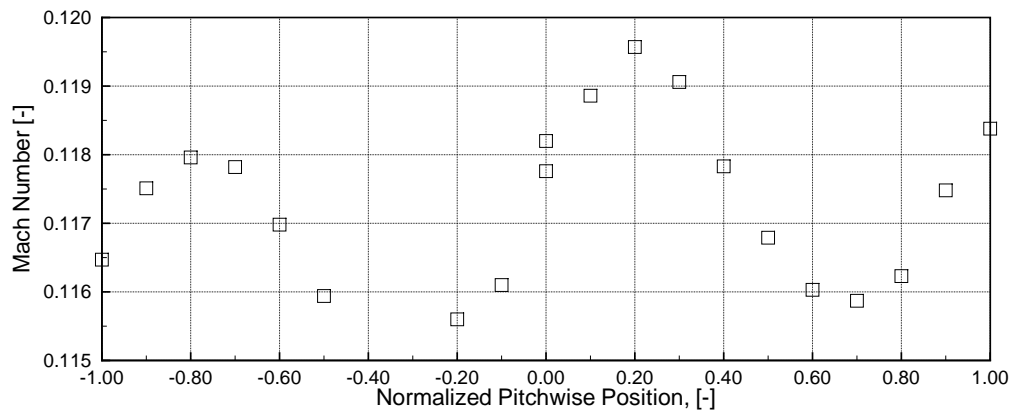
The detailed outlet traverses taken of the blade wake showed that the periodicity of



(a) Total pressure



(b) Flow angle



(c) Mach number

Figure 3.18: Midspan inlet traverses at $Ma = 1.16$

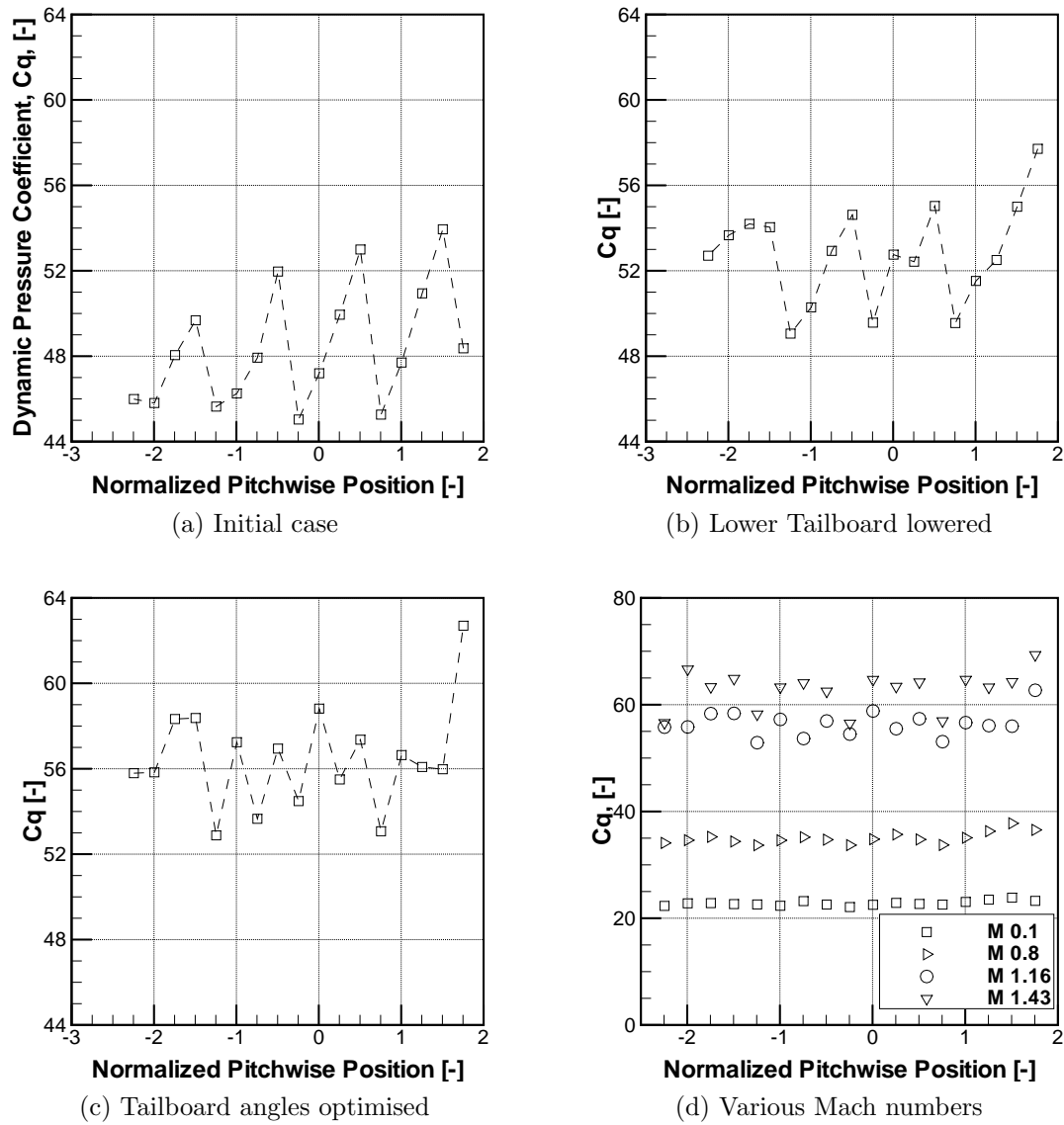


Figure 3.19: Sidewall dynamic pressure coefficients in the exit plane

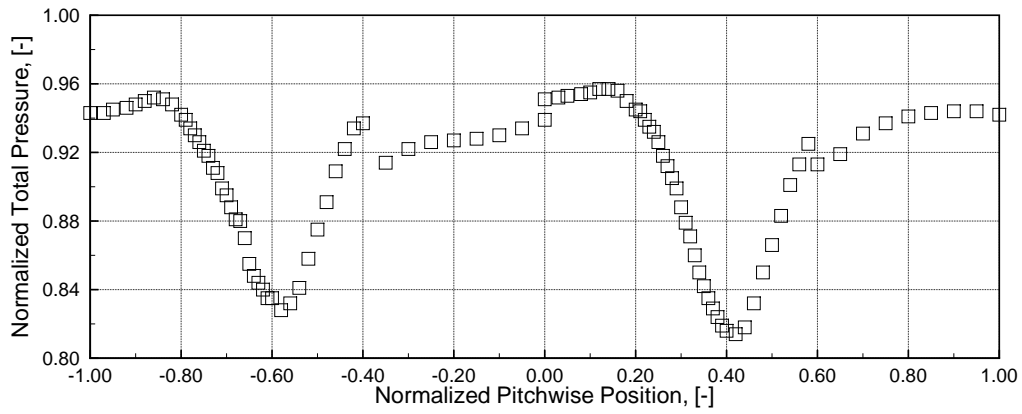
the cascade was not perfect. Both the depth and the width of the total pressure deficit within the wake were slightly different between the two measured passages. However, significant flow features such as shock waves, which appeared as discontinuities in the data, were in similar locations in both passages. To quantify the overall performance of the blades in both passages, the mixed-out and mass-averaged total pressure losses, described in Section 3.6, were computed for each passage. The relative difference between the north and south passages was presented in Table 3.2. The difference in losses between the two passages were on the order of 2.5%. It could be concluded that there was an acceptable degree of flow similarity was achieved in the cascade.

Table 3.2: Comparison of Averaged Wake Values From North and South Passages

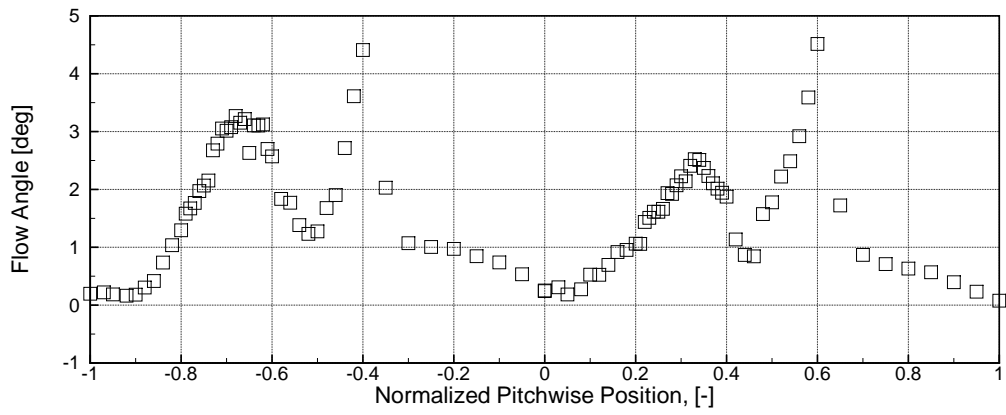
	Mixed Out	Mass Averaged
North	0.1501	0.1521
South	0.1538	0.1560
Diff.	-2.47%	-2.56%

3.7.2 Suction Surface Static Pressures

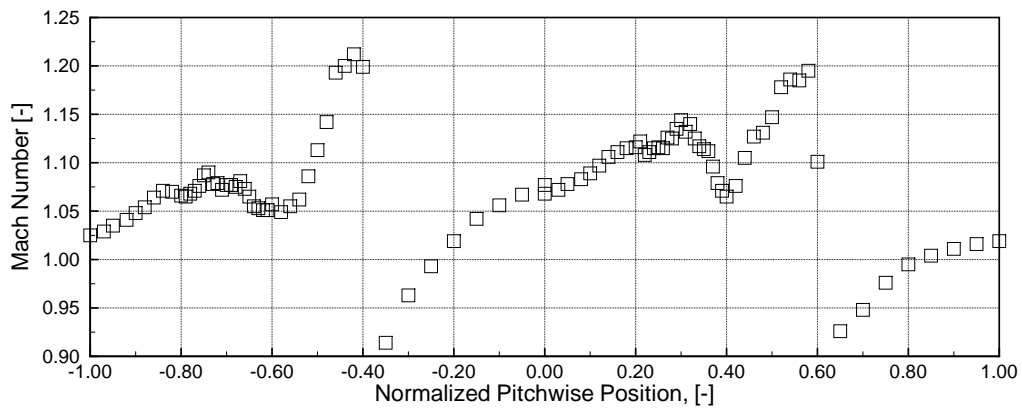
An additional indication of flow periodicity was to examine the difference between the surface static pressure distribution on two different blades within the cascade. This method was used by Lepicovsky [39] in his examination of the periodicity of the NASA transonic flutter cascade. This approach showed not only the overall similarity between the the flow in the two passages, but highlighted where the major differences occurred. Figure 3.21 shows the effect of three different tailboard settings on the differences between the suction surface static pressure distribution on blades 3 and 5. The location of these blades was shown in Figure 3.2. Figure 3.21a shows the distribution for the initial case. Figure 3.21b shows the effect of lowering the tailboard. Figure 3.21b shows the effect of optimizing the upper and lower tailboard angles. The vertical axis in Figure 3.21 showed the difference in the static pressure on both blades normalized by the pressure measured on blade 5. The attenuation of fluctuations in the normalized Mach number error due to optimizing the tailboard



(a) Total Pressure

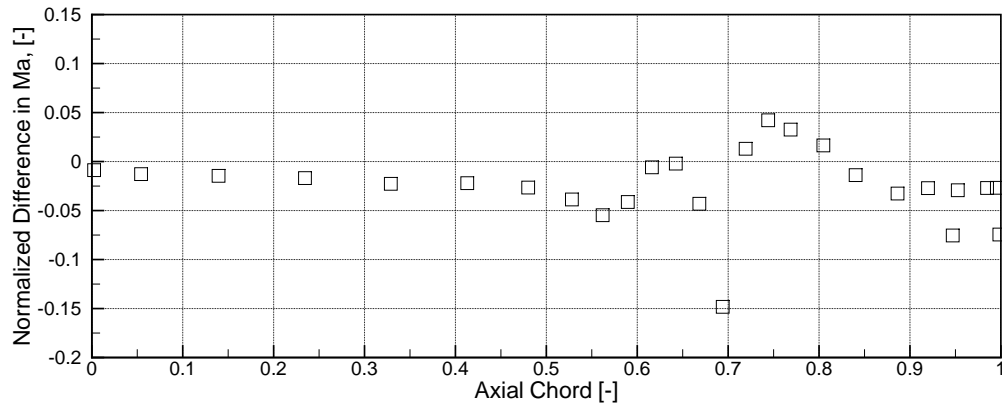


(b) Flow Angle

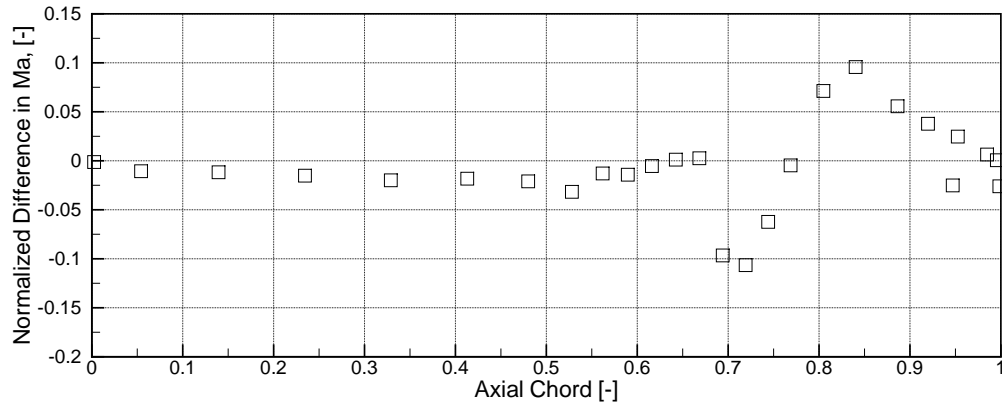


(c) Mach Number

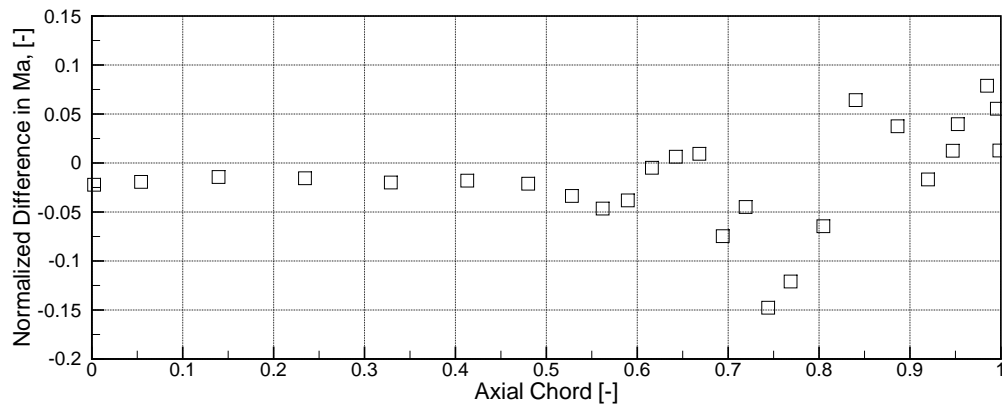
Figure 3.20: Mid-passage Traverses with optimal tailboard positions



(a) Initial case



(b) Tailboard lowered



(c) Tailboard angles optimized

Figure 3.21: Difference in suction surface static pressures at $Ma = 1.16$

angles was not as apparent as the resulting improvement in the periodicity of the sidewall static pressure taps.

The suction side static pressure measurements, together with the sidewall static pressure measurements, provided a reasonable measure of the outlet flow periodicity. It was important to note that the region of the largest discrepancies in the suction surface pressures occurred between 60 and 70 % of the pitch, (0.6 s to 0.7 s).

3.7.3 Flow Two Dimensionality

In addition to having a periodic flow within the passages being examined, it was also necessary to confirm the assumption that the flow could be approximated as two-dimensional at the mid-span plane. A qualitative measure of flow two-dimensionality was obtained using surface oil-flow visualization. The results for a variety of Mach numbers are shown in Section 5.1. However the the pattern obtained at $Ma = 0.7$ is shown in Figure 3.22.

In this image, the flow direction is from top to bottom. The secondary flow regions on two extremes of the span were clearly visible. It could be seen that the secondary flow presented a certain amount of blockage to the main flow. This blockage affected streamlines outside the secondary flow zone slightly. However, it was noted that that by the time that the flow reached the mid-span, the surface streamlines were all parallel and the flow appeared to be two-dimensional. Two dimensional flow appeared to exist for more than 50% of the span A more qualitative measure of flow two-dimensionality was obtained by examining the Axial Velocity-Density Ratio ($AVDR$), defined in Equation 3.18.

$$AVDR = \frac{\int_0^1 \Delta \dot{m}_2 d\frac{y}{s}}{\dot{m}_1} \quad (3.18)$$

This ratio sought to quantify the amount of blockage that secondary flows introduced into the passage. In a passage without blockage, the integral of the axial momentum, or product of axial velocity and density, would be identical at inlet and exit. However, in any real blade passage, the blockage introduced by secondary flows

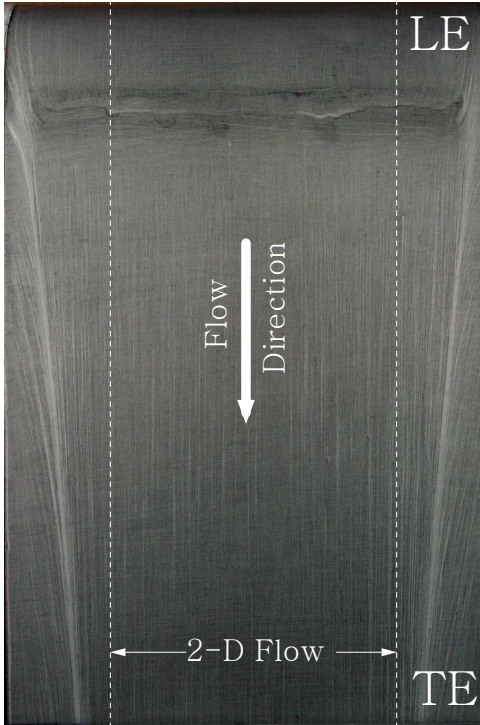


Figure 3.22: Blade surface flow pattern at $Ma = 0.7$

would cause the axial momentum at the midspan of the exit plane to be higher than at the inlet to allow for equal mass flux in both these planes. The *AVDR* quantified this increase.

The *AVDR* measured in the current experiments is shown in Figure 3.23. The *AVDR* was slightly less than unity for all measured Mach numbers. This was not a physically meaningful result since it implied that less mass was exiting from the mid-passage plane than was entering. However, the uncertainty bands on the measured values of *AVDR* were sufficiently wide that they extended to values greater than unity. The calculations for the propagation of uncertainty for the *AVDR* measurements are shown in Appendix C. The measured *AVDR* values close to unity indicated that secondary flows had a limited effect on the overall flow through the blade passage. The combination of flow visualization and *AVDR* measurements showed that the cascade had two dimensional flow over a significant portion of the blades' span.

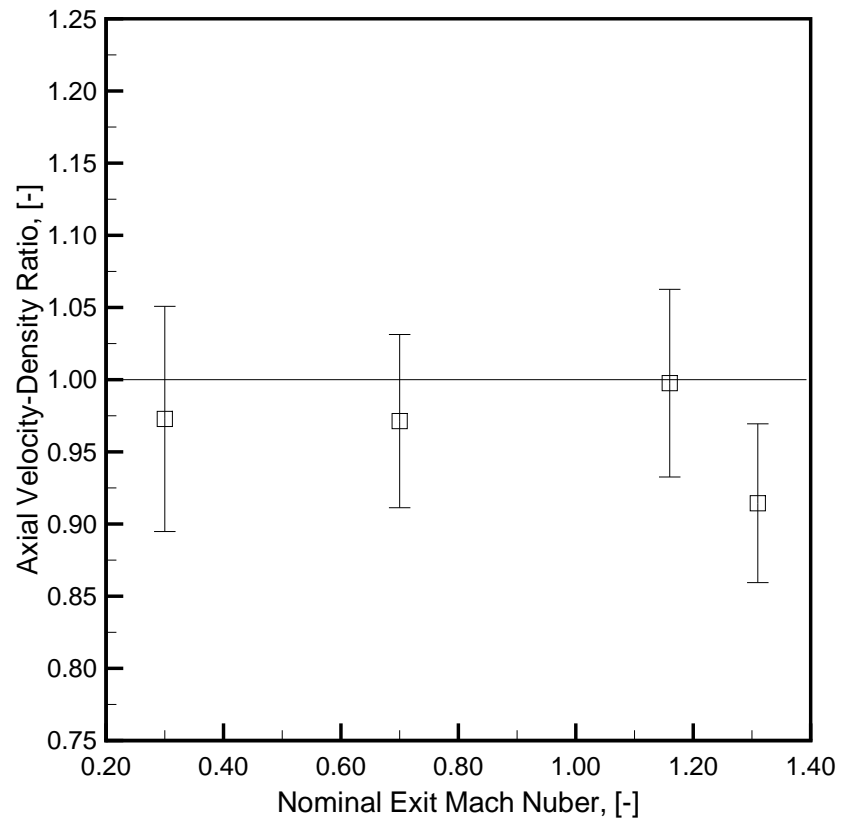


Figure 3.23: Axial Velocity-Density Ratio changes with Mach number

3.7.4 Probe Interactions

Intrusive measurements, such as pressure probes, had the potential to significantly affect the flowfield by creating a blockage, especially in transonic flows. The effect of the probe on the blade surface Mach number distribution was shown in Figure 3.24. This figure compared the surface Mach number distribution on the fourth and fifth blades when the finger probe was located at three different positions along its traverse plane. The positions were: $0.0 s$, the mid-wake position, $1.0 s$, and a position labeled *whistle*. This was a point where, at high Mach numbers, a audible whistle was heard. This figure shows that there were some differences between the Mach number distributions, but they were small and concentrated in the shock affected region of the blade which was a region of highly unsteady flow.

Another way of examining the effect of the probe on the overall flow was to show the history of the characteristic exit Mach number as the probe was traversed across the outlet measurement plane. This is presented in Figure 3.25 for a test at a nominal exit Mach number of $Ma = 1.16$. It could be seen that there was an increase in the global Mach number as the probe entered the wake region. When the probe stem was within the blade wake, the effective displacement thickness of the probe wake and blade wake were coincident, thus the blockage caused by the probe was reduced. As the probe re-entered the mid-pitch flow there was a corresponding deceleration in the characteristic exit Mach number. This showed that the probe did slightly affect the overall flow through the cascade. However, it was important to note that the effect only changed the Mach number by approximately Mach 0.03 at worst.

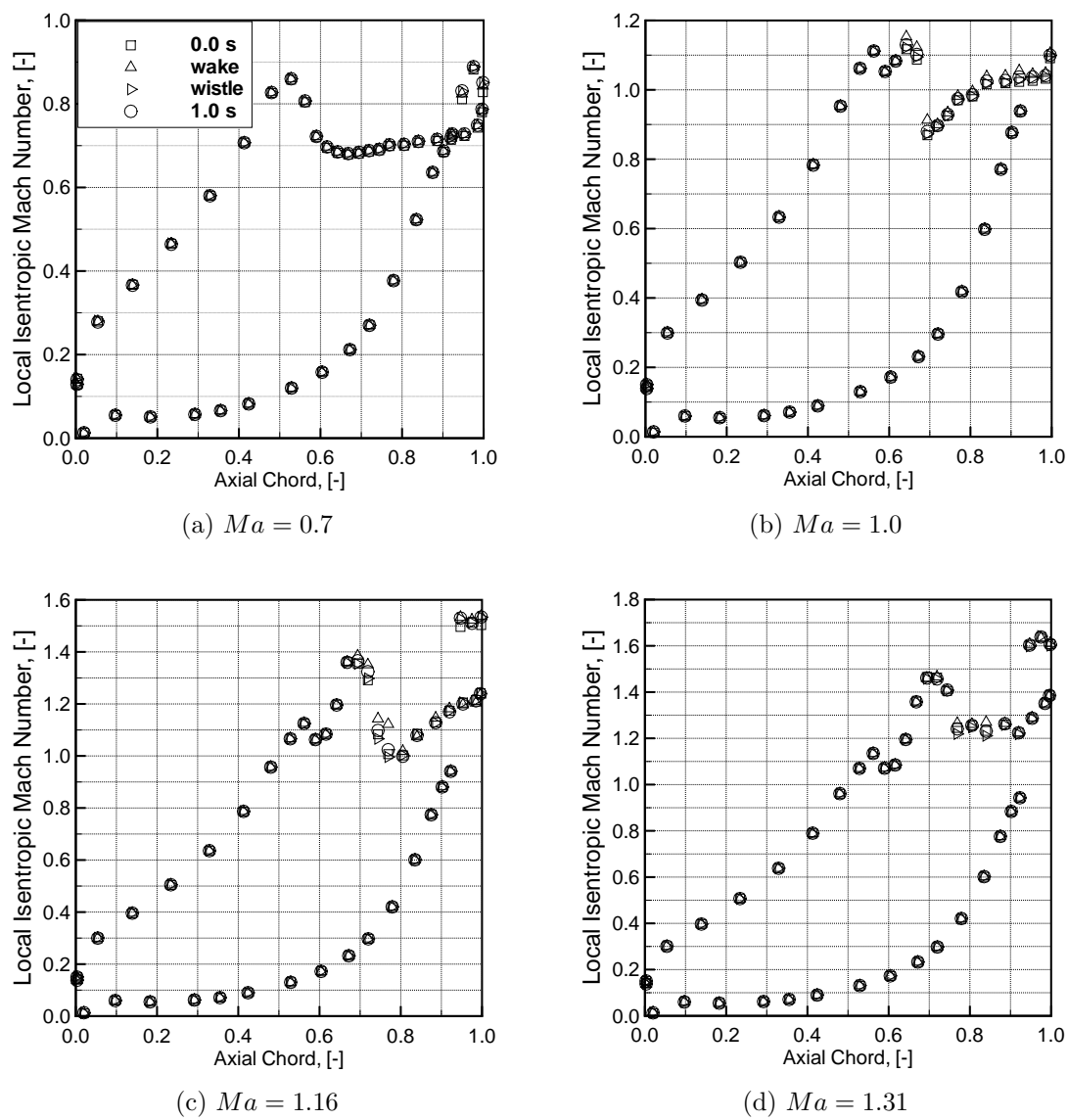


Figure 3.24: Effect of probe position on surface Mach number distributions

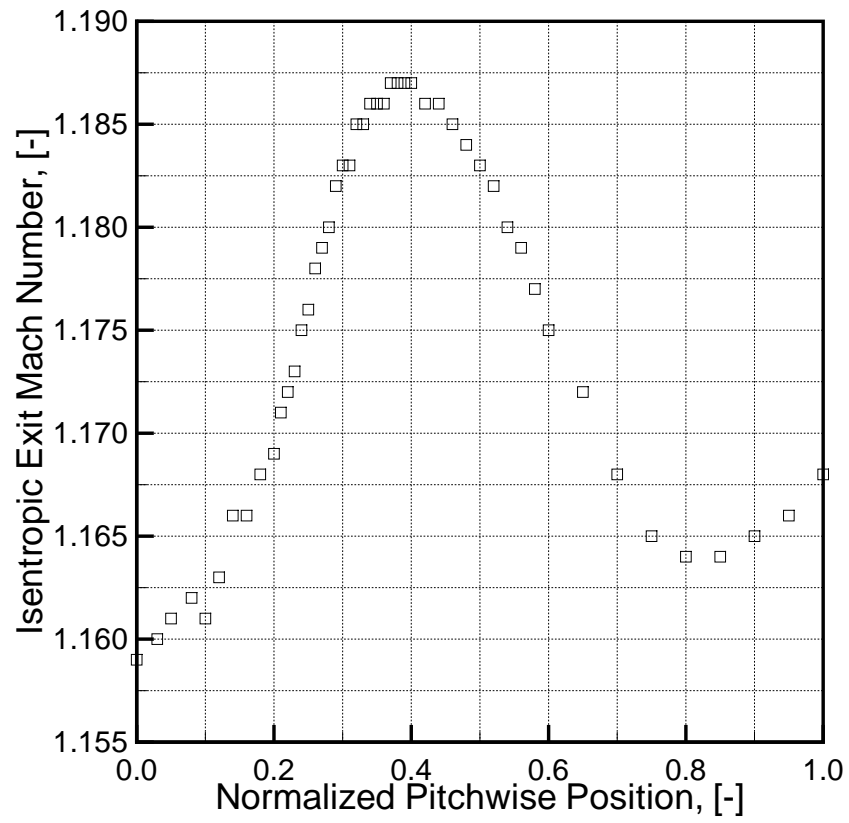


Figure 3.25: Effect of probe position on cascade Mach number

Computational Setup

Numerical investigations were performed to supplement the experimental data by allowing the flow within the blade passage to be examined quantitatively, as well as to provide some inference on the unsteady flow phenomenon. All the computations were carried out using a commercial Computational Fluid Dynamics (CFD) software package, *Fluent 6.3*, without any modifications to the code. Therefore, the computational results also demonstrated the predictive ability of modern CFD software.

4.1 Governing Equations

The *Fluent* software solved for the conservation of mass, momentum and energy at each cell. The governing equations for two dimensional compressible flow in Cartesian coordinates are given in Equation 4.1 through 4.4 in the manner used by Vuillez and Veuillot [66].

$$\frac{\partial U}{\partial t} + \frac{\partial E}{\partial x} + \frac{\partial F}{\partial y} = 0 \quad (4.1)$$

where:

$$U = \begin{bmatrix} \rho \\ \rho u \\ \rho v \\ E_t \end{bmatrix} \quad (4.2)$$

$$E = \begin{bmatrix} \rho u \\ \rho u^2 + P - \tau_{xx} \\ \rho uv - \tau_{xy} \\ (E_t + \rho)u - u\tau_{xx} - v\tau_{xy} \end{bmatrix} \quad (4.3)$$

$$F = \begin{bmatrix} \rho v \\ \rho uv - \tau_{xy} \\ \rho v^2 + P - \tau_{yy} \\ (E_t + \rho)v - u\tau_{xy} - v\tau_{yy} \end{bmatrix} \quad (4.4)$$

and:

$$\tau_{xx} = \frac{2}{3}\mu \left(2\frac{\partial u}{\partial x} - \frac{\partial v}{\partial y} \right) \quad (4.5)$$

$$\tau_{xy} = \mu \left(\frac{\partial u}{\partial y} - \frac{\partial v}{\partial x} \right) \quad (4.6)$$

$$E_t = e_o + \frac{1}{2}\rho(u^2 + v^2) \quad (4.7)$$

The solver modeled the turbulence within each cell using a Reynolds Averaged Navier Stokes (RANS) approach, which required some form of turbulence model. The $k - \omega$ model was found to be more appropriate for use with internal compressible flows. This turbulence model used two equations to track the transport, generation and destruction of two properties: the turbulent kinetic energy, k , and the specific turbulent dissipation rate, ω [27]. These two properties could be used to model how turbulence affected the flow. The specific implementation of the $k - \omega$ model which was chosen was the Shear Stress Treatment (SST). Menter *et al.* [31] stated that this model was better suited for transonic flows with shock waves than the standard $k - \omega$ model. The SST model, developed by Menter [42], used the standard $k - \omega$ model of Wilcox [67] near the wall, and the $k - \epsilon$ model in the free-stream. This formulations allowed each turbulence model to be used in the regions of flow where it was most applicable.

Several fluid properties were allowed to vary based on local conditions, while others remained fixed. The density was modeled using the ideal gas law and the viscosity related to the local temperature with the Sutherland viscosity law. Other properties; such as the specific heat capacity and thermal conductivity, were set as constants and initialized at sea level ambient values.

4.2 Numerical Model

A finite volume approach was used to solve the governing equations. The solver used the conservation of mass and energy to evaluate the density rather than the pressure. Such density-based solvers are more suitable for transonic and supersonic flows [27]. In *Fluent 6.3* the density-based solver was a coupled solver, meaning that it solved the

conservation of mass, momentum and energy in a single step rather than sequentially. The solver also formulated the governing equations implicitly rather than explicitly.

The solver evaluated the gradients between cells using the Green-Gauss *node-based* approach which, in an unstructured grid, is preferable to a *cell-based* approach [27]. The governing equations were discretized using a second-order upwind scheme. This second-order scheme reduced the magnitude of the discretization error of the model compared to a lower-order scheme. In the unsteady solutions, second-order accurate discretization over time was employed.

Simulations were performed on flows which were invariant in time as well as those which were time-dependent as shown in Table 4.1. The time-invariant solutions were referred to as *steady* or RANS solutions while the time-dependent solutions were termed *unsteady* or URANS. Variations of flow properties over time were computed in both the steady and unsteady solutions. In the steady solutions, the effects of the boundary conditions propagated through the domain until a converged time-invariant solution was obtained. Essentially, one iteration was treated as a time step in the steady solution. For the unsteady solutions, the fluctuating behavior of the flow was modeled at fixed time steps. Between each time step, the solution was iterated until a converged and locally time-invariant solution was obtained. Therefore, in unsteady solutions, there were effectively two time steps: one *true* time step which was used to model the unsteady behavior, and one *local* time step which modeled how the changes between true time steps propagated through the domain.

Tests showed that the size of the local time steps taken by the solver, when obtaining a time-invariant solution, was a very important criterion for the stability of the solution and for the rate of convergence. This time step was quantified by the Courant-Friedrichs-Lewy (*CFL*) number [37]. It is defined in Equation 4.8.

$$CFL = u_i \frac{\Delta t_i}{\Delta x_i} \quad (4.8)$$

The *CFL* number relates how far the flow traveled in one local time step ($u_i \Delta t_i$) to the local grid spacing, (Δx_i). Note that time steps were analogous to iterations when computing a time-invariant solution. If the *CFL* number was less than unity, the flow

would take more than one iteration to pass through each cell. This increased both the stability and the convergence time. In the present simulations a CFL number of 5 was found to combine fast and accurate solution convergence with good stability.

4.3 Boundary Conditions

The solution domain was a single blade, bounded by upper and lower periodic boundaries which followed the blade's chord line. The domain is shown in Figure 4.1 with the mesh suppressed. The flow rate through the domain was set by the constant pressure inlet and exit surfaces. The total pressure at the inlet was set as the sea level ambient total pressure, 101.325 kPa. The pressure at the exit was set to be the static pressure which corresponded to the desired exit Mach number for the specified inlet total pressure.

Initial tests showed that the computational results did not correctly predict the stagnation point on the blade. Section 3.7 showed that there was a significant, 5 to 6°, off-design incidence angle in the cascade. Therefore, the inlet flow was set at the measured mass-averaged inlet flow angle, which is given in Table 4.2 for each Mach number examined. For cases where no inlet flow angle was available, the angle measured at the closest exit Mach number was used. This resulted in a much improved prediction of the flow over the blades. The Mach numbers at which the steady and unsteady simulations were performed are given in Table 4.1.

The turbulence properties were set at the inlet. A turbulence intensity of 0.2% and a length scale of 0.001 m were chosen. These values were similar to the turbulence properties which would be expected to be present at the inlet of a suction-type cascade drawing from a room filled with still air. These same values were used by Currie and Carscallen [18] in their simulation of an identical blade.

4.4 Solution Procedure

Each case was initialized so that the entire domain was at the exit static pressure, and the velocity vector was set at the inlet angle. The solution was initially unstable

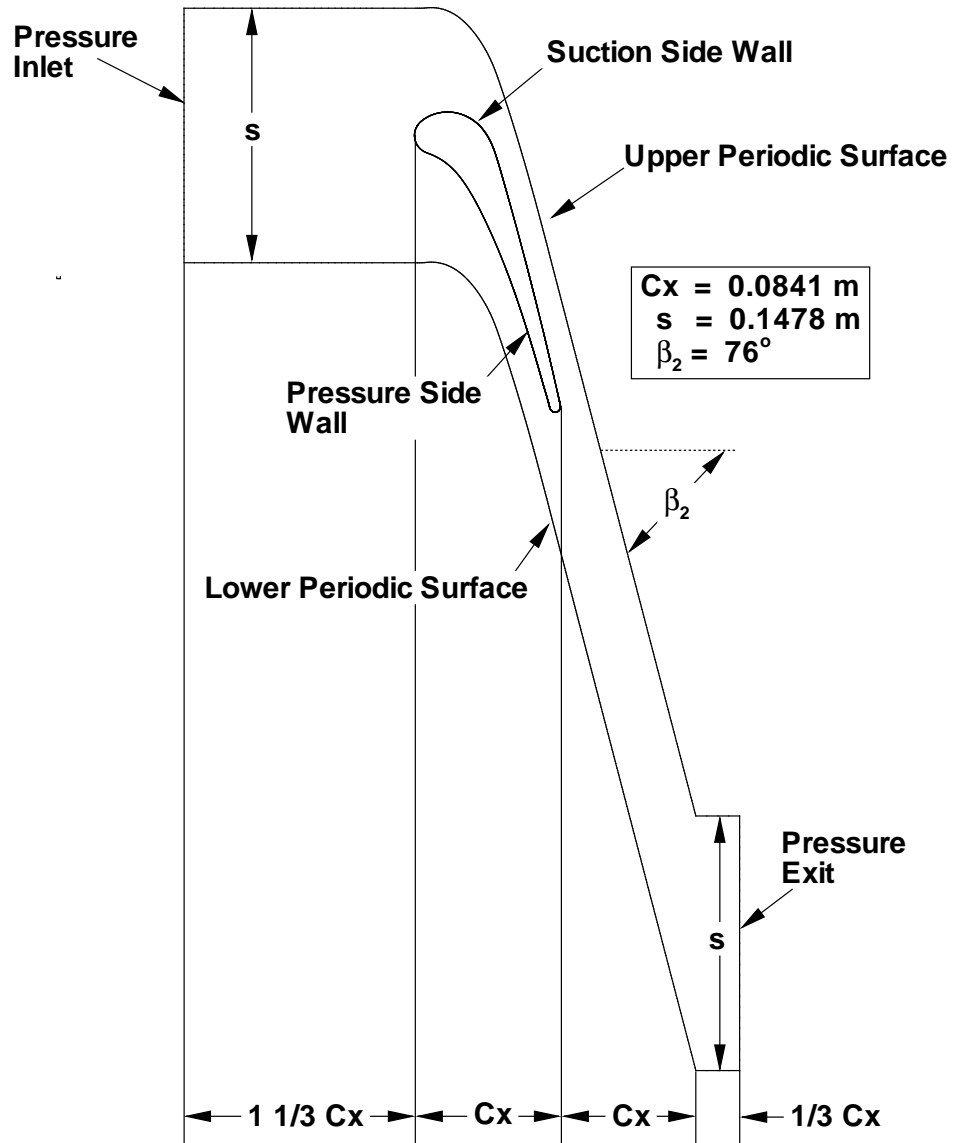


Figure 4.1: Computational domain

Table 4.1: Exit Mach numbers for CFD simulations

Mach Number	Steady	Converged Residual	Unsteady
0.3	✓	2.54×10^{-5}	
0.5	✓	3.23×10^{-4}	
0.7	✓	3.79×10^{-4}	✓
0.9	✓	3.23×10^{-4}	
1.0	✓	2.02×10^{-3}	
1.16	✓	3.26×10^{-4}	✓
1.31	✓	1.98×10^{-6}	
1.40	✓	2.81×10^{-6}	
1.50	✓	8.07×10^{-5}	
1.60	✓	8.22×10^{-5}	

Table 4.2: Inlet flow angles

Mach Number	0.3	0.7	1.16	1.31
Mass-Averaged α_1	-3.99	-4.49	-4.37	-4.94

and required the CFL number to be reduced to 0.5 and for first-order upwind discretization to be used. After every 1000 iterations, the CFL number was increased by approximately 150% until it reached a value of 5. This value was chosen since it was large enough to allow the solution to converge but was small enough to prevent uncontrolled oscillations. After 3000 iterations, the discretization scheme was changed to second-order upwind to improve the accuracy of the solution.

Each case was run until convergence. At low Mach numbers, convergence was defined as the point past which the normalized residuals from the continuity equation were close to 10^{-4} in magnitude and had stopped decreasing appreciably after multiple iterations. As the Mach number was increased, no plateau in the residual was observed after many thousands of iterations. In these cases, convergence was defined as the point where the residual in the continuity equation became less than 10^{-6} . The normalized residual after the final iteration for each steady case is given in Table 4.1.

The unsteady simulations were initialized using the converged steady solutions. Carscallen *et al.* [10] determined that the shedding frequency of the blades was approximately 10 kHz. To obtain around twenty time steps per shedding cycle, a time

step of 2.5×10^{-6} s was used. During each time step, the solution was iterated until the residual in the continuity equation dropped below 10^{-7} . This residual threshold was typically obtained after 100 iterations. The *CFL* number was retained at 5 for the unsteady simulations. With a *CFL* number of unity, initial tests failed to develop vortex shedding. The unsteady simulations converged to a periodically unsteady solution. This was determined by monitoring the base pressure. Once this pressure began to behave in a sinusoidal manner with increasing time steps the unsteady solution was deemed converged.

4.5 Mesh Quality

The mesh applied to the domain is shown in Figure 4.2. The majority of the mesh was unstructured with quadrilateral cells. However, there were structured regions of the mesh placed at the inlet, in an internal zone downstream of the trailing edge as well as in the boundary layer region around the blade. The structured zone in the wake extended almost to the trailing edge boundary layer mesh, as seen in Figure 4.2. This section of structured grid also extended twenty trailing edge diameters downstream.

The boundary layer properties are also shown in Figure 4.2. These properties are before grid refinement. The only grid refinement used was to reduce the dimensionless near-wall grid spacing, y^+ , on the pressure and suction surface such that its value was less than unity. This was necessary for the $k - \omega$ scheme to work accurately.

4.5.1 Grid Independence study

To ensure that the mesh was sufficiently fine that the solution was a function of only the boundary conditions rather than the mesh density, a grid independence study was conducted. A Mesh was generated with 157% the number of cells as the mesh used for the steady and unsteady solutions. This refinement resulted in a 7.7% change in the mixed-out losses at $Ma = 1.16$, from $Yt = 1.69$ in the coarse grid to $Yt = 1.77$ in the refined grid. This showed that the mesh was sufficiently dense to be independent of grid spacing effects.

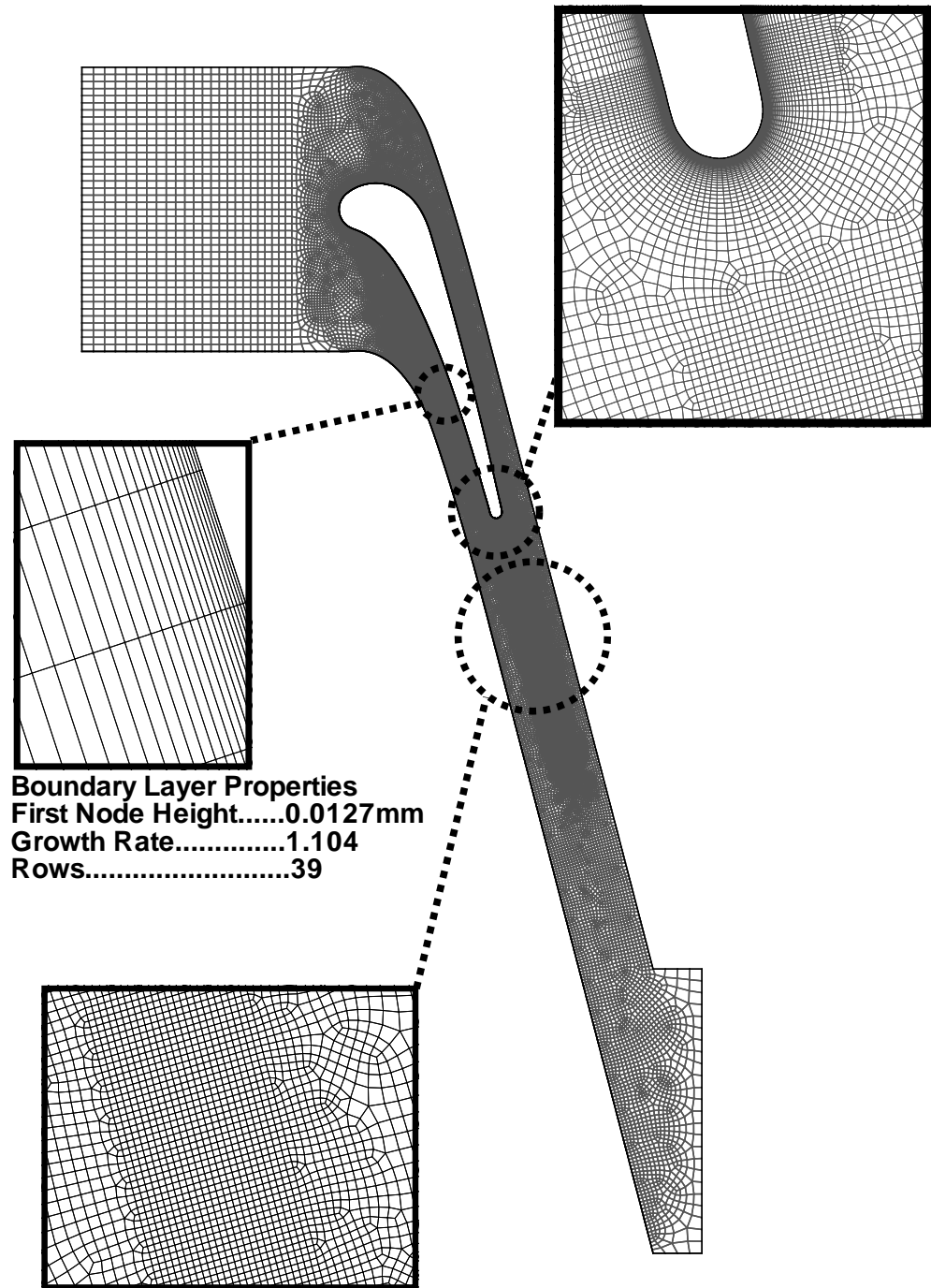


Figure 4.2: Computational mesh

4.6 Post-Processing

The results from the unsteady predictions of the flow within the blade passage were analyzed to create images similar to those produced by the schlieren photographic method. Schlieren photography creates an image whose intensity is proportional to the rate of change of the density field in a direction perpendicular to a knife-edge placed in the light beam which is traversing the flow. For most of the images presented in subsequent sections the knife-edge was simulated as being set at the exit angle of 79° , as in the high quality schlieren images produced by Sieverding [57]. However, in some cases, rotating the knife-edge 90° from this setting led to better definition of the shock waves.

Chapter 5

Results

Several different experimental and computational investigations were performed on the cascade to examine the behaviour of the flow through the blading under investigation. The details of how the various experimental methods were implemented were addressed in Chapter 3. This chapter will focus on the results from the individual tests while Chapter 6 will assemble the entire set of experimental and computational results to describe the overall flow through the blade passage.

There were five different investigations performed on the blades: blade surface static pressure and base pressure measurements, traverses of the inlet and exit flow and oil-film and schlieren flow visualization. The experimental data were supplemented by steady (RANS) and unsteady (URANS) computational simulations. Table 5.1 shows the Mach numbers at which the various tests were performed.

Table 5.1: Test Conditions

Exit Mach Number	0.10	0.20	0.30	0.40	0.50	0.60	0.70	0.80	0.90	1.00	1.10	1.20	1.30	1.40	1.50	1.60	1.70	
Surface Pressure	✓	✓	✓	✓	✓	✓	✓	✓	✓	✓	✓	✓	✓	✓				
Base Pressure	✓	✓	✓	✓	✓	✓	✓	✓	✓	✓	✓	✓	✓	✓				
Exit Traverse			✓				✓			✓		✓	✓					
Inlet Traverse			✓				✓					✓	✓					
Flow Visualization							✓			✓		✓	✓	✓				
RANS			✓		✓		✓		✓	✓		✓	✓	✓	✓	✓	✓	✓
URANS							✓					✓	✓					

Due to the design of the cascade, the Reynolds number was varied along with the exit Mach number. Table 5.2 shows the Reynolds number corresponding to each test's exit Mach number assuming an exit plane temperature of 298 K. The Reynolds number computed in Table 5.2 was based the nominal exit velocity and the true chord length as the characteristic properties, as shown in Equation 5.1.

Table 5.2: Variations of Reynolds number

Ma	Re _{Model}	Re _{Engine}
0.70	2.65×10^6	0.0903×10^6
1.00	3.79×10^6	0.129×10^6
1.16	4.40×10^6	0.150×10^6
1.31	4.50×10^6	0.169×10^6
1.40	5.31×10^6	0.181×10^6

$$Re = \frac{Ma_2 \sqrt{\gamma R T_{char}} C}{\nu} \quad (5.1)$$

Table 5.2 also lists the Reynolds number at the same exit Mach number but with air at 1400 K and using an engine representative length scale. This was meant to be an approximation of the blade Reynolds number in a real engine.

Between $0.7 \leq Ma \leq 1.4$ the model Reynolds number varied between 2.65×10^6 and 5.31×10^6 . Though this represented a doubling of the Reynolds number, values remained in a range characteristic of fully turbulent flow. However, the model Reynolds number was an order of magnitude larger than the engine Reynolds number. This may mean that the behaviour of the flow over the blades, especially within the boundary layer, may be different between the cascade model and the engine. This could have an effect on how the flow would react to adverse pressure gradients on the blade and to shock-boundary layer interactions.

5.1 Surface Flow Visualization

The oil-film images, taken at four different Mach numbers, are shown in Figure 5.1. The oil flow technique gave a qualitative measure of the wall shear stress on the suction surface of the blade. Darker regions on the blade represented regions where there was a low wall shear stress, while lighter regions showed a higher shear stress. However, very light regions also occurred where the vortical structures within regions of separated flow entrained the oil from the blade surface.

There are two scales placed along the right hand side of the images. The outer-most scale shows the normalized suction surface length, while the inner-most scale

shows the percent of axial chord. The static pressure tap locations are shown as red lines on the inner-most scale.

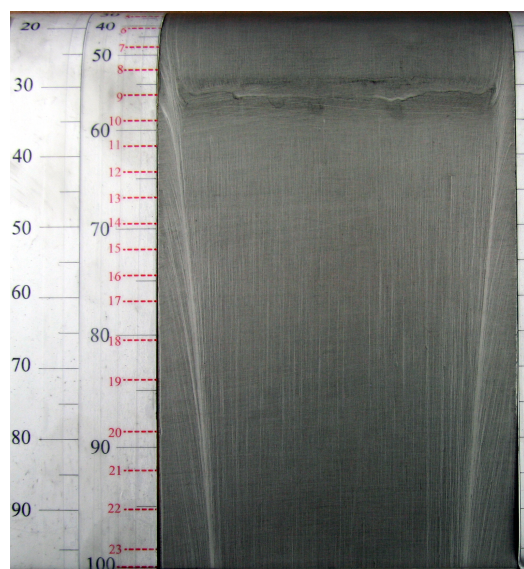
5.1.1 Subsonic Flow at $Ma = 0.7$

The subsonic flow over the blade is shown in Figure 5.1a for a nominal Mach number of 0.70. This figure showed that the flow was two dimensional at the midspan as the secondary flows at the two endwalls only extended 14% of the span into the passage. At approximately $0.55 C_x$, there was a dark, low shear stress, region which persisted across the span of the airfoil. This feature showed that at this axial location, some feature of the flow or the blade's geometry disturbed the boundary layer so that the wall shear stress was reduced, perhaps sufficiently to promote separation. The cause of this disturbance will be discussed in detail with reference to the static pressure measurements in Section 5.3.

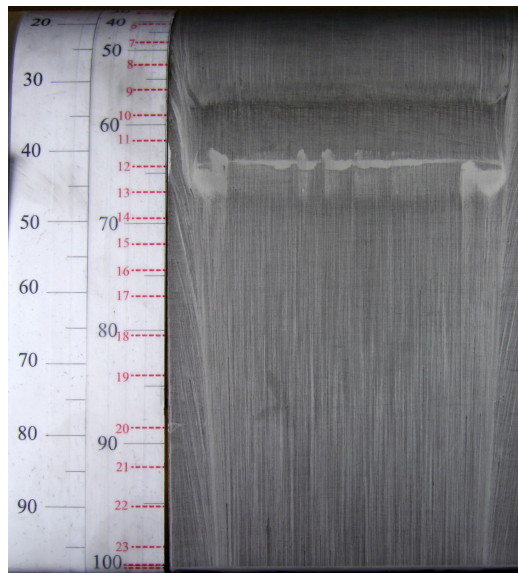
5.1.2 Transonic Flow at $Ma = 1.16$

The behaviour of the blade at design conditions is shown in Figure 5.1c. At approximately $0.58 C_x$ there is a dark line visible on the blade. The throat of the blade passage is approximately at this location. This discontinuity in the oil-flow pattern occurred at approximately the same location as the low-shear region observed in Figure 5.1a. The origins of the discontinuity observed at supersonic Mach numbers will also be addressed in Section 5.3.

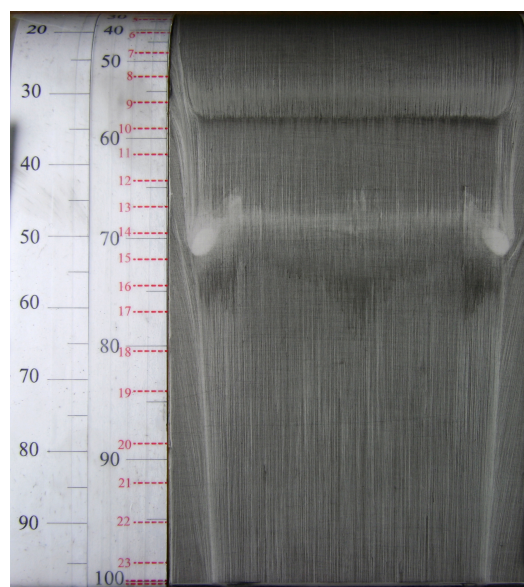
Further downstream, at $0.68 C_x$, a lighter zone was visible. This is the region of shock impingement from the adjacent blade which caused the flow to separate. One interesting phenomenon which was observed in the oil-flow images at this Mach number was the presence of a vortex whose axis of rotation appeared to be normal to the blade surface. This vortex occurred in the region where the developing horseshoe vortex interacted separated flow. A detailed oil flow image of this feature is shown in Figure 5.2. This phenomenon did not appear in the subsonic flow shown in Figure 5.1a, however there was some evidence of it in Figure 5.1b and Figure 5.1d.



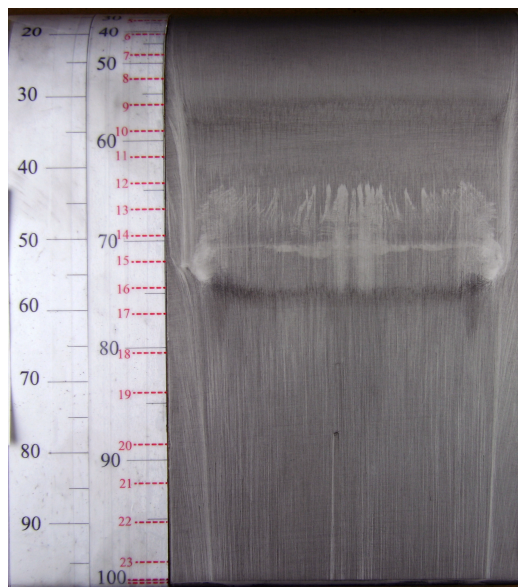
(a) Mach 0.70



(b) Mach 1.00



(c) Mach 1.16



(d) Mach 1.31

Figure 5.1: Oil-film flow visualization results

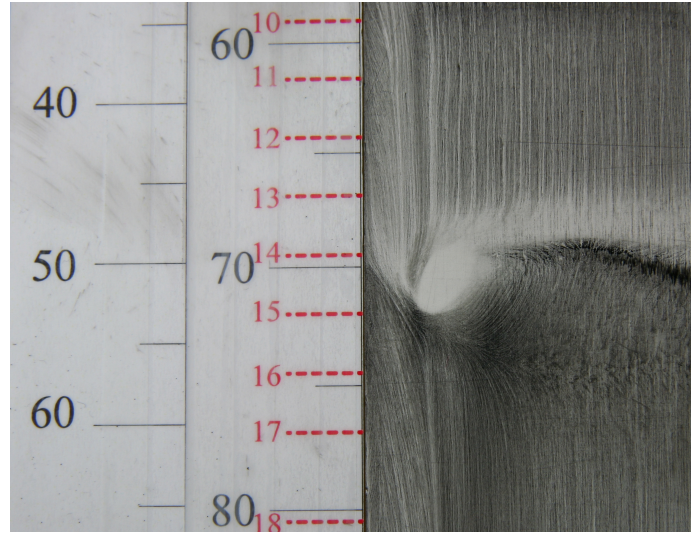


Figure 5.2: Vortex observed at Mach 1.16

The mechanism driving this vortex's formation is not yet understood. Since these vortices were located close to the cascade sidewalls, they were not detected by any of the subsequent tests which focused primarily on the mid-passage flow.

5.2 Passage Flow Visualization

It was important to investigate the general behaviour of the flow within the passage to understand the details of the local flow-fields on the blade surface and in the wake. This was accomplished using new computational studies and archival schlieren images from previous studies performed on the same cascade.

5.2.1 Experimental Schlieren Images

Previous experimental programs undertaken in the NRC transonic linear cascade have produced many high quality schlieren images. In Chapter 3, it was noted that there was a small difference between the old and new blades in the as-manufactured geometry of the trailing edge. The details of how the schlieren images were produced were given by Fleige [26]. These images have been previously published in [26, 10, 18, 29]. Figures 5.3a, 5.3b and 5.3c show the passage flow at $Ma = 0.7$, $Ma = 1.0$ and $Ma = 1.16$, respectively. These images showed the salient features of the passage

flow. These features will be examined in more detail with reference to computational results which allowed a more qualitative comparison with the experiments.

5.2.1.1 Subsonic Flow

The subsonic flow thorough the passage is shown in Figure 5.3a. This image shows a distinct von Kármán vortex street in the wake of the blade as well as a series of acoustic waves which traveled upstream through the passage. These waves were observed experimentally by Sieverding [57] using high speed schlieren photography. Sieverding stated that the waves were formed by the outward motion of the the separating shear layer on the trailing edge. This meant that as the flow traveled around the trailing edge, it would eventually lack sufficient momentum to remain attached in the face of the large adverse pressure gradient. This would cause the flow to separate. The separated shear layers oscillated due to the vortex formation at the trailing edge. As the shear layer moved towards the pressure or suction surface, it compressed some of the core flow which formed a subsonic compression, or acoustic, wave. Since the passage flow was subsonic these waves could propagate upstream. This behaviour was also observed in the unsteady computational simulations of the flow at $Ma = 0.7$.

5.2.1.2 Transonic Flow

At sonic conditions, $Ma = 1.0$, Figure 5.3b shows a normal shock wave across the passage. As in the subsonic case, the flow at $Ma = 1.0$ exhibited von Kármán vortex street in the wake of the blade.

As the Mach number was increased to design conditions of $Ma = 1.16$, the characteristic supersonic wake structure, described in Section 2.1.2 was observed. Lighter regions at the start of the trailing edge, labeled (B) showed the expansion waves formed as the flow was turned around the trailing edge. Before these expansion waves, an oblique shock labeled (A) was observed, of which there was no evidence in either the oil-flow images, the surface static pressures or the computational results.

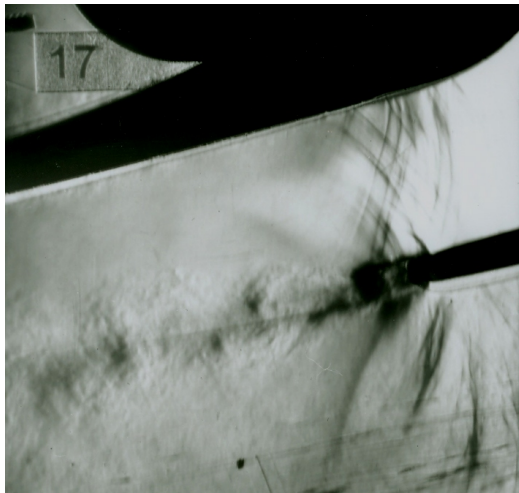
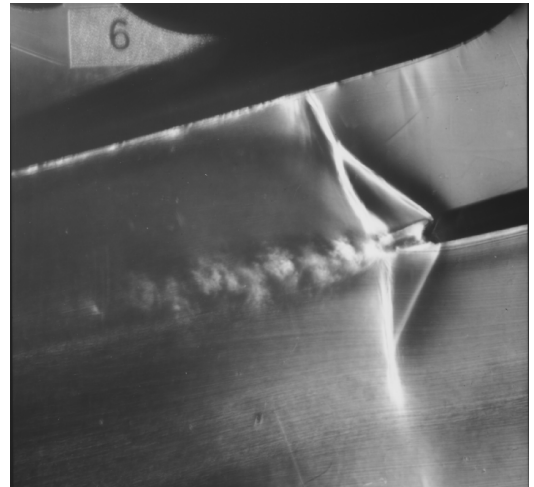
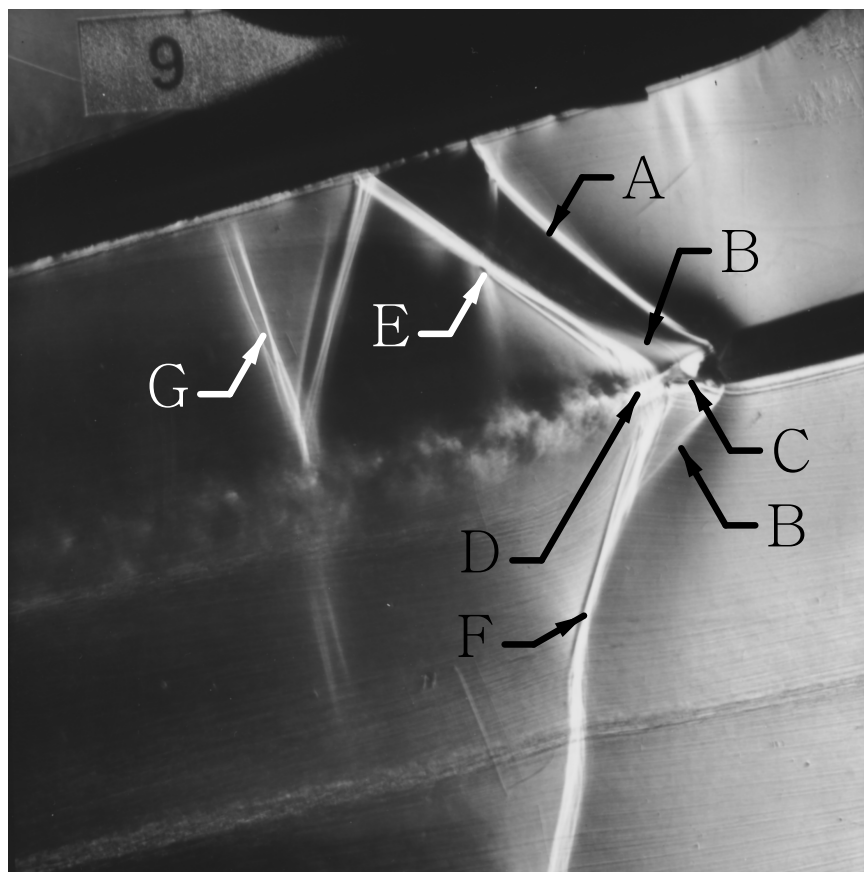
(a) $Ma = 0.70$ (b) $Ma = 1.00$ (c) $Ma = 1.16$

Figure 5.3: Experimental schlieren images

This shock will be discussed subsequently. Distinct lines (C) defined the strong shear layers which separated the base triangle from the rest of the flow. The base triangle was concluded by two oblique shock waves which originated at the point of confluence (D). The oblique shock which emanated from the pressure side of the blade (E) impinged on the adjacent suction surface. The suction side oblique shock (F) did not interact with any blades.

Section 3.1.2 noted that there was a slight variation in geometry between the experiments of Carscallen [8] and Fleige [26] and the current blade. This imperfection at the trailing edge may have been the cause of the first oblique shock emitted from the pressure surface. This behaviour has been observed by Sonoda *et al.* [61] who noted that a small, in this case negative, step on the pressure surface caused an oblique shock to form upstream of the trailing edge at supersonic exit Mach numbers. It is therefore likely that the small positive step on the pressure surface of the blades used in previous experiments may have caused the flow to turn away from the blade surface and initiated the oblique shock wave which was labeled (A) in Figure 5.3c.

The images in Figure 5.3 also showed the development of the vortex structure in the blade's wake. Figures 5.3a and 5.3b both showed a von Kármán vortex street in the wake of the blade. Figure 5.3c also showed distinct vortices in the wake but they did not have the same *classical* von Kármán structure as was observed at lower Mach numbers. This behaviour was discussed in Chapter 2.

5.2.2 Computed Schlieren Images

The experimental passage flow visualization was supplemented by computational predictions of the passage flow. Chapter 4 discussed the calculation procedure and post-processing for the computational results. The unsteady passage flow at $Ma = 0.7$ and $Ma = 1.16$ are shown in Figure 5.4 and Figure 5.5 respectively. The results from the remaining steady simulations are shown in Appendix D. These images were annotated with the percent axial chord attached to the blade's suction surface and the percent pitch attached to an axial plane $1.40 C_x$ downstream of the blade's leading edge. This allowed a qualitative comparison with the experimental measurements.

Additionally, the simulated angle of the knife edge was shown by a roundel placed on one of the blades.

5.2.2.1 Subsonic Flow at $Ma = 0.7$

The computational prediction of the unsteady flow field at $Ma = 0.7$ is shown in Figure 5.4 for a converged solution at a time step where the flow was exhibiting periodically unsteady behaviour. The same distinct von Kármán-type vortex structures were seen in this image as in those taken by Fleige [26].

Additionally, Figure 5.4 shows the unsteady acoustic waves, discussed with reference to Figure 5.3a, propagating upstream through the passage and interacting with the adjacent blade's suction surface. It appears that an acoustic wave was reflected off the suction surface when the adjacent blade's acoustic wave interacted with it. Though Figure 5.4 showed this interaction occurring at $0.57 C_x$, the unsteady results showed that the acoustic wave first impacted the suction surface at $0.65 C_x$ and both the incident and reflected wave traveled upstream along the suction surface. Therefore, this interaction cannot be solely responsible for the low shear stress observed locally at $0.57 C_x$ in Figure 5.1a.

5.2.2.2 Transonic Flow at $Ma = 1.16$

The results from the unsteady computations performed at $Ma = 1.16$ are shown in Figure 5.5. An additional shock is observed in Figure 5.5 of which there was no evidence in the oil flow images, though it was visible in the experimental schlieren. This shock occurred about $0.85 C_x$ and joined with the reflected pressure surface shock wave to intersect the traverse plane at approximately $0.1 s$. Some of the experimental schlieren images taken at $Ma = 1.16$, such as Figure 5.3c, did show a normal shock occurring at this location. This shock is labeled (G) in Figure 5.3c. However, there were several other images gathered at the same speed where the normal shock did not appear.

Figure 5.5 also showed an interesting region of low gradient which stretched across

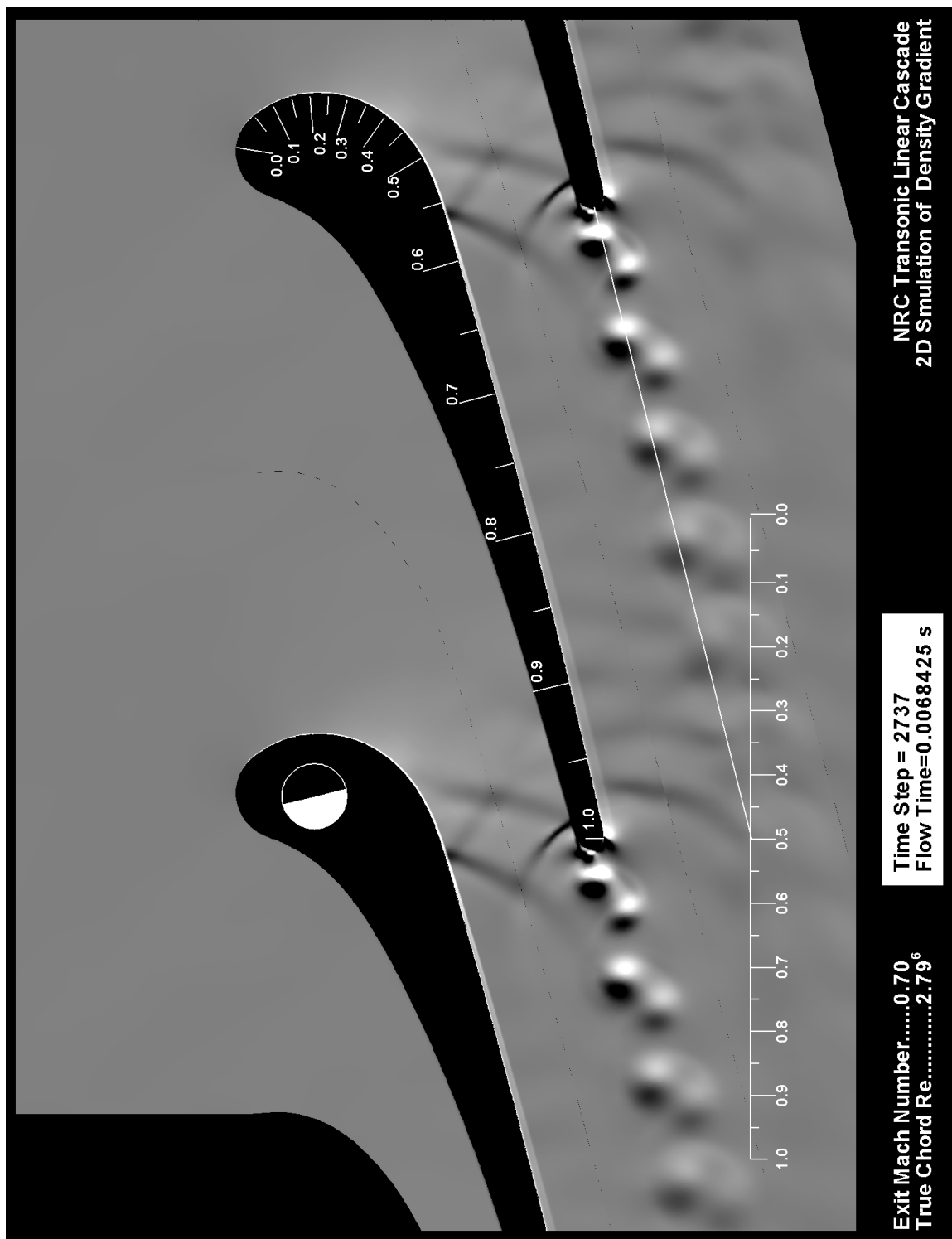


Figure 5.4: Computed passage flow field at $Ma = 0.70$

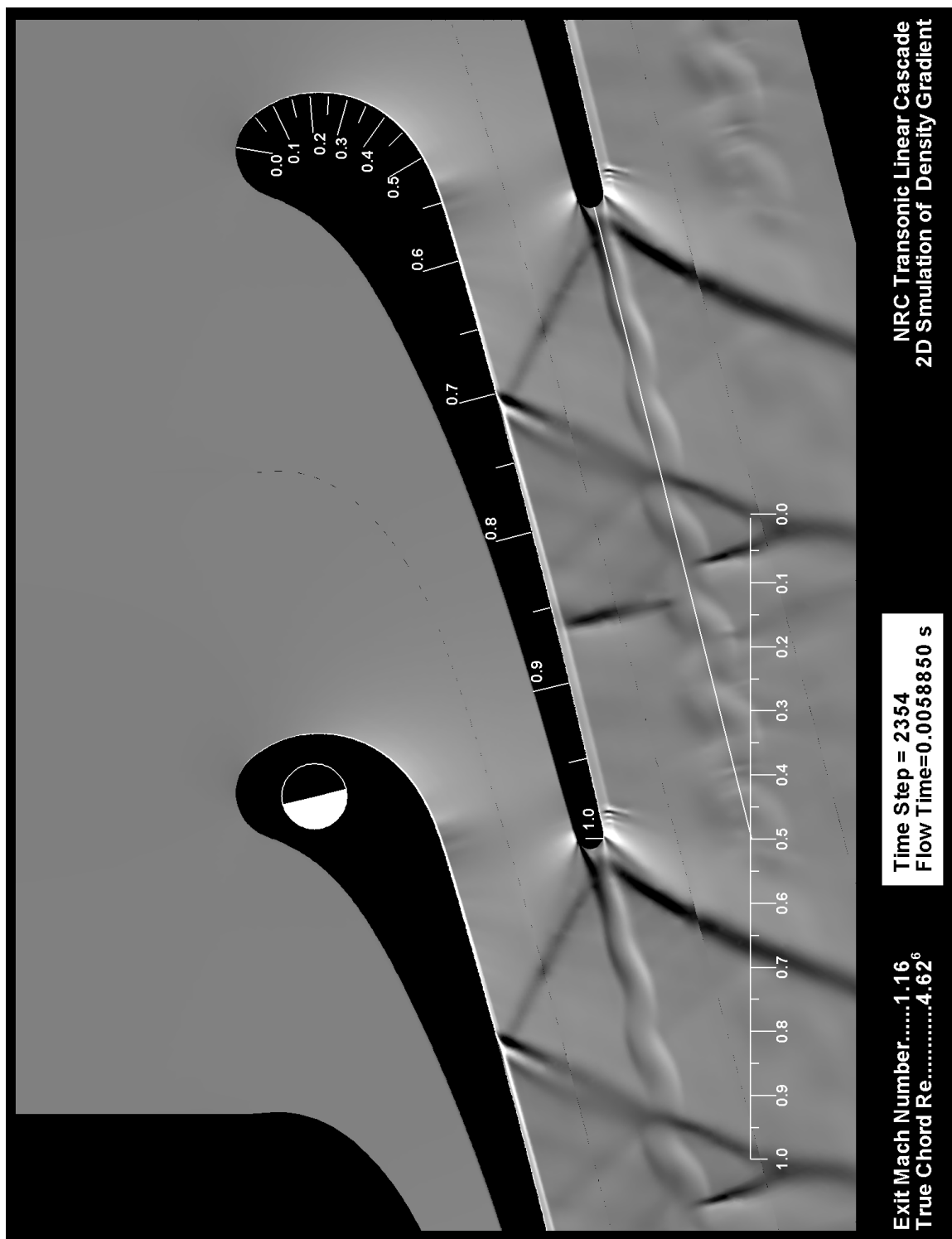


Figure 5.5: Computed passage flow field at $Ma = 1.16$

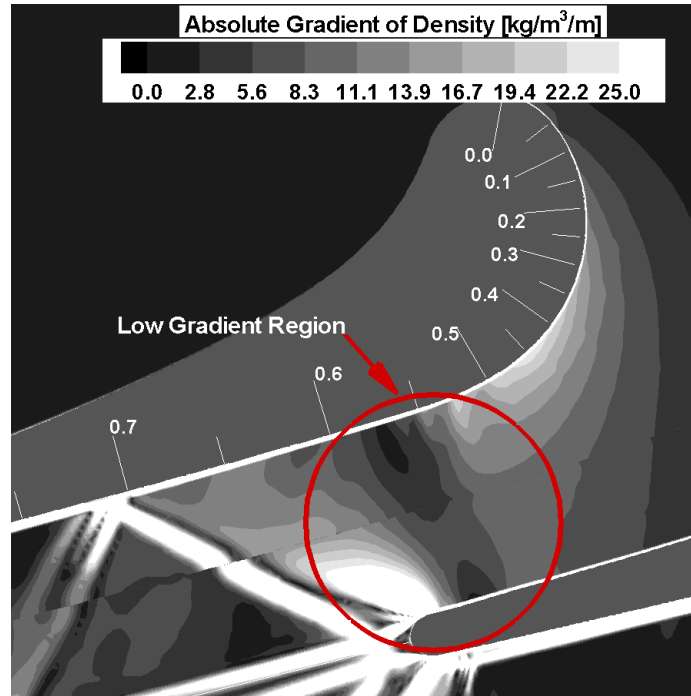


Figure 5.6: Detailed view of Total Gradient at the Passage Throat for $Ma = 1.16$

the passage between 55 and $60\%C_x$. This region was where there was an unexplained dark line deposited in Figure 5.1c. Figure 5.6 shows a closeup view of the magnitude of the two dimensional density gradient within the passage. There is a local region of low total density gradient centered at $0.57 C_x$ which was coincident with both the passage throat and the discontinuity in Figure 5.1c. This behaviour will be discussed with reference to the static pressure distributions in Section 5.3. The slight discontinuity in the contours at the mid-passage was an unavoidable artifact of the post-processing.

5.3 Blade Surface Static Pressure Distribution

Pressure and suction surface static taps permitted a detailed examination of the flow over a blade. Due to manufacturing limitations, only one side of a blade was instrumented. Therefore, the data which will be presented contain measurements from the pressure surface of the third blade and the suction surface of the fourth blade. Additional computational data on the behaviour of the flow over the blade were available from the computational studies described in Chapter 4. When available, the computational results were compared to the experimental data.

There were various methods for normalizing static pressure data. In low-speed flow, the static pressure coefficient has typically been used. However in transonic and supersonic flows it was more useful to determine a local Mach number, which was an approximation of the local velocity on the blade. The local Mach number gave a good indication of the flow behaviour since it shows both the acceleration of the flow and approximately how close the local flow was to becoming sonic. The uncertainty in the measurements of the local Mach number were found to be negligible (see Appendix C).

5.3.1 Subsonic Flow

Figure 5.7 shows the surface Mach number distributions for the test conditions with a subsonic exit Mach number. The flow accelerated up to the throat of the blade, at $0.57 C_x$, and proceeded to slow as it entered the expanding region of uncovered flow turning. Past $0.65 C_x$ the low suction surface curvature created a parallel channel, resulting in an essentially constant velocity region up to the trailing edge. In this region, the large total pressure losses in the wake made the Mach number defined in the base region meaningless. The flow in the base region will be more thoroughly examined in Section 5.4.

Both steady and unsteady RANS calculations were performed with a nominal exit Mach number of $Ma = 0.7$. Figure 5.8 compares the measured surface Mach number distribution to the RANS prediction. This figure shows that excellent agreement was obtained across the blade at a subsonic Mach number of 0.7. By using the experimentally measured mass-averaged inlet flow angle, the stagnation point was properly predicted. The agreement remained excellent across the pressure and suction surface, this will be contrasted to the behaviour at supersonic Mach numbers.

In Section 5.1.1 it was noted that oil flow image produced at $Ma = 0.7$ showed that there was a dark region extending across the span of the blade in the region of $0.57 C_x$. The cause of this disturbance could not be explained by the oil flow images alone. However, the local static pressure data allowed better inferences about the flow in this region. Another factor which explained this region of flow was the slope of the suction surface profile, which is shown in Figure 5.9. Though the flow near a curved

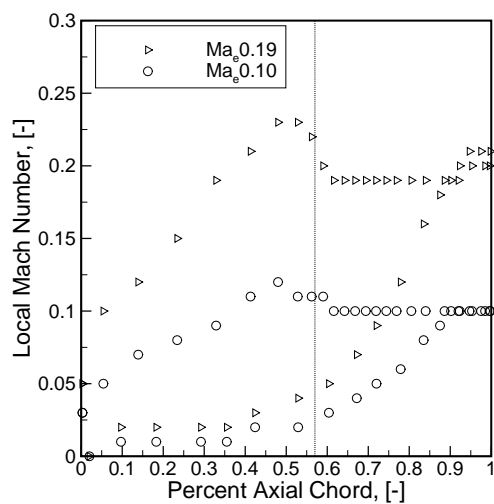
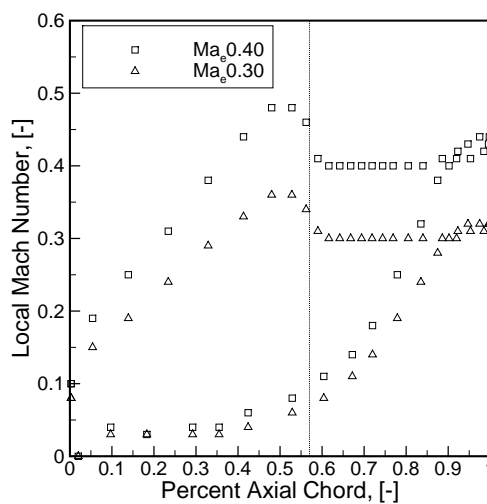
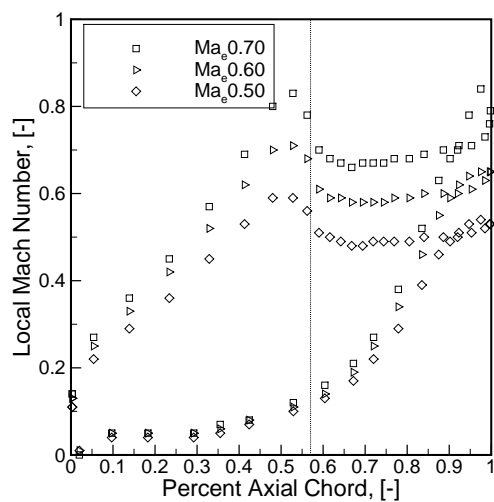
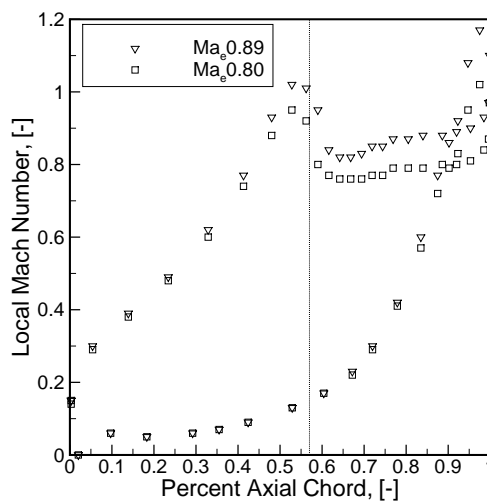
(a) $Ma = 0.1$ to $Ma = 0.2$ (b) $Ma = 0.3$ to $Ma = 0.4$ (c) $Ma = 0.5$ to $Ma = 0.7$ (d) $Ma = 0.8$ to $Ma = 0.9$

Figure 5.7: Local Mach numbers for subsonic flow

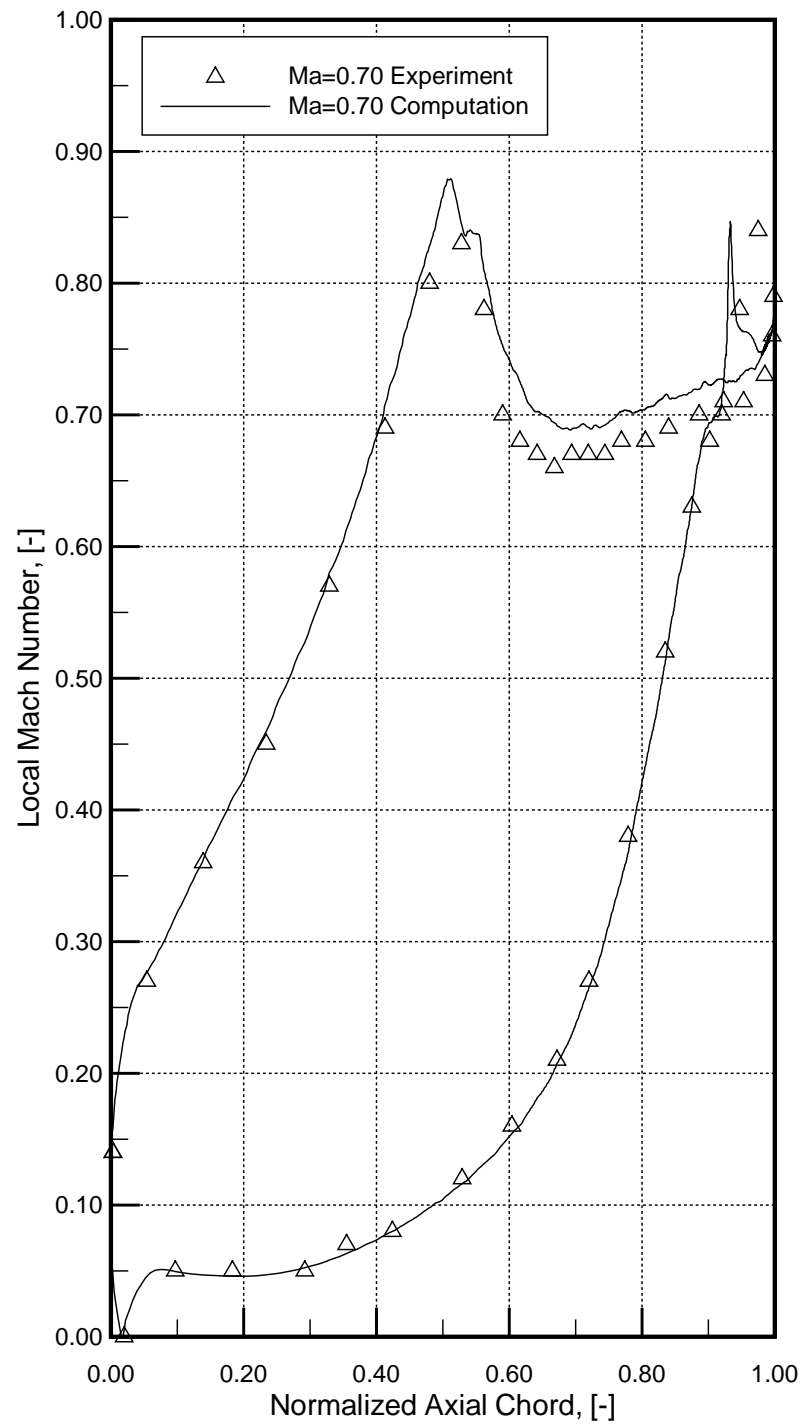


Figure 5.8: Measured and predicted surface Mach number at $Ma = 0.7$

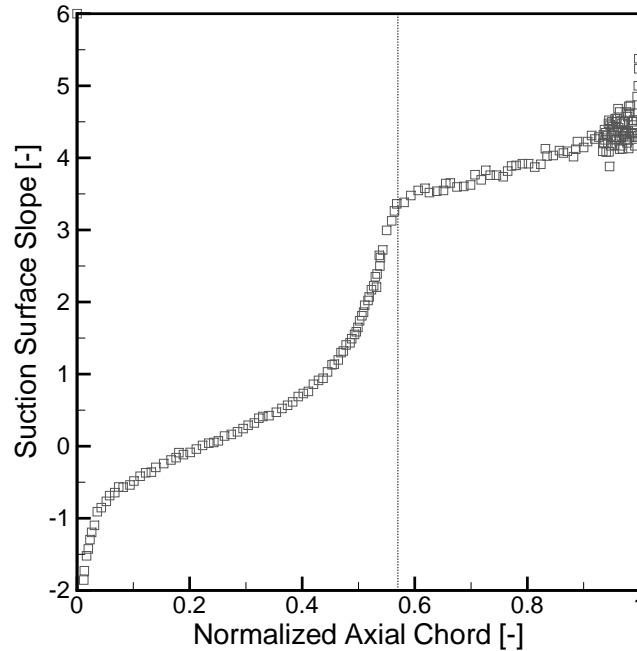


Figure 5.9: Local slope of suction surface

wall reacts to the local radius of curvature, the local slope of the suction surface was found to be a quantity which was easier to calculate and was strongly related to the local radius of curvature. Therefore, the slope of the suction surface profile Figure 5.9 shows how the blade was influencing the flow close to the wall, which was what the oil flow and local static pressure measurements were sensing. It could be seen that the slope changed abruptly at the throat.

This change in curvature could cause a local deceleration, which would, in turn, cause an adverse pressure gradient. Past $0.57 C_x$, the measured and computed loadings in Figure 5.8 showed just such a deceleration and increase in static pressure. This could result in a local decrease in the velocity gradient normal to the wall, and thus the wall shear stress, as the flow came close to separating. It appeared as though the flow did not separate since there was no isobaric region on the measured blade loadings and the oil flow did not show a light region across the span, indicative of a separated shear layer at higher Mach numbers. A low shear stress region would not have the ability to remove as much oil from the surface as elsewhere on the blade and would leave a dark region on the surface, as was seen in Figure 5.1a. Additionally, if

the flow did not separate, the wall static pressure would not be significantly affected by a low shear region. This may explain why there were no notable discontinuities in Figure 5.8 at the throat.

5.3.2 Transonic Flow

Data taken at an exit Mach numbers between $Ma = 1.0$ and 1.4 showed a new pattern of loading which was driven by the unique behaviour of transonic flows. These experimental results are shown in Figure 5.10. The Mach number distribution up to the passage throat was identical in all the supersonic cases, showing that the passage was choked.

The local Mach numbers diverged past the throat, where the expanding passage in the uncovered region accelerated the supersonic flow. As in the subsonic cases, oil flow images showed a discontinuity at the throat, which will be discussed shortly.

The acceleration along the suction surface ended abruptly. The oil flow results indicated that the acceleration was terminated by an oblique shock wave impinging on the suction surface. The location of this impingement point as seen in the oil flow, computational passage visualization, and the surface Mach number distribution are shown in Table 5.3. The surface static pressures also showed evidence of this shock wave impingement. The shock waves appeared as sharp decreases in the local surface Mach number. However, the shock was not a sharp discontinuity, as inviscid theory would predict [63]. Viscous effects spread the property changes across the shock over a finite area. After the initial pressure rise across the shock wave, there was also some evidence for a small region of separated flow. This was indicated by having two points with a similar static pressure, which was lower than the surrounding fluid, as would be present in a separation bubble. This behaviour was seen in the $Ma = 1.16$ data. However, recall that Section 3.7.2 showed the greatest blade-to-blade variations in surface static pressure occurring in this region. Therefore, there was also greater uncertainty in the local static pressure downstream of the shock.

For many of the supersonic exit Mach numbers, after the shock-affected region, the static pressures stabilized at a nearly constant level up to the beginning of the

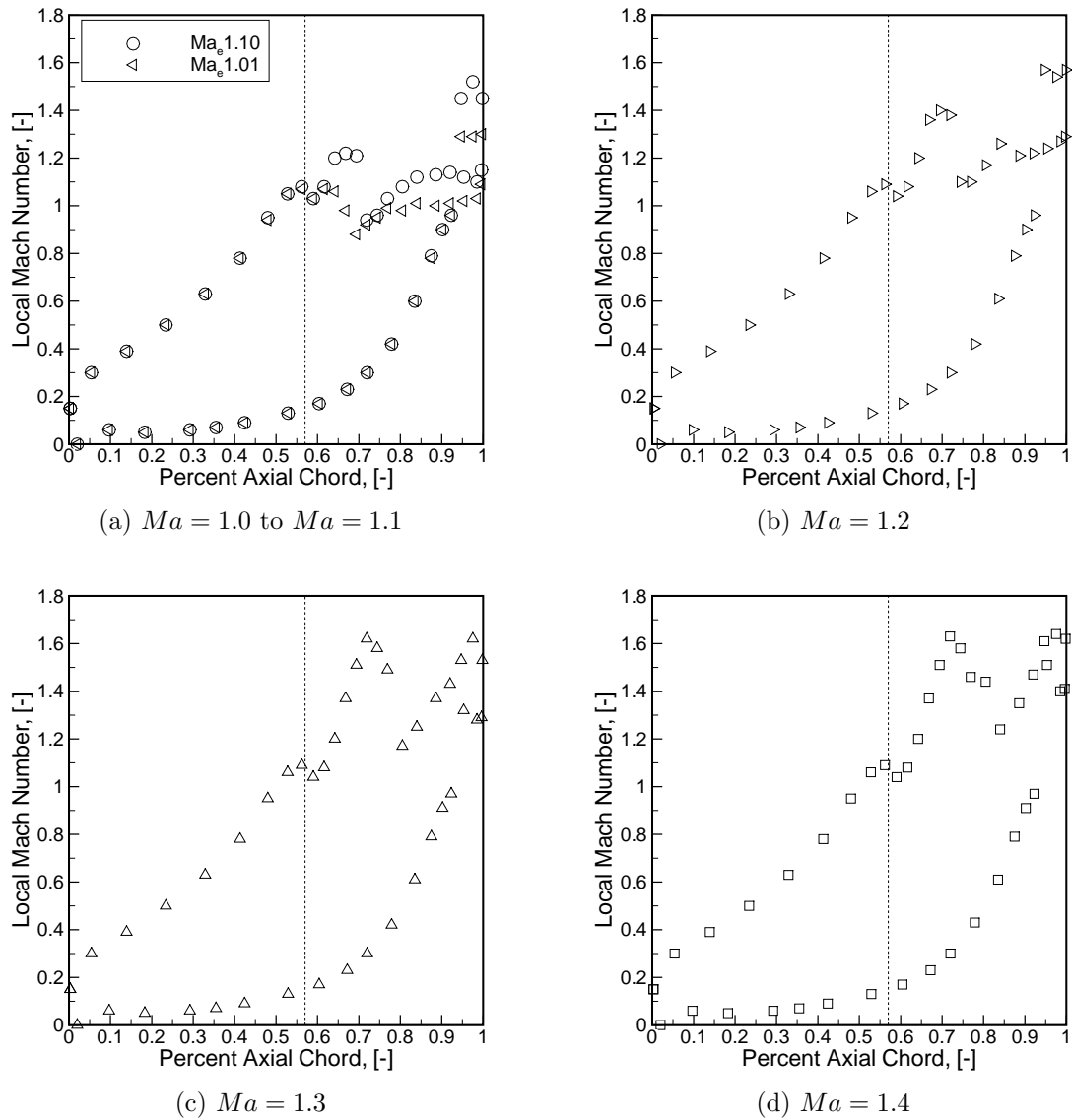


Figure 5.10: Local Mach numbers for transonic flow

Table 5.3: Shock position determined by various methods

Method	Uncertainty	M1.0	M1.16	M1.3
Oil Flow	$\pm 2.5\% C_x$	0.65	0.7	0.7
Computation	$\pm 0.05\% C_x$	0.65	0.71	0.73
Surface Pressure	$\pm 2.5\% C_x$	0.64	0.7	0.72

trailing edge. For the $Ma = 1.0$ to $Ma = 1.2$ cases a Mach number plateau had been reached by $0.80 C_x$. However, in the $Ma = 1.3$ and $Ma = 1.4$ cases, there was no Mach number plateau and the flow continued accelerating up to the trailing edge.

The comparison between the steady computational results and experimental results for $Ma = 1.00$, 1.16 and 1.31 can be seen in Figure 5.11. Figure 5.12 shows a more detailed view of the region downstream of the shock wave impingement, where the isobaric region indicative of flow separation can be seen more clearly. The agreement between the predictions and experiment was not as good as for the subsonic case shown in Figure 5.8. Though the computations accurately predicted the stagnation point as well as the pressure surface and most of the suction surface, they failed to properly model the shock boundary layer interaction and the flow that developed downstream of it.

The computations performed at $Ma = 1.16$ and $Ma = 1.31$ showed an isobaric region downstream of the shock, similar to that predicted in the theoretical models of shock induced boundary layer discussed in Section 2.1.2. However, the magnitude of this predicted behaviour was not in agreement with the measurements. For all cases, after the predicted point of reattachment, the computed local Mach number distribution did not return to the levels measured experimentally.

5.3.2.1 Flow Behaviour at Throat

At transonic speeds, the oil flow images showed a thin line of oil remaining on the blade at the throat. Unapparent in the subsonic flow, the local static pressures showed a discontinuity at this location. In all the Mach numbers shown in Figure 5.10 there was a small drop in Mach number past the throat before the flow continued accelerating in the expanding region. This drop could be explained by again examining the suction surface slope shown in Figure 5.9, where there was a sharp discontinuity at $0.57 C_x$. For supersonic exit Mach numbers, the flow was sonic at the throat and thus the flow behaved differently than in the subsonic case described in Section 5.3.1. Supersonic flow reacts to any form of discontinuity by creating a shock or expansion wave. In the design of supersonic aircraft, great pains are taken to ensure that the

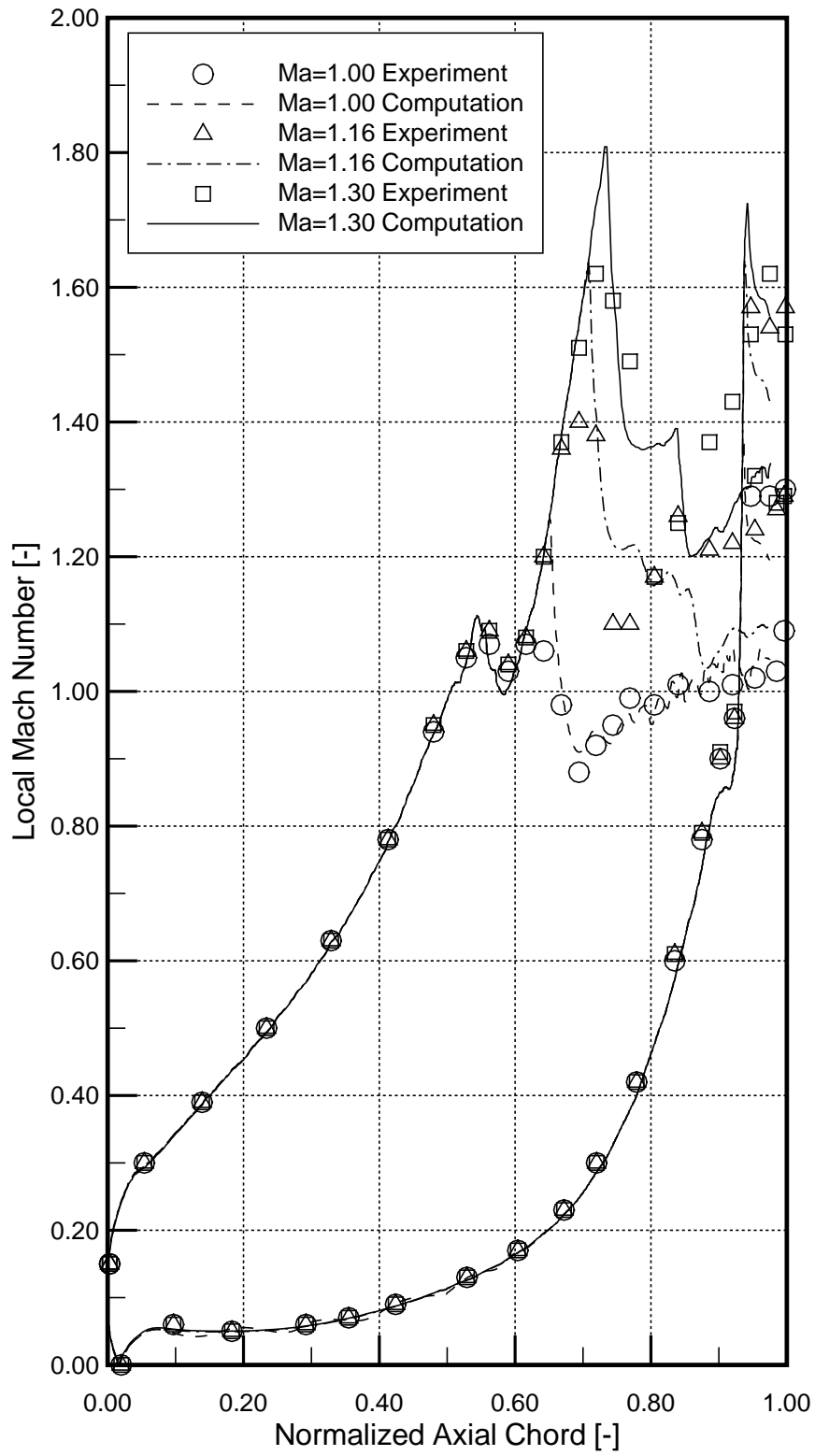


Figure 5.11: Measured and predicted surface Mach number at $Ma = 1.0- 1.31$

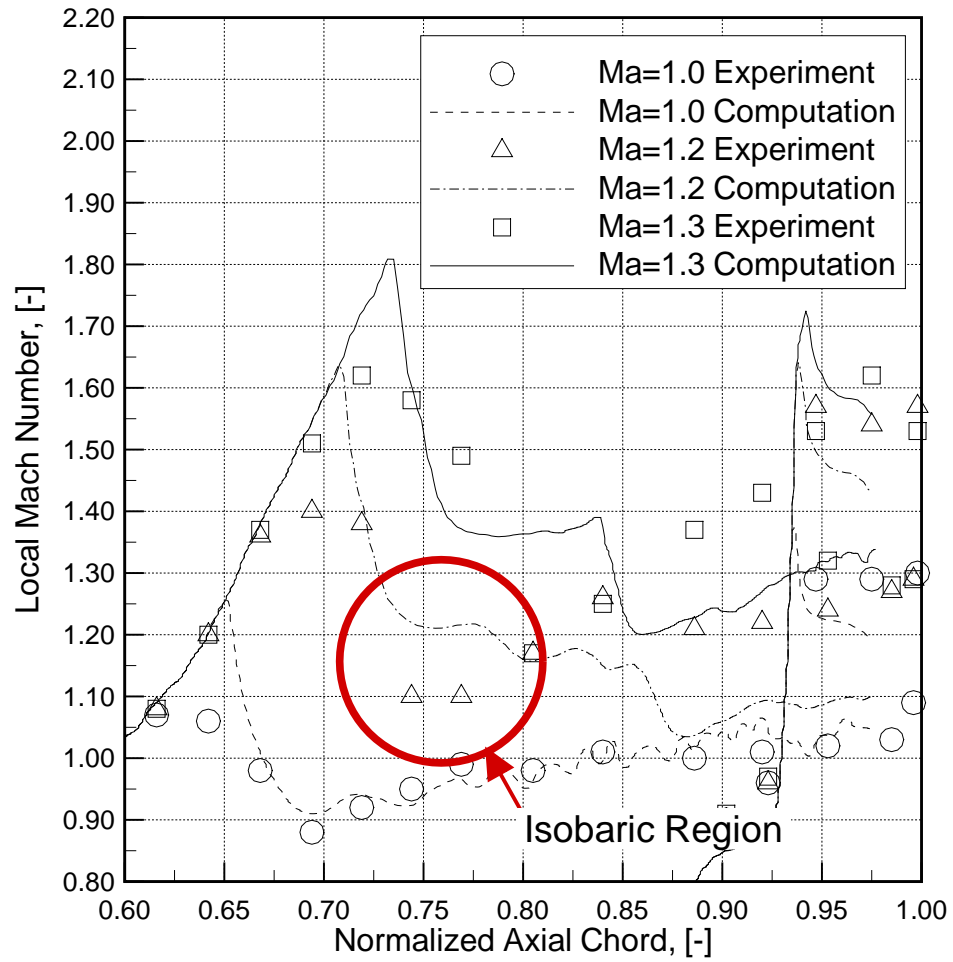


Figure 5.12: Detail of Figure 5.11

rate of growth of the craft's streamwise cross section has no discontinuities to avoid generating unnecessary shocks; this is known as the *area rule* [5]. A similar effect may be influencing the behaviour at the throat of this vane, where the rapid change in the slope may have induced a shock wave to form. However, as the Mach number was very close to unity in this region, the shock wave would have to be quite weak. It was only able to slightly reduce the Mach number and perturb the boundary layer sufficiently to effect a small decrease in wall shear stress.

5.4 Base Pressure

The base pressure was measured using three static taps located in the trailing edge region. One tap was located at the point where the chord line intersected the trailing edge arc and was referred to as the trailing edge tip location. The other two were located towards the pressure and suction sides of the trailing edge.

The three static taps in the trailing edge region showed distinctly different behaviour than those on the rest of the blade once the exit Mach number exceeded $Ma = 0.8$, as seen in Figure 5.7. At these speeds, the low static pressure in the trailing edge region caused the three trailing edge static taps to read a Mach number significantly higher than that in the constant velocity region observed along the final $0.40 C_x$ of the suction surface. The three pressures measured in the trailing edge region were not always similar for each Mach number. This was predicted by the experiments performed by Sieverding[57], which were discussed in Section 2.1.3.

Since there were large spatial variations of static pressure within the trailing edge region, the mean of the three measured static pressures would be characteristic of no one location on the trailing edge but rather of the entire trailing edge flow. However, in almost every experiment which measured the base pressure, the pressure was recorded using a single static pressure tap at the trailing edge tip [7, 69]. Therefore, to obtain a measurement of base pressure which was most comparable to that of other researchers, only the pressure at the trailing edge tip was used.

The most common method of normalizing the base pressure was the base pressure coefficient, Cp_b , defined in Equation 2.5. The base pressure was recorded experimen-

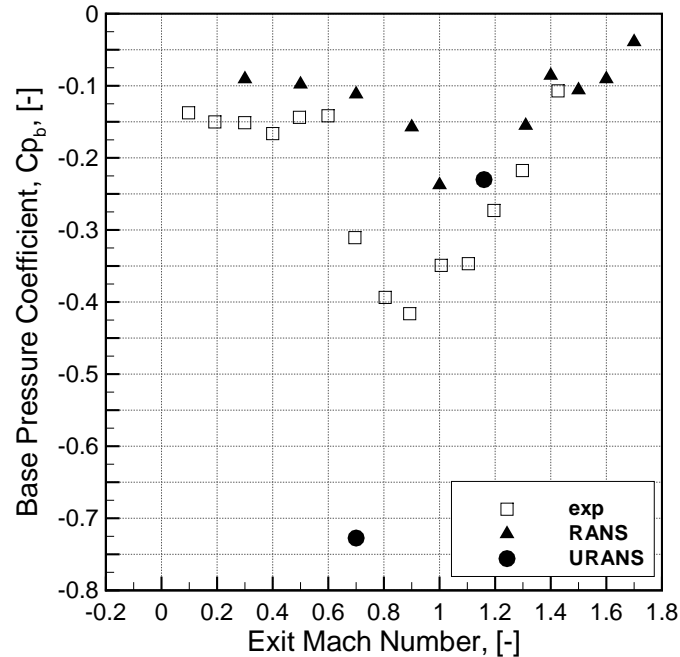


Figure 5.13: Base pressure coefficient as measured and computed at various Mach numbers

tally for a range of Mach numbers between $Ma = 0.1$ and 1.4 . The CFD predictions extended the upper end of the range to $Ma = 1.7$. Figure 5.13 shows the results from the current experiments, as well as the steady and unsteady computations.

The experimentally determined base pressures remained roughly constant up until $Ma = 0.6$. Past this point, there was a sharp decrease in base pressure with a minimum occurring at $Ma = 0.8$. This was followed by a recovery of base pressure back to the $Ma = 0.6$ levels at $Ma = 1.4$. This behaviour was in good agreement with Carscallen *et al.*'s [10] previous measurements on this cascade. For a different cascade, Corriveau and Sjolander [16] observed a minimum in base pressure at an exit Mach number of $Ma = 1.0$ followed by a mild recovery with increasing Mach number.

The computational results showed a similar behaviour. However, the base pressure coefficient only began to decrease sharply past $Ma = 0.8$, and the magnitude of the C_{p_b} minimum was smaller than experimentally observed. It is important to note that while there was no vortex shedding in the steady simulations, the base pressure

minimum was still observed at approximately $Ma = 1.0$. The base pressures time histories from the two unsteady simulations are shown in Figure 5.14. The mean base pressure over two periods from both the URANS simulations were computed and shown in Figure 5.13. The subsonic and supersonic base pressures showed significantly different behaviour. The unsteady $Ma = 0.7$ simulation predicted a significantly lower base pressure than was those measured experimentally. The $Ma = 1.16$ simulations, however, predicted an almost identical base pressure.

The frequency of the periodically unsteady behaviour was 7.91 kHz at $Ma = 0.70$ and 13.91 kHz at $Ma = 1.16$. These frequencies corresponded to Strouhal numbers, defined in Equation 5.2, of $St = 0.207$ at $Ma = 0.70$ and $St = 0.220$ at $Ma = 1.16$.

$$St = \frac{f \phi_{te}}{Ma_2 \sqrt{\gamma} R T s_2} \quad (5.2)$$

These values agreed well with the behaviour expected from a cylinder, where the Strouhal number remains around $St = 0.21$ for a wide range of flow conditions [37]. The $Ma = 0.70$ values also agreed well with frequency measurements performed by Carscallen *et al.* [10] which recorded a Strouhal number of 0.20 at this speed. However, at $Ma = 1.16$, Carscallen *et al.*'s measured Strouhal number of 0.35 did not agree the CFD prediction.

The experimental data on the blade's base pressure were compared to the empirical correlation developed by Sieverding [58]. Though Section 2.1.3 showed that there was another applicable base pressure correlation developed by Bölcs and Sari [7], the Sieverding correlation is more commonly used, was easier to implement and predicted the base pressure more accurately. This correlation determined the base pressure using the exit Mach number and blade geometry. The blade geometry was characterized by the suction side curvature angle, ϵ , and the trailing edge wedge angle, δ_{te} . Both these values were defined in Section 3.1.2. The blade under investigation had a value of $\frac{1}{2}(\epsilon + \delta_{te}) = 7.5$. Figure 5.15 compares the experimental data to the trend predicted by the Sieverding correlation for a blade with $\frac{1}{2}(\epsilon + \delta_{te}) = 8$. Note that the horizontal axis is the ratio of the static-to-total pressure at the cascade exit and is thus inversely proportional to Mach number. The computed and measured base pressures agreed

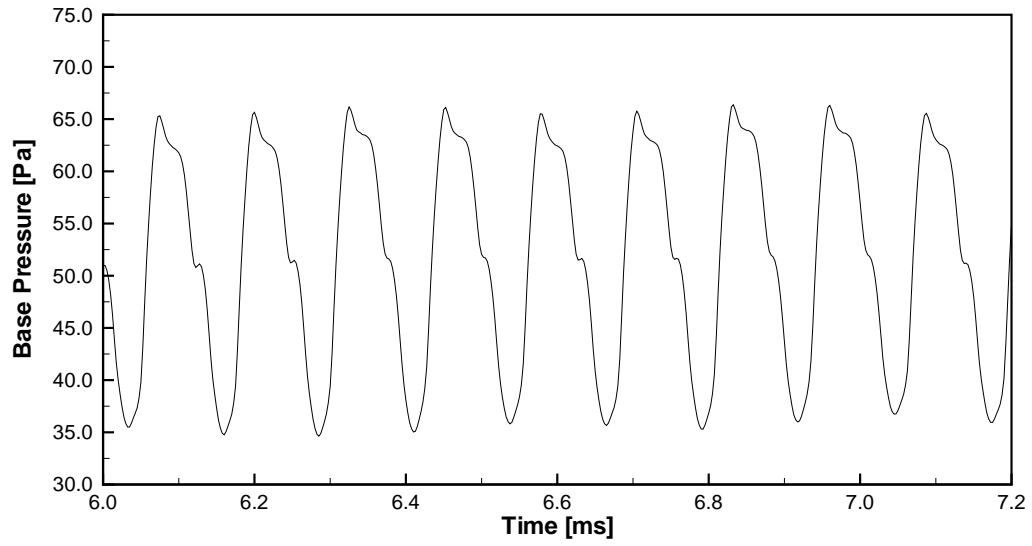
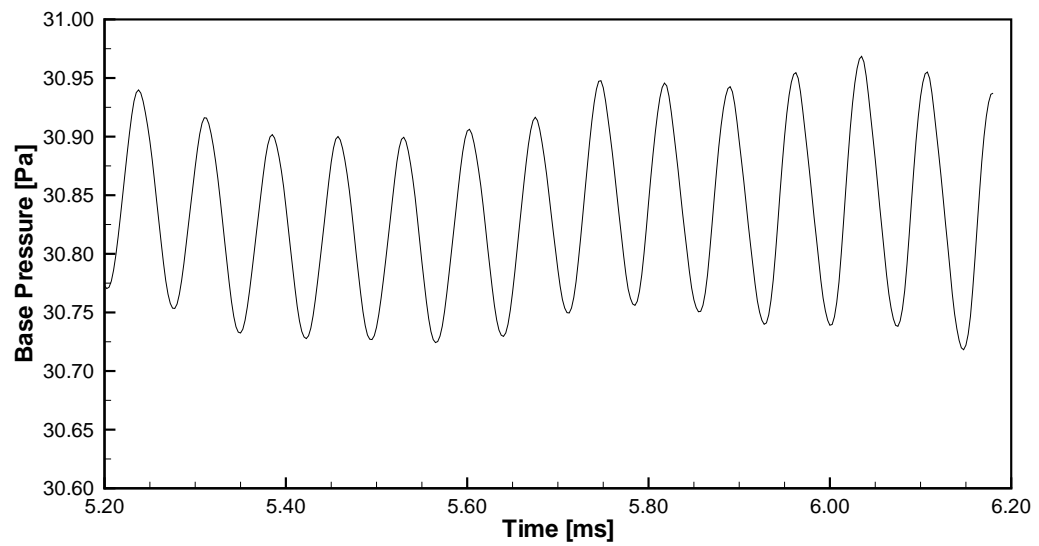
(a) $Ma = 0.70$ (b) $Ma = 1.16$

Figure 5.14: Base pressure history over time for unsteady simulations

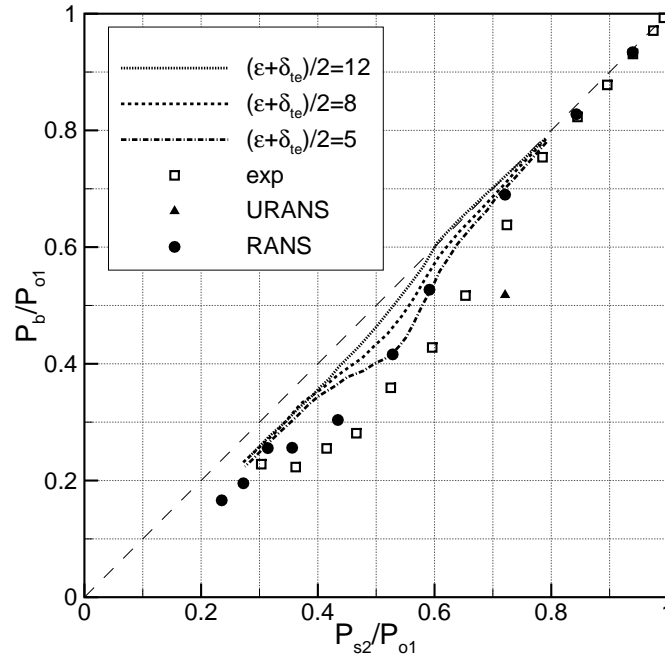


Figure 5.15: Comparison of Sieverding correlation to experimental and computational results

quite well with the Sieverding correlation compared to the agreement obtained by other investigations.

5.5 Wake Traverses

Although blade surface pressure distributions were important in understanding the passage flow behaviour, they could not fully describe loss generation of the blade. Chapter 2 showed that the flowfield downstream of the blade's trailing edge is complex. To examine the behaviour of the trailing edge flow, the wake properties downstream of the blade-row were measured over a range of subsonic and transonic Mach numbers. To evaluate the losses, the traverse data were mass-averaged using the two methods discussed in Section 3.6. These traverses covered only the third passage. The experimental data were also used to examine the accuracy of the computational results.

Traverses were performed at five different exit Mach numbers, though only three sets of data will be discussed in detail. The data taken at $Ma = 0.3$ and $Ma = 0.7$

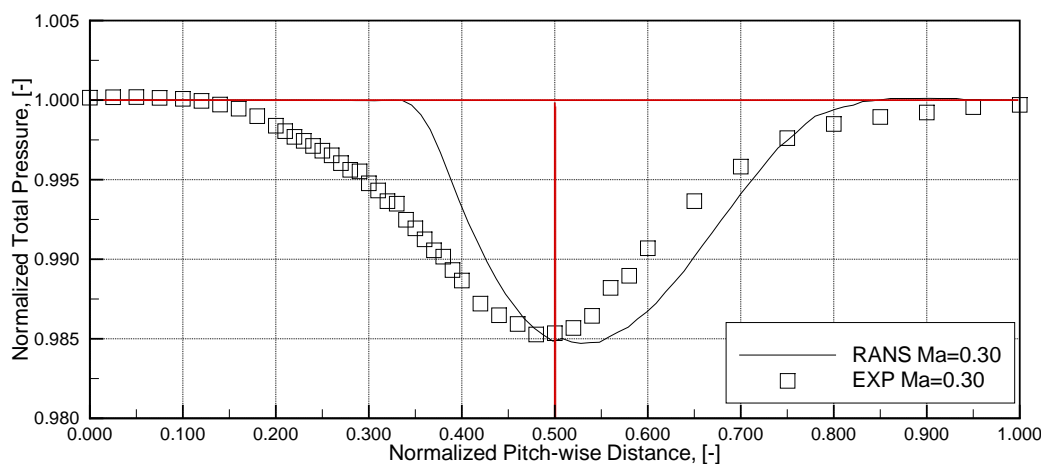
were characteristic of the subsonic flow while the data taken at $Ma = 1.16$ showed all the major features of transonic flow. The local values of the normalized total pressure, flow angle and Mach number for these three exit Mach numbers are given in Figures 5.16 to 5.18. Data from the other traverses can be found in Appendix D. Detailed analysis of the wake traverses was necessary to confirm that the experimental and computational results showed physically meaningful behaviour before averaging the wake data.

The normalized pitchwise distance, used as the independent variable in all the wake plots, corresponded to the scale and datum attached to the traverse plane in Figure 5.4. The normalized pitchwise distance started at the mid-passage before the suction side of the blade and extended to the mid-passage past the pressure surface. The midpoint of this axis, $0.5s$, was the location where a line projected at the metal angle from the trailing edge intersected the traverse plane. A layout of the traverse region was shown in Figure 3.7.

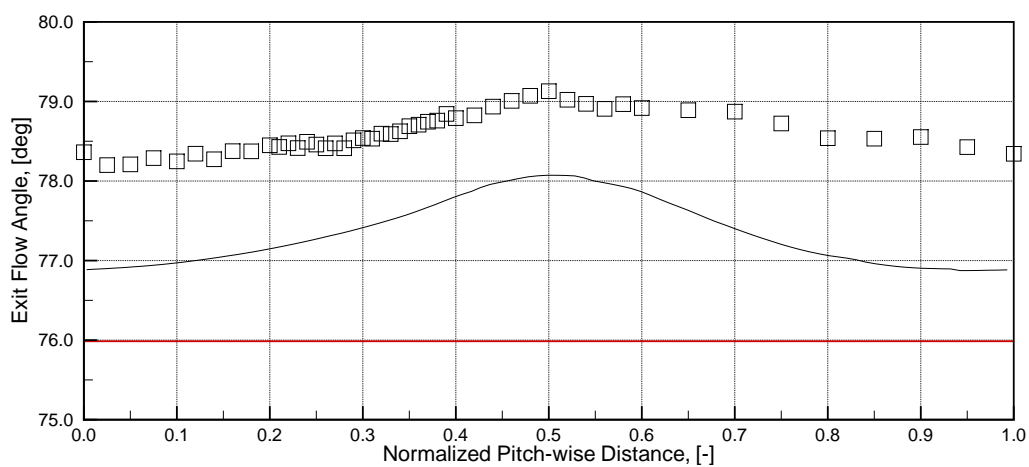
Recall from Chapter 3 that the probe was mechanically aligned with the exit metal angle of the blade at the traverse plane. There was an inherent error of approximately $\pm 1^\circ$ in this method. This uncertainty led to a bias error between the experimental and computational results. This error was easiest to quantify using the $Ma = 0.3$ data, since they showed the smallest variations of flow angle across the pitch. Figure 5.16b shows that there was a constant positive one degree bias across the pitch. It was decided however, not to adjust the experimental results to account for this bias. This error was one factor in the disagreement between the experiments and computations.

5.5.1 Outlet Flow Angles

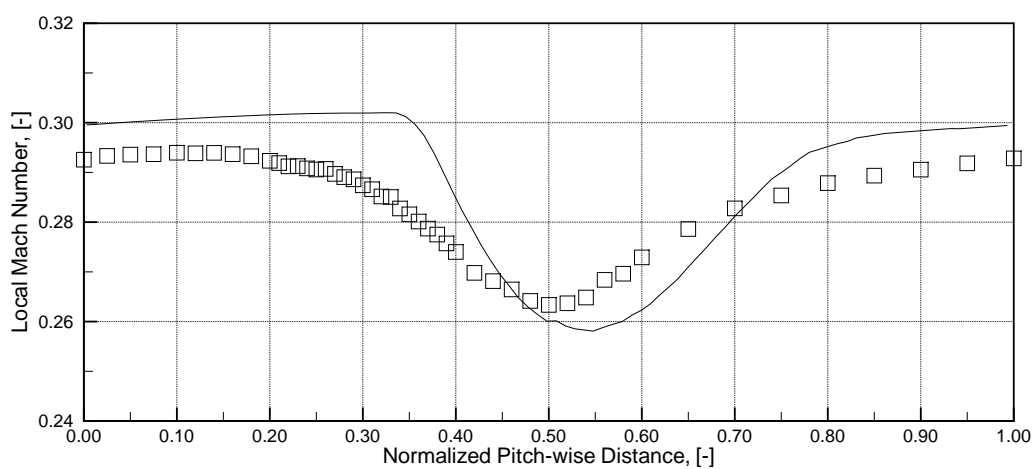
The mixed-out flow angles, computed according to the method of Amecke and Šafařík[4], are shown in Figure 5.19. The experimental and computed angles were plotted as a function of the exit Mach number, along with three different empirical predictions of the blade's outlet angle. Almost all the measured and computed flow angles were larger than the blade metal exit angle, implying over-turning of the flow by the blade. This was an unexpected result as Dixon [24] stated that flow over-turning



(a) Total pressure

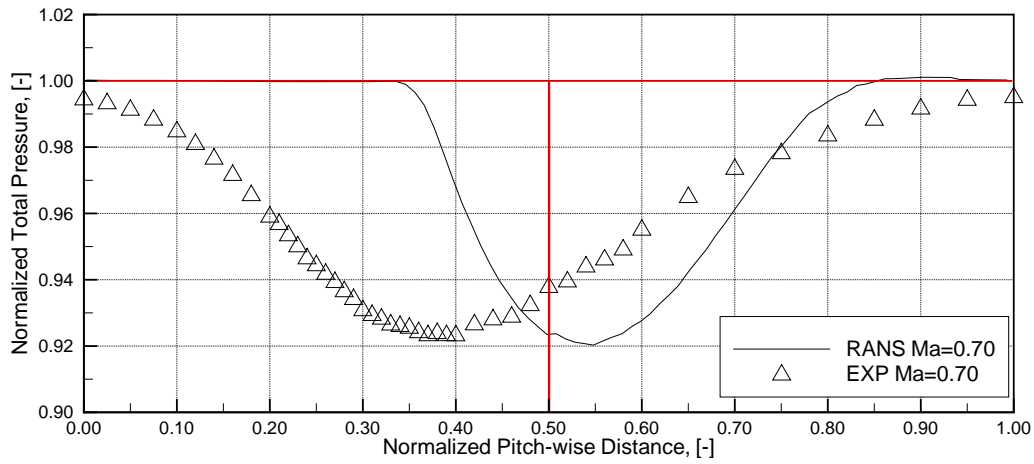


(b) Flow angle

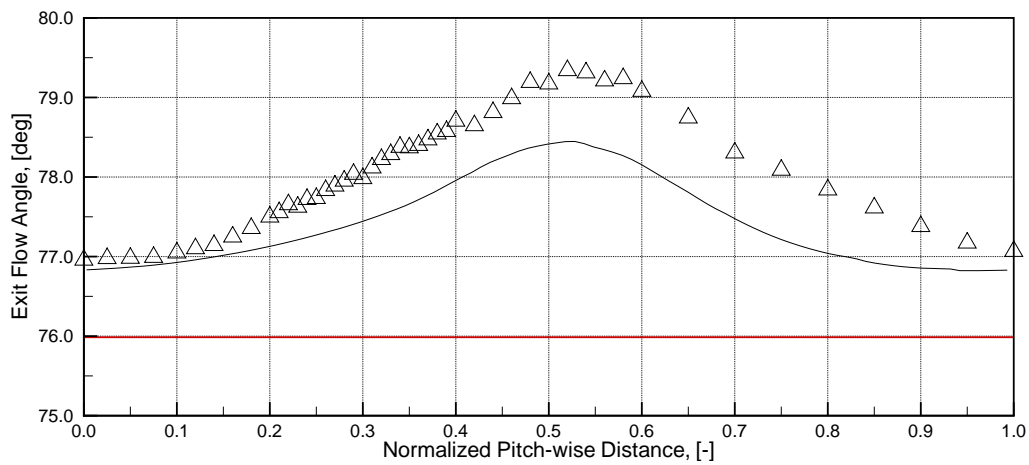


(c) Mach number

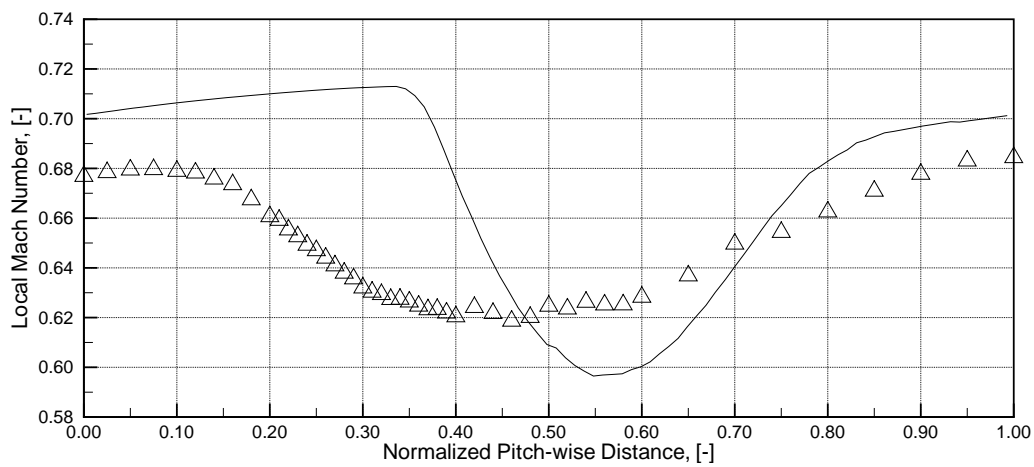
Figure 5.16: Measured and computed Wake flowfield for $Ma = 0.30$



(a) Total pressure

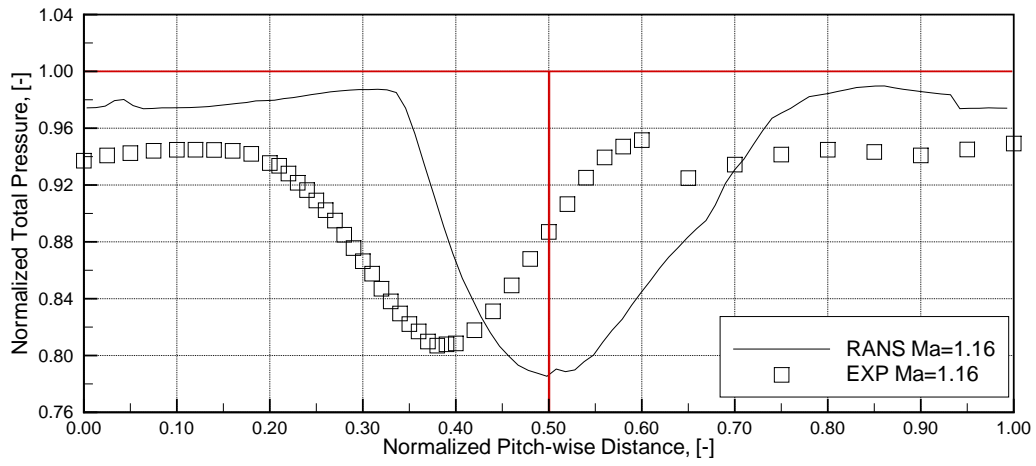


(b) Flow angle

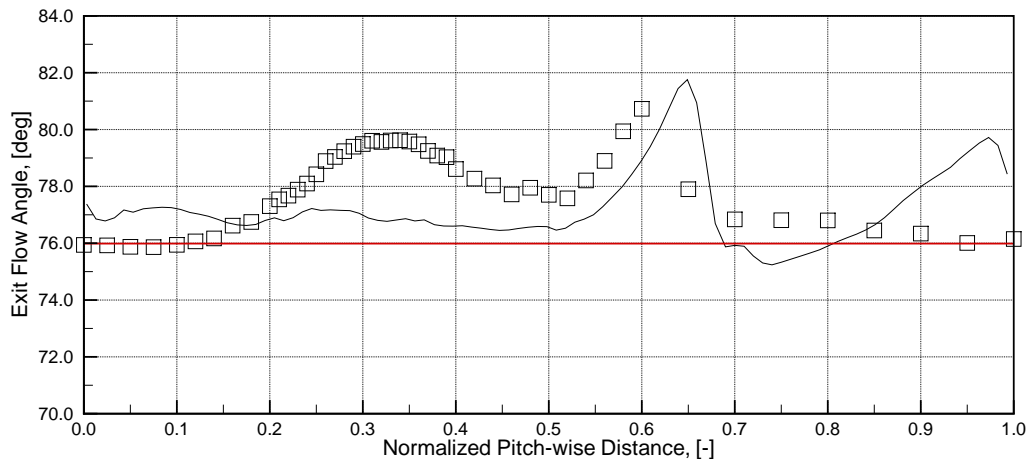


(c) Mach number

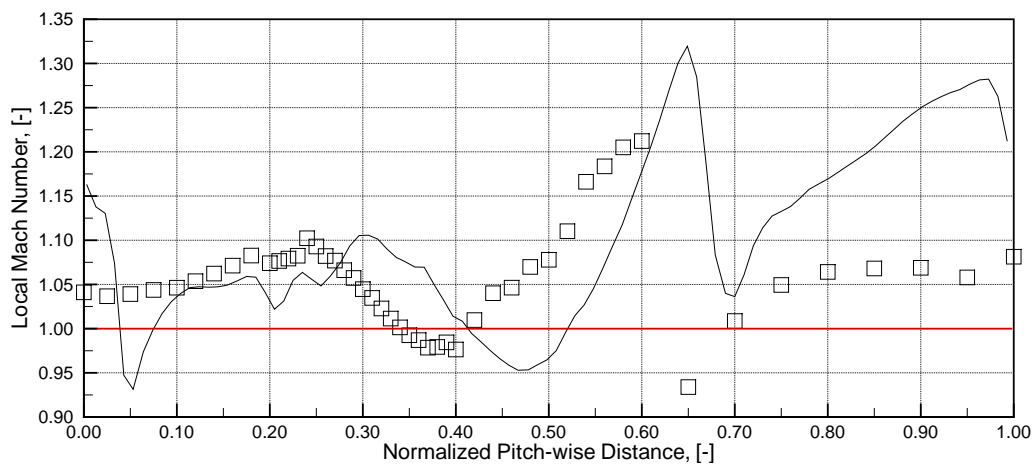
Figure 5.17: Measured and computed wake flowfield for $Ma = 0.70$



(a) Total pressure



(b) Flow angle



(c) Mach number

Figure 5.18: Measured and computed wake flowfield for $Ma = 1.16$

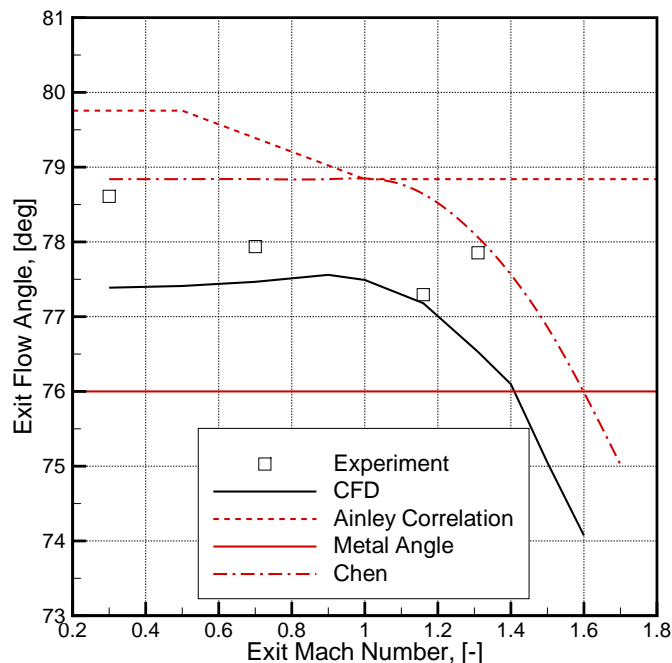


Figure 5.19: Effect of Mach number on mixed out flow angle

almost never occurs in a turbine blade. When over-turning does occur, it is almost always in regions close to the hub or tip which are strongly affected by secondary flows. This apparent over-turning was also observed by Moustapha *et al.* [44] in their examination of the flow within the blade passage currently under investigation.

Since it was not physically sensible for over-turning to occur at the midspan of the blade, the derivation of the metal angle was re-examined. The stated value of the exit metal angle, 76° , was obtained from the work of Carscallen [8]. To check this value, the metal angle was calculated graphically, as shown in Figure 5.20. In this figure, a line was extended perpendicular to the suction surface in a region, close to the trailing edge of the blade, where the pressure and suction surface were almost parallel. This line would be intersected by the chord line close to its midpoint. Therefore, the midpoint of this line was connected with the trailing edge tip to approximate the exit metal angle. This method produced an exit metal angle of 78.3° , closer to the gauging angle of 78.8° than to the original metal angle.

There was additional evidence that the original value for the blade's metal angle was incorrect. Almost all correlations to predict the exit flow angle are based the

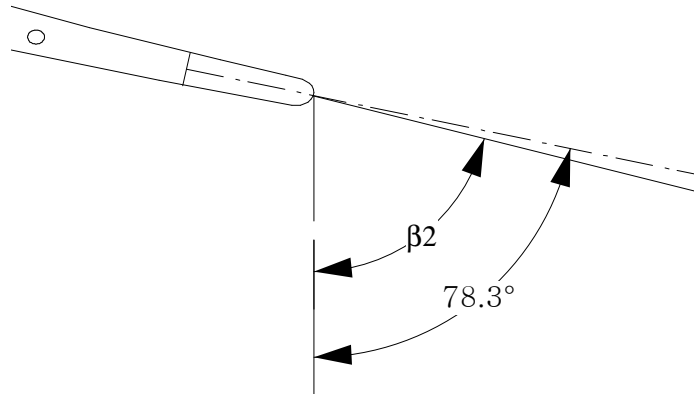


Figure 5.20: Graphical determination of the exit metal angle

gauging angle, defined in Equation 3.1. One of the original correlations between gauging angle and exit flow angle was developed by Ainley [2]. A more modern correlation, designed to be extended to higher Mach numbers, was developed by Chen [13]. Both these correlations, shown in Figure 5.19 predicted an exit flow angle *greater* than current blade's metal angle while on almost all other blades, they predict and exit angle less than the metal angle. This suggests that the original value of the exit metal angle was not indicative of how far the blade was actually turning the flow.

Therefore, though the blade had a metal angle of 76° , there was evidence that the blade was trying to turn the flow closer to the gauging angle of 78.8° . In light of this, it was understandable that majority of the mixed out flow angles fell between these two bounds.

If the the gauging angle of 78.8° was treated as the metal angle, the flow behaved as would be expected in the wake of transonic blading. In the mid-passage there was a region of constant under-turning. The flow began to approach the gauging angle within in the wake region. This was the behaviour observed by Corriveau [15] in the wake of several different designs of transonic blading. At $Ma = 1.16$, the local flow angle exceeded the gauging angle within the wake. This local over-turning has also been observed in other cascades with transonic exit Mach numbers by Prust [50].

Another feature seen in the $Ma = 1.16$ data was the presence of a shock wave at $0.65 s$. This resulted in an abrupt change in flow angle. This shock can be seen to pass through the traverse plane at the same pitchwise position in Figure 5.5.

This examination of the local flow angle showed that the flow behaved in a physically sensible manner, despite the initial appearance of an unusual degree of overturning.

5.5.2 Total Pressure

The total pressure was presented as the local total pressure normalized by the cascade inlet pressure, so as to remove the effect of day-to-day variations in ambient conditions from the results. The total pressure deficits observed in the experimental and computational wakes was an indication of loss generated within the wake. The local minimum total pressure was the location of the center of the wake, where the most entropy had been generated.

There was a discrepancy in the location of the total pressure minimum between the experimental measurements and computed predictions which grew with increasing Mach number, as shown from a comparison of Figures 5.16a, 5.17a and 5.18a. The experimental results showed the wake center intersecting the traverse plane at less than 50% of the pitch ($0.5 s$), implying that the wake was turned less than 76° . This contradicted the flow angle measurements. The computational results had the wake centre located past $0.5 s$, showing better agreement with the flow angle data.

The discrepancies between the experimental total pressure and angle data could be described by a simple reversal of the horizontal axis. However, this was most likely not the source of the error, due to the excellent agreement in the pitch-wise location of shock waves in Figure 5.18b. The reason for this discrepancy, therefore, remains unresolved. However, it should be noted that the position of the wake centre was quite sensitive to the exit flow angle. A change of 1.5° in α_2 could result in a $0.1 s$ change in the wake centre location.

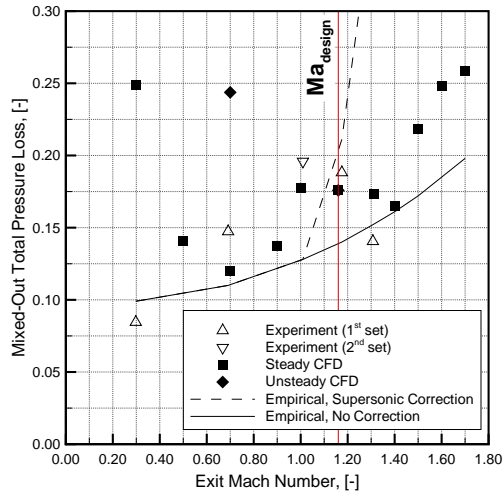
5.5.3 Mass-Averaged and Mixed-Out Results

Using the two data reduction methods described in Section 3.6, the performance of the blade was examined over the range of investigated Mach numbers. Blade performance could be defined either as the total pressure losses, shown in Figures 5.21a and 5.21c, or the normalized entropy generation, shown in Figures 5.21b and 5.21d.

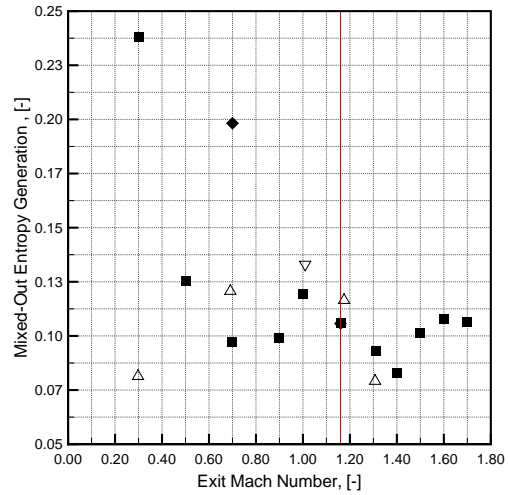
Examining the total pressure losses, the mixed-out losses were always greater or equal to the mass-averaged losses. This was to be expected as the mass-averaged losses did not examine the mixing required to transform the inhomogeneous flow in the traverse plane into a homogeneous flow at some distant point downstream.

The measured total pressure losses and entropy generation recorded at $Ma = 1.31$ showed an unusual trend in Figure 5.21. The magnitude of these losses were extremely small considering the exit Mach number at which they were measured. Additionally, they were significantly smaller than predicted by the computational models. These abnormally small losses may have partially been the result of the probe calibration. The maximum Mach number at which the probe was calibrated was $Ma = 1.22$. Figure 3.11 showed that the total pressure correction, K_1 , was strongly dependent on Mach number past $Ma = 1.00$. The data reduction algorithm linearly extrapolated to find calibration coefficients when the local Mach number fell outside the calibration range. Examining the trend in K_1 versus Mach number in Figure 3.11, it could be seen that it exhibited almost exponential growth with Mach number. Therefore, the probe data reduction may have been significantly under-estimating the amount of compression occurring in the bow shock which formed upstream of the probe, and thus reporting an erroneously large total pressure across the traverse. This would lead to an under-prediction of the losses.

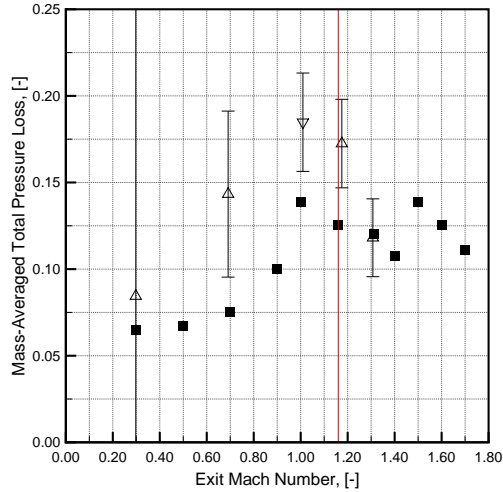
Aside from the data at $Ma = 1.31$, the computational predictions of the losses showed fair agreement with the experimental values in the transonic range, especially the mixed-out values. However, the computational prediction of mixed-out losses was significantly higher than the measurements in the lower subsonic range ($Ma = 0.3$ and $Ma = 0.5$).



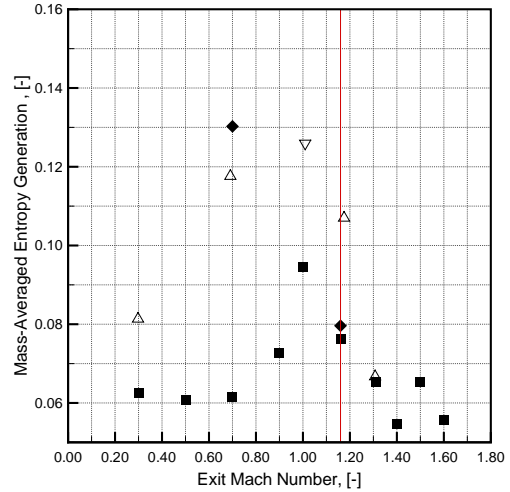
(a) Mixed-out total pressure loss



(b) Mixed-out entropy generation



(c) Mass-averaged total pressure loss



(d) Mass-averaged entropy generation

Figure 5.21: Blade performance

The mass-averaged loss from the computations showed a consistent under-prediction of the loss. The large discrepancies, seen at low Mach numbers between the predicted and measured mixed-out losses, were not present in the mass-averaged data. However, at the highest Mach numbers ($Ma = 1.6$ and $Ma = 1.7$) the mass-averaged losses showed a decrease which was opposite to that of trends reported from other cascades such as [30, 15]. Therefore, as the exit Mach number differed significantly from the design Mach number of $Ma = 1.16$, for which the solver settings had been optimized, the accuracy of computed mixed-out and mass-averaged losses were questionable.

Figure 5.21c shows the uncertainty bands on the mass-averaged total pressures losses. At low Mach numbers, the uncertainty in the losses was extremely large, while in the transonic range the uncertainties were more reasonable. The propagation of uncertainties for the mass averaged total pressure losses is shown in Appendix C.

The focus of the present work was the flow behaviour in the region between $Ma = 0.7$ and $Ma = 1.16$. In this region, the computational and experimental results revealed an interesting behaviour. The magnitude of both the total pressure losses, Y_t , and entropy generation, ζ , grew with increasing Mach number to reach a local maximum at $Ma = 1.0$. Past $Ma = 1.0$ there was a slight decrease in losses. This decrease was most pronounced in the entropy generation and the least pronounced in the computed mixed-out total pressure losses. The trend in the computed mixed-out losses, Y_t , showed that the losses began to increase rapidly past $Ma = 1.40$.

The most interesting part of these data was the apparent decrease, or plateau, in loss between $Ma = 1.0$ and $Ma = 1.4$. The mechanism driving this behaviour will be discussed in Chapter 6, as well as how to exploit this behaviour in designs of other transonic blades.

Discussion

6.1 Transonic loss Behaviour

In Section 5.5, it was reported that both the mass-averaged and mixed-out losses reached a local maxima about $Ma = 1.0$. Depending on the type of investigation and averaging method, the losses decreased, or at least remained constant up until $Ma = 1.4$. This loss behaviour was a very interesting phenomenon. It implied that there would be a negligible penalty or even a slight benefit to increasing the exit Mach number of this vane to values greater than the design point of $Ma = 1.16$. Higher exit Mach numbers from this stator vane would allow the turbine stage to extract more work from the flow as this would increase the tangential momentum entering the rotor.

6.1.1 Confirming the Behaviour of the Losses

Before discussing the possible causes of this loss behaviour, it was important to ascertain that it was a real effect. In the present experiments, two repeats of wake measurements were performed, though only the latter set had been presented in detail. Between the two sets of measurements, the cascade was disassembled and re-assembled. The magnitude of the total pressure loss coefficient measured in each set differed between 5% and 12%. Therefore, the plateau was an repeatable phenomenon in the data.

Additionally, in 1990, Carscallen[8] measured the losses from an almost identical cascade. He employed an entirely different type of instrumentation, and reported area-averaged rather than mass-averaged or mixed-out loss values. The data presented in [11, 8, 10] showed a distinct loss minimum at close to $Ma = 1.3$. Graham and Kost[30], using a different cascade, also observed a local loss maximum about $Ma = 1.0$ and a local minimum at a higher transonic Mach number. For a mid-loaded

turbine cascade, Corriveau [15] measured and computed a loss plateau in this Mach number range. Also, Povey *et al.* [48] noted a plateau in loss past $Ma = 1.05$. The fact that four independent experiments observed a loss decrease, or plateau, past $Ma = 1.0$ adds credence to the argument that the current observation of a transonic loss plateau was a real effect.

6.1.2 Possible Causes for the Minimum

Chapter 2 outlined the major sources of two-dimensional midspan losses, namely: boundary layers, shock waves and their interaction with the suction side boundary layer, and the base pressure and associated wake mixing. The following discussion will address how each effect could contribute to the trend in the total pressure loss from the vane examined in this investigation.

6.1.2.1 Boundary Layer Losses

Mee *et al.* [41] described the relative importance of boundary layer losses on the overall loss from transonic turbine blades. They showed that the contribution of the undisturbed boundary layers to the overall loss varied little over the range of Mach numbers investigated, and those variations were monotonically decreasing. It was assumed that the boundary layer losses on the current blades would exhibit similar behaviour of those examined by Mee *et al.* [41], due to their general flow and geometric similarity. Therefore, it was likely that the origin of the overall loss behaviour was not due to the losses incurred by the undisturbed boundary layers.

6.1.3 Shocks and Shock Boundary Layer Interaction

Though the shock waves lead directly to the generation of a great deal of entropy, their effect was monotonically increasing and thus could not be the driving force behind the transonic loss plateau. For this reason, the more complex phenomenon of shock-boundary layer interactions has been identified as a more likely source of the loss behaviour.

Graham and Kost [30] attributed the decrease in losses observed in their cascade past $Ma = 1.0$ to the shock boundary-layer interactions on the suction surface of the blade. They suggested that the expansion wave, which formed at the peak of the separation bubble, turned the flow towards the blade and accelerated reattachment (Figure 2.4). When the shocks were perpendicular to the blade at $Ma = 1.0$, there was no reflected wave and thus the separation bubble was largest. As the shock angle increased, the expansion wave became stronger, reducing the size of the separation bubble. This led to a reduction in losses up to $Ma = 1.15$. Past this minimum value, though there was a strong expansion wave to promote reattachment, the incident oblique shock interacted with the boundary layer so far along the blades's suction surface that there was insufficient blade surface left for reattachment to occur. The losses grew continuously past this point, due both to the separated flow and the increasing amount of entropy generated by the shock waves.

The shock-boundary layer interaction appeared to affect the current blading differently. Though the point of shock wave impingement did move downstream as the Mach number increased, the effect was to move the impingement point from $0.65 C_x$ at $Ma = 1.0$ to $0.74 C_x$ at $Ma = 1.4$. This behaviour was observed in the oil film images, local static pressure distributions and computational results. All three techniques showed that the separated shear layer re-attached on the suction surface of the blade. The highest experimental Mach number was 1.40, and the RANS computations showed that past this Mach number, the losses began to increase. The computational results predicted that by $Ma = 1.7$ the point of shock-boundary layer interaction would be at $0.80 C_x$ and the flow would reattach to the suction surface. This indicated that the mechanism driving the growth of the losses past the local minimum was most likely not the departure of the separated shear layer from the blade surface observed in the blading used by Graham and Kost [30].

However, it was difficult to determine whether the incident shock angle had an effect on the size of the separation bubble as Graham and Kost claimed [30]. The static pressure taps were too coarse in the separated flow zone to describe the size of the separation bubble accurately. The images in Figure 5.1 show that there were, at

best, three static taps in the region where the oil flow images showed evidence of separation bubbles. Dietrichs [23] had better success at characterizing shock-boundary layer interactions on turbine blades. He had nine static taps in this region. The computational predictions gave clearer indications of the flow behaviour in the separated shear layer, but their poor agreement with experiments downstream of the shock wave made the information they provided suspect.

One attribute of shock-boundary layer interactions which may have had a mitigating effect on the overall losses was the effect of shock waves on the downstream boundary layer. In cases when flow reattached to the blade, the boundary layer which developed downstream of the impingement point would be thicker and generate more entropy than an undisturbed boundary layer. As the shock wave impinged further downstream, the blade area under the influence of this thicker boundary layer decreased, reducing the boundary layer losses [30]. However, this effect could only cause the losses to decrease with a growing exit Mach number, and therefore cannot be solely responsible for the more complex trend which was observed.

Though there was unquestionably shock-induced boundary layer separation occurring on the suction surface, there was evidence that it was not the only driving factor of the loss behaviour in the current cascade. At all Mach numbers examined, the separated shear layers re-attached to form separation bubbles. Additionally, the oil film visualization and surface Mach number measurements showed that the separation bubbles were relatively small.

6.1.4 Base Pressure

The final of source of losses within the cascade was the base pressure loss. Recall from Section 5.4 that the base pressure coefficient decreased past $Ma = 0.6$, increasing the magnitude of the base pressure loss. The base pressure coefficient experienced a minimum at $Ma = 0.9$ before returning to its subsonic value at $Ma = 1.4$.

This decrease in base pressure loss past $Ma = 0.9$ may have helped offset the ever-increasing amounts of entropy generated in shock waves as the exit Mach number increased. Past $Ma = 1.4$ the steady computational predictions of base pressure

showed that it did not grow as rapidly with increasing Mach number. This meant that past $Ma = 1.4$ there was less of a decrease in base pressure losses to offset the growing increase in entropy across shock waves. This may have been one of the key reasons that the losses began to grow past $Ma = 1.4$, as shown in Figure 5.21a.

6.1.4.1 Interactions

The potential existed for the base pressure loss to be influenced by the shock-boundary layer interaction occurring on the suction surface. To discuss how this may occur, it is necessary to describe the relationship between boundary layer thickness at the trailing edge and the base pressure.

A model of how separated shear layers from a cylinder interact to form a vortex street was given by Gerrard [28]. The details of his theory are beyond the scope of this work, but Cicatelli and Sieverding [14] noted one significant implication: Gerrard [28] defined the formation point of a vortex as the location where the vorticity present at the outer part of one shear layer had migrated across the wake and interacted with the opposite shear layer which had opposing vorticity. This behaviour is shown in Figure 6.1. At the point where the two shear layers met, the opposing vorticity of the interacting shear layers would cancel each other and a distinct vortex would be shed. Gerrard [28] stated that the frequency of vortex shedding would be reduced by the growth of the diffusion length, defined as the sum of the cylinder diameter and boundary layer displacement thicknesses.

However, the current computational studies appear to show the opposite trend. From the URANS base pressure time histories, the frequency of the $Ma = 1.16$ simulations was greater than at $Ma = 0.7$, when the boundary layer was much thinner. However, it should be noted that at $Ma = 1.16$ the two shear layers within the wake did not merge until they traveled some distance downstream, showing that the thick boundary layer had suppressed aggressive vortex shedding at $Ma = 1.16$. This is despite the high frequency, low amplitude fluctuations in base pressure from the $Ma = 1.16$ unsteady calculations.

The effect of the shedding frequency on the base pressure is less well understood.

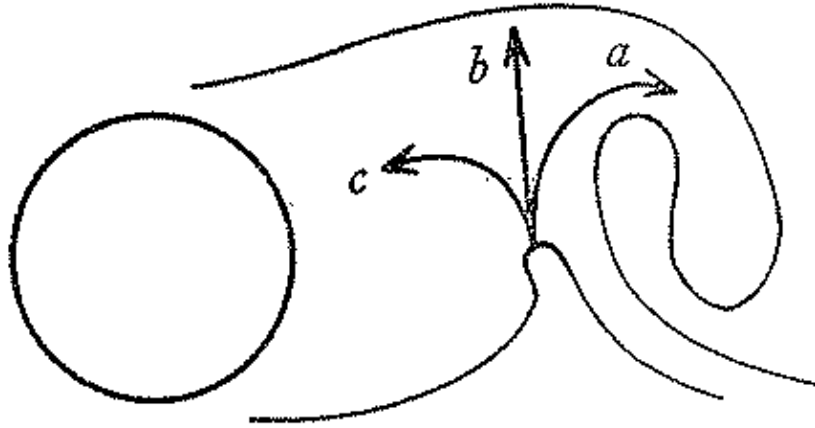


Figure 6.1: Gerrard[28] model of vortex formation.

Sieverding and Heinemann [59] noted that the base pressure could vary by as much as 20% between blades with the same dimensionless shedding frequency. Motallebi and Norburry [43] also measured the base pressure and shedding frequency, or the Strouhal number, at a range of Mach numbers in the transonic regime. They found that a large drop in base pressure was accompanied by an increase in shedding frequency. Past $Ma = 1.2$ there was an increase in base pressure corresponding to a slight decrease in shedding frequency. This trend has also been observed by Rowe *et al.* [53]. Using a blunt-ended flat plate, they were able to examine the effect of increasing boundary layer thickness on the Strouhal number and the base pressure coefficient. They noted that an increasing displacement thickness caused a decrease in Strouhal number and a corresponding increase in base pressure. Therefore, there was strong evidence that the disruption of vortex shedding caused by a thicker suction surface boundary layer may have led to an increase in base pressure.

The implications of this theory extends to the design of subsonic blading. If the disruption of trailing edge vortex shedding has a benefit in terms of base pressure loss reduction, then all designs of blading may benefit from an increased boundary layer thickness at the trailing edge. For subsonic blades, where there are no incident shock waves to disturb the boundary layer, a similar effect may be obtained by promoting early transition using high local curvature early on the blade, as done by Sonoda [61] or by increasing the blade's surface roughness. The increased penalty in terms of

Table 6.1: Comparison of experiments to computational and empirical predictions

Mach	RANS		URANS		K&O	K&O no CFM
	Mass-Avg. [%]	Mixed-Out [%]	Mass-Avg. [%]	Mixed-Out [%]	Mixed-Out [%]	Mixed-Out [%]
0.30	-23.07	194.38			17.03	17.03
0.69	-47.56	-18.70	8.16	65.34	-15.73	-15.73
1.01	-24.97	-9.86			-31.28	-31.28
1.18	-27.22	-6.02	-23.82	-6.04	14.63	-19.54
1.31	1.92	22.91			216.26	28.74

boundary layer losses may be offset if a significant reduction in base pressure loss was realized. Mee *et al.* [41] showed that at subsonic speeds, the boundary layer loss was of the same magnitude as the base pressure and mixing losses.

It may be, that the shock-boundary layer interactions were one of the driving factors behind the transonic loss plateau. Though the shock-induced boundary layer separation was not as dominant and effect as observed by Graham and Kost [30], the thickened boundary layer resulting from these interaction may have been the driver for the reduced base pressure loss.

6.2 Empirical and Computational Predictions of Losses

In Chapter 5, it was shown that there was a notable disagreement between the computational predictions of loss and the experimental results. The empirical Kacker and Okapuu (K&O) [34] loss correlation also only showed fair agreement with the measured mixed-out total pressure loss. These differences are quantified in Table 6.1. Evidently, no technique was able to predict the loss within $\pm 10\%$ across the measured Mach number range, though it would appear that the RANS prediction of the mixed-out loss came closest. The following sections will examine the strengths and weaknesses of the empirical and computational predictions.

6.2.1 Empirical Predictions of Total Pressure Loss Coefficient

The K&O [34] total pressure loss correlation, discussed in Chapter 2 was compared to the experimental and numerical data. The empirical data presented in Table 6.1 was calculated using the adjustments to the K&O method proposed by Zhu and Sjolander [70]. Two different versions of the correlation were examined: one where a compressible flow modifier (CFM), was added, and one with no correction.

Without the supersonic correction, the K&O correlation predicted the mixed-out losses within 20% at $Ma = 0.3$. As the losses grew, the correlation failed to predict the sharp rise in loss between $Ma = 0.7$ and $Ma = 1.0$ and the discrepancy between correlations and experiments grew. The addition of the supersonic correction factor did not improve the agreement, the correlation still under-predicted the subsonic losses and produced significant over-predictions of losses in supersonic flows. Additionally, neither implementation of the K&O correlations predicted the transonic loss plateau observed both experimentally and computationally.

Overall, the K&O [34] correlation gave a rough order-of-magnitude estimate of the losses. It predicted the mixed-out total pressure loss with a root-mean-squared error of approximately 20%. The use of the supersonic correction factor was not found to improve the accuracy of the correlation in transonic flow and lead to unacceptable over-predictions in supersonic flow.

6.2.2 Empirical Predictions of Base Pressure Coefficient

Sieverding *et al.*'s [58] base pressure correlation was discussed in Chapter 2. The experimental results from Chapter 5 compared favourably to this correlation. However, below an outlet static-to-total pressure ratio of 0.8, corresponding to an exit Mach number of 0.6, there was a consistent bias between the experiments and the empirically predicted trend for $\frac{(\epsilon + \delta_{te})}{2} = 8$. Jouini *et al.* [33] achieved much better agreement with the Sieverding correlation up to $Ma = 1.0$, after which they also noted an appreciable bias. Jouini *et al.* [33] noted that there may be other geometric parameters which strongly influenced the base pressure aside from the trailing edge

wedge angle and suction surface curvature. Comparing that work and the present results to the Sieverding correlation indicated that the trailing edge diameter to throat opening ratio, $\frac{\phi_{te}}{o}$, may be another important indicator of geometry.

The present blades had a $\frac{\phi_{te}}{o}$ ratio of 0.27, while the blading used by Jouini *et al.* had a ratio of 0.08. The Sieverding correlation was made up of data from a group of sixteen blade geometries. The $\frac{\phi_{te}}{o}$ ratio of this family ranged between 0.04 and 0.19, with a mean of 0.11. Therefore, the better agreement of the data from Jouini *et al.* up to $Ma = 1.0$ may have been due to the fact that their $\frac{\phi_{te}}{o}$ ratio was within the range of values used to make up the correlation. The present blade's $\frac{\phi_{te}}{o}$ ratio was 100% larger than the mean $\frac{\phi_{te}}{o}$ ratio observed in the correlation family of blades and 16% larger than the maximum. The $\frac{\phi_{te}}{o}$ ratio of the current blade was somewhat larger than that seen in other designs [33, 61], however it remains a realistic value for future blade designs. The large $\frac{\phi_{te}}{o}$ ratio for the present blade may have been the reason why the present results diverged from the correlation past $Ma = 0.6$.

Sieverding *et al.* attempted to incorporate the $\frac{\phi_{te}}{o}$ ratio into their correlation, but were unable to do so from the data-set they had available [58]. However, since this correlation was produced in 1980, there have been many other published investigations of base pressure data with corresponding blade geometries, *e.g.* [16, 33, 10, 7, 69, 19, 35, 43]. This additional data may allow a more robust correlation to be developed in the future which would take into account the $\frac{\phi_{te}}{o}$ ratio, as well as other important geometric parameters to allow a more accurate prediction of the base pressure.

6.2.3 Predictive Ability of Computational Methods

The computational predictions of the flow behaviour were more accurate than empirical correlations for both the base pressure and the mixed-out total pressure losses. The computations were able to predict the intriguing transonic loss behaviour, discussed in Section 6.1. Additionally, the agreement between experimental and computed base pressures was much better than the agreement with Sieverding *et al.*'s correlation. However, there were also cases where the flow behaviour was not well predicted.

By far, the most obvious disagreements between the computational and experi-

mental results were observed at exit Mach numbers which differed significantly from the design conditions. The mixed-out losses showed a unanticipated growth in magnitude below $Ma = 0.7$, while the mass-averaged losses showed an unrealistic decrease in loss past $Ma = 1.5$. These discrepancies could be better understood by examining the normalized total pressure loss, defined in Equation 6.1.

$$\Delta P_o = \frac{P_{o1} - P_{o2}}{P_{o1}} \quad (6.1)$$

Figure 6.2 shows that at $Ma = 0.3$ the mixed-out normalized total pressure loss was over-predicted. The combination of this over prediction in normalized total pressure loss and the lower dynamic pressure made the predicted values of Y_t and ζ unrealistically high below $Ma = 0.7$. One reason why the computations may have over-predicted the mixed-out total pressure loss was that the computational model was optimized for transonic flow. This may have influences its accuracy outside the transonic range. Additionally, it was noted previously that the uncertainty in the mass-averaged properties at low Mach numbers was much larger than at transonic speeds.

The mass-averaged computational results showed not only an unexpected decrease in total pressure loss past $Ma = 1.5$, but also consistently under-predicted the normalized total pressure loss. For this reason, the mixed-out losses, though they had difficulty producing accurate predictions of the loss in lower speed flow, were treated as the most reliable computational prediction of the loss behaviour. Between $Ma = 0.7$ and $Ma = 1.3$, the root-mean-squared error in the prediction of Y_t was 16%, better than the agreement between the experiments and the empirical correlations.

A more detailed investigation of the results showed local regions of the flow which did not agree well with experiments. One such region was downstream of the shock impingement on the suction surface. The computational predictions of the local Mach number in this region showed very poor agreement with experiments. This was most likely due to the importance of transition on the behaviour of a separation bubble. It was established in Chapter 2 that shock-boundary layer interactions can differ significantly depending on the state, laminar or turbulent, of the boundary

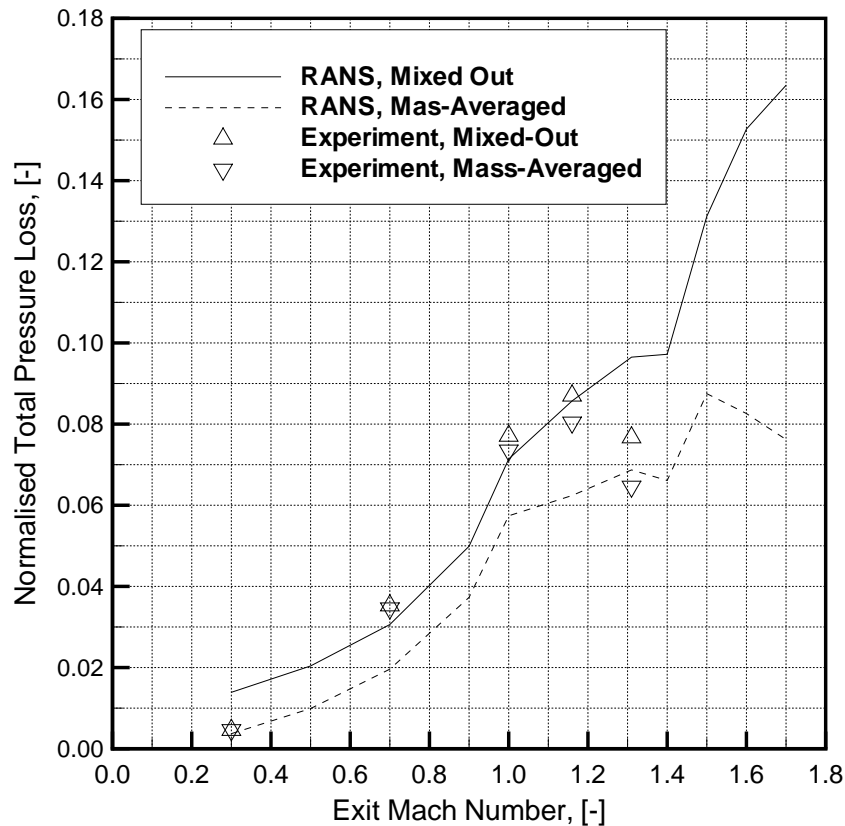


Figure 6.2: Comparison of experimental and computed normalized total pressure loss

layer. The RANS approach used in the present work treated the entire flow as being turbulent, while actually, the local Reynolds number near the stagnation point was quite low and thus laminar flow would exist over part of the blade's surface until transition to turbulence occurred. The $k - \omega$ turbulence model attempted to adjust for this effect empirically [27]. However, the phenomenon of transition is enormously complex, especially in a blade passage which has with strong and varying pressure gradients. The empirical adjustments to the turbulence model were not capable of predicting how the boundary layer would behave at the point of shock impingement. In reality, the strong favorable pressure gradient along in the blade passage may have postponed transition sufficiently that the incident shock wave interacted with a laminar boundary layer. For this reason, the computational models could not accurately predict the behaviour within or after the separation bubble.

Another discrepancy was in the magnitude of the unsteady base pressure. The

$Ma = 0.70$ URANS simulations significantly under-predicted the base pressure, while the unsteady behaviour in the $Ma = 1.16$ URANS simulations had no effect on the time-averaged base pressure. The subsonic shedding frequency was quite close to the value measured experimentally by Carscallen [10] while there was a large discrepancy at $Ma = 1.16$. Rowe *et al.* [53] noted that the Strouhal number was strongly dependent on the trailing edge boundary layer thickness. Therefore, this indicated that the boundary layer thicknesses at the trailing edge was well modeled in the subsonic case, but not so at supersonic speeds. This was to be expected from the poor prediction of the flow downstream of shock-boundary layer interactions. However, this did not explain the poor agreement in base pressure at subsonic speeds. The reasons for this discrepancy in base pressure may have lain in the modeling of the mechanics of vortex formation and its influence on the base pressure. This could be a result of the mesh density in the wake region, the size of the unsteady time step, or another consequence of the turbulence model chosen.

The preceding discussions of errors in the predicted flow behaviour all noted that the $k - \omega$ turbulence model may have been one of the causes of the discrepancies. However, despite its shortcomings, the $k - \omega$ model was the most appropriate choice for the type of flow being examined. Phenomena such as flow separation and vortex shedding may require a much denser grid and a more complex treatment of turbulence, such as Large Eddy Simulation, in order to be predicted in detail.

Aside from the errors in the predicted losses at Mach numbers much larger or smaller than the design value, the computational results were able to predict the loss behaviour much better than empirical correlations. The computations used commercially available software, *Fluent 6.3*, and did not employ any user-defined functions or arbitrary adjustments to turbulence model constants. This shows both the strengths and weaknesses of this software. Though it was able to model the behaviour of the losses with Mach number to a fair degree of accuracy, there were several local flow phenomena which it could not predict.

Conclusions and Recommendations

A combination of experimental and computational techniques were used to investigate the flow through a linear cascade of first stage nozzle guide vane at speeds ranging from low subsonic to supersonic. Detailed measurements of the midspan downstream flow field, allowed the examination of losses with increasing Mach number and the identification of flow features responsible for the behaviour of these losses.

The experimental facility was a suction-type open circuit wind tunnel. Despite a flow bias at the inlet plane, the exit flow from the cascade had acceptable periodicity. The mixed-out total pressure loss measured in two adjacent passages differed by only 2.5%. Surface static pressure measurements quantified the flow over the blade surface, while qualitative measurements were provided by oil-film and schlieren flow visualization. The blade wakes were recorded using a pressure probe which was traversed across one blade pitch. This probe was designed for use in transonic flows, though it experienced difficulties recording flow properties close to $Ma = 1.0$.

The computational investigations were performed using *Fluent 6.3*. This solver used a two dimensional, density-based coupled algorithm with an unstructured mesh to predict the flow thorough the blade passage. Both steady and time-dependent cases were investigated. The results showed overall agreement with the experiments. The steady computational results predicted the mixed-out total pressure loss within 16%, for Mach numbers greater than 0.3.

Empirical correlations for the total pressure losses and base pressure had only fair success in predicting the experimental values. Commonly used correlations could only predict the losses within 25%. In addition to the coarse agreement with the experimental data, the empirical results did not show the experimentally observed trends with increasing Mach number.

The overall behaviour of the blade losses showed an intriguing trend in performance at transonic speeds. Between Mach 1.00 and 1.40, depending on the measure-

ment and averaging method, a slight decrease or plateau was observed in the losses. This transonic loss plateau was preceded and followed by large increases in losses with a growing Mach number. This behaviour was most likely driven by the losses due to shock-boundary layer interactions and the base pressure.

Oblique shocks, originating from the pressure side of an adjacent blade, impinged on the suction surface. Some degree of shock-induced boundary layer separation was observed experimentally at all supersonic Mach numbers. The separated shear layer caused by these trailing edge shocks was seen to re-attach at all Mach numbers examined experimentally and computationally. The steady growth in losses due to trailing edge shocks and their interactions with the boundary layer appeared to be offset with a decrease in base pressure loss at transonic speeds.

The base pressure losses increased past $Ma = 0.6$ and reached a maximum at $Ma = 0.9$. Beyond this point, the base pressure losses continually decreased with a growing exit Mach number. The rapid decrease in the the base pressure losses, to levels observed at low subsonic speeds, may have been caused, in part, by the thickening of the boundary layer at the trailing edge by incident shocks upstream.

There were two major findings from the present work. The first was that the blading under investigation could operate with an exit Mach number greater than its design value of 1.16 without experiencing any loss penalty. A higher exit Mach number would result in more tangential momentum being transferred to the downstream rotor. If the rotor were designed appropriately, this could result in an increase in stage efficiency. The second finding was that this intriguing behaviour in losses could be predicted computationally with an acceptable degree of accuracy using commercially available software, without additional empirical corrections to the code.

7.1 Recommendations for Future Work

The analysis of the results from the present investigation highlighted three major areas where improvements could have been made, in the test section design, the probe design, and in computational methods.

The boundary layer flaps on the north and south endwalls were found to be ineffective at adjusting the inlet flow. These should be re-designed to reduce the appreciable inlet flow bias. The test section had blades with quite a large true chord length. This allowed greater spatial resolution for pressure measurements within the wake and on the blade surface, however it limited the number of blades within the cascade to six. If the true chord of the blades was reduced, more blades could be used in the cascade while maintaining the same maximum exit Mach number. Though this would have an effect on the measurement resolution, it would help to reduce the 2.5% difference in losses measured between passages. The only region where better measurement resolution was required was within the separated flow region, downstream of the incident trailing edge shock wave. Though this region moved downstream with increasing Mach number, its location at the design conditions of $Ma = 1.16$ was established experimentally and computationally. Therefore, additional static taps in this region will allow a better examination of the shock-boundary layer interactions at the design Mach number.

The finger probe encountered many difficulties in determining accurate measurements when the local Mach number was close to unity. In Section 3.5.4, it was recommended that the probe be re-manufactured to allow for a fifth static tap to help correct for the errors introduced at these speeds. Additionally, the maximum calibration Mach number for the probe should be extended from $Ma = 1.22$ to $Ma = 1.4$ so that it can record flow properties more accurately at higher Mach numbers. This could be accomplished by placing De Laval nozzles in the calibration tunnel to increase its maximum Mach number, as was done by Povey *et al.* [48].

The computational methods could be improved by incorporating a transition model in the computational code. Many of the errors in predicting the local flow behaviour were attributed to the $k-\omega$ turbulence model which had no laminar-to-turbulent transition capability. Alternatively, the RANS based approach to turbulence modeling could be abandoned in favor of a more accurate yet computationally intensive approach such as Large Eddy Simulation.

The empirical models used to predict total pressure and base pressure losses leave

much to be desired in terms of accuracy, especially at transonic speeds. The large body of data on the losses from cascade measurements could warrant some of these correlations being revisited, especially the Sieverding base pressure correlation. In the case of the base pressure correlation, the trailing edge to throat-opening ratio may be an additional important parameter.

Two additional topics for future research arose from the the present results. It was proposed in Chapter 6 that the losses on subsonic blading may be reduced by increasing the trailing edge boundary layer thickness to suppress vortex shedding. This behaviour should be confirmed experimentally. Another interesting behaviour, which stemmed from the oil-film visualization, was the observation of a vortex whose axis of rotation was normal to the blade's suction surface, at the point where the separation bubble interacted with the sidewall boundary layer. The origins and effects of this vortex are not known at present and should be investigated.

References

- [1] Adamczyk, J. J., 1991. “Wake Mixing in Axial Flow Compressors”. ASME Paper No. 96-GT-29.
- [2] Ainley, D. G., 1948. “Performance of Axial Flow Turbines”. *Proc. Instn. Mech. Engrs.*, **159**.
- [3] Ainley, D. G., and Mathieson, 1951. “A Method of Performance Estimation for Axial-Flow Turbines”. Reports and Memoranda 2974, British Ministry of Supply, December.
- [4] Amecke, J., and Šafářik, P., 1995. “Data Reduction of Wake Flow Measurements with Injection of an Other Gas”. Forschungsbericht 95-32, DLR, Göttingen, Germany.
- [5] Anderson, J. D., 1990. *Modern Compressible Flow With Historical Perspective*, 2nd ed. McGraw-Hill, Boston, MA.
- [6] Benner, M., 2003. *The Influence of Leading-edge Geometry on Profile and Secondary Losses in Turbine Cascades*. PhD Thesis, Carleton University, Ottawa, Ontario, May.
- [7] Bölcs, A. and Sari, O., 1991. “A New Base Pressure Correlation for Transonic and Supersonic Flows”. ASME Paper No. 91-GT-324.
- [8] Carscallen, W. E., 1990. *An Experimental Investigation of the Redistribution of Gas Stream Total Temperature in a High Turning Angle Transonic Planar Cascade*. PhD Thesis, Queen’s University, Kingston, Ontario, April.
- [9] Carscallen, W. E., Currie, T. C., Hogg, S. I., and Gostelow, J. P., 1999. “Measurement and Computation of Energy Separation in the Vortical Wake Flow of a Turbine Nozzle Cascade”. *J. Turbomachinery*, **121**, pp. 703–708.
- [10] Carscallen, W. E., Fleige, H. U., and Gostlow, J. P., 1996. “Transonic Turbine Vane Wake Flows”. ASME Paper No. 96-GT-419.
- [11] Carscallen, W. E., and Oosthuizen, P. H., 1989. “The Effect of Secondary Flow on the Redistribution of the Total Temperature Field Downstream of a Stationary Turbine Cascade”. In AGARD-CP-469 Secondary Flows In Turbomachines, pp. 27–1–27–13.
- [12] Cebeci, T., and Carr, L., 1987. “A Computer Program for Calculating Laminar and Turbulent Boundary Layers for Two-Dimensional Time-Dependant Flows”. Technical Memorandum TM-78470, NASA.

- [13] Chen, S., 1987. “A Loss model for the Transonic Flow Low-Pressure Steam Turbine Blades”. IMechE Paper No. C269/87.
- [14] Ciccattelli, G., and Sieverding, C. H., 1997. “The Effect of Vortex Shedding on the Unsteady Pressure Distribution Around the Trailing Edge of a Turbine Blade”. *J. Turbomachinery*, **119**, pp. 810–818.
- [15] Corriveau, D., 2005. *Influence of Loading Distribution on the Performance of High Pressure Turbine Blades*. PhD Thesis, Carleton University, Ottawa, Ontario, July.
- [16] Corriveau, D., and Sjolander, S. A., 2007. “Influence of Loading Distribution on the Off-Design Performance of High Pressure Turbine Blades”. *J. Turbomachinery*, **129**, pp. 563–571.
- [17] Craig, H. R. M., and Cox, H. J. A., 1971. “Performance Estimates of Axial Flow Turbines”. *Proc. Inst. Mech. Eng.*, **185** (32), pp. 407–424.
- [18] Currie, T. C., and Carscadden, W. E., 1998. “Simulation of Trailing Edge Vortex Shedding in a Transonic Turbine Cascade”. *J. Turbomachinery*, **120**, pp. 10–19.
- [19] Dawes, W. N., Camus, J.-J., Xu, L. P., and Graham, C. G., 1987. “Measured and Predicted Loss Generation in Transonic Turbine Blading”. In AGARD-CP-401, pp. 8–1–8–11.
- [20] Denton, J. D., 1993. “Loss Mechanisms in Turbomachines”. *J. Turbomachinery*, **115**, pp. 621–656.
- [21] Denton, J. D., and Cumpsty, N. A., 1987. “Loss Mechanisms in Turbomachines”. IMechE Paper No. C260/87.
- [22] Denton, J. D., and Xu, L., 1990. “The Trailing Edge Losses of Transonic Turbine Blades”. *J. Turbomachinery*, **112**, pp. 277–285.
- [23] Dietrichs, H., Hourmouziadis, J., Malzacher, F., and Braunling, 1987. “Flow Phenomenon in Transonic Turbine Cascades Detailed Experimental and Numerical Investigation”. International Symposium on Air Breathing Engines. ISABE 87-7031.
- [24] Dixon, S. L., 2005. *Fluid Mechanics and Thermodynamics of Turbomachinery*, 5th ed. Butterworth-Heinemann, Burlington, MA.
- [25] Dunham, J., and Came, P. M., 1970. “Improvements to the Ainley/Mathieson Method of Turbine Performance Prediction”. *J. of Eng. for Power*, **92**, pp. 252–256.
- [26] Flige, H. U., 1992. *Investigation of Unsteady Wakes from Transonic Turbine Nozzle Guide Vanes*. Diploma Thesis, Institute for Turbomachinery, University of Hanover (Gottfried Wilhelm Leibniz Universitat), Hannover, Germany, May.

- [27] Fluent Inc., 2004. Fluent 6.3 Documentation.
- [28] Gerrard, J. H., 1965. “The Mechanics of the Formation Region of Vortices Behind Bluff Bodies”. *J. Fluid Mech.*, **25** (6), pp. 401–413.
- [29] Gostelow, J. P., 2006. “On Vortex Formation in the Wake of Flows of Transonic Turbine Vanes and Oscillating Airfoils”. *J. Turbomachinery*, **128**, pp. 528–535.
- [30] Graham, C. G., and Kost, F. H., 1979. “Shock Boundary Layer Interaction on High Turning Transonic Turbine Cascades”. ASME Paper No. 79-GT-37.
- [31] Hanjalic, K., Nagano, Y., and Tummers, M., Eds., 2003. Ten Years of Industrial Experience with the SST Turbulence Model, vol. 4.
- [32] Huey, L. J., 1978. “A Yaw-Insensitive Static Pressure Probe”. *Journal of Fluids Engineering*, **100**, pp. 229–231.
- [33] Jouini, D. B. M., Sjolander, S. A., and Moustapha, S. H., 2002. “Midspan Flow-Field Measurements for Two Transonic Linear Turbine Cascades at Off-Design Conditions”. *J. Turbomachinery*, **124**, pp. 176–186.
- [34] Kacker, S. C., and Okapuu, U., 1982. “A Mean Line Prediction Method for Axial Flow Turbine Efficiency”. *J. Turbomachinery*, **104**, pp. 111–119.
- [35] Kiock, R., Lethaus, F., Baines, N. C., and Sieverding, C. H., 1986. “The Transonic Flow Through a Plane Turbine Cascade as Measured in Four European Wind Tunnels”. *J. Turbomachinery*, **108**, pp. 277–284.
- [36] Kost, F., 2008. “Probes in Transonic Flow”. XIX Biannual Symposium on Measuring Techniques in Turbomachinery: Transonic and Supersonic Flow in Cascades and Turbomachines, pp. 1–4.
- [37] Kundu, P. K., and Cohen, I. M., 2004. *Fluid Mechanics*, 3rd ed. Elsevier Academic Press, London, UK.
- [38] Lawaczeck, O., 1970. “Der Prüfstand für ebene Schaufelgitter der Aerodynamischen Versuchsanstalt Göttingen”. Bericht 70 A 46, DFVLR-AVA.
- [39] Lepicovsky, J., Chima, R. V., McFarland, E. R., and Wood, J. R., 2001. “On Flowfield Periodicity in the NASA Transonic Flutter Cascade”. *J. Turbomachinery*, **123**, pp. 501–508.
- [40] Lewis, W. E., 1965. “Fixed Direction Probes for Aerodynamic Measurements”. *Proc. Instn. Mech. Engrs.*, **180**, Part 3J, pp. 141–151.
- [41] Mee, D. J., Baines, N. C., Oldfield, M. L., and Dickens, T. E., 1992. “An Examination of the Contributions to Loss on a Transonic Turbine Blade in Cascade”. *J. Turbomachinery*, **114**, pp. 155–162.

- [42] Menter, F. R., 1993. “Zonal Two-Equation $k - \omega$ Turbulence Models for Aerodynamic Flows”. Paper No. AIAA-93-2906.
- [43] Motallebi, F., and Norbury, J. F., 1981. “The Effect of Base Bleed on Vortex Shedding and Base Pressure in Compressible Flow”. *J. Fluid Mech.*, **110**, pp. 273–292.
- [44] Moustapha, S. H., Carscallen, W. E., and McGeachy, J. D., 1993. “Aerodynamic Performance of a Transonic Low Aspect Ratio Turbine Nozzle”. *J. Turbomachinery*, **115**, pp. 400–415.
- [45] Moustapha, S. H., Okapuu, U., and Williamson, R. G., 1987. “Influence of Rotor Blade Loading on the Performance of a Highly Loaded Turbine Stage”. *J. Turbomachinery*, **109**, pp. 155–161.
- [46] Moustapha, S. H., and Williamson, R. G., 1986. “Effect of Two Endwall Contours on the Performance of an Annular Nozzle Cascade”. *AIAA Journal*, **24** (9), pp. 1524–1530.
- [47] Oosthuizen, P. H., and Carscallen, W. E., 2007. *An Introduction to Compressible Flow*. P&CC, Kingston, ON.
- [48] Povey, T., Oldfield, M. L., and Haselbach, F., 2008. “Transonic turbine vane tests in a new miniature cascade facility”. *Proc. Instn. Mech. Engrs. Part A: J. Power and Energy*, **222**, pp. 529–539.
- [49] Pratt and Whitney Canada, 1992. “PT6A-41/42/45 Training Guide”. Tech. rep.
- [50] Prust, H. W., and Helon, R. M., 1972. “Flow Conditions Around the Exit and Downstream of Certain Stator Blading With Various Trailing-Edge Thickness and Geometries”. Technical Memorandum TM-X-2659, NASA.
- [51] Raffel, M., and Kost, F., 1998. “Investigation of Aerodynamic Effects of Coolant Ejection at the Trailing Edge of a Turbine Blade Model by PIV and Pressure Measurements”. *Experiments in Fluids*, **24**, pp. 447–461.
- [52] Reiss, H., and Blocs, A., 2000. “Aerodynamic Loss Measurement in a Linear Cascade with Film Cooling Injection”. 15th Bi-annual Symposium on Measurement Techniques in Transonic and Supersonic Flow in Cascades and Turbomachines.
- [53] Rowe, A., Fry, A. L. A., and Motallebi, F., 2001. “Influence of Boundary-Layer Thickness on Base Pressure and Vortex Shedding Frequency”. *AIAA Journal*, **39** (4), pp. 754–756.
- [54] Schlichting, H., 1966. *Boundary Layer Theory*. McGraw-Hill, New York.
- [55] Sieverding, C., 1975. “Pressure Probe Measurements in Cascades”. In *Modern Methods of Testing Rotating Components in Turbomachines (Instrumentation)*, M. Pianko, Ed., no. AGARD-AG-207. pp. 20–30.

- [56] Sieverding, C., Maretto, L., Lehthaus, F., and Lawaczeck, O., 1974. “Design and Calibration of Four Probes for Use in the Transonic Turbine Cascade Testing”. Technical Note 100, VKI, Rhode Saint Genese, Belgium.
- [57] Sieverding, C., Richard, H., and Desse, J., 2003. “Turbine Trailing Edge Flow at High Subsonic Outlet Mach Number”. *J. Turbomachinery*, **125**, pp. 298–309.
- [58] Sieverding, C., Stanislas, M., and Snoeck, J., 1980. “The Base Pressure Problem in Transonic Turbine Cascades”. *J. of Eng. for Power*, **102**, pp. 711–718.
- [59] Sieverding, C. H., and Heinemann, H., 1990. “The Influence of Boundary Layer State on Vortex Shedding From Flat Plates and Turbine Cascades”. *J. Turbomachinery*, **112**, pp. 181–187.
- [60] Solomon, G. E., 1955. “Transonic Flow Past Cone Cylinders”. Technical Report 1242, NACA.
- [61] Sonoda, T., Arima, T., Olhofer, M., Sendhoff, B., Kost, F., and Giess, P.-A., 2006. “A Study of Advanced High-Loaded Transonic Turbine Airfoils”. *J. Turbomachinery*, **128**, pp. 620–657.
- [62] Spaid, F. W. and Hurley, F. X., and Hellman, T. H., 1975. “Miniature Probe for Transonic Flow Direction Measurements”. *AIAA Journal*, **13**, pp. 253–255.
- [63] Stanewsky, E., 1973. “Transonic Flows in Turbomachinery”. Lecture Series 59, von Karman Institute for Fluid Dynamics, May.
- [64] Taylor, G. I., and Maccoll, J. W., 1933. “The Air Pressure on a Cone Moving at High Speed”. *Proc. Roy. Soc. (London) ser. A*, **139**, pp. 278–311.
- [65] Truckenbrodt, E., 1955. “A Method of Quadrature for the Calculation of Laminar and Turbulent Boundary Layers in Plane and Rotation Symetric Flow”. Technical Memorandum TM 1379, NACA.
- [66] Vuillez, C., and Veuillot, J. P., 1990. “Quasi-3D Viscous Flow Computations in Subsonic and Transonic Turbomachinery Blading”. Paper No. AIAA-90-2126.
- [67] Wilcox, D. C., 1993. “A Two-Equation Turbulence Model for Wall-Bounded and Free-Shear Flows”. Paper No. AIAA-93-2905.
- [68] Williamson, R. G., and Moustapha, S. H., 1986. “Annular Cascade Testing of Turbine Nozzles at High Exit Mach Numbers”. *J. Turbomachinery*, **108**, pp. 313–320.
- [69] Xu, L., and Denton, D. J., 1988. “The Base Pressure and Loss for a Family of Four Turbine Blades”. *J. Turbomachinery*, **110**, pp. 9–17.
- [70] Zhu, J., and Sjolander, S. A., 1987. “Improved Profile Loss and Deviation Correlations for Axial Turbine Blade Rows”. ASME Paper No. GT2005-69077.

Flow Quality in Transonic Calibration Tunnel

A.1 Calibration Tunnel Design

The *finger* type three-hole probe was calibrated in the NRC transonic calibration tunnel. A schematic of the tunnel is shown in Figure A.1. The tunnel was a suction type design with perforated sidewalls which allowed it to operate at a wide range of transonic Mach numbers without the need for the test section geometry to be changed. The same 2MW Brown-Boveri exhauster which serviced the transonic linear cascade was connected to the calibration tunnel. This allowed the test section to reach a maximum Mach number of 1.22.

The same instrumentation used on the transonic linear cascade was used in the calibration tunnel to measure the inlet total temperature and pressure as well as the probe pressures and endwall static pressures. The probe was rotated using an angular traverse mechanism actuated by a computer controlled stepper motor. In order to eliminate the accumulation of any position errors as the probe moved through its calibration points, the angles were measured in pairs, first the positive angle then its negative counterpart. The resulting uncertainty in angular position was found

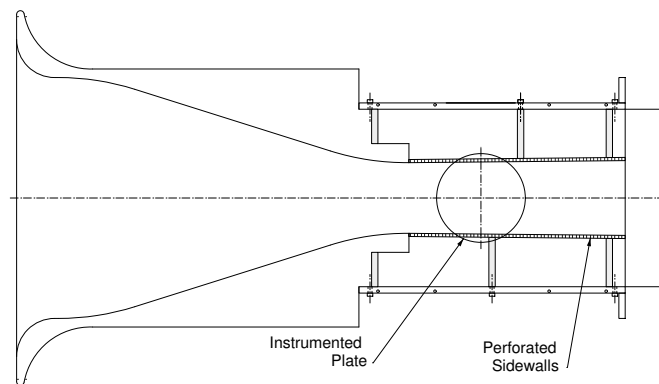


Figure A.1: Schematic of the NRC transonic probe calibration tunnel

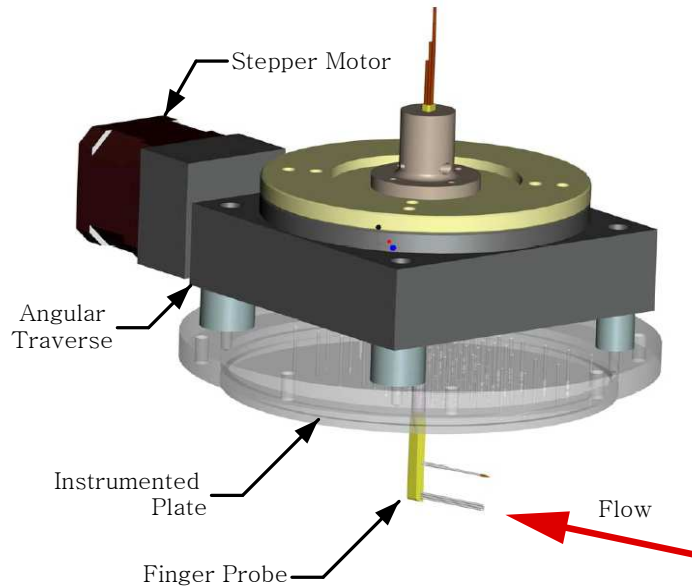


Figure A.2: Finger probe installed in traverse mechanism

to be negligible relative to other sources of error in the calibration procedure. The angles were set in increments of 1° between $\pm 12^\circ$ for the pre-traverse calibration and $\pm 10^\circ$ for the post-traverse calibration.

The finger probe, installed in the angular traverse mechanism is shown in Figure A.2.

A.2 Flow Quality in the Calibration Tunnel

The quality of the data which any pneumatic probe could provide was sensitive to the quality of the flow in which it was calibrated. The calibration procedure used with the finger probe employed calibration coefficients to relate the measured pressures from the probe to the known *true* calibration tunnel conditions. When the probe was placed in a flow where the true flow properties were unknown, these calibration coefficients allowed the true values to be determined from the measured pressures. Therefore, the probe could only measure flow properties as accurately as the true tunnel conditions were known.

The three flow properties which were measured were the total pressure, flow angle and Mach number. The true total pressure of the flow was the ambient room pressure.

This was measured with a precision barometric indicator. The flow angle was set with the angular traverse mechanism. The third flow property, the Mach number, was the property with the largest potential for uncertainty. The errors in Mach number were of a much larger magnitude than those in total pressure or flow angle. Therefore, the remaining focus will be to ascertaining the ability of the calibration tunnel to record an accurate and constant indication of the Mach number in the test section and to maintain the flow at this Mach number for the duration of the calibration.

A.2.1 Test Section Mach Number

In order to determine the test section Mach number, a characteristic static pressure was compared to the inlet total pressure to calculate the true test section isentropic Mach number. In order for the tunnel isentropic Mach number to be most indicative of the mean test section flow, it was necessary that the static pressure be measured in a region of homogeneous flow. This required some form of flow visualization within the test section. Sieverding *et al.* [56] examined the flow in their test section using a Schlieren system. Unfortunately the NRC transonic calibration tunnel lacked optical access to the test section due to the need for perforated sidewalls. Therefore, in order to obtain a coarse picture of the shock structure in the test section, an array of static pressure taps was installed on the upper endwall of the tunnel. The layout of the pressure ports relative to the probe is shown in Figure A.3. Each static pressure reading was referenced to the inlet total pressure to create a local isentropic Mach number. The local isentropic Mach number distributions are shown in Figure A.4. It can be seen that a normal shock appeared at Mach one at the probe tip. As the Mach number was increased, the shock impingement point moved downstream. The position of this shock had a significant impact on the determination of the true tunnel Mach number.

During the calibration tests, the reference static port for computing the tunnel Mach number was located directly above the probe tip. This position is shown as *Ref A* in Figure A.3. Figure A.4 showed that at transonic speeds, the static port was in a shock affected area and thus it recorded a highly fluctuating and incorrect static

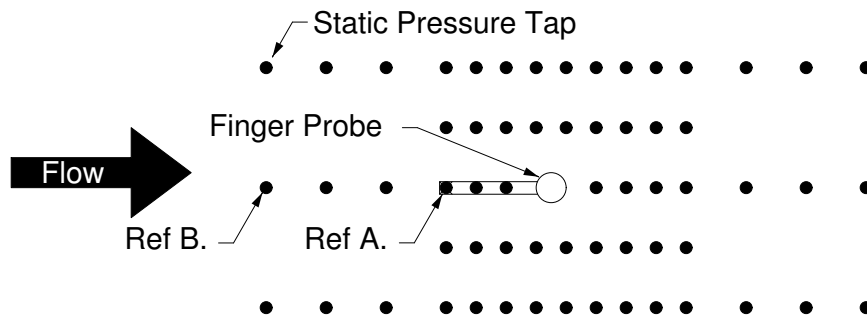


Figure A.3: Layout of static pressure taps on calibration tunnel endwall

pressure. By switching to a reference static pressure tap further upstream, *Ref B*, the magnitude of the fluctuations were decreased. This had an additional effect of changing the computed value of the tunnel Mach number. The new reference static pressure tap was chosen at the furthest upstream location in line with the probe tip, shown as *Ref B* in Figure A.3. The true values of the tunnel Mach number were much more closely spaced than was intended, however they covered a sufficient range to produce an adequate calibration. All probe calibration data were presented using the new reference static pressure to quantify the tunnel conditions. Table A.1 shows the test section Mach numbers computed using the original and new reference static pressures.

Table A.1: Test Section Mach Numbers Calculated with Different Reference Static Pressures

Ref A	Ref B
0.30	0.30
0.51	0.51
0.72	0.69
1.07	0.89
1.16	1.01
1.18	1.07
1.19	1.14
1.22	1.19

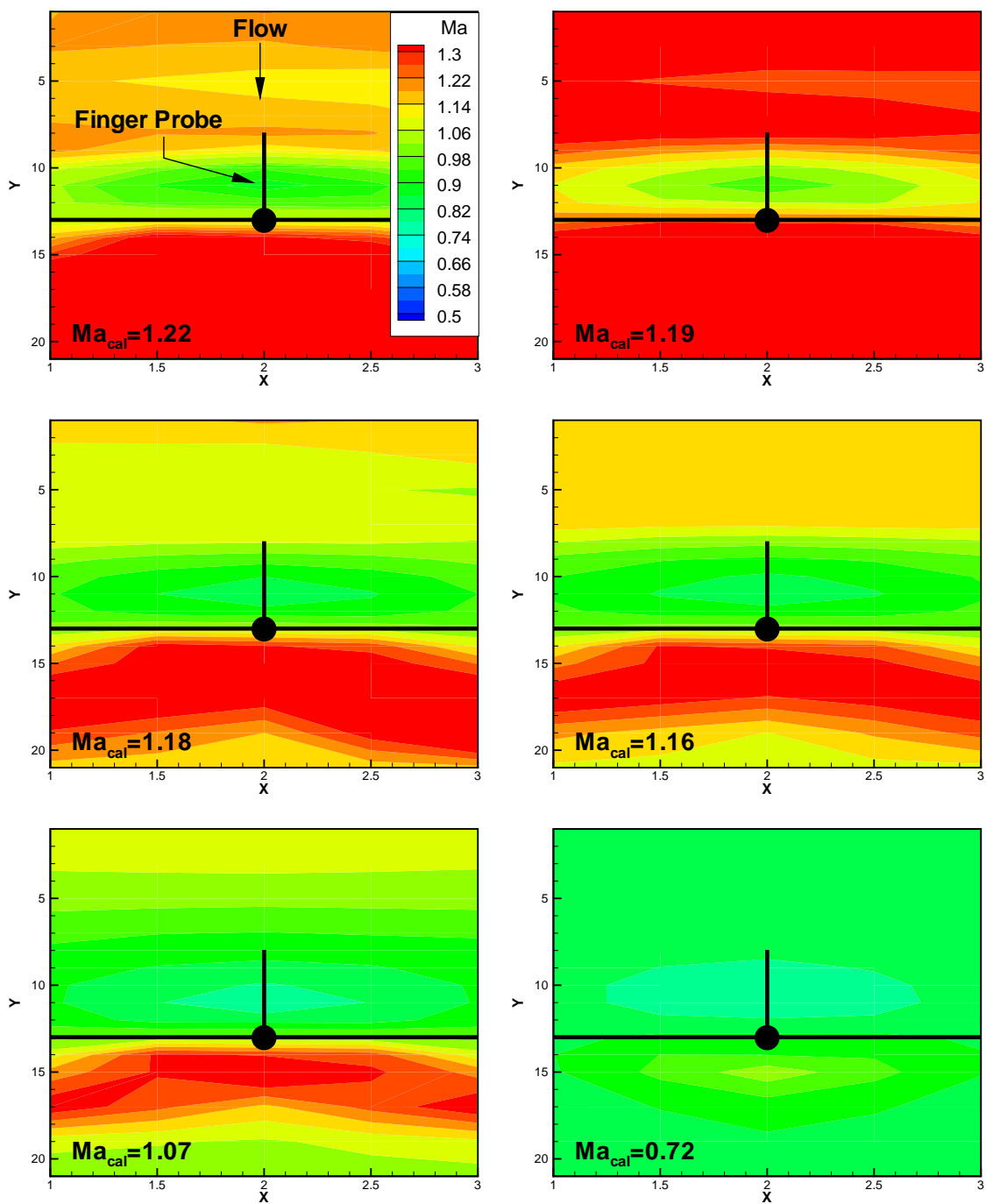


Figure A.4: Static pressure distribution on calibration tunnel endwalls

A.2.1.1 Mach Number Consistency Over Time

During the calibration tests, there was a small oscillation in the measured test section Mach number over time. It was important to quantify the magnitude of this oscillation to quantify the error in the *true* tunnel Mach number.

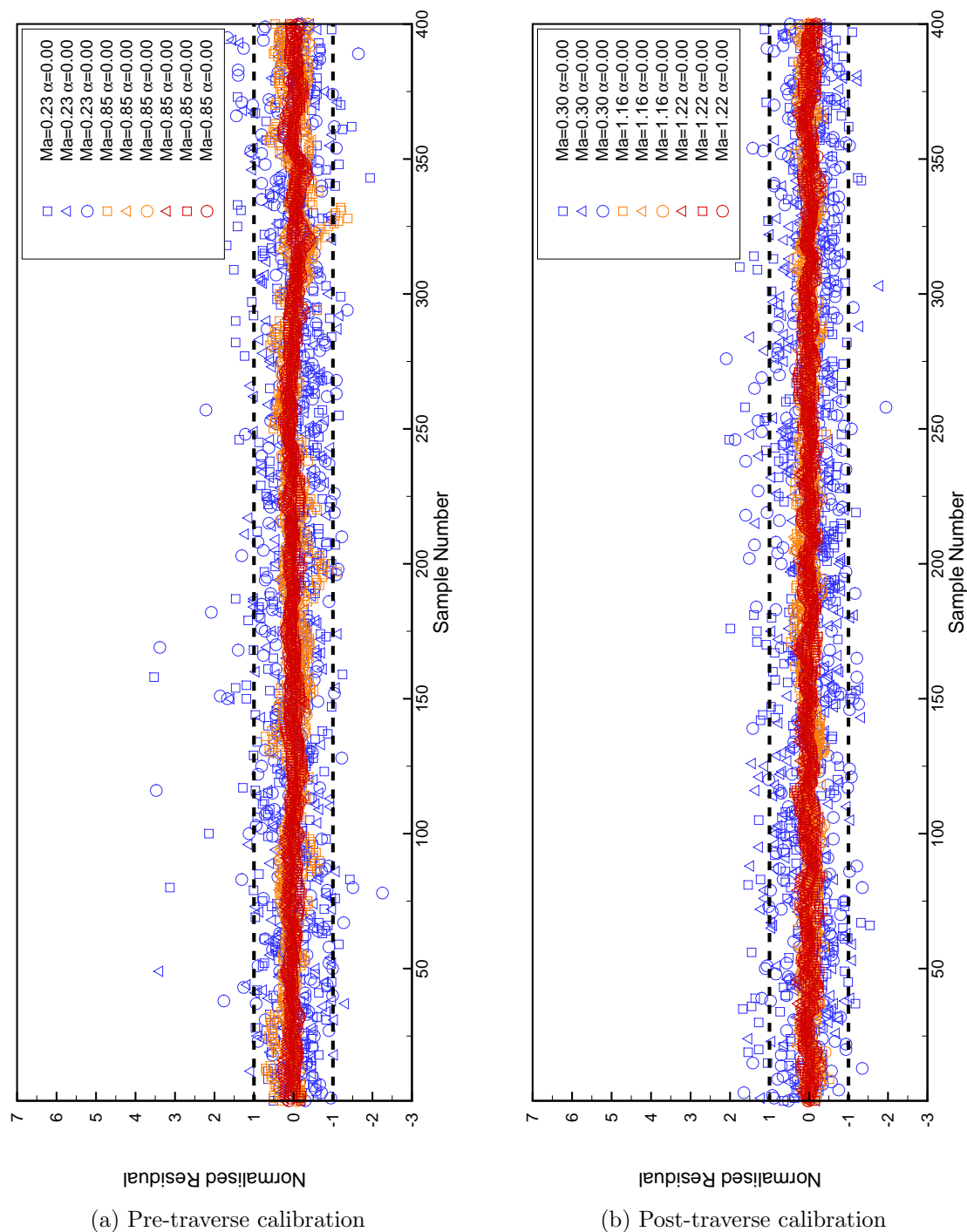
The instantaneous Mach number was computed for each sample which made up the average tunnel Mach number for a given calibration point. The difference between the instantaneous Mach number and the mean Mach number at that calibration point was normalized by that mean Mach number and was plotted in Figure A.5. It could be seen that there were greater fluctuations at the supersonic calibration Mach numbers. However, in all cases the fluctuations in this normalized residual remained within $\pm 1\%$. This was an acceptable degree of error for the calibration Mach number, however it should be noted that due to moving the reference static tap, two calibration Mach numbers were, in fact, within 1% of each other. These two calibration points, Mach 1.18 and 1.19 could not be treated as distinct. Therefore the Mach 1.19 calibration data was not used as this Mach number showed greater scattering over time than the Mach 1.18 data.

A.2.2 Angle History

One common challenge in transonic testing is that small changes in the blockage of a passage can have large effects on the flow. There was a possibility that as the probe moved through its range of motion, the varying blockage would change the test section Mach number. To examine the magnitude of this effect, the time-averaged tunnel Mach number was computed for every Mach number and angle combination and the results are shown in Figure A.6. In this figure, the residual was computed using Equation A.1.

$$Res = \frac{Ma_{(Ma,\alpha)} - \frac{1}{n_\alpha} \sum_{i=1}^{n_\alpha} Ma_{(Ma,\alpha_i)}}{\frac{1}{n_\alpha} \sum_{i=1}^{n_\alpha} Ma_{(Ma,\alpha_i)}} \quad (\text{A.1})$$

It can be seen that in the pre-traverse calibration calibration, the extreme angles investigated did have an effect on the tunnel Mach number, especially in the high

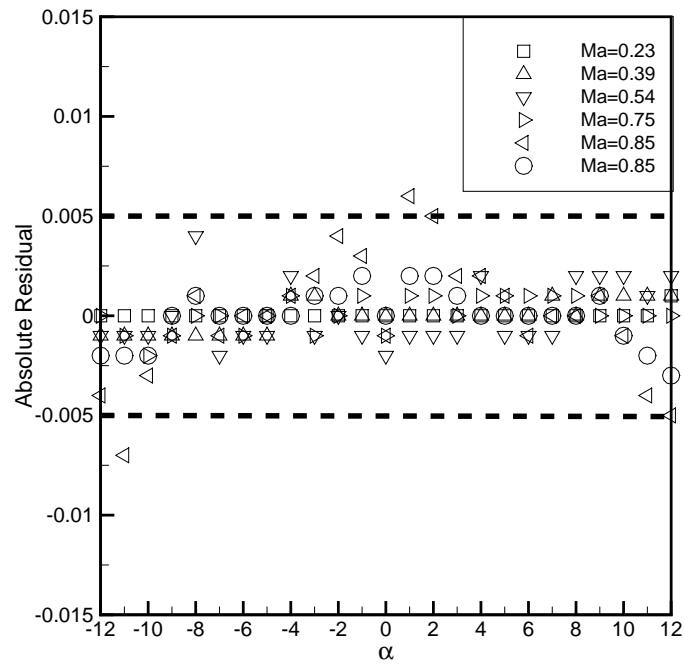


(a) Pre-traverse calibration

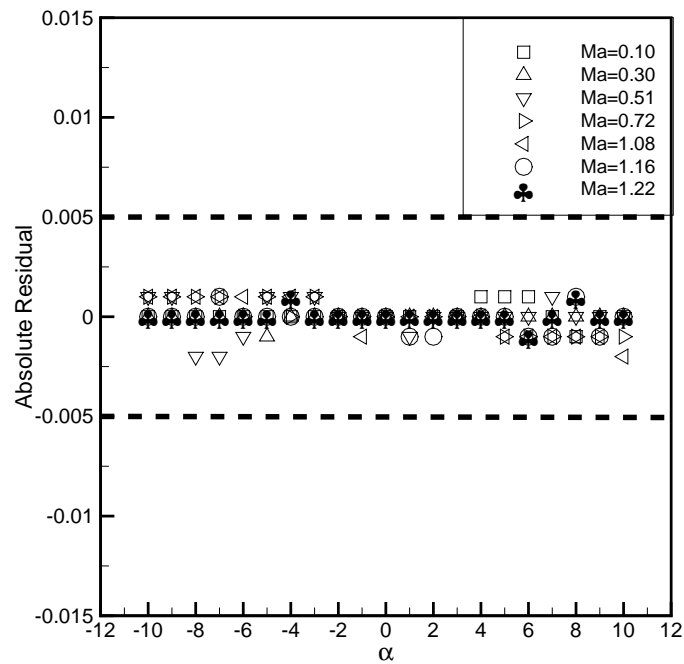
(b) Post-traverse calibration

Figure A.5: Effect of probe angle on tunnel Mach number

transonic range. This effect was not nearly as pronounced in the post-traverse calibration data. However, in both cases the majority of the data was within $\pm 0.005\%$ of a Mach number, showing that the changes in angle did not seriously affect the test section Mach number.



(a) Pre-traverse calibration



(b) Post-traverse calibration

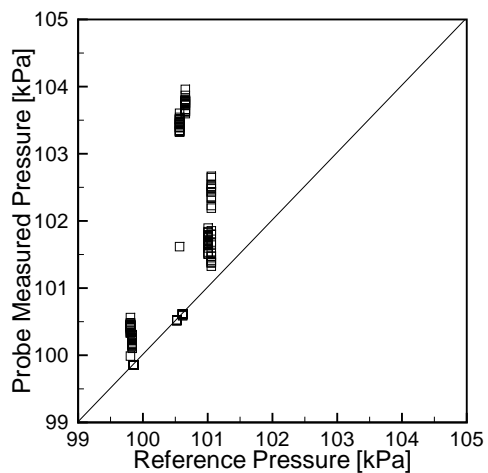
Figure A.6: Effect of probe angle on tunnel Mach number

Appendix B

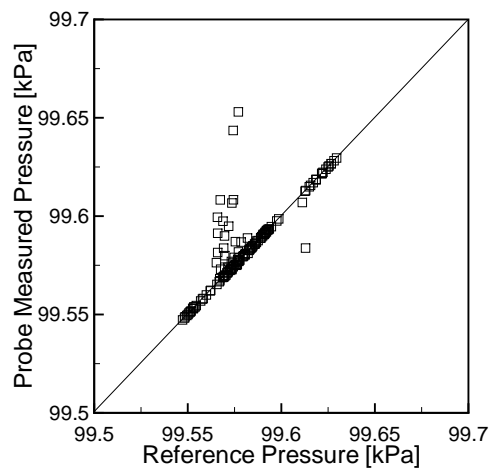
Probe Accuracy

In order to examine how effective the calibrated probe was at measuring flow properties, it was tested in two ways. First, the original calibration data were reduced using the algorithm presented in Section 3.6.2 and the results were compared to the known tunnel conditions. The results from this test are shown in Figure B.1. The second, more rigorous, test was to take data measured at Mach numbers and flow angles not used for calibration, and to examine how the probe results compared to the known tunnel conditions. This was shown in Figure B.2. Unfortunately, validation data were only available for the pre-calibration.

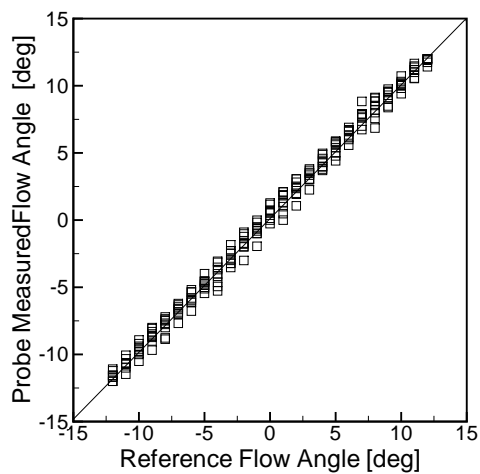
The post-traverse data were seen to have a much greater ability to extract the true tunnel conditions from the measured probe pressures. However, only the data used to create the calibration tables were used to validate the post-traverse results. The pre-traverse calibration was performed at more Mach numbers than were used to create the calibration tables, and these data were included in Figure B.1 to test the predictive ability of the pre-traverse calibration. It can be seen that in transonic range the pre-traverse calibration had significant errors in predicting the Mach number, as was expected from the way that the static pressure anomaly was dealt with. Additionally, the pre-traverse calibration was validated with data taken from angles and Mach numbers not used in the calibration tables. Figure B.2 corroborates the fact that the probe had difficulty measuring in the transonic range.



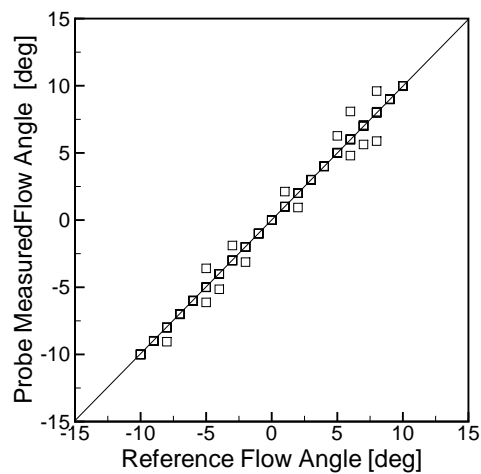
(a) Pre-traverse calibration, Total Pressure



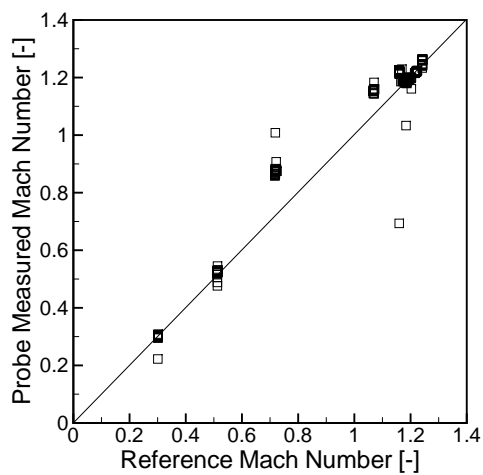
(b) Post-traverse calibration, Total Pressure



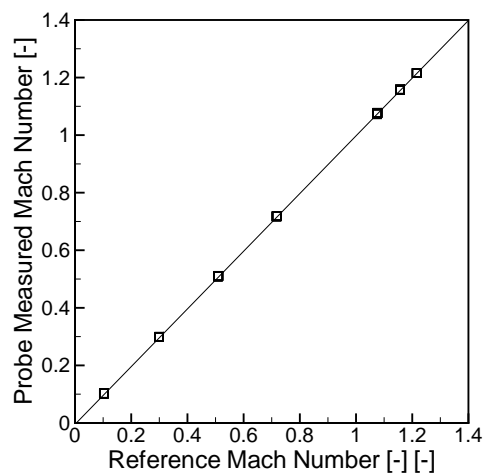
(c) Pre-traverse calibration, Flow Angle



(d) Post-traverse calibration, Flow Angle

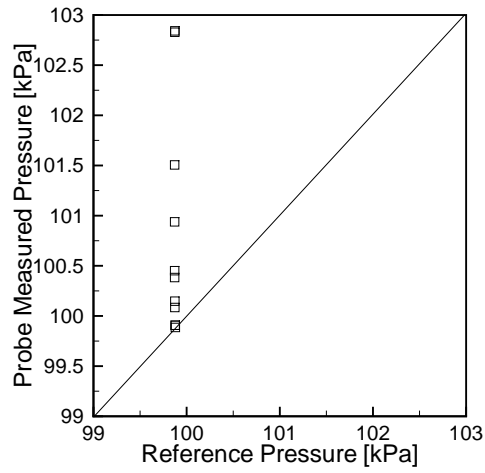


(e) Pre-traverse calibration, Mach Number

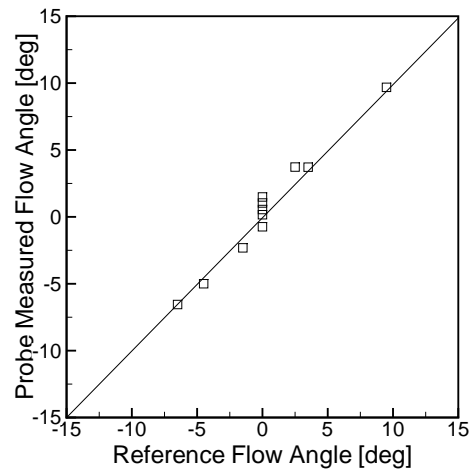


(f) Post-traverse calibration, Mach Number

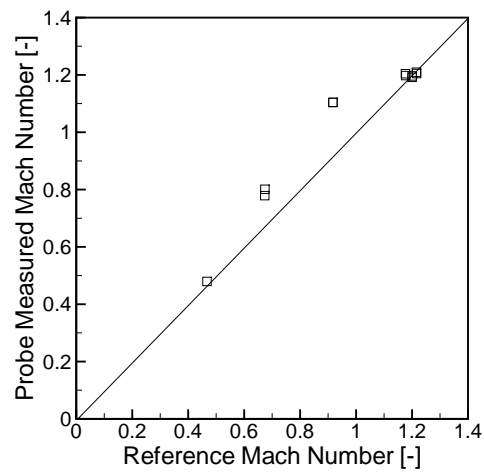
Figure B.1: Validation using calibration data



(a) Total Pressure



(b) Flow Angle



(c) Mach Number

Figure B.2: Pre-traverse calibration validation using new data

Uncertainty Calculations

C.1 Uncertainty in Measurements

Errors in total pressure and flow angle were found to be normally distributed. Therefore, the 95% confidence interval was determined from the data shown in Figure B.1. The errors in mach number were not normally distributed, so the worst case error identified in Section 3.5.4 was used. The uncertainty in measurements of the total pressure and temperature were considered negligible as they were made with recently calibrated instruments which were secondary standards. The 95% confidence interval on the basic quantities from which more abstract values were derived are shown in Table C.1. Using the method of partial differentials, the uncertainty in most of the measured quantities could be made.

Table C.1: 95% confidence intervals on measured quantities

Property	95% Confidence Interval
P_{o_2}	± 6 kPa
α	$\pm 0.7^\circ$ (0.012 rad)
Ma	± 0.6
P_{o_1}	± 0.0 kPa
T_{o_1}	± 0.0 K

The uncertainty in the static pressure was determined from the uncertainty in the total pressure and Mach number using Equation C.1.

$$\mu_{P_{s_2}} = \sqrt{\left(\frac{\partial P_{s_2}}{\partial P_{o_2}} \mu_{P_{o_2}}\right)^2 + \left(\frac{\partial P_{s_2}}{\partial Ma} \mu_{Ma}\right)^2} \quad (\text{C.1})$$

where:

$$\frac{\partial P_{s_2}}{\partial P_{o_2}} = \left(1 + \frac{\gamma - 1}{2} Ma^2\right)^{\frac{-\gamma}{\gamma - 1}}$$

$$\frac{\partial P_{s_2}}{\partial Ma} = -\gamma P_{o_2} Ma \left(1 + \frac{1 + \gamma}{2} Ma^2\right)^{\frac{-(\gamma + 1)}{\gamma - 1}}$$

C.2 Uncertainty in Mass Averaged Quantities

To begin to define the uncertainty in the mass averaged quantities, the uncertainty in the differential mass flow at each measurement point, $\Delta\dot{m}$, had to be computed. The formula for $\Delta\dot{m}$ is given in Equation 3.11.

$$\mu_{\Delta\dot{m}} = \sqrt{\left(\frac{\partial\Delta\dot{m}}{\partial P_o}\mu_{P_o}\right)^2 + \left(\frac{\partial\Delta\dot{m}}{\partial\alpha}\mu_{\alpha}\right)^2 + \left(\frac{\partial\Delta\dot{m}}{\partial Ma}\mu_{Ma}\right)^2} \quad (\text{C.2})$$

where:

$$\begin{aligned} \frac{\partial\Delta\dot{m}}{\partial P_o} &= \frac{\Delta\dot{m}}{P_o} \\ \frac{\partial\Delta\dot{m}}{\partial T_o} &= \frac{2\Delta\dot{m}}{T_o} \\ \frac{\partial\Delta\dot{m}}{\partial\alpha} &= \cot\alpha\Delta\dot{m} \\ \frac{\partial\Delta\dot{m}}{\partial Ma} &= \frac{P_o}{\sqrt{T_o}}\sqrt{\frac{\gamma}{R}}\sin\alpha\left(1 + \frac{\gamma-1}{2}Ma^2\right)^{\frac{1+\gamma}{2-2\gamma}}\left(1 - \frac{\frac{(1+\gamma)Ma^2}{2}}{1 + \frac{\gamma-1}{2}Ma^2}\right) \end{aligned}$$

The integral of the differential mass-flow across the pitch was calculated using the trapezoid rule as shown in Equation C.3. The uncertainty in the overall mass flow is shown by Equation C.4. This equation weighted the uncertainty for each differential mass flow by the area which is represented. The root of the sum of the squares of these weighted uncertainties was the overall uncertainty in the mass flow

$$\dot{m} = \sum_{i=2}^n \frac{1}{2}(\Delta\dot{m}_{(i)} + \Delta\dot{m}_{(i-1)})(x_{(i-1)} - x_{(i)}) \quad (\text{C.3})$$

$$\mu_{\dot{m}} = \sqrt{\sum_{i=2}^n \left(\left(\frac{1}{2}(\mu_{\Delta\dot{m}_{(i)}})(x_{(i-1)} - x_{(i)}) \right)^2 + \left(\frac{1}{2}(\mu_{\Delta\dot{m}_{(i-1)}})(x_{(i-1)} - x_{(i)}) \right)^2 \right)} \quad (\text{C.4})$$

The mass-averaged value of any property, ψ , could be calculated with Equation C.5. The same principle used to evaluate the uncertainty in the mass flow was applied to the mass-averaged quantities, as shown in Equation C.6. The algorithm for calculating the mixed-out properties was too complex to apply the partial differential method of error propagation.

$$\psi_{ma} = \sum_{i=2}^n \frac{\frac{1}{2}(\psi_{(i)}d\dot{m}_{(i)} + \psi_{(i-1)}d\dot{m}_{(i-1)})(x_{(i-1)} - x_{(i)})}{\dot{m}} = \sum_{i=2}^n \Phi_{(i)} \quad (\text{C.5})$$

$$\mu_{\psi_{ma}} = \sqrt{\left(\sum_{i=2}^n \mu_{\Phi(i)}\right)^2} \quad (\text{C.6})$$

$$\mu_{\Phi(i)} = \sqrt{\left(\frac{\partial\Phi(i)}{\partial\dot{m}}\mu_{\dot{m}}\right)^2 + \left(\frac{\partial\Phi(i)}{\partial\psi(i)}\mu_{\psi(i)}\right)^2 + \left(\frac{\partial\Phi(i)}{\partial\Delta\dot{m}(i)}\mu_{\Delta\dot{m}(i)}\right)^2 + \left(\frac{\partial\Phi(i)}{\partial\psi(i-1)}\mu_{\psi(i-1)}\right)^2 + \left(\frac{\partial\Phi(i)}{\partial\Delta\dot{m}(i-1)}\mu_{\Delta\dot{m}(i-1)}\right)^2} \quad (\text{C.7})$$

where:

$$\begin{aligned} \frac{\partial\Phi(i)}{\partial\dot{m}} &= \frac{-\frac{1}{2}(\psi(i)\Delta\dot{m}(i) + \psi(i-1)\Delta\dot{m}(i-1))(x_{(i-1)} - x_{(i)})}{\dot{m}^2} \\ \frac{\partial\Phi(i)}{\partial\psi(i)} &= \frac{\frac{1}{2}(\Delta\dot{m}(i))(x_{(i-1)} - x_{(i)})}{\dot{m}} \\ \frac{\partial\Phi(i)}{\partial\Delta\dot{m}(i)} &= \frac{\frac{1}{2}(\psi(i))(x_{(i-1)} - x_{(i)})}{\dot{m}} \\ \frac{\partial\Phi(i)}{\partial\psi(i-1)} &= \frac{\frac{1}{2}(\Delta\dot{m}(i-1))(x_{(i-1)} - x_{(i)})}{\dot{m}} \\ \frac{\partial\Phi(i)}{\partial\Delta\dot{m}(i-1)} &= \frac{\frac{1}{2}(\psi(i-1))(x_{(i-1)} - x_{(i)})}{\dot{m}} \end{aligned}$$

Once the uncertainty in the mass-averaged values of P_{O_2} and P_{S_2} were known, the uncertainty in the mass-averaged total pressure loss coefficient, defined in Equation 2.3, could be found.

$$\mu_{Yt_{ma}} = \sqrt{\left(\frac{\partial Yt_{ma}}{\partial P_{O_2}}\mu_{P_{O_2}}\right)^2 + \left(\frac{\partial Yt_{ma}}{\partial P_{S_2}}\mu_{P_{S_2}}\right)^2} \quad (\text{C.8})$$

where:

$$\begin{aligned} \frac{\partial Yt_{ma}}{\partial P_{O_2}} &= \frac{(P_{O_1} - P_{S_2})}{(P_{O_2} - P_{S_2})^2} \\ \frac{\partial Yt_{ma}}{\partial P_{S_2}} &= \frac{-(P_{O_1} - P_{O_2})}{(P_{O_s} - P_{S_2})^2} \end{aligned}$$

C.3 Uncertainty in Local Mach Number

The uncertainty in the value of local Mach number measured on the blades was calculated using Equation C.9. The total and static pressures used in Equation C.9

were measured directly by the HyScan pressure scanner rather than indirectly through the the calibrated finger probe. Therefore, the uncertainty in the static pressure measurements was 0.05% of the HyScan unit's range of ± 103.42 kPa (15 psi), which was 51 Pa. As stated previously, the uncertainty in the total pressure was considered as negligible. Using Equation C.9, the uncertainty in the largest measured surface Mach number of 2 was ± 0.002 , which was smaller than the symbols used to represent the local Mach number. For this reason there were no error bars placed on plots of local Mach number.

$$\mu_{Ma} = \sqrt{\left(\frac{\partial Ma}{\partial P_o} \mu_{P_o}\right)^2 + \left(\frac{\partial Ma}{\partial P_s} \mu_{P_s}\right)^2} \quad (\text{C.9})$$

where:

$$\frac{\partial Ma}{\partial P_o} = \frac{\frac{1}{\gamma} \frac{1}{P_s} \left(\frac{P_o}{P_s}\right)^{\frac{-1}{\gamma}}}{\left(\frac{2}{\gamma-1} \left(\frac{P_o}{P_s}\right)^{\frac{\gamma-1}{\gamma}} - 1\right)^{\frac{1}{2}}}$$

$$\frac{\partial Ma}{\partial P_s} = \frac{\frac{1}{\gamma} \frac{P_o}{P_s^2} \left(\frac{P_o}{P_s}\right)^{\frac{-1}{\gamma}}}{\left(\frac{2}{\gamma-1} \left(\frac{P_o}{P_s}\right)^{\frac{\gamma-1}{\gamma}} - 1\right)^{\frac{1}{2}}}$$

C.4 Uncertainty in Axial Velocity-Density Ratio

The uncertainty in the inlet and outlet mass flows could be found using Equation C.4. This information allowed the uncertainty in the axial velocity-density ratio to be computed using Equation C.10.

$$\mu_{AVDR} = \sqrt{\left(\frac{1}{\dot{m}_1} \mu_{\dot{m}_2}\right)^2 + \left(\frac{-\dot{m}_2}{(\dot{m}_1)^2} \mu_{\dot{m}_1}\right)^2} \quad (\text{C.10})$$

Appendix D
Supplemental Figures

D.1 Traverses

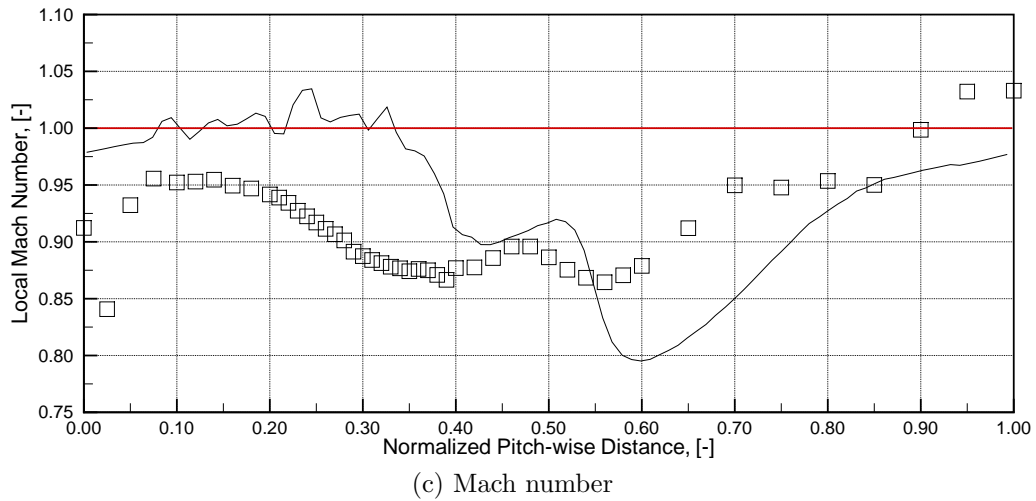
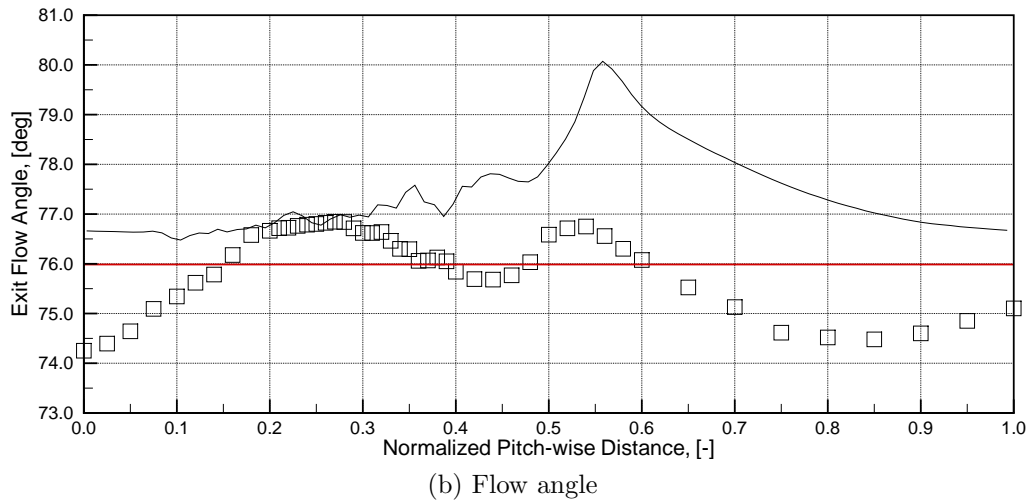
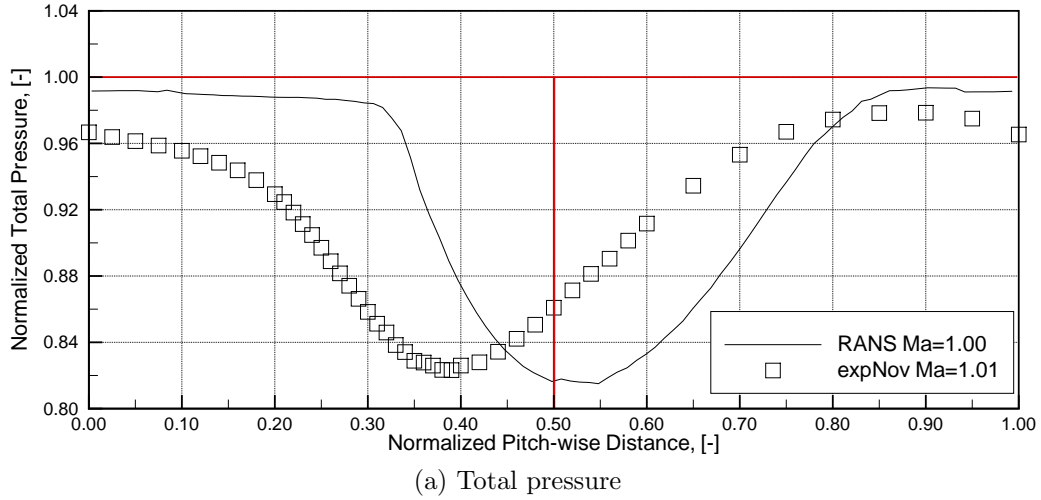
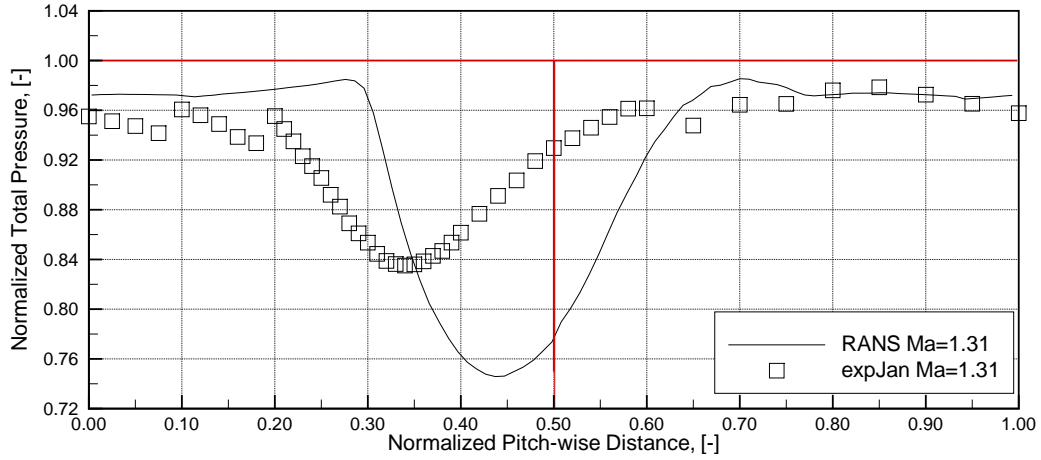
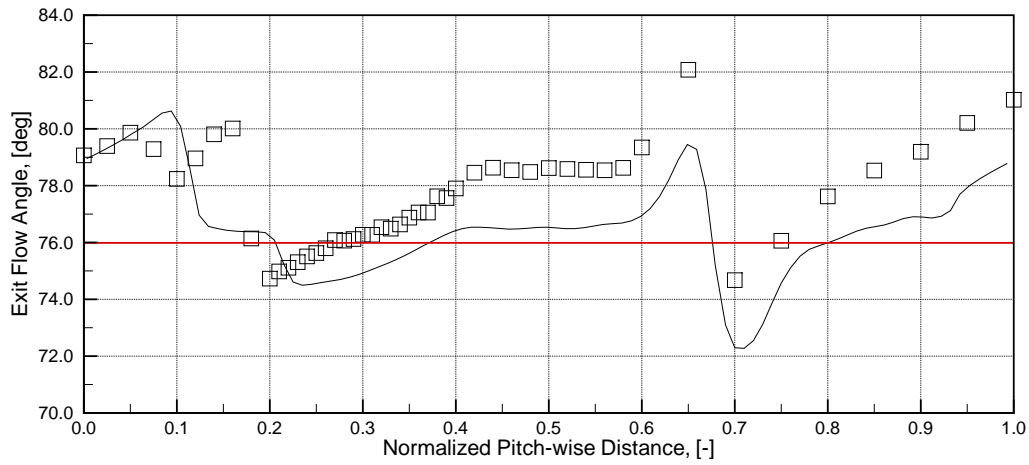


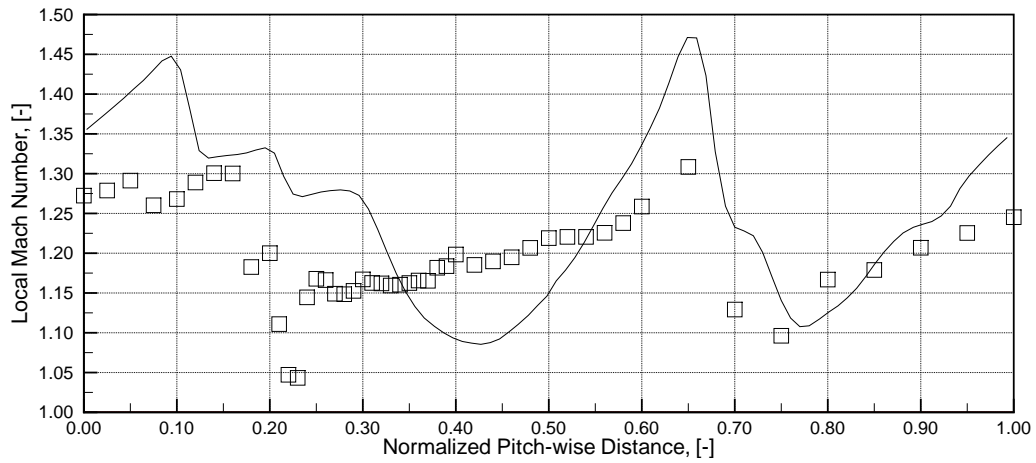
Figure D.1: Experimental and computed wake flowfield for $Ma = 1.0$



(a) Total pressure



(b) Flow angle



(c) Mach number

Figure D.2: Experimental and computed wake flowfield for $Ma = 1.31$

D.2 Blade Loadings

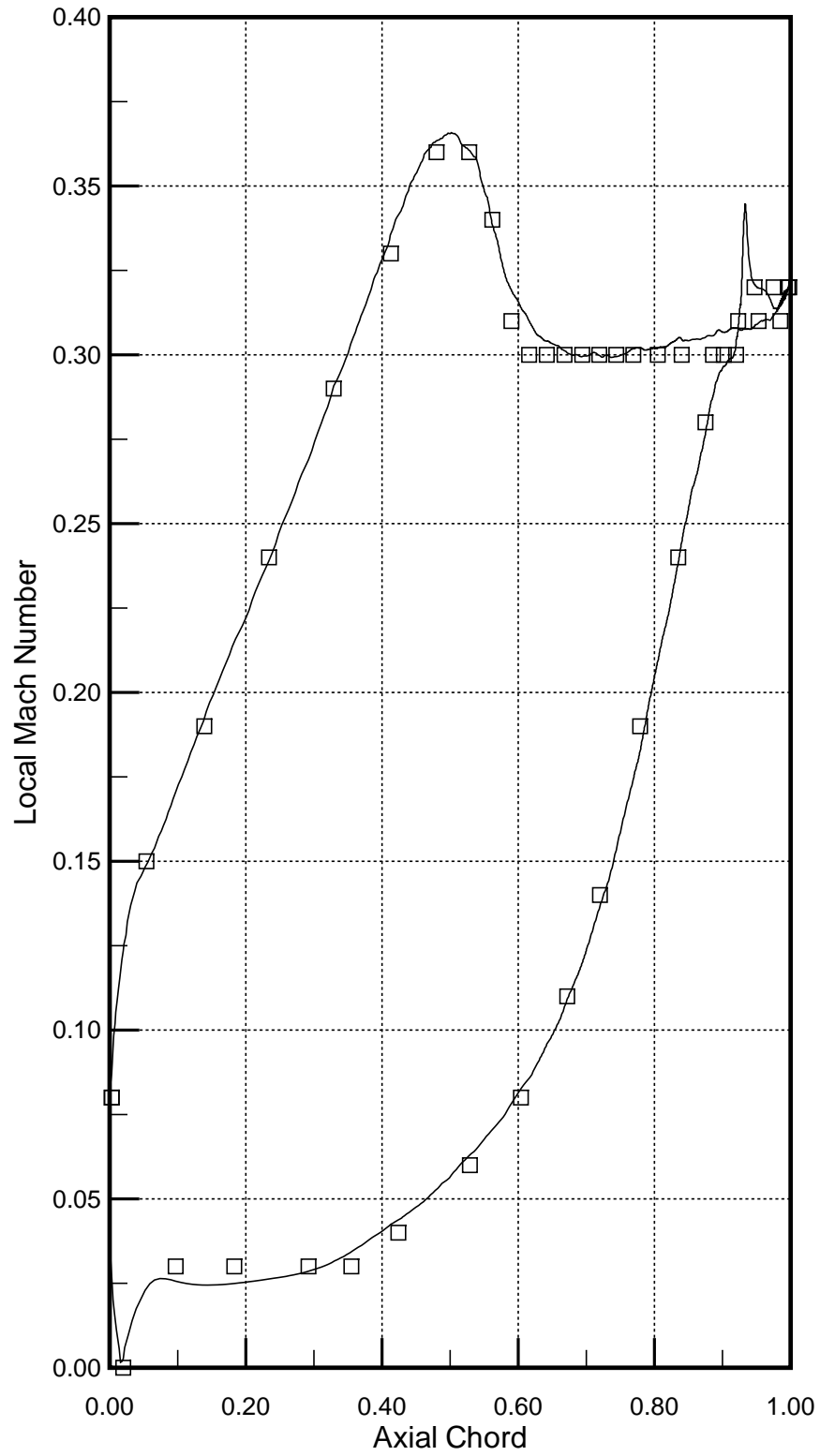


Figure D.3: Measured and predicted surface Mach number at $Ma = 0.3$

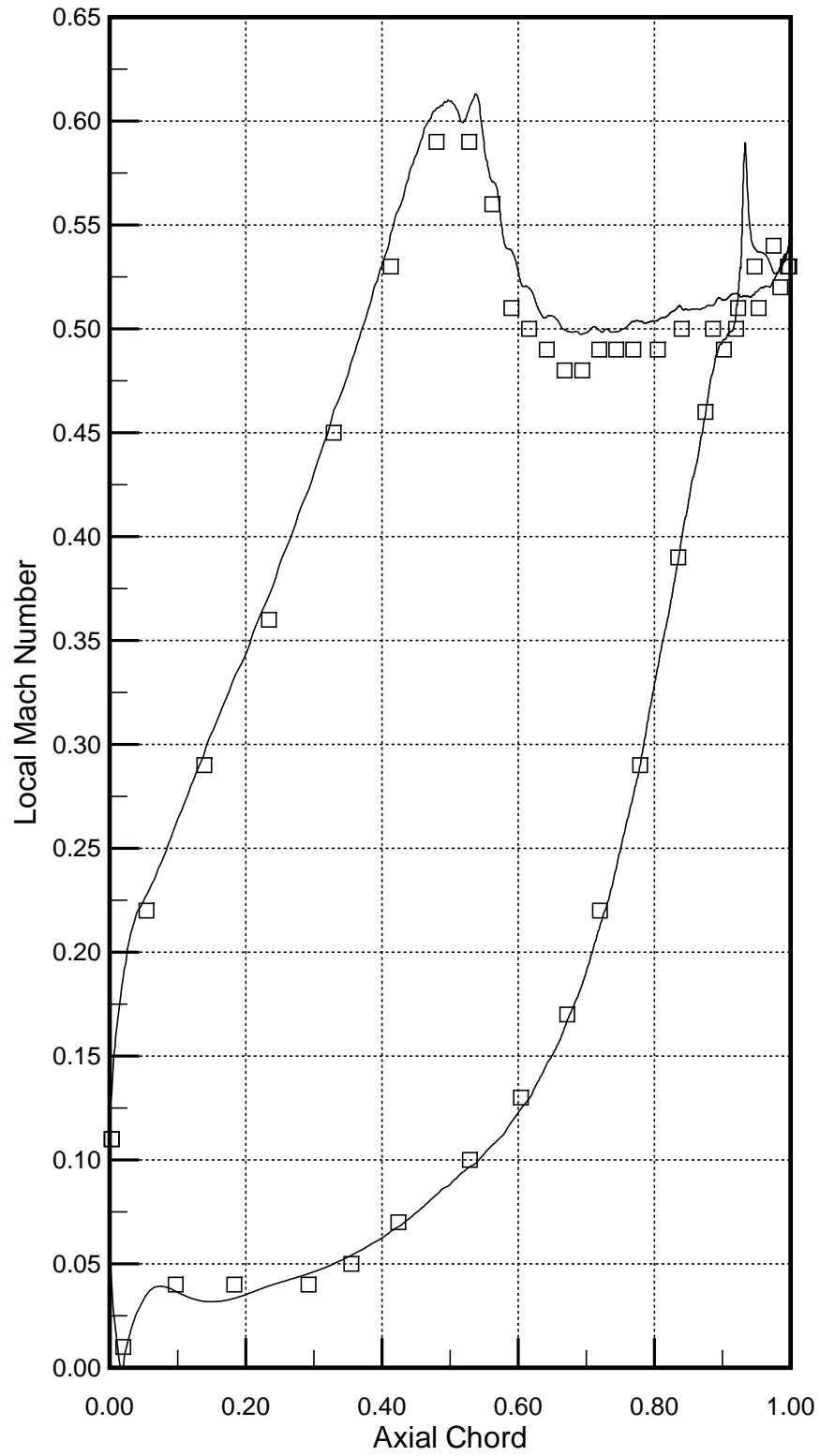


Figure D.4: Measured and predicted surface Mach number at $Ma = 0.5$

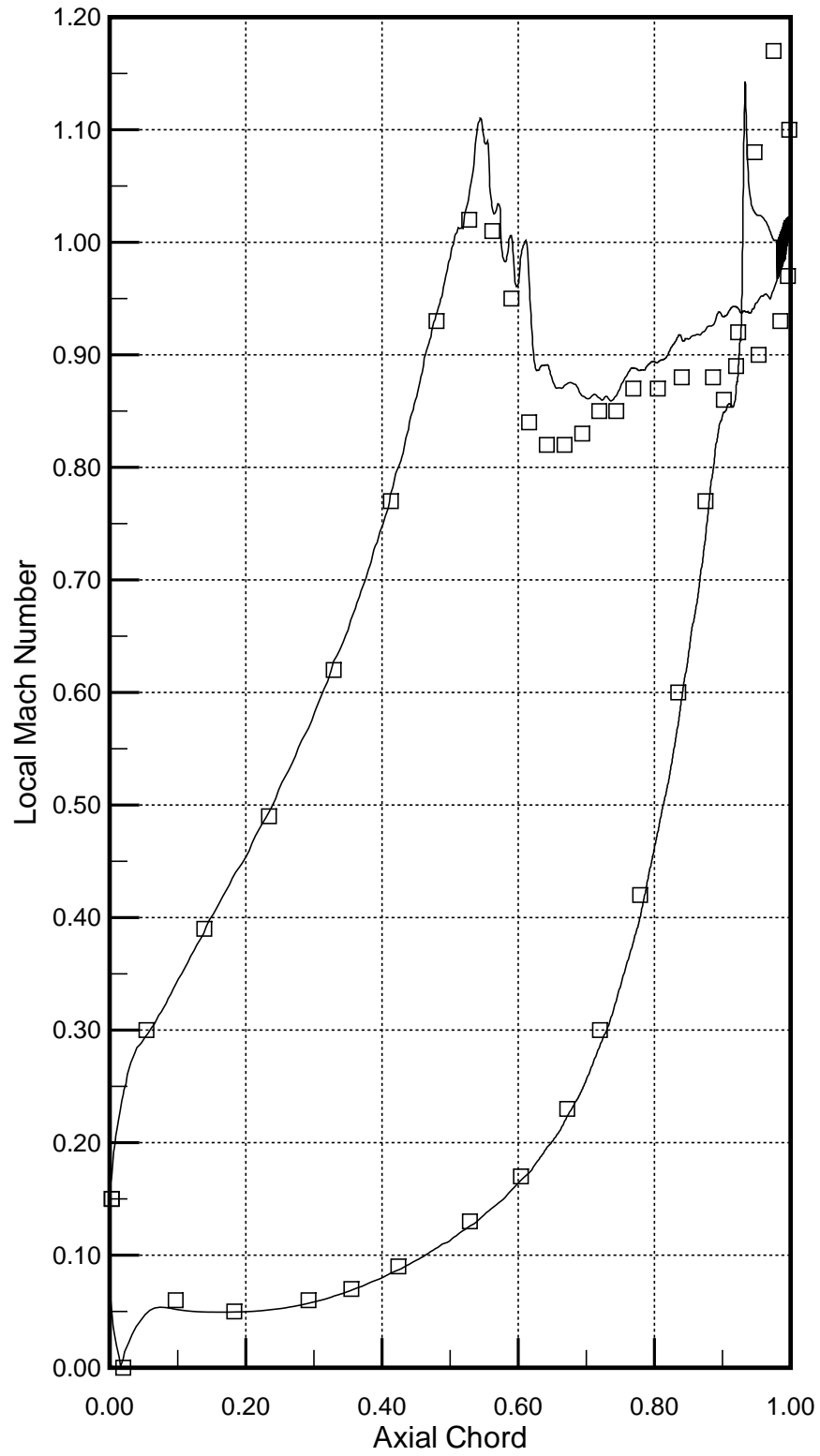


Figure D.5: Measured and predicted surface Mach number at $Ma = 0.9$

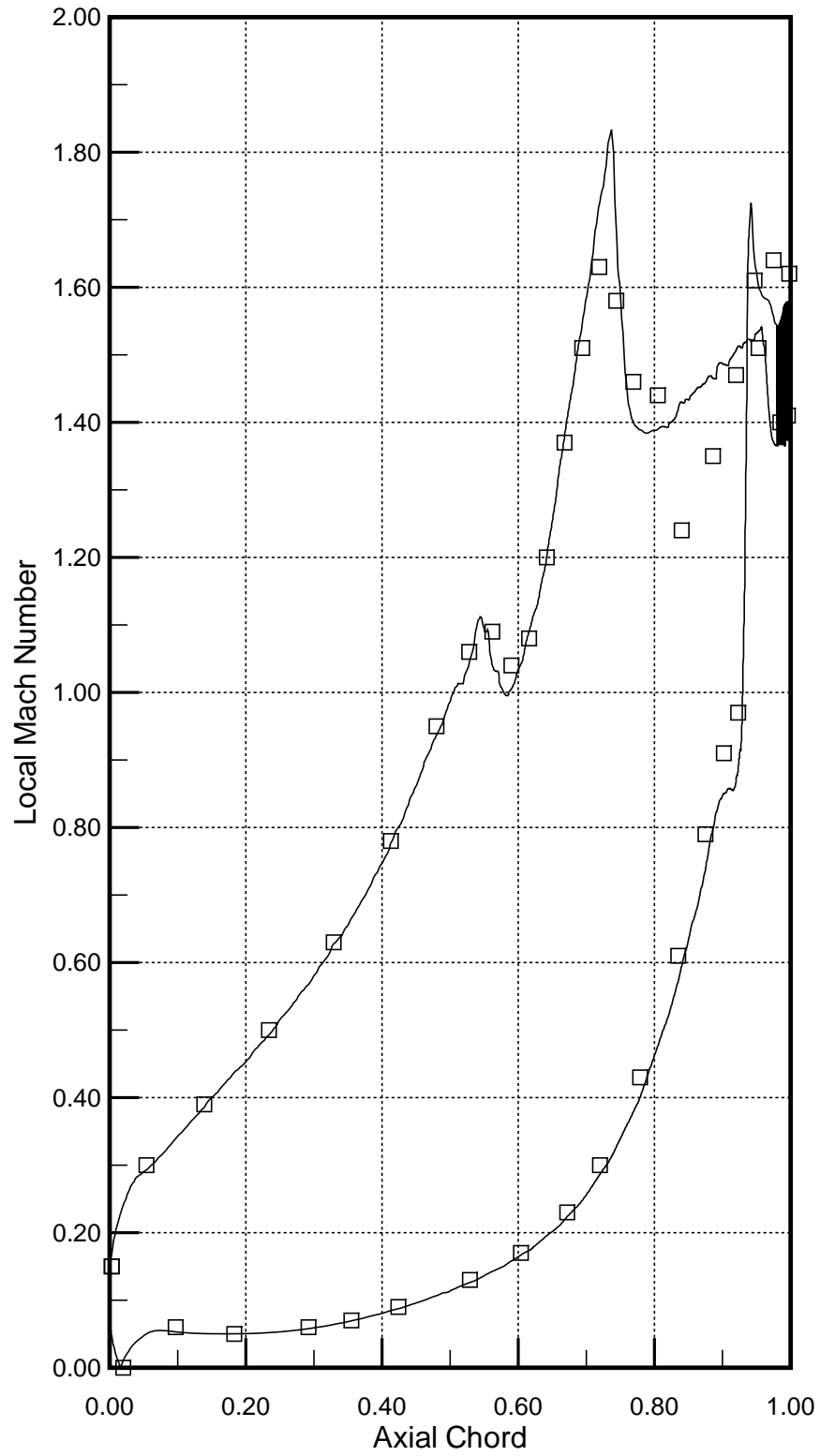
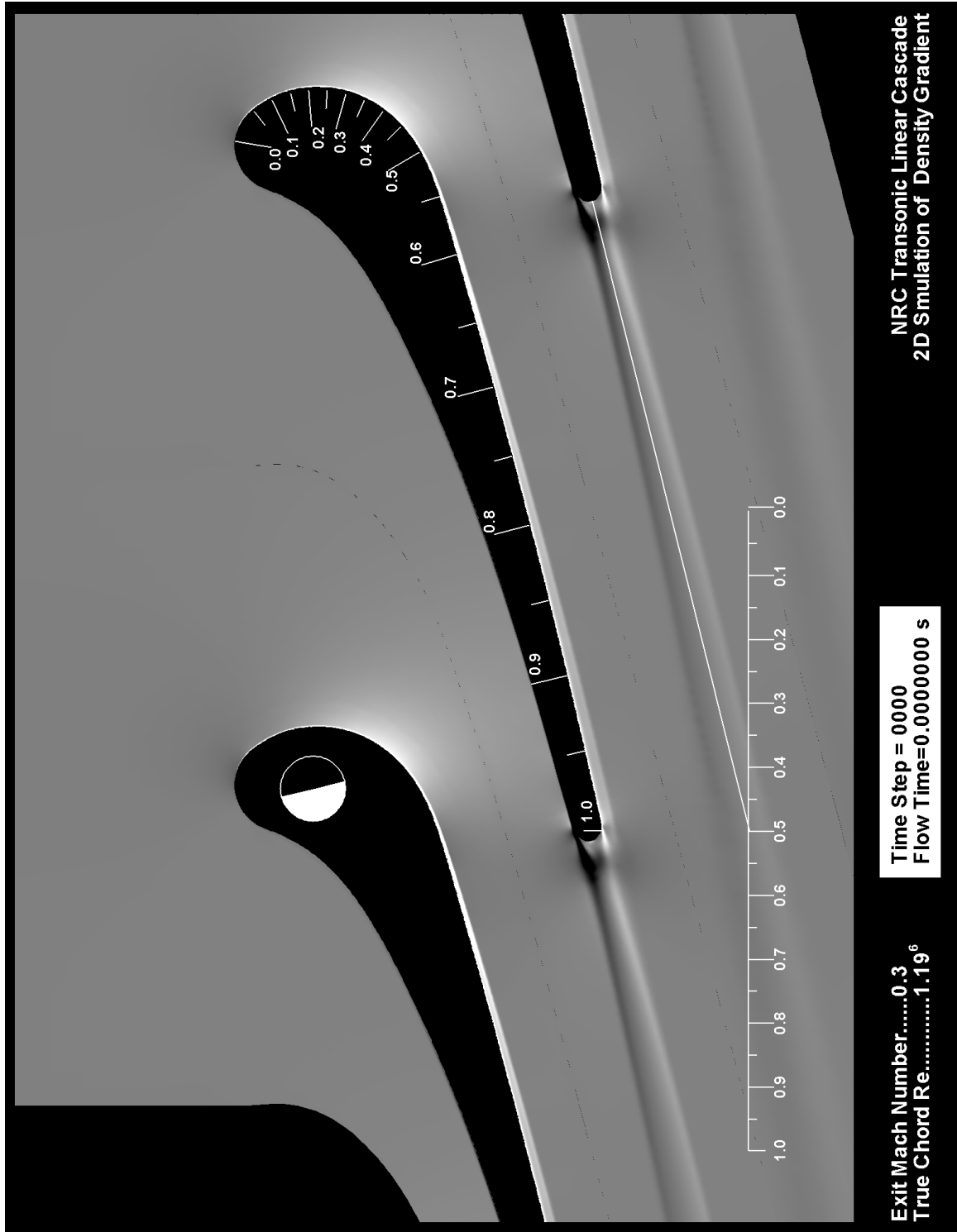


Figure D.6: Measured and predicted surface Mach number at $Ma = 1.4$

D.3 Computed Passage Flow Visualization

Figure D.7: Computed steady passage flow field at $Ma = 0.3$

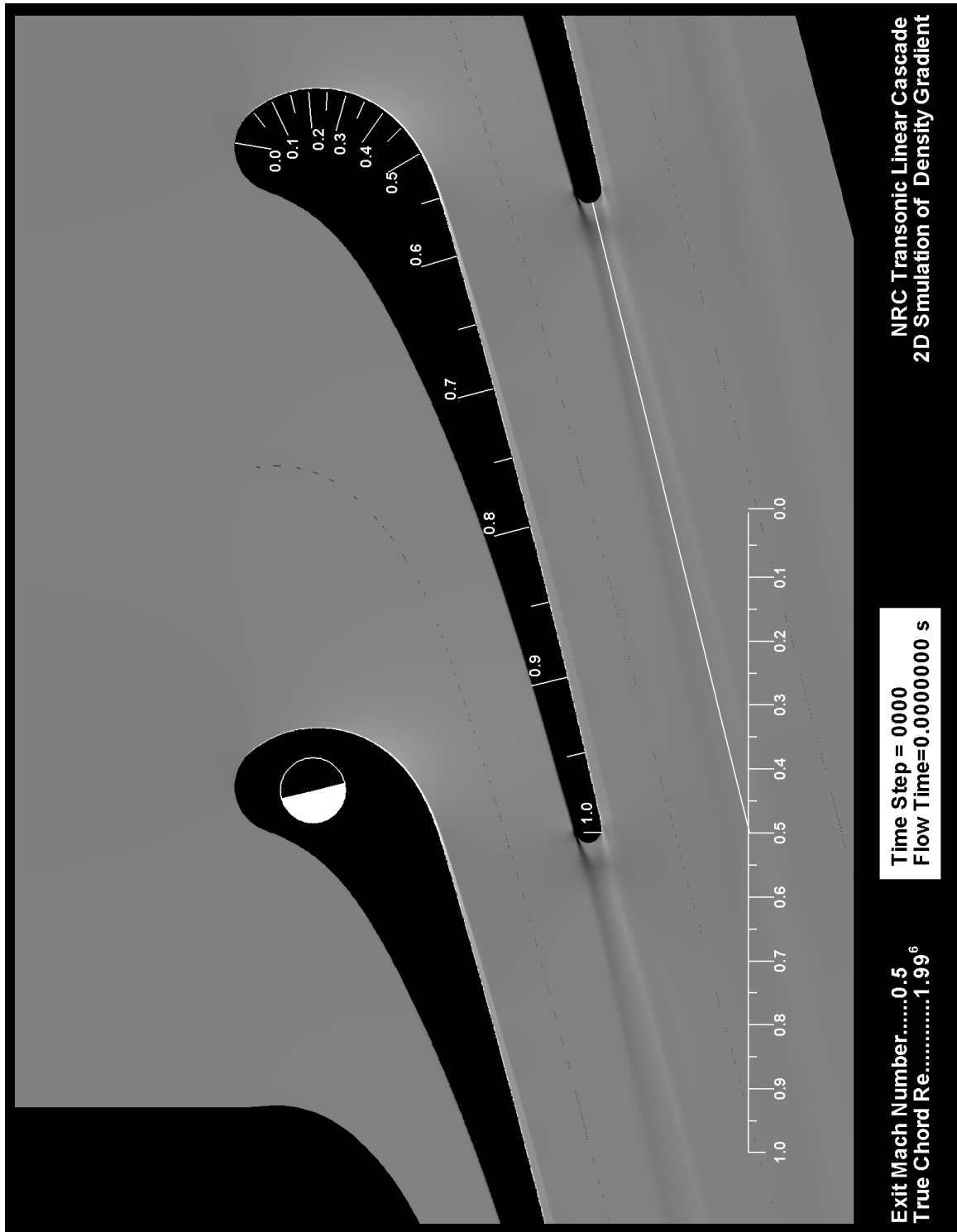


Figure D.8: Computed steady passage flow field at $Ma = 0.5$

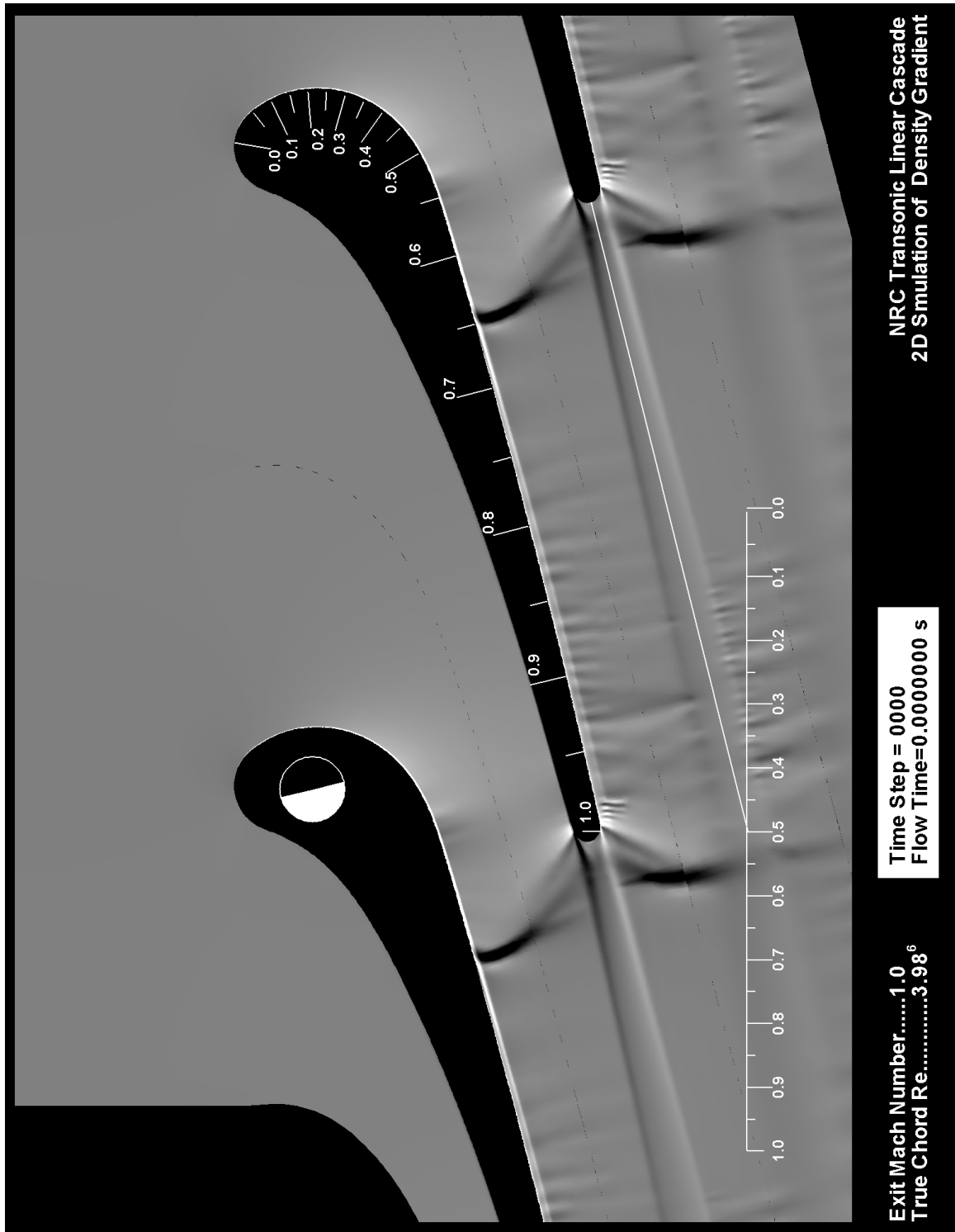


Figure D.10: Computed steady passage flow field at $Ma = 1.00$

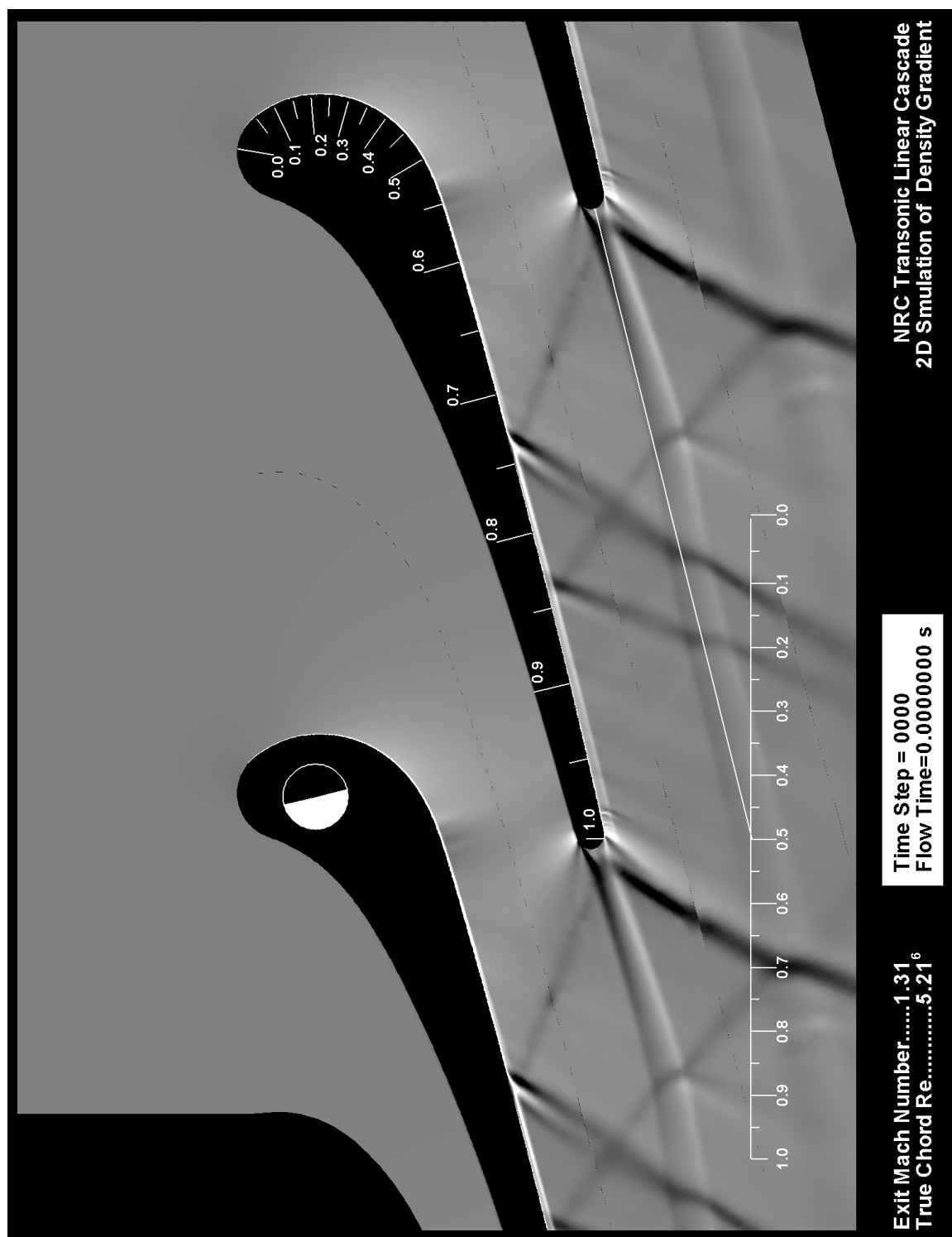


Figure D.11: Computed steady passage flow field at $Ma = 1.31$

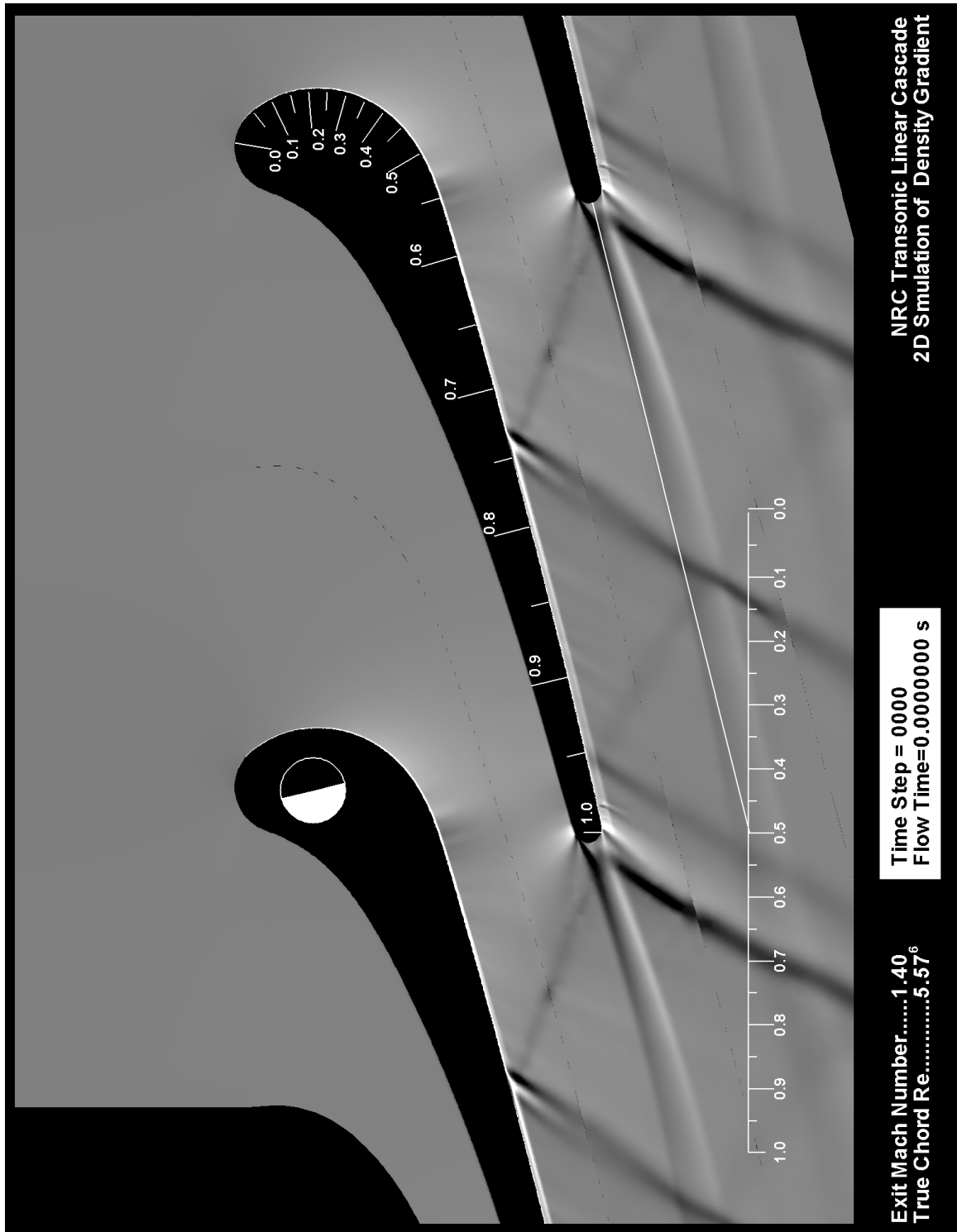


Figure D.12: Computed steady passage flow field at $Ma = 1.4$

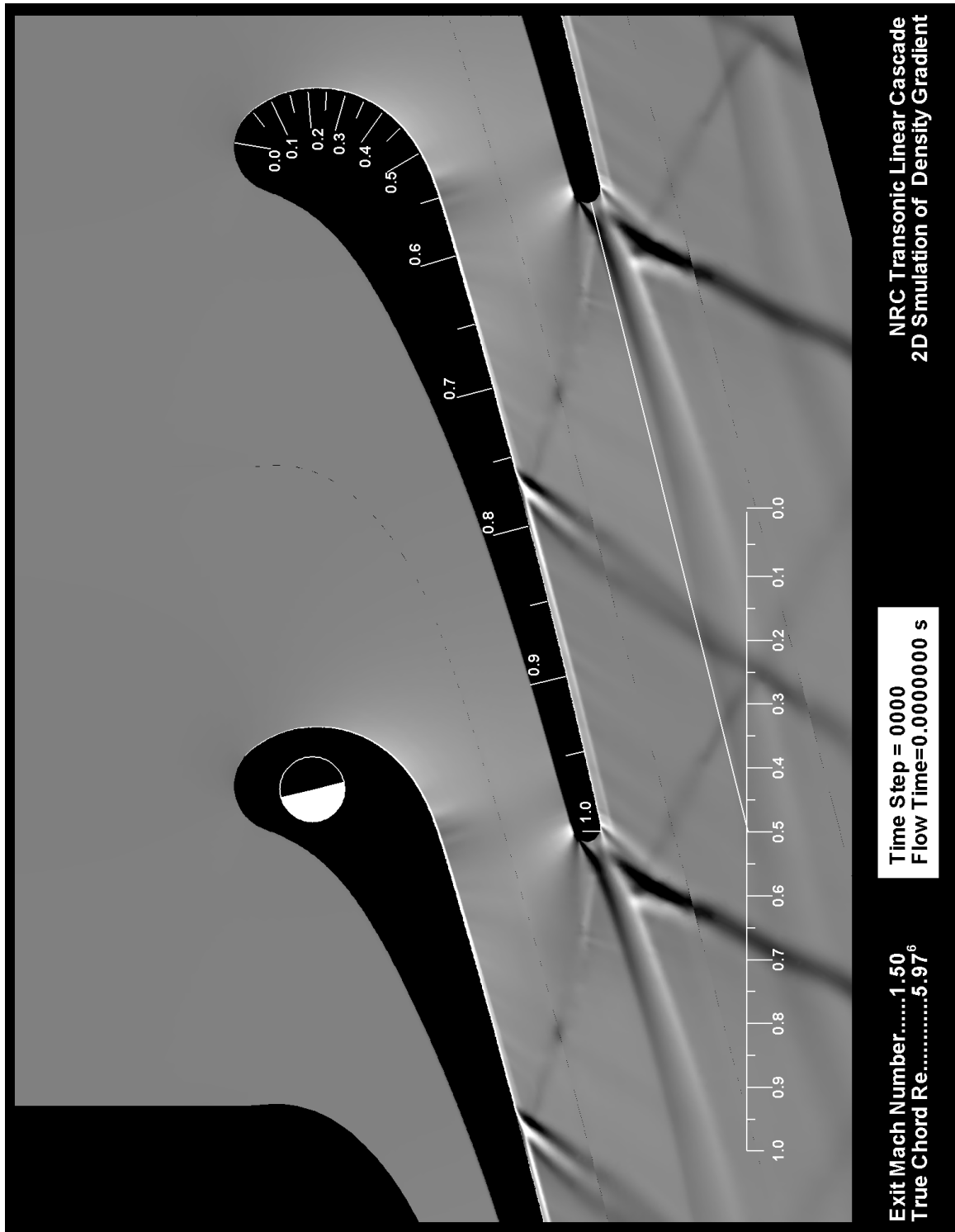


Figure D.13: Computed steady passage flow field at $Ma = 1.5$

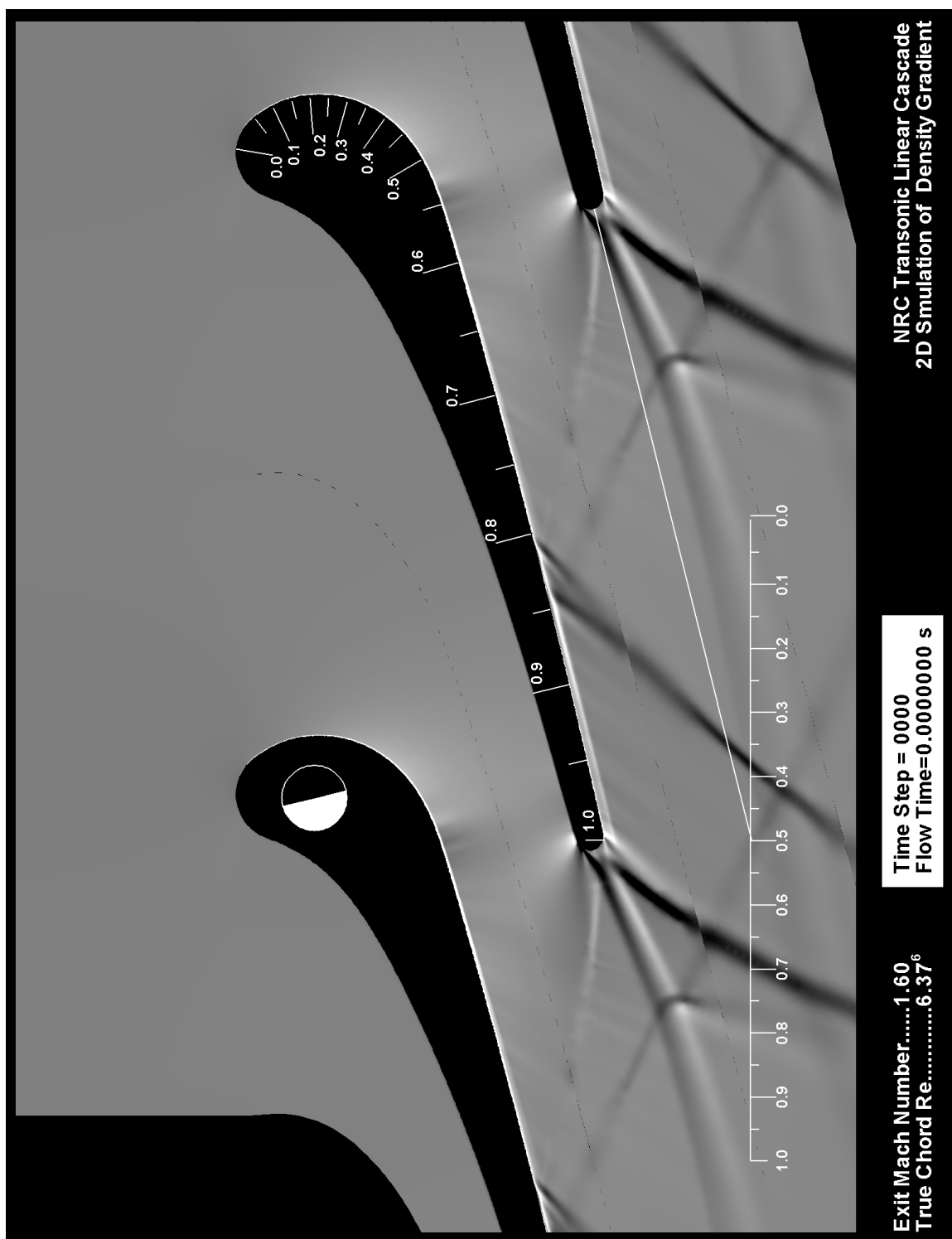


Figure D.14: Computed steady passage flow field at $Ma = 1.6$

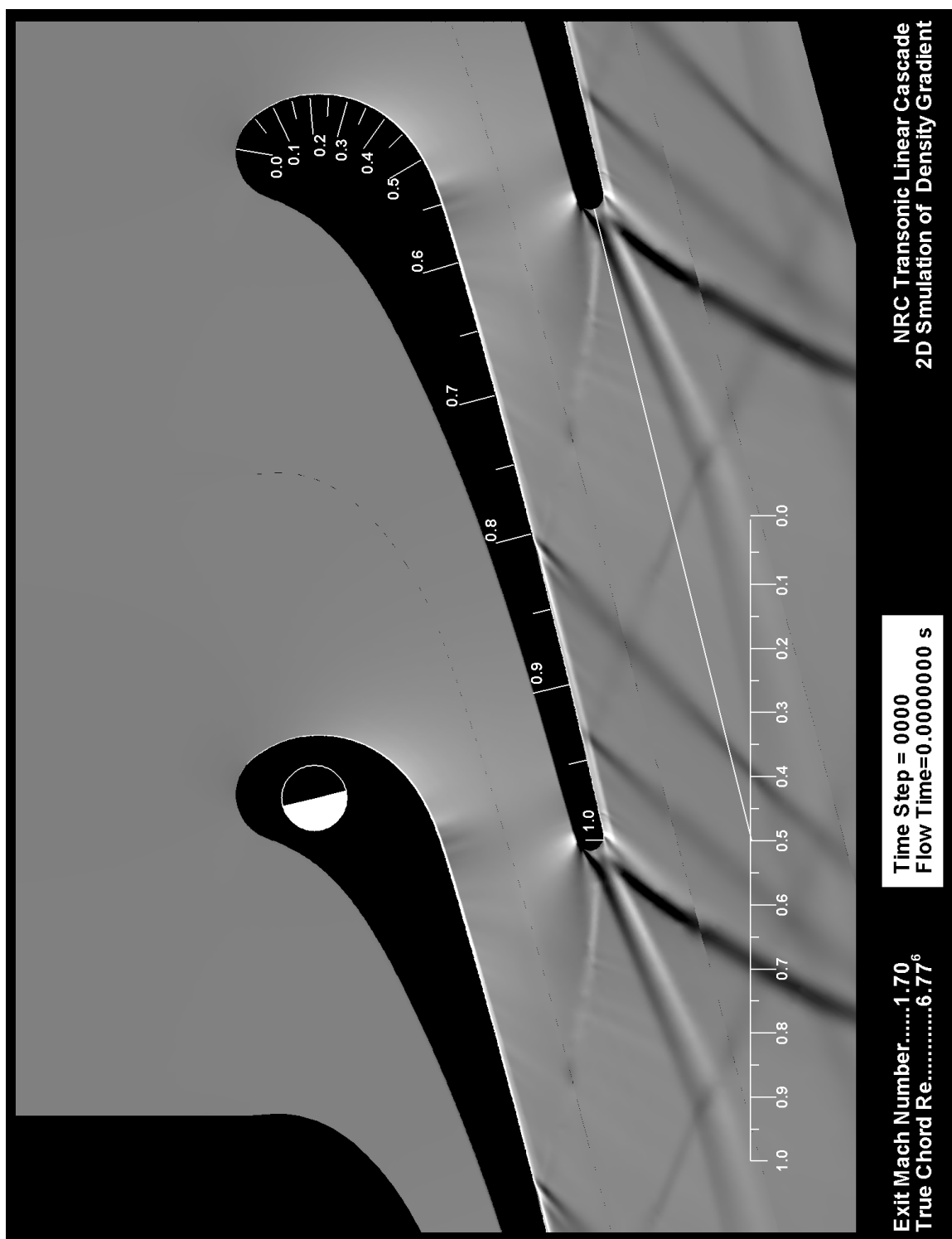


Figure D.15: Computed steady passage flow field at $Ma = 1.7$

Appendix E

MatLab Data Reduction Code

E.1 Mixed out Profile Loss

```
1 function [M_m, Yt, alpha_m]=mixedOutLoss(x_nd, Po, Po_c, Ps_c, alpha_c, useAlpha)
2   %CONSTANTS
3   pitch=147.8; %[mm]
4   gamma=1.4;
5
6   Po_i=mean(Po);
7
8   %Decides if the measured values of alpha should be used. if not selected
9   %a nominal value of 14 deg (the blade metal angle) is substituted
10  if useAlpha>0
11    alpha_k=alpha_c+14;
12  else
13    alpha_k=14*ones(length(Po_c),1);
14  end
15
16  %Caluclates the differnetial dimensionless flow properties
17  theta_e=sqrt(2/(gamma-1)*((gamma+1)/2)^((gamma+1)/(gamma-1)))*
18    ... (Ps_c./Po_c).^ (1/gamma) .*sqrt(1-(Ps_c./Po_c).^((gamma-1)/gamma));
19  q=Po_c.*gamma/(gamma-1) .* (Ps_c./Po_c).^ (1/gamma) .*
20    ... (1-(Ps_c./Po_c).^((gamma-1)/gamma));
21
22  %Calcualtes the differentials
23  int_m=(Po_c./Po_i) .*theta_e.*sind(alpha_k);
24  int_A=(Po_c./Po_i) .* (2*q./Po_c.*(sind(alpha_k)).^2+Ps_c./Po_c);
25  int_C=(Po_c./Po_i) .*2.*q./Po_c.*sind(alpha_k) .*cosd(alpha_k);
26
27  %Integrates using the trapezoid rule
28  Im=trapz(x_nd,int_m);
29  IA=trapz(x_nd,int_A);
30  IC=trapz(x_nd,int_C);
31  Imb=Im;
32
33  %Calcualtes the 'critical mach number'
34  Mhi= ((gamma+1)/2)^(2/(gamma-1))*(IA/Imb)^2*(0.5-(2/(gamma+1))^
35    ... (2/(gamma-1))*(Imb/IA)^2+(gamma+1)/(2*gamma)*(IC/IA)^2+
36    ...sqrt(0.25-(2/(gamma+1))^ (2/(gamma-1))*(Imb/IA)^2+(gamma^2-1)/
37    ... (4*gamma^2)*(IC/IA)^2));
38  Mlow= ((gamma+1)/2)^(2/(gamma-1))*(IA/Imb)^2*(0.5-(2/(gamma+1))^
39    ... (2/(gamma-1))*(Imb/IA)^2+(gamma+1)/(2*gamma)*(IC/IA)^2-
40    ...sqrt(0.25-(2/(gamma+1))^ (2/(gamma-1))*(Imb/IA)^2+(gamma^2-1)/
41    ... (4*gamma^2)*(IC/IA)^2));
42
```

```

43     Mhi=sqrt(Mhi);
44     Mlow=sqrt(Mlow);
45
46     %In most cases the lower mach number is more physically meaningfull,
47     %however in some cases the high mach number may need to be used. refer
48     %to Ameke and Safarik
49     M_m=Mlow;
50
51     %Calculates the mixed out properties
52     M_true_m=M_m*sqrt(2/((gamma+1)-(gamma-1)*M_m^2));
53     alpha_m=acosd(1/(gamma*M_m)*((gamma+1)/2)^(gamma/(gamma-1))*(IC/Imb));
54     phi=(1-(gamma-1)/(gamma+1)*M_m^2)^(1/(gamma-1))*(1-(gamma-1)/(gamma+1)
55         ...*M_m^2);
56     theta_m=(1-(gamma-1)/(gamma+1)*M_m^2)^(1/(gamma-1))*((gamma+1)/2
57         ...^(1/(gamma-1))*M_m;
58     %zeta is the loss term used by Ameke and Safarik, however Yt is more
59     %often used in literature. Stephen Andrews derived the conversion
60     %equation (phi=Po_m/Ps_m)
61     zeta=1-abs(Imb)/(theta_m*sind(alpha_m));
62 %Definition 1
63     Yt=(zeta)/((1-zeta)*(1-phi));
64 %Definition 2
65     %Yt=(zeta)/(1-(1-zeta)*phi);
66 end

```

E.2 Mass Averaged Loss

```

1 function [M_ma, Yt_ma, alpha_ma]=massAveragedLoss(x,Po,To,Po_c,Ps_c,Ma_c
2     ...,alpha_c,useAlpha)
3     %CONSTANTS
4     gamma=1.4;
5     R=287;
6     %Decides if the measured values of alpha should be used. if not selected
7     %a nominal value of 14 deg (the blade metal angle) is substituted
8     if useAlpha>0
9         alpha_k=alpha_c+14;
10    else
11        alpha_k=14;
12    end
13
14    %The differential mass flow
15    d_m_dot=Po_c./sqrt(To).*sqrt(gamma/R).*Ma_c.*sind(alpha_k).*
16        ... (1+0.5*(gamma-1)*Ma_c.^2).^((1+gamma)/(2-2*gamma));
17    %Total mass flow
18    m_dot=trapz(x,d_m_dot);
19    %Mass averaged flow properties
20    M_ma=trapz(x,Ma_c.*d_m_dot)/m_dot;
21    Po_ma=trapz(x(:,1),d_m_dot.*Po_c)/m_dot;
22    Ps_ma=trapz(x(:,1),d_m_dot.*Ps_c)/m_dot;
23    alpha_ma=trapz(x(:,1),d_m_dot.*alpha_k)/m_dot;
24

```

```

25 %   Definition 1
26   Yt_ma=(mean(Po)-Po_ma)/(Po_ma-Ps_ma);
27 %   Definition 2
28 %   Yt_ma=(mean(Po)-Po_ma)/(mean(Po)-Ps_ma);
29
30 end

```

E.3 Finger Probe Analysis

```

1 function [Po,Ps,U,alpha,Ma]=reduceFingerProbe(P_U,P_c,P_D,P_st,To,gamma)
2 %%%%%%%%%%%%%%%%%%%%%%%%%%%%%%%%%%%%%%%%%%%%%%%%%%%%%%%%%%%%%%%%%%%%%%%%%
3 %%%%%%%%%%%%%%%%%%%%%%%%%%%%%%%%%%%%%%%%%%%%%%%%%%%%%%%%%%%%%%%%%%%%%%%%%
4 %           ::Finger Probe Data Reduction::
5 %           verison 1.0 (24-Sept-2008)
6 %           Programmed by: Stephen Andrews
7 %
8 %:::Use:::
9 %   Calcualtes the follwing flow variables given the measured values of
10 %   P_U,P_c,P_D,P_st,To and gamma (see Nomenclature below)
11 %   *Total Pressure (Po)
12 %   *Static Pressure (Ps)
13 %   *Magnitude of Flow Velocity (U)
14 %   *Flow Direction (alpha)
15 %   *Local Mach Number (Ma)
16 %
17 %:::Algorythim:::
18 %   Reads the file coeffs.mat which is a table of 7 different pressure
19 %   correlations sorted so rows show ascending Mach numbers, columns
20 %   ascending probe angles and frames show each presure corelation
21 %   (see Note below)
22 %   1) The program first determines the corect flow angle and Mach
23 %   number by guessing a flow angle of zero and calculating the
24 %   Mach number. Using this first guess at a Mach number, the
25 %   program then re-calculates the flow angle and using this new
26 %   flow angle again calculaes the Mach number. The program
27 %   examines the difference between the two guesses of Mach number
28 %   and once the error is less than some global tolerance, the
29 %   program takes that Ma/alpha combination as being the best
30 %   approximation to the true Ma/alpha locust
31 %   2) Knowing the flow angle and mach number, the program can then
32 %   calucalte the pressure correlation K23 which
33 %   yeilds the dynamic pressure (q=(Po-Ps))
34 %   3) Knowing the flow angle angle and mach number, the program can
35 %   then calculate the coefficent K1 and find the true static
36 %   pressure (Ps)
37 %   4) Knowing the static pressure and q, the total pressure (Po) can
38 %   be calculated
39 %   5) Assuming adiabatic flow in the cascade, the local flow velocity
40 %   can be calculated by the total-to-static-pressure ratio
41
42 %:::Major Assumptions:::

```



```

43 %      1) Linear behaviour of pressure coefficients between calibration
44 %         points
45 %      2) Calibration encompasses entire range of mach numbers and angles
46 %      4) Flow is adiabatic (i.e. local  $T_o=T_{atm}$ )
47 %
48 %:::Note:::
49 %      FORMATTING OF THE COEFF.MAT FILE
50 %      coeffMtx(1, :, :)=[NAN, alpha(:)]
51 %      'alpha' is a list of calibration angles in ascending order.
52 %      coeffMtx(:, 1, :)= [NAN;Ma(:)]
53 %      'Ma' is a list of tunnel mach numbers in ascending order.
54 %      coeffMtx(2:end, 2:end, 1)
55 %           $K1=(P_c-P_s)/(P_o-P_s)$ 
56 %      coeffMtx(2:end, 2:end, 2)
57 %           $K12=(P_c-P_U)/(P_o-P_s)$ ;
58 %      coeffMtx(2:end, 2:end, 3)
59 %           $K13=(P_c-P_D)/(P_o-P_s)$ ;
60 %      coeffMtx(2:end, 2:end, 4)
61 %           $K23=(P_U-P_D)/(P_o-P_s)$ ;
62 %      coeffMtx(2:end, 2:end, 5)
63 %           $K_{phi\_2}=K12/K13$ ;
64 %      coeffMtx(2:end, 2:end, 6)
65 %           $K_{phi\_3}=1/K_{phi\_2}$ ;
66 %      coeffMtx(2:end, 2:end, 7)
67 %           $K_m=P_{st}/P_c$ 
68 %
69 %:::Nomenclature:::
70 %       $P_o$ =True total pressure
71 %       $P_s$ =True static pressure
72 %       $P_c$ =Measured total pressure
73 %       $P_U$ =Measured upper pressure
74 %       $P_D$ =Measured lower pressure
75 %       $P_{st}$ =Measured static pressure
76 %       $Ma_{meas}$ =Mach number corresponding to stinger static, to probe
77 %      total, pressure ratio.
78 %%%%%%%%%%%%%%%%%%%%%%%%%%%%%%%%%%%%%%%%%%%%%%%%%%%%%%%%%%%%%%%%%%%%%%%%%
79 %%%%%%%%%%%%%%%%%%%%%%%%%%%%%%%%%%%%%%%%%%%%%%%%%%%%%%%%%%%%%%%%%%%%%%%%%
80
81
82 %%%%%%%%%%%%%%%%%%%%%%%%%%%%%%%%%%%%%%%%%%%%%%%%%%%%%%%%%%%%%%%%%%%%%%%%%
83 %      MAIN FUNCTION
84 %%%%%%%%%%%%%%%%%%%%%%%%%%%%%%%%%%%%%%%%%%%%%%%%%%%%%%%%%%%%%%%%%%%%%%%%%
85 %:::Initialising of program controls:::
86 %Defines constants
87     R= 287;    %[J/kgK]    ONLY TRUE IF PURE AIR IS WORKING FLUID
88
89 %reads file created by Finger_Probe_v100.m
90 %current directory must contain folder called 'cal' which has a
91 %coeff.mat file containing the output created by this procedure
92     coeffMtx=ones(6,12,7);
93     load 'cal/coeff.mat'
94
95 %Sets the tolerances for the iteration on Ma/alpha
96     tol=0.01;

```

```

97 %Guesses the difference (could be eliminated with a do..while loop)
98     diff=1;
99 %Guesses the first angle, by default is zero
100     alpha_guess=0;
101
102 %Calculates K values
103     Ktheta1=(P_c-P_U)/(P_c-P_D);
104     Ktheta2=1/Ktheta1;
105     Km=P_st/P_c;
106
107 %Iterates the guessed flow angle and Mach until solution converges
108 %within tolerance
109     iter=0;
110     while(diff>tol)
111         Ma_guess=findMach(alpha_guess,Km, coeffMtx);
112         alpha_guess=findAlpha(Ma_guess,Ktheta1,Ktheta2,coeffMtx);
113         diff=Ma_guess-findMach(alpha_guess,Km,coeffMtx);
114         iter=iter+1;
115     end
116
117     Ma=Ma_guess;
118     alpha=alpha_guess;
119
120 %Uses Ma and alpha to compute flow variables
121     K23=findK(alpha, Ma, 4, coeffMtx);
122     q=(P_U-P_D)/K23 ;
123     K1=findK(alpha, Ma, 1, coeffMtx);
124     Ps=P_c-K1*q;
125     Po=q+Ps;
126     a=sqrt(gamma*R*To*(Ps/Po)^(-1*(gamma-1)/gamma));
127     Ma=sqrt((2/(gamma-1))*((Po/Ps)^((gamma-1)/gamma)-1));
128     U=Ma*a;
129 end
130 %%%%%%%%%%%%%%%%%%%%%%%%%%%%%%%%%%%%%%%%%%%%%%%%%%%%%%%%%%%%%%%%%%%%%%%%%
131
132     %%%%%%%%%%%%%%%%%%%%%%%%%%%%%%%%%%%%%%%%%%%%%%%%%%%%%%%%%%%%%%%%%%%%%%%%%
133     % LOCAL FUNCTIONS
134     %%%%%%%%%%%%%%%%%%%%%%%%%%%%%%%%%%%%%%%%%%%%%%%%%%%%%%%%%%%%%%%%%%%%%%%%%
135
136 %%%%%%%%%%%%%%%%%%%%%%%%%%%%%%%%%%%%%%%%%%%%%%%%%%%%%%%%%%%%%%%%%%%%%%%%%
137 % ::findMach::
138 % "returns a mach number given a Km value and angle"
139 %*Linearly interpolates between adjacent calibration points to get Ma
140 %*will deal with being at the final calibration angle
141 %*will extrapolate outside the bounds of calibration without warning
142
143 function [M]=findMach(alpha,Km,coeffMtx)
144     alphaHiIdx=find(coeffMtx(1,2:end,1)>=alpha,1,'first')+1;
145     %Note the '+1' was necessary as search was from 2:end
146     if isempty(alphaHiIdx)
147         %If alpha is outside the bounds of the calibration range, then
148         %alpha index is set to the extrem to which alpha is closest
149         if alpha>0
150             alphaHiIdx=length(coeffMtx(1,:,1));

```



```

205 %                                     ::findAlpha::
206 %                                     "returns a flow angle given a Mach Number and both Ktheta"
207 %*Searches for the angle corresponding to the smaller Ktheta value
208 %   (smaller the Ktheta the smaller the error)
209 %*Linearly interpolates between adjacent calibration angles and mach
210 % numbers to get alpha
211 %*will deal with being at the final calibration Mach Number and angle
212 %*algorhythm very similar to findMach
213
214 function [A]=findAlpha(Ma,Ktheta1,Ktheta2,coeffMtx)
215     %Choses the correct Ktheta
216     if(Ktheta1>Ktheta2)
217         Ktheta=Ktheta2;
218         KIdx=6;
219     else
220         Ktheta=Ktheta1;
221         KIdx=5;
222     end
223
224     %Subtracts the target from the values to change problem to a zero
225     %search
226     searchMtx=[coeffMtx(1, :, 1); [coeffMtx(2:end, 1, 1),
227                                     ... (coeffMtx(2:end, 2:end, KIdx)-Ktheta)]];
228
229     %Finds the Mach numbers bounding the desired mach number
230     MaHiIdx=find(coeffMtx(2:end, 1, 1)≥Ma, 1, 'first')+1;
231     if isempty(MaHiIdx)
232         if Ma>1
233             MaHiIdx=length(coeffMtx(:, 1, 1));
234         else
235             MaHiIdx=3;
236         end
237     elseif MaHiIdx==2
238         MaHiIdx=3;
239     end
240     MaHi=searchMtx(MaHiIdx, 1);
241     MaLowIdx=MaHiIdx-1;
242     MaLow=searchMtx(MaLowIdx, 1);
243
244     %finds the non-integer index of the zero solution along a line of
245     %constant mach number
246     holdIdx=findInVect(searchMtx(MaLowIdx, 2:end))+1;
247     ALow=searchMtx(1, floor(holdIdx));
248     AHigh=searchMtx(1, ceil(holdIdx));
249
250     %calualates the angle coresponding to the measured Ktheta at the low
251     %mach number
252     if(AHigh==ALow)
253         AMaLow=AHigh;
254     else
255         AMaLow=ALow+(holdIdx-floor(holdIdx))*(AHigh-ALow)/
256                                     ... (ceil(holdIdx)-floor(holdIdx));
257     end
258     %repeats last two steps for the high mach number

```


Appendix F

Coordinates

$$X_{nd} = \frac{X_i - X_{LE}}{C_x} \quad (\text{F.1})$$

$$Y_{nd} = \frac{Y_i - Y_{LE}}{s} \quad (\text{F.2})$$

F.1 Blade Geometry

Table F.1: Blade coordinates

Suction surface		Pressure surface	
$X_{nd}[-]$	$Y_{nd}[-]$	$X_{nd}[-]$	$Y_{nd}[-]$
0.0102	0.0007	-1.8795	-0.5546
0.0225	0.0009	-1.8789	-0.5496
0.0355	0.0004	-1.8762	-0.5442
0.0478	-0.0008	-1.8716	-0.5399
0.0599	-0.0028	-1.8649	-0.5364
0.0717	-0.0055	-1.8555	-0.5330
0.0832	-0.0090	-1.8448	-0.5308
0.0937	-0.0130	-1.8311	-0.5288
0.1038	-0.0176	-1.8158	-0.5265
0.1126	-0.0226	-1.8010	-0.5243
0.1214	-0.0285	-1.7858	-0.5218
0.1294	-0.0346	-1.7713	-0.5194
0.1373	-0.0414	-1.7568	-0.5169
0.1444	-0.0482	-1.7424	-0.5144
0.1510	-0.0553	-1.7279	-0.5119
0.1570	-0.0626	-1.7137	-0.5094
0.1623	-0.0699	-1.6993	-0.5070
0.1670	-0.0774	-1.6849	-0.5046
0.1708	-0.0849	-1.6706	-0.5023
0.1742	-0.0927	-1.6562	-0.5000
0.1769	-0.1007	-1.6417	-0.4977
0.1789	-0.1086	-1.6270	-0.4953
0.1802	-0.1167	-1.6126	-0.4929
0.1809	-0.1247	-1.5980	-0.4905
0.1809	-0.1327	-1.5834	-0.4881
0.1803	-0.1408	-1.5383	-0.4805

Table F.1: (Continued)

Suction surface		Pressure surface	
$X_{nd}[-]$	$Y_{nd}[-]$	$X_{nd}[-]$	$Y_{nd}[-]$
0.1789	-0.1489	-1.4661	-0.4684
0.1770	-0.1569	-1.3942	-0.4558
0.1743	-0.1649	-1.3223	-0.4432
0.1711	-0.1727	-1.2506	-0.4300
0.1672	-0.1804	-1.1789	-0.4167
0.1626	-0.1881	-1.1078	-0.4029
0.1575	-0.1956	-1.0365	-0.3887
0.1518	-0.2029	-0.9656	-0.3740
0.1456	-0.2101	-0.8952	-0.3587
0.1387	-0.2171	-0.8249	-0.3428
0.1313	-0.2240	-0.7550	-0.3263
0.1234	-0.2306	-0.6858	-0.3093
0.1150	-0.2372	-0.6170	-0.2915
0.1060	-0.2434	-0.5692	-0.2786
0.0968	-0.2494	-0.5009	-0.2596
0.0869	-0.2552	-0.4335	-0.2394
0.0766	-0.2608	-0.3675	-0.2178
0.0659	-0.2661	-0.3029	-0.1940
0.0549	-0.2712	-0.2415	-0.1669
0.0433	-0.2761	-0.1857	-0.1351
0.0315	-0.2808	-0.1395	-0.0981
0.0195	-0.2852	-0.1220	-0.0794
0.0070	-0.2894	-0.1153	-0.0711
-0.0055	-0.2933	-0.1091	-0.0627
-0.0188	-0.2972	-0.1035	-0.0544
-0.0317	-0.3008	-0.0984	-0.0466
-0.0450	-0.3042	-0.0928	-0.0393
-0.0584	-0.3075	-0.0867	-0.0331
-0.0720	-0.3105	-0.0795	-0.0273
-0.0820	-0.3126	-0.0712	-0.0217
-0.1517	-0.3258	-0.0614	-0.0164
-0.2235	-0.3380	-0.0517	-0.0120
-0.2954	-0.3498	-0.0410	-0.0082
-0.3678	-0.3615	-0.0295	-0.0050
-0.4399	-0.3733	-0.0174	-0.0024
-0.5123	-0.3847	-0.0050	-0.0006
-0.5848	-0.3962		
-0.6571	-0.4075		
-0.7299	-0.4186		
-0.8028	-0.4297		
-0.8754	-0.4407		

Table F.1: (Continued)

Suction surface		Pressure surface	
$X_{nd}[-]$	$Y_{nd}[-]$	$X_{nd}[-]$	$Y_{nd}[-]$
-0.9484	-0.4514		
-1.0214	-0.4621		
-1.0944	-0.4729		
-1.1674	-0.4833		
-1.2407	-0.4936		
-1.3140	-0.5039		
-1.3872	-0.5141		
-1.4605	-0.5241		
-1.5339	-0.5339		
-1.5570	-0.5369		
-1.5722	-0.5390		
-1.5871	-0.5410		
-1.6023	-0.5430		
-1.6172	-0.5450		
-1.6323	-0.5470		
-1.6472	-0.5490		
-1.6622	-0.5509		
-1.6773	-0.5528		
-1.6924	-0.5548		
-1.7073	-0.5568		
-1.7224	-0.5588		
-1.7374	-0.5607		
-1.7523	-0.5627		
-1.7673	-0.5646		
-1.7825	-0.5666		
-1.7975	-0.5686		
-1.8123	-0.5705		
-1.8268	-0.5723		
-1.8386	-0.5733		
-1.8480	-0.5729		
-1.8574	-0.5712		
-1.8657	-0.5684		
-1.8723	-0.5647		
-1.8769	-0.5604		

F.2 Static Pressure Taps

Table F.2: Blade surface pressure tap locations

(a) Suction Surface		(b) Pressure Surface	
X_{nd}	Y_{nd}	X_{nd}	Y_{nd}
0.0025	-0.0141	0.9736	0.0867
0.0542	-0.0593	0.9219	0.0583
0.1393	-0.0846	0.9010	0.0157
0.2342	-0.0920	0.8738	-0.0373
0.3284	-0.0818	0.8339	-0.1170
0.4125	-0.0553	0.7781	-0.2227
0.4794	-0.0158	0.7189	-0.3279
0.5274	0.0320	0.6716	-0.4062
0.5611	0.0837	0.6033	-0.5096
0.5888	0.1367	0.5283	-0.6114
0.6154	0.1898	0.4231	-0.7356
0.6416	0.2430	0.3546	-0.8022
0.6675	0.2962	0.2914	-0.8509
0.6931	0.3495	0.1828	-0.9051
0.7182	0.4028	0.0964	-0.9293
0.7430	0.4562	0.0201	-0.9611
0.7677	0.5096	0.0025	-1.0141
0.8036	0.5899		
0.8391	0.6703		
0.8851	0.7776		
0.9186	0.8582		
0.9513	0.9389		
0.9835	1.0198		
0.9943	1.0470		
0.9970	1.0738		
0.9457	1.0844		

Curriculum Vitae

The author was born on September 16th 1984 in Bridgetown, Barbados. He completed his primary and secondary education in Guelph, Ontario, graduating from St. John's Kilmarnock School in 2003. He went on to study mechanical engineering at Queen's University in Kingston, Ontario. While at Queen's he was awarded the Dean's Scholarship in 2003, 2004, 2005 and 2006. He graduated from Queen's in 2007 with first class honours, achieving a cumulative average in the top tenth percentile of his year.

He then began his graduate studies at the Royal Military College of Canada, pursuing a degree of Master of Applied Science in Aeronautical Engineering. He performed initial research into heat transfer enhancement devices in the trailing edge of turbine blades. This work was presented at the 2008 ASME Turbo-Expo in Berlin, Germany and at the 2008 International Mechanical Engineering Congress and Exhibit in Boston, Massachusetts.

In the coursework portion of his degree, the author achieved a cumulative average of 85%. He then traveled to the National Research Council of Canada's Gas Turbine Laboratory, in Ottawa, Ontario, to perform the experimental portion of his degree. This research resulted in a further two publications, presented at the 2009 ASME Turbo-Expo in Orlando, Florida and at the 19th Conference of the International Society for Air Breathing Engines in Montréal, Québec.